ZIRCONIA-BASED ELECTROCERAMIC MATERIALS FOR SOFC APPLICATIONS

Alan John Feighery

A Thesis Submitted for the Degree of PhD
at the
University of St Andrews

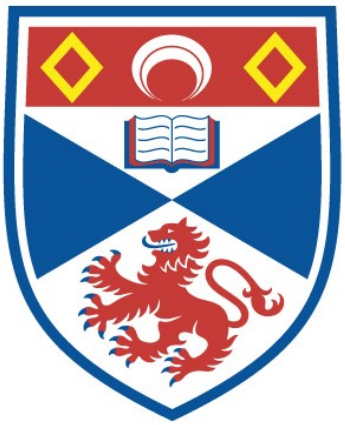

1999

University of St Andrews

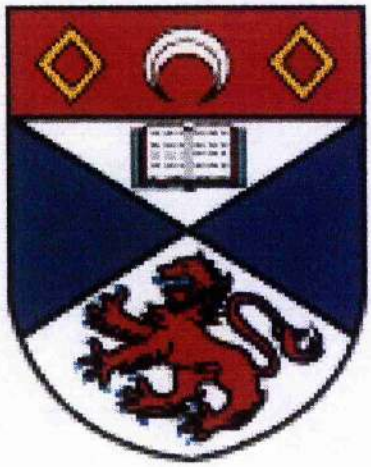

School of Chemistry

Zirconia-based Electroceramic Materials for SOFC Applications

Alan John Feighery

A thesis presented for the degree of
Doctor of Philosophy

DECLARATION

I, Alan J. Feighery, hereby certify that this thesis, which is approximately 50000 words in length, has been written by me, that it is the record of work carried out by me and that it has not been submitted in any previous application for a higher degree.

Date 26/10/98 Signature of Candidate

I was admitted as a research student in October 1995 and as a candidate for the degree of Doctor Philosophy in October 1996; the higher study for which this is a record was carried out in the University of St. Andrews between 1995 and 1998.

Date 26/10/98 Signature of Candidate

I hereby certify that the candidate has fulfilled the conditions of the Resolution and Regulations appropriate for the degree of Doctor of Philosophy in the University of St. Andrews and that the candidate is qualified to submit this thesis in application for that degree.

Date 26/10/98 Signature of Supervisor

In submitting this thesis to the University of St Andrews I understand that I am giving permission for it to be made available for use in accordance with the regulations of the University Library for the time being in force, subject to any copyright vested in the work not being affected thereby. I also understand that the title and abstract will be published, and that a copy of the work may be made and supplied to any bona fide library or research worker.

Date 26/10/98 Signature of Candidate

ACKNOWLEDGEMENTS

I would like to thank Dr John Irvine for his supervision, guidance and encouragement over the last three years. Thanks also to Dr Iain Gibson of Queen Mary and Westfield College for his advice and Professor Chaogui Zheng of the University of Beijing for his assistance with the phase diagram work.

I would like to thank Dr Ron Smith at ISIS for assistance in performing Neutron Diffraction experiments and Drs Andy Dent, Ian Harvey and Andy Smith at the Daresbury SRS for assistance with EXAFS experiments.

Many thanks to the technical support staff Brian Walker, Colin Smith, Jim Rennie and of course Bobby Cathcart for his unique brand of humour.

Thanks also to the EPSRC and Tioxide Specialities Ltd for funding.

And last but not least, all the various members of the group, who have often annoyed but mostly entertained me over the years. Particular thanks must go to Dr Peter Slater, Dr Andreas Kaiser and Dr Duncan Fagg for their advice, useful discussions and ability to talk about things other than chemistry in the pub. And of course Dr Brian Mitchell must be thanked for his constant barrage of politically incorrect, gross generalisations about all things that annoy him, which were highly entertaining.

ABSTRACT

The phase relations, electrical properties and structural characteristics of doped cubic stabilised Zirconia based electroceramic materials have been investigated using a number of characterisation techniques.

The phase relations of the ternary systems ZrO_2-Y_2O_3-TiO_2 and ZrO_2-Gd_2O_3-TiO_2 at 1500°C have been investigated. Electrical characterisation in air and in low oxygen partial pressures has been carried out using 2-probe A.C. Impedance Spectroscopy and 4-probe D.C. resistivity measurements to ascertain whether compositions within these systems could be utilised as the anode materials in Solid Oxide Fuel Cells. The effect of porosity on the ionic and electronic conducting properties of the ZrO_2-Y_2O_3-TiO_2 system has been investigated to provide a clearer understanding of the effect of the porosity within candidate anode materials.

The effect of Al_2O_3 additions on the electrical properties and stability of the Solid Oxide Fuel Cell material of choice, 8 mol% Yttria stabilised Zirconia, has been investigated. Al_2O_3 has been found to remain primarily as a second phase within the 8YSZ, however a small quantity of Al^{3+} does dissolve into the fluorite matrix. Al_2O_3 has been found to have a negligible effect on the high temperature ionic conductivity of 8YSZ and improves the resistance of 8YSZ to hydrothermal degradation by stabilising the cubic structure.

High temperature Time of Flight Neutron Diffraction has been used to link the change in activation energy observed in 8YSZ to a break down in local ordering of oxygen ions. Extended X-ray absorption Fine Structure Spectroscopy has been used to characterise the local structure of the cations in 8 mol% Yttria-stabilised Zirconia. Analysis of the high temperature data reveals that the local structure is quite different from the average crystallographic structure. The oxygen vacancies were determined to be associated with Zirconium ions and found to disorder at high temperatures.

CONTENTS

CHAPTER 1

Introduction

1.1. Fuel Cells

Fuel cells offer a means of electrochemical conversion of hydrogen or hydrocarbon fuels, (such as methane), to directly produce electricity. In theory electrochemical conversion processes offer a much higher efficiency for the generation of electricity than conventional methods.

1.1.1. Thermodynamics

The most common methods, to produce electricity are either by oil or gas fired processes, where the combustion of the fuel drives a turbine in which mechanical work is indirectly converted to electricity. These conventional processes are subject to the Carnot limitation. This is where the efficiency of an engine is given by the equation:-

$$\eta = \frac{T_1 - T_2}{T_1}$$

where η is the efficiency of the process, T_1 is the temperature of the combustion process and T_2 is the temperature of the heat sink. For the second law of thermodynamics to be obeyed $T_2 \neq 0$, therefore, energy must always be lost as heat in the surroundings for the process to be spontaneous.

Electrochemical combustion, however, is not confined by the Carnot limitation. This is because this process gives a direct method of energy conversion e.g. The thermodynamic data for the reaction of hydrogen and oxygen, at standard conditions are $\Delta H^\circ = -285$ kJmol^{-1} and $\Delta G^\circ = -237$ kJmol^{-1} [1,2]. Therefore in a fuel cell at constant pressure it would be theoretically possible to obtain 237kJ of electrical work, which is only slightly less than the heat evolved from combustion at constant pressure (-285kJ). This variation in energy is solely due to the loss in entropy on the formation of liquid water from gaseous hydrogen and oxygen. Theoretical efficiency of a H_2 based fuel cell would therefore be given by

$$\frac{-237 \text{ kJ}}{-285 \text{ kJ}} \times 100 = 80\%$$

In practice the amount of energy is around 70%. Figure 1.1 compares this result with the efficiencies which are obtainable from common energy production methods. Recent developments in combined cycle gas turbine design have boosted efficiency to 55-60% [3].

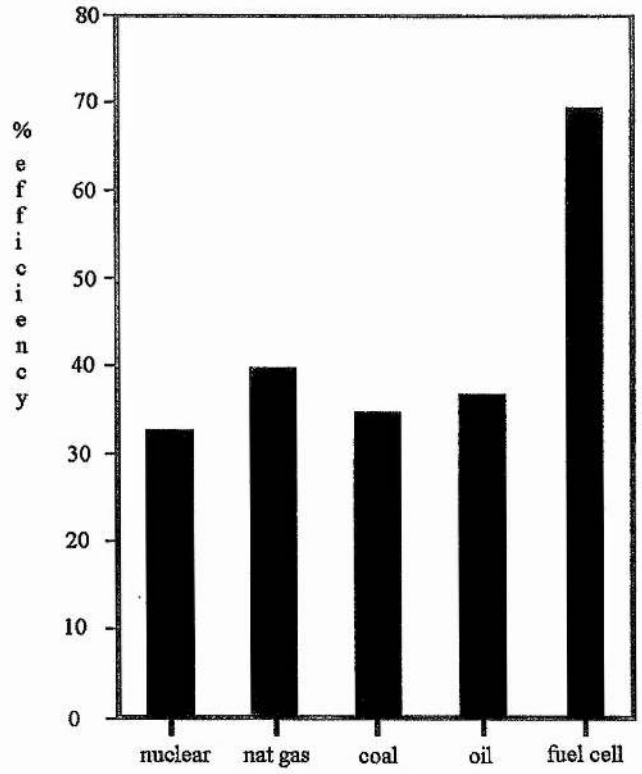

Figure 1.1. Comparison of the efficiencies obtainable from different energy production methods [4].

1.1.2. Fuel Cell Technology

Since the discovery of a simple hydrogen/oxygen fuel cell, which used sulphuric acid as the electrolyte, by Grove in 1839 [5], and the discovery of a solid-oxide electrolyte by Nernst in 1899 [6], a variety of devices have been produced. The many different types of fuel cell are differentiated by the nature of the electrolyte, which largely dictate the cell's operating temperature range. These are the Molten Carbonate Fuel Cell (MCFC), the Solid Polymer Fuel Cell (SPFC), the Phosphoric Acid Fuel Cell

(PAFC) and the Solid Oxide Fuel Cell (SOFC) [7]. For transportation, the proton exchange membrane fuel cell (PEMFC) has a clear advantage because it has a low operating temperature (60-90°C) allowing rapid start-up and its high power density lends itself to the stringent space and weight requirements required for the automotive market. For stationary applications, where the efficiency of power generation is most important, both low and high temperature fuel cells compare favourably with conventional generating methods below 500 kW. For larger, multi-megawatt power plants, the high temperature fuel cells, such as the SOFC are favoured. This is because the heat generated can be used in a combined gas turbine cycle and can provide efficiencies of over 70%, some 10% higher than conventional technology. In recent years, significant advances have been made in the development of SOFCs [8-10] and many test systems are currently undergoing long tem tests.

Despite the inherent benefits of fuel cell technology, the commercialisation of fuel cells, particularly the SOFC, has been a slow process. The reasons vary and depend both on the fuel cell type and the requirements of the application. The challenge faced by the automotive industry as far as PEMFCs are concerned is to reduce the materials and manufacturing costs. In addition hydrogen fuel is not yet economically available from renewable sources. It is currently produced by reforming hydrocarbon-based fuels such as natural gas and methanol. Further, extensive fuel clean-up is needed before the hydrogen-rich reformate enters the fuel cell. The SOFC, which is less developed than the other fuel cell types, does not have the same fuel problems because the reformate components can be oxidised directly at the higher operating temperature (750-1000°C). There are, however, still materials issues to be addressed. These are associated with thermal mismatches that produce sealing and fabrication problems for the ceramic materials used in each cell in the fuel cell stack. However there is an increasing market pull for cleaner, more efficient energy production, which has intensified the effort devoted to fuel cell research and development.

1.2. The Solid Oxide Fuel Cell

The solid oxide fuel cell (SOFC) is an all ceramic fuel cell which means there are few constraints on design. This gives it distinct advantages over other types of fuel cells because it does not require the use of either precious materials or corrosive liquids. This means it has both a low maintenance cost and also the possibility of a long running lifetime. The basic operation of a SOFC is shown in Figure 1.2.

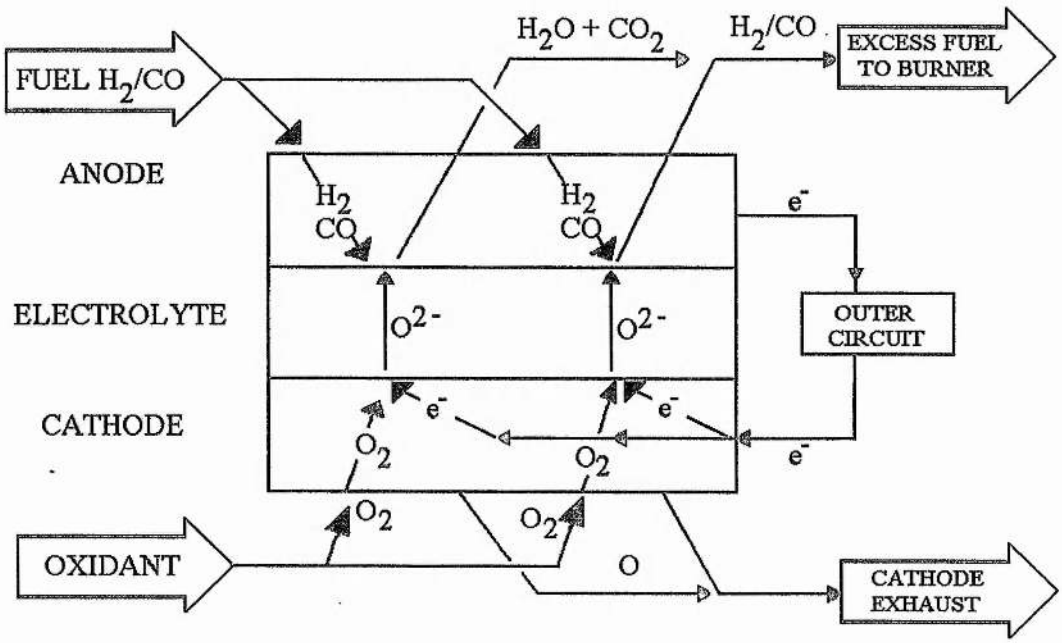

Figure 1.2. The basic operation of a SOFC.

The fuel gases can be H_2, CO or alkanes such as methane, or more realistically natural gas. Electrochemical oxidation of alkanes can occur at the anode at the normal temperature of operation between 900 and 1000°C but other processes are more important. For example, methane, in the presence of oxygen can thermally decompose to carbon and water at high temperatures (>1000°C). Thus, the fuel gases are first converted into H_2 and CO by steam reforming. The steam reforming of hydrocarbon fuels involves the endothermic reaction

$$CH_4\,(g) + H_2O\,(g) \leftrightarrow CO\,(g) + 3H_2\,(g) \qquad \Delta H = +206.2\ kJmol^{-1}$$

which is obviously favoured by low pressure and high temperature. The water gas shift equilibrium, which is pressure independent is represented by the equation

$$CO\,(g) + H_2O\,(g) \leftrightarrow CO_2\,(g) + H_2\,(g) \qquad \Delta H = -41.1\ kJmol^{-1}$$

Thus overall, these reactions are favoured by high temperatures, a high steam ratio and low pressures. The higher hydrocarbons in natural gas also react with steam in a similar fashion.

If insufficient steam is present, carbon may be deposited according to the following equations

$$2CO\,(g) \leftrightarrow CO_2\,(g) + C\,(s) \quad \Delta H = -172\ kJmol^{-1} \qquad \text{(Boudouard Reaction)}$$

and

$$CH_4\,(g) \leftrightarrow 2H_2\,(g) + C\,(s) \qquad \Delta H = +86.2\ kJmol^{-1}$$

The decomposition of methane to carbon and hydrogen is obviously favoured by high temperatures, but is much less endothermic than the reforming reaction and hence will not occur in the presence of steam. The decomposition for both reactions is termed cracking and the deposition of carbon is called coking. Coking is undesirable because deposited carbon can block the flow of gas and covers the anode, lowering reforming activity. The steam reforming treatment can be done by one of three methods. These are external, integrated or internal reforming [11].

External reforming takes place in a separate reforming reactor which comprises of heated tubes filled with Nickel or Noble metal catalysts through which steam and the fuel gas is passed. The maximum efficiency of this type of arrangement is 60%.

Integrated reforming uses the waste heat of the fuel cell by the integration of reformer cells containing the catalyst material arranged inside the fuel cell stack. The reforming device is alternate with a stack of about 5 single fuel cells. Steam must still be passed with fuel cell gas. Good exchange of heat is only realised between the

reforming unit and the directly contacting fuel cells. The efficiency of this set up is still around 60%.

Internal reforming takes place in every cell at the anode. The advantage of this system is that the steam produced by the fuel cell reaction contributes to the partial pressure of water vapour in the gas mixture at the anode. This therefore prevents the cracking reaction. However, the main drawback of this arrangement is that the reforming reaction is endothermic whilst the cell reaction is exothermic. This can lead to large temperature gradients over the anode which may cause damage to the cell in the form of cracks. For a natural gas fired SOFC with internal reforming, an efficiency of up to 68% can be realised if the waste heat is used for additional production of electricity with a steam turbine.

1.2.1. Solid Oxide Fuel Cell Design

Westinghouse in the U.S.A. were the first major company to carry out major research on SOFCs but in recent years many other organisations have been involved in the research and development of this field [12], many stack designs have been proposed for SOFCs but the two most common and distinct types are the tubular and planar designs.

1.2.2. Tubular Design

This is the type of structure used by Westinghouse [13]. A schematic representation of this cell is shown in Figure 1.3 [14]. Fuel flows on the outside of the support tube whilst the oxidant is introduced into the centre of the cell through an injector tube. The porous tube is normally that of 15 mol% CaO-stabilised Zirconia. This tube is overlaid with the cathode layer. An electrolyte layer covers the cathode except for a narrow strip along the cell length. The exposed cathode strip is covered with a gas tight interconnect layer, whilst the electrolyte surface is covered by the anode material. The electrolyte/electrode and interconnect layers are fabricated by the use of the electrochemical vapour deposition (EVD) technique. These cells are then bundled together to make a fuel cell stack, where each individual cell is connected to the next in series or parallel by the use of a material called 'nickel felt'. This consists of nickel metal

fibres sinter bonded with each other and also to the nickel metal in the fuel electrode. This is shown in Figure 1.4 [15]. State of the art cells have been shown to exhibit high performance and stability, and have been tested for up to 70000 hours. Typical output is 0.68V at a current density of 250 mA/cm^2 on hydrogen fuel 89% H_2, 11% H_2O with an 85% fuel utilisation [13,16-18]. This therefore gives a power density of 0.17 Wcm^{-2}.

The advantages of the tubular design are that the respective gases are kept separate from each other by the actual nature of the cell design thus eliminating the necessity of finding a material to make gas tight seals. The oxidant gas is passed through the centre of the tube by use of an injector tube whereas the fuel gas remains distinct around the outside of the fuel cell tube. There is therefore no need for any seals. Another advantage is that the long cell length is beneficial for in-situ reforming. The fuel/spent fuel mixture can be distributed along the cell and thus reduce the amount of local cooling that arises from the endothermic reforming reaction. The catalytic reforming reaction, especially using Nickel, is more rapid than the exothermic combustion reaction which leads to local cooling of the cell. The distribution of the gas mixture therefore avoids the possibility of severe local thermal stresses within the ceramic components. The nature of multi cell stacking also means that individual cells can slide along the Nickel felt when thermal expansion and contraction results in mismatches. This set up means that the formation of cracks will be limited to just one cell.

The major disadvantages are that there can be high polarisation losses due to the cathode collection path being very long and that CVD and/or EVD dictates somewhat the choice of materials used and this may be against requirements [19]. For example the cathode used in the Westinghouse design is $La_{0.85}Sr_{0.15}MnO_{3-\delta}$. However, it is known that the electronic conductivity of $La_{0.5}Sr_{0.5}MnO_3$, or $La_{0.5}Mn_{0.15}O_{3-\delta}$ is higher than the composition used and the cathodic polarisation produced during oxygen reduction is also lower than for the highly doped material. Thus the Westinghouse design incorporates a composition with inferior properties. The choice of material is due to problems with the CVD technique limiting the Strontium Oxide doping concentrations to relatively low levels due to the gaseous chemical reactions involved or due to

interfacial reactions involving Strontium Oxide at the high temperatures involved in the CVD deposition process.

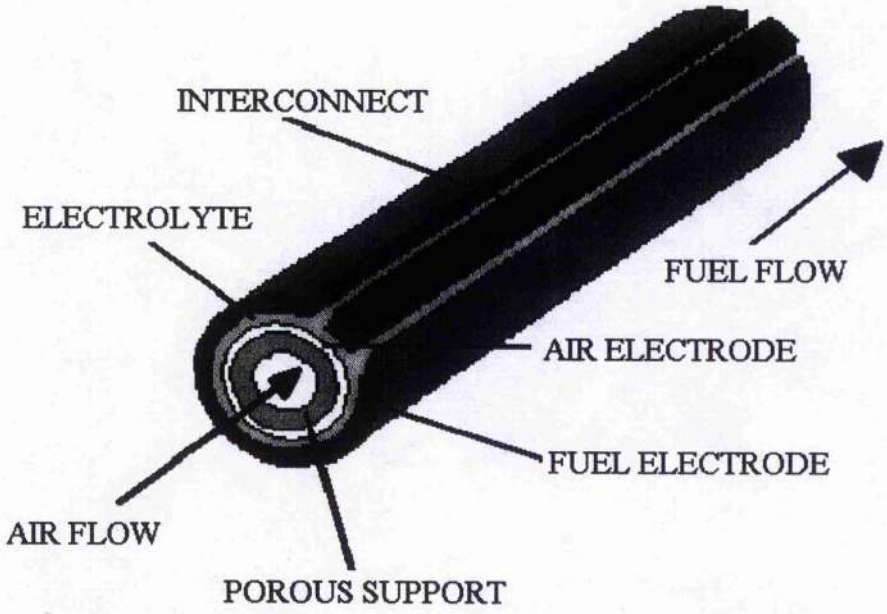

Figure 1.3. Sealless tubular design of SOFC (Westinghouse) [14].

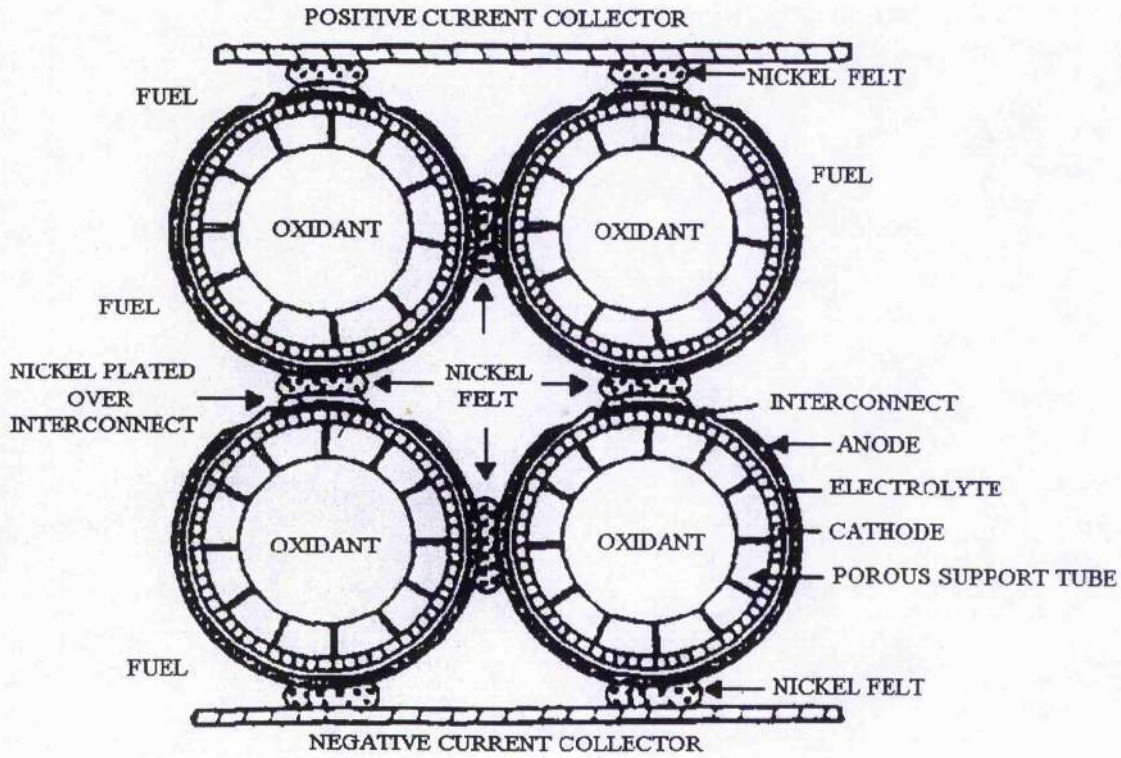

Figure 1.4. The stacking mechanism for tubular fuel cells [15].

1.2.3. Planar Design

The planar design is the simplest configuration of components and is stated to offer 10-100 times greater volumetric power density than the tubular designs [13]. A representation of this design is given in Figure 1.6. [14]. A single cell comprises of a three layer structure of anode, electrolyte and cathode, which are sandwiched together. The fuel cell stack is made by separating subsequent cells by a bipolar interconnect which has ribs on each side to allow the passage of the gases. Different geometries can be obtained by the direction of these interconnects, either co-flow or cross-flow. A complete SOFC planar stack is formed by the continued stacking of the layers to the desired height. The nature of the planar design allows many fabrication methods to be employed. Some examples are CVD, EVD [20,21], plasma spraying [22], laser evaporation [23] or most simply screen printing of electrodes onto a tape cast electrolyte. Typical output of a single cell with the planar arrangement is 0.7 V at a current density of 260 $mAcm^{-2}$. This therefore shows a power density of 0.18 Wcm^{-2}. This is similar to that of the tubular cell but shows a higher volumetric power density than that of the tubular design [14].

The other major advantages of the planar design are that the electrode production process can easily be accomplished by mass production methods such as screen printing and tape casting. These processes are easier and cheaper than the CVD/EVD methods utilised in the tubular design.

The major disadvantage of this design is that there is a need for a high temperature gas seal. The different types of seal possible are compressive seals, cement seals, glass seals and glass-ceramic seals. Compressive seals can lead to non-uniform stress distribution on the ceramic and therefore lead to the formation of cracks. Cements and glasses must be carefully chosen so that the reaction with the cell materials occur at the operating temperature and thermal expansion mismatch is minimised. The planar design results in less efficient distribution of gases across the cell than in the tubular case. This results in localised cooling due to the endothermic reforming reactions, which in turn may lead to thermal stresses and cracking. Another disadvantage is that the position of the contact areas between the anode of one cell and the cathode of the next

via the interconnect is important. A limited contact area will lead to a long path for the current in the plane of each electrode. This can lead to high ohmic losses.

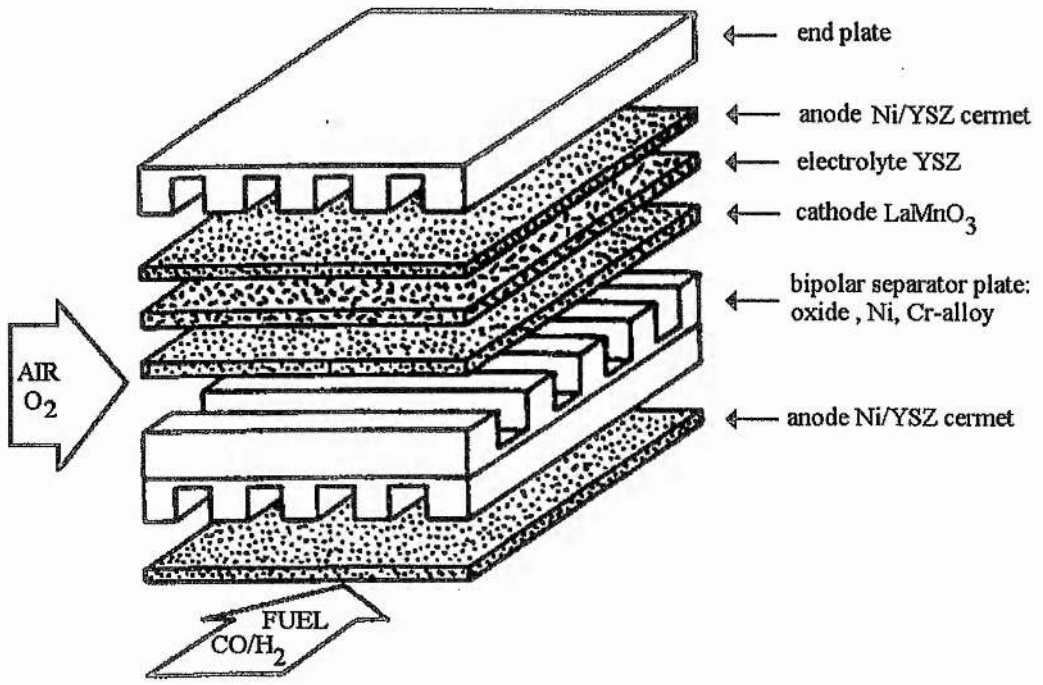

Figure 1.6. Planar Design of the SOFC [19].

1.2.4. Monolithic Design

The monolithic design, designed by Argonne National Laboratory, incorporates a complex corrugated structure which allows separated gas flows, as for the tubular design, eliminating the need for gas-tight seals, Figure 1.5. This design offers a high power density with low resistive losses, which allows the cell to be operated at high currents [14]. The main disadvantage is the complicated fabrication of the corrugated layer and the subsequent problems in scale-up to large SOFC devices. Monolithic cells have been operated at 2.2 Acm^{-2} [24], 1.5 Wcm^{-2} at 0.7 V

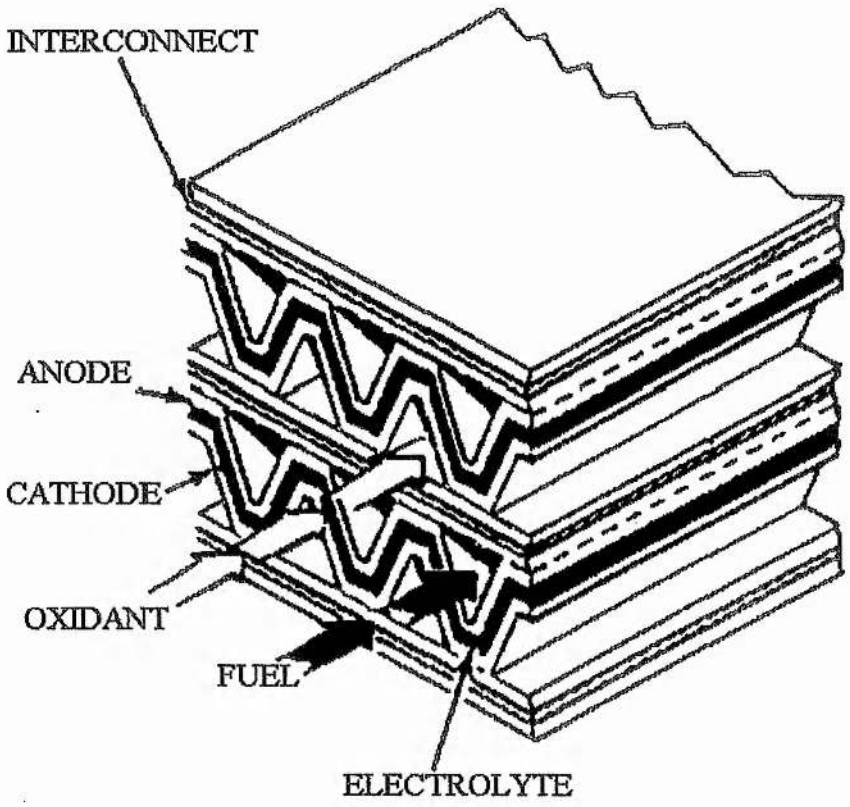

Figure 1.5. The Monolithic design of a SOFC.

1.3. Solid Oxide Fuel Cell Materials

1.3.1. The Electrolyte

The electrolyte, typically formed by the sintering of a compacted powder, has to be dense, preventing any gaseous diffusion through the electrolyte and contain very low levels of impurities, which can have a detrimental effect on the oxide ion conduction. Either of these factors would produce ohmic losses, with a corresponding decrease in the cell voltage, E and the efficiency of the cell. The electrolyte must also be a purely ionic conductor over a wide range of oxygen partial pressures. The current solid electrolyte of choice is Yttria stabilised Zirconia. Several manufacturers produce YSZ by different routes resulting in products with often vastly different properties. For example Tosoh produce 8YSZ by a co-precipitation route and Tioxide used a plasma processing route. Further details of theses processing routes are given in sections 2.1.1.3 and 2.1.1.4.

For planar solid oxide fuel cells, which have a higher power density and lower fabrication costs than the tubular design, tape casting is well suited for the production of thin membranes. For example, the production route used by Dornier consisted of mixing the ceramic raw materials ZrO_2, Y_2O_3 and Al_2O_3 together and processing with organic components such as solvents, plasticizer and binder to form a slurry [25]. Pore formation prevention is achieved by deaerating the slurry and then metering it to a casting head. The slurry is drawn out to form a tape between two adjustable blades and Mylar carrier foil. The solvents are then evaporated from the cast tape in a drying tunnel using infrared radiators. The 'green' sheets which are obtained are then punched out from the dried flexible tapes. The punching residue can then be dissolved and mixed-in with the fresh slurry for re-utilisation. The punched-out substrates are then sintered at greater than 1500°C for several hours.

1.3.1.1. Yttria-stabilised Zirconia

Pure Zirconia can exist in three polymorphs at ambient pressures. The differences in the structures of the three polymorphs are illustrated by the changes in cell angle and lattice parameter shown in Table 1.1.

Table 1.1. Crystallographic data for the three polymorphs of Zirconia[26, 27, 28].

Monoclinic	**Tetragonal**	**Cubic**
Space Group $P2_1/c$	Space Group $P4_2/nmc$	Space Group Fm3m
a = 5.3129 Å	a = 5.094 Å	a = 5.090 Å
b = 5.2125 Å	c = 5.177 Å	
c = 5.1471 Å		
β = 99.218 °		
$\rho_o = 5.820\ gcm^{-3}$	$\rho_o = 6.090\ gcm^{-3}$	$\rho_o = 6.206\ gcm^{-3}$

The monoclinic polymorph is stable at room temperature and undergoes a reversible phase transformation to the tetragonal polymorph at 1170°C [29,30]. Further heating to above 2370°C causes the tetragonal polymorph to undergo a phase transformation to the cubic polymorph, which has the fluorite structure.

Metastable, or kinetically stable, tetragonal Zirconia has been obtained at room temperature, but its formation is dependent upon crystallite size and cooling regime [31]; metastable tetragonal Zirconia requires crystallite sizes less than 30 nm. A metastable tetragonal Zirconia phase is commonly obtained from the preparation of Zirconia by wet chemical processing routes e.g. sol-gel [32], where crystallites with diameters between 10 and 30 nm are readily obtained.

The instability of the cubic Zirconia polymorph at room temperature is unusual compared to other $M^{2+}F_2$ and $M^{4+}O_2$ compounds with the fluorite structure e.g. ThO_2, CaF_2, which are cubic at room temperature. The fluorite structure is illustrated in Figure 1.7. It consists of a cubic close packed array of Zirconium ions, with oxygen occupying all the tetrahedral sites between the close packed layers. The cubic close packed layers of metal ions are oriented parallel to the {111} planes of the unit cell. In the fluorite structure with space group Fm3m, Zirconium and Oxygen ions are located at the following positions:

Zr	4(a)	0 0 0
O	8(c)	¼¼¼ + (000, ½½0, ½0½, 0½½) + ¾¾¾

Alternatively, redefining the origin of the unit cell by displacing the unit cell along one of the body diagonals by one quarter of the length of the diagonal, i.e. ¼¼¼, the Fluorite structure can be described as a primitive cubic array of anions in which the eight co-ordinate sites at the cube body centres are alternatively empty and occupied by a cation.

As the unit cell of the fluorite structure is orthogonal, calculation of the interatomic distances is straightforward and involves simple trigonometric calculations. The formulae for the interatomic distances in the cubic fluorite structure are thus:

Cation - Anion distances: $d^2 = ((a/2)^2+(a/2)^2)+(a/2)^2 = 3a^2/16 \therefore d = 3^{½}a/4 = 0.433a$

Cation - Cation distances: $d^2 = (a/2)^2 + (a/2)^2 = a^2/2 \therefore d = a/2^{½} = 0.707a$

Anion - Anion distances: $d = 1 - (a/4 + a/4) = 0.5a$

Zirconia usually shatters on heating because of the changes in volume that accompany the monoclinic ⇔ tetragonal transition. The tetragonal to monoclinic transition is accompanied by a 5% contraction in volume. The phase transition and the shattering may be avoided by doping with MgO, CaO, Y_2O_3, Gd_2O_3 and rare earth oxides [29]. These oxides form solid solutions with the high temperature, cubic polymorph of ZrO_2 (stable only at > 2400°C in pure ZrO_2) and these cubic solid solutions are stabilised to much lower temperatures.

The stabilisation involves the substitution of the aliovalent cation for Zirconium, with a corresponding introduction of oxygen vacancies as the charge compensating species. Stabilised Zirconia has reversible expansion/contraction behaviour on thermal cycling without any disruptive phase transitions. The substitution of Zirconium with Yttrium is summarised below using Kröger-Vink notation [33], which is commonly used to describe the reaction of point defects. The introduction of oxygen vacancies leads to oxide-ion conductivity in doped Zirconia.

$$Y_2O_3 \xrightarrow{ZrO_2} 2Y_{Zr}^{'} + V_O^{\cdot\cdot} + 3O_O$$

$Y_{Zr}^{'}$ represents a negatively charged defect of a Y^{3+} ion on a Zr^{4+} ion lattice site, $V_O^{\cdot\cdot}$ a positively charged oxygen vacancy and O_O an oxygen ion on its lattice site.

Because of the larger ionic radius of the aliovalent dopant (1.15Å for Y^{3+} compared to 0.98Å for Zr^{4+}, in eight fold co-ordination) the tetragonal and cubic polymorphs of Zirconia are stabilised to lower temperatures due to an increase in the average cation radius. This subsequently allows an increase in the co-ordination number of the cation from 7 in the monoclinic structure to almost 8 in cubic stabilised Zirconia; however, not all of the co-ordinated sites are occupied. The most widely-studied stabilised Zirconia system is the binary ZrO_2 -Y_2O_3 system due to the wide range of properties obtained with different solid solution compositions and heat treatments. The binary ZrO_2 -Y_2O_3 system is discussed in more detail in chapter 3 and the less widely studied system ZrO_2 -Gd_2O_3 is studied in chapter 4.

1.3.1.2. Other Electrolyte Materials

An alternative to stabilised Zirconia is the use of Ceria based electrolytes. CeO_2 solid solutions show higher oxygen ion conductivity values than doped Zirconia (see Figure 1.8) and also higher values of oxygen surface exchange coefficient [34]. These factors suggest that similar power densities can be obtained from stacks incorporating CeO_2 electrolytes at lower temperatures than similar stacks incorporating ZrO_2 based electrolytes. This reduced temperature of operation will be beneficial in terms of a decrease in the number of thermally related materials problems such as exchange of ions between component layers and/or the introduction of cracks between component layers due to thermal cycling. However all of these beneficial properties are offset by the redox behaviour of Ce^{4+}, and the resulting introduction of electronic conductivity when is the oxygen partial pressure is low i.e.

$$O_o^x \rightarrow \tfrac{1}{2} O_2 + V_o^{\bullet\bullet} + 2e' \ (Ce^{3+})$$

The increase of electronic conductivity due to the presence of Ce^{3+} severely decreases the magnitude of the ionic domain of CeO_2 based electrolytes. Recent work on the doping of the basic CeO_2 material with small amounts of dopant ions have been shown to widen the ionic domain [35]. Other researchers suggested coating the CeO_2 with a stabilised ZrO_2 layer which effectively suppresses the reduction of CeO_2 [36,37].

Bi_2O_3 based oxides also exhibit high oxide ion conduction e.g. $Bi_2V_{0.9}Cu_{0.1}O_{5.35}$ (BiCuVOx) has an oxide ion conductivity 50 to 100 times greater than any other electrolyte at 300°C but like the CeO_2 based oxides, n-type semiconduction is dominant at low oxygen partial pressures and the thermal stability in the region of 700°C is not satisfactory [38,39].

a)

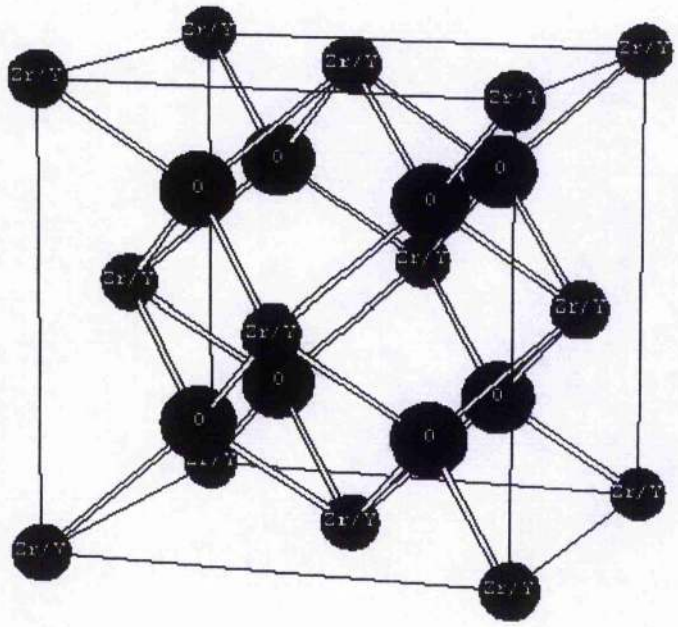

b)

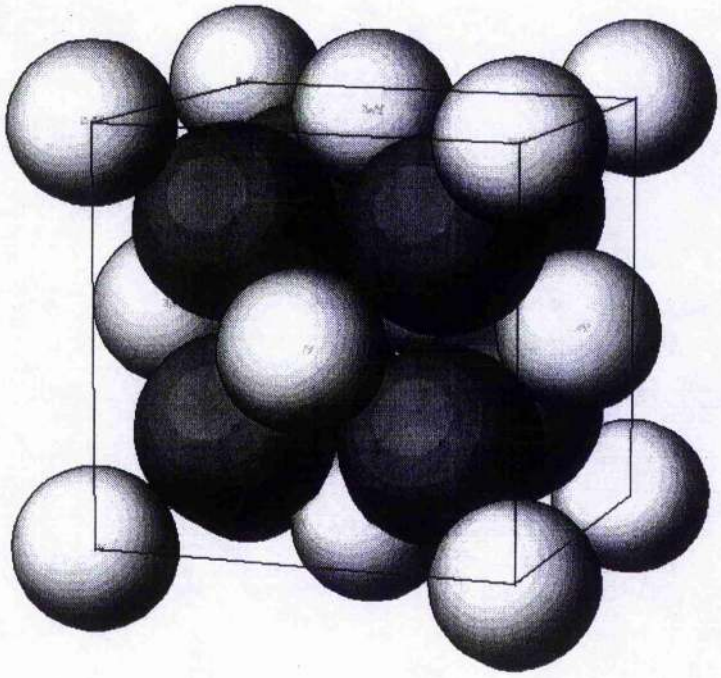

Figure 1.7 a)The face centred cubic fluorite structure of Yttria-stabilised Zirconia with the cations Y/Zr at the 000 position, shown as a 'ball and stick' model and as b) a 'filled sphere' model.

Ishihara et al reported that $LaGaO_3$ exhibits high oxide ion conductivity when Sr is doped for the La site and Mg for the Ga site [40]. $La_{0.9}Sr_{0.1}Ga_{0.8}Mg_{0.2}O_3$, which has the perovskite structure exhibits an oxide ion conductivity higher than that of Sc-doped ZrO_2 and lower than that of Bi_2O_3. The conductivity of doped $LaGaO_3$ is 10 Sm^{-1} at 850°C, i.e. the same as the conductivity in 8 mol% Yttria Stabilised Zirconia at 1000°C. However, recent structural studies indicated that several phase transitions occur in doped $LaGaO_3$ between room temperature and 1000°C [41,42], which indicates that it is unlikely that it will replace YSZ as the material of choice for SOFC devices.

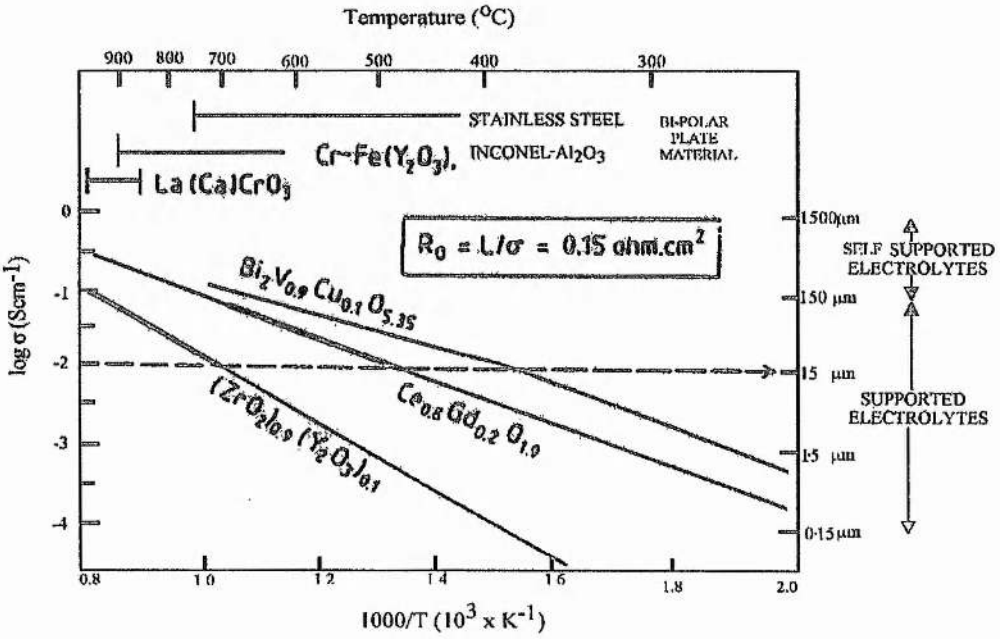

Figure 1.8. Comparative conductivities of CeO_2 and ZrO_2 based electrolyte materials [34].

1.3.2. The Anode

Metals are used in the anode material as high electronic conduction is required under the highly reducing conditions of the anode, although the metals must be oxidation resistant due to the high oxidation partial pressures observed near the gas outlets of the anode compartment. Suitable metals at 1000°C are Cobalt, Nickel, Palladium and Platinum. Nickel is used due to its low cost and high catalytic properties [43].

1.3.2.2. Ni/YSZ Cermets

The anode currently used in SOFC development is a Nickel/YSZ cermet, which incorporates active particles of Nickel in an inactive YSZ support. The fuel oxidation occurring at the anode involves the adsorption of the fuel onto the Nickel, e.g.

$$H_2 + 2Ni \leftrightarrow 2NiH$$

$$2NiH + O_o^x \leftrightarrow H_2O + 2Ni + V_o^{\circ\circ} + 2e^-$$

The Nickel metal is dispersed in YSZ to support the Nickel particles, to prevent the fusion of the Nickel particles at high temperatures, to match similar thermal expansion of the anode and electrolyte and to provide a porous structure. The porous structure is required so that the reaction of the fuel gas with the oxygen ions and the electrons can occur over a large surface area. Electronic conductivity [44] and the thermal expansion [45] both increase with Nickel content, so to prevent the thermal expansion from becoming too different from that of the electrolyte a compromise has to be made. A typical Nickel content of 30 vol% is used, producing a porosity of 30% and a conductivity significantly greater than the accepted minimum value of 50 Scm^{-1} [46]. The Nickel is usually introduced to the YSZ powder as NiO and is reduced in situ in the fuel cell, providing an enhanced porous microstructure [47].

There are, however, several problems associated with Ni/YSZ cermets. These include the sintering of Nickel [48], which reduces the active surface area available for oxidation to occur, Nickel Sulphide formation due to Sulphur being present in the natural gas [49] and carbon deposition, especially from higher hydrocarbons [50]. The carbon deposition also catalysed by Nickel which means that steam must be present to prevent coking from occurring. This coking is reduced by steam reforming but anode degradation in the form of Nickel sintering occurs with high partial pressures of steam [51]. Lithium addition to the anode has been reported to significantly lower the activation energy for surface carbon removal from the anode [52].

The anode is usually applied to the electrolyte plates by screen printing, which involves making a paste from a mixture of the desired anode ceramic powder, a solvent

and a binder. Thickness of the applied films and the grain size can be controlled by varying the ratio of the components in the mixture.

1.3.2.3. Other Anode Materials

Ruthenium/Stabilised ZrO_2 cermets have been studied and shown to have a higher resistance to sintering whilst still possessing a high reforming activity [53]. Cobalt/stabilised ZrO_2 cermets have also been investigated and shown to have a higher tolerance to Sulphur than Nickel/YSZ cermets [54]. The cost of Co, however, is much higher. The suitability of mixed valence states such as found in $LiTi_2O_4$, $Mg_xTi_{3-x}O_5$, $CrTi_2O_5$ and Nb doped $MgTi_2O_5$, Mg_2TiO_4 and $Sm_2Ti_2O_7$ have been studied by Steele et al [55]. Of these the mixed Niobium, Magnesium pseudobrookites looked the most promising. However these materials are unstable over a wide range of oxygen partial pressures.

1.3.2.4. Mixed Conducting Anode Materials

Mixed conducting oxides have been proposed for use as SOFC anodes [56]. These have been said to offer theoretical improvements in performance over purely electronic conductors. This is because in cermet anodes based on electronic conductors the oxidation of fuel can only occur at the so called triple point regions between the electrolyte, electrode and the gas, Figure 1.10a. In a mixed conductor, however, the oxygen ions can move through the electronic conducting matrix and the electrochemical combustion of hydrogen can occur over the whole particle surface area, Figure 1.10b. This larger surface area for reaction results in lower polarisation losses at the electrode.

The most common mixed conductor studied is that of oxides based on solid solutions in the ZrO_2-Y_2O_3-TiO_2 system [56-62]. Due to the presence of a variable valence Titanium ions, it is possible that a catalytic process for the conversion of hydrocarbons can occur as observed in the Ni-cermet anode. Irvine et al have studied Nb doped stabilised Zirconias but these were found to have conducting properties which were not suitable for SOFC applications [63]. The contribution of Ni cermet anodes to current SOFCs in terms of resistivity is lower than any of the other components in a

SOFC stack, Figure 1.11. Any potential replacement for Ni/YSZ cermets must have high conductivity although not necessarily as good as conventional Ni cermets.

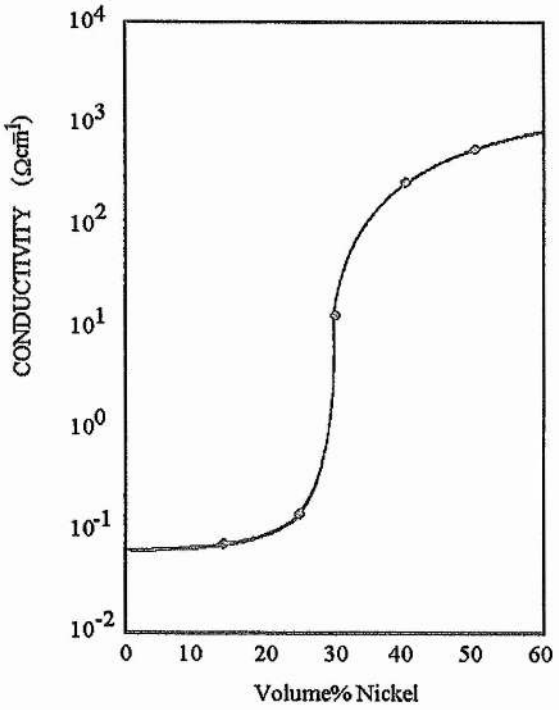

Figure 1.9a Conductivity of Ni/YSZ cermet versus Ni content at 1000°C [14].

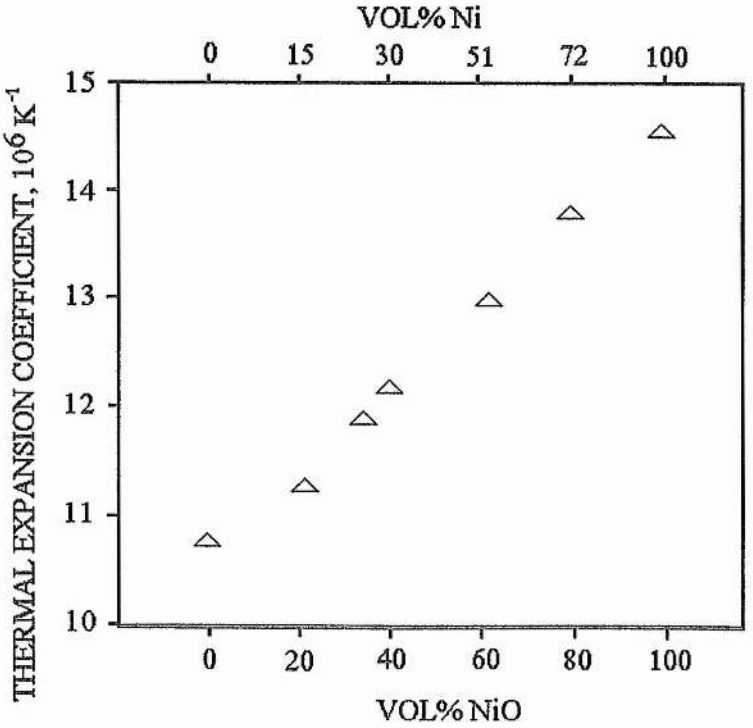

Figure 1.9b Thermal expansion coefficient of Ni/YSZ cermet as a function of Ni content [58].

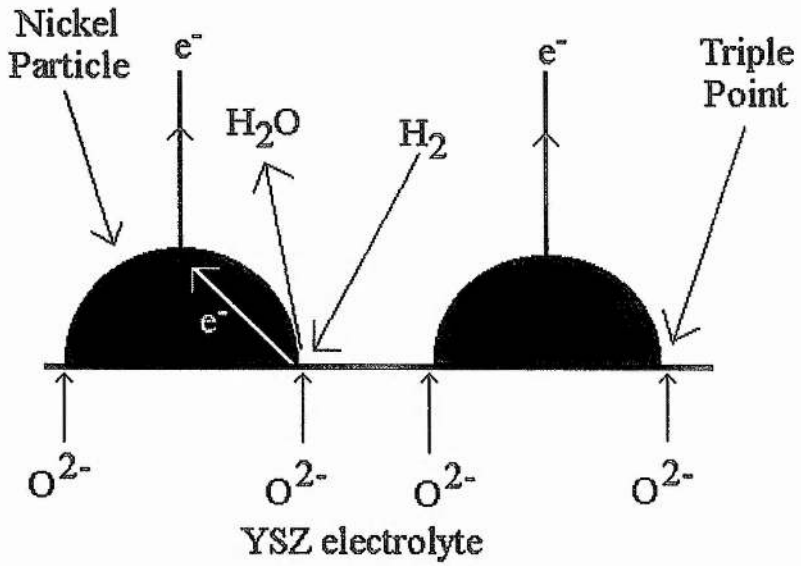

Figure 1.10a. Reaction area for a cermet composed of ionic conducting and electronic conducting components.

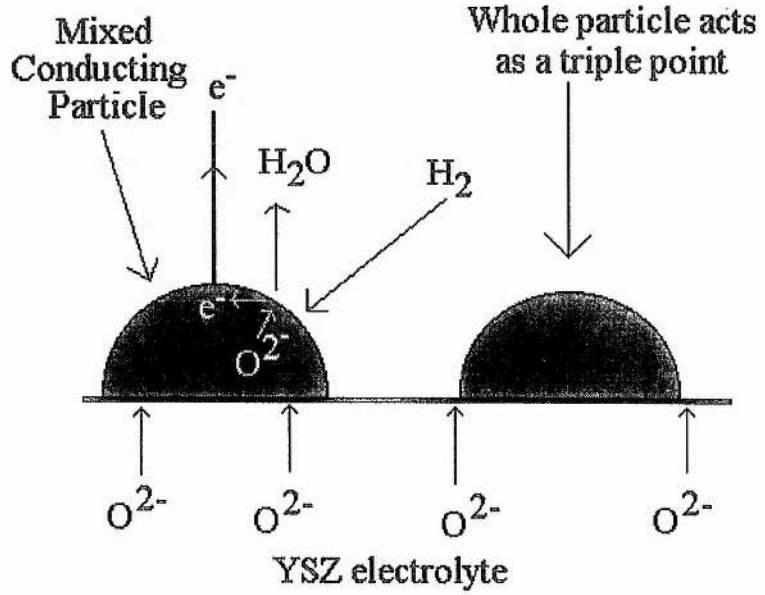

Figure 1.10b. Reaction area for a mixed ionic and electronic conducting material.

1.3.3. The Cathode

Doped Lanthanum Manganite is the cathode material currently used in SOFC's due to its high electronic conductivity in oxidising atmospheres [64-66]. Replacing some La^{3+} in $LaMnO_3$, with Sr^{2+} can improve the conductivity, by increasing the Mn^{4+} content [67].

i.e. $$LaMnO_3 \text{ — } SrO \longrightarrow La^{3+}_{1-x}Sr^{2+}_{x}Mn^{3+}_{1-x}Mn^{4+}_{x}O_3$$

A substitution of 10 mol% Sr^{2+} produces an increase in electronic conductivity from 75 to 125 Scm^{-1} at 1000°C [68]. The thermal expansion coefficient of $LaMnO_3$ is quite similar to that of Yttria stabilised Zirconia ($11.2 \times 10^{-6}\ °C^{-1}$) and increases slightly with the addition of strontium [69]. Accurate tailoring of the thermal expansion can be made by the substitution of smaller Ca^{2+} for La^{3+}/Sr^{2+}. A significant problem which has recently received much attention [70-73] is the reaction of the cathode and electrolyte during co-sintering and in reducing atmospheres at fuel cell temperatures, producing poorly conducting phases e.g. $La_2Zr_2O_7$ [74] which increase the ohmic losses and reduce the performance of the fuel cell.

1.3.4. The Interconnects

The properties required for the interconnecting material are probably the most stringent of all of the components. In addition to having electronic conductivity and comparable thermal expansion to the YSZ electrolyte and electrodes, the interconnect must be stable in both oxidising and reducing atmospheres and have a high sintered density to prevent cross-diffusion and mixing of fuel and oxidant gases. The interconnect must also have a flatness better than 100μm, i.e. better than 0.1% [75]. The only material which is chemically stable within both atmospheres and sufficiently conducting is doped Lanthanum Chromite, which is quite similar to the cathode material. Its conductivity and thermal expansion can be varied in a similar manner to those of the cathode by substituting La^{3+} with divalent cations [76,77]. One of the major differences between the cathode and the interconnect material is the high density required for the latter and this has proved to be very difficult to obtain [78,79]. By

producing highly reactive powders, sintering of $LaCrO_3$ to near full density in air has been possible [80].

Reaction spraying is an efficient means of powder processing [81]. This technique utilises aqueous solutions of chlorides and nitrates, which are pumped into a reactor, which has a temperature above 1000°C. Atomisation is carried out by means of pressure and the powder is separated by filters. When falling from the top to the bottom of the reactor, the droplets undergo the stages of solvent evaporation, decomposition of the salts and formation of the perovskite phase, which has a small crystallite size. The small crystallites result in good sintering behaviour.

The powder obtained from the reaction spraying can then be ball milled to prepare a tape casting slurry. Slurry preparation is usually performed in an annular ball mill by mixing the powder with solvents, plastisizers and organic binders.

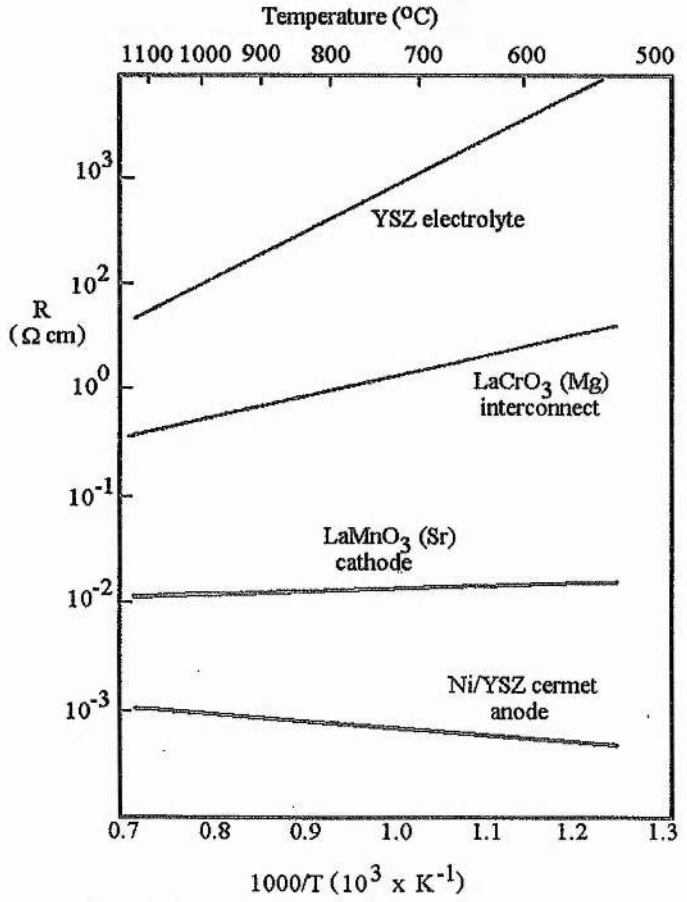

Figure 1.11. Typical resistivity values for each individual component of a SOFC stack [19].

1.4. Aim of Project

Yttria-stabilised Zirconia (YSZ) is likely to remain the material of choice for the electrolyte in Solid Oxide Fuel Cells (SOFC), due to its high oxide-ion conductivity at 800-1000°C. Nickel/YSZ cermets are currently used as the anode materials in SOFCs because of their compatibility with the YSZ electrolyte and their high electronic conductivity. However, 8 mol% YSZ is metastable resulting in degradation of conductivity with time at fuel cell operating temperatures and is fragile, restricting the thickness and thus conductivity of YSZ plates required for use in the planar design of SOFCs. The cermet anodes also have several problems associated with them, particularly the build up of carbon on the nickel. Thus for SOFCs to become commercially viable devices, the electrolyte 8YSZ must be stabilised to reduce degradation in conductivity with time and strengthened. New anodes must be found in order to replace the current Nickel/YSZ cermets.

The aims of this study are to address these materials problems to aid SOFC commercialisation. The aims are essentially threefold:

1. In the search for viable alternatives to Ni/YSZ cermets as anode materials, determine and characterise the single phase cubic regions of two rare earth stabilised Zirconia systems, which have been doped with reducible Ti^{4+}, in terms of their structural and electrochemical properties (chapters 3 and 4).

2. To strengthen the YSZ electrolyte so that it may be used in planar SOFCs, determine the effect of Alumina additions on the electrical, structural and mechanical properties of 8 mol% YSZ. Also included in the this work is the addition of the Calcium Aluminate oxide ion conductor $Ca_{12}Al_{14}O_{33}$ to 8YSZ (chapter 5).

3. To increase the knowledge and understanding of the conduction mechanism of fully stabilised cubic fluorite materials in terms of their crystallography by using Neutron Diffraction and EXAFS as structural probes (chapters 6 and 7).

1.5. References

[1] P.W. Atkins, Physical Chemistry 3rd edition, Oxford University Press (1988)

[2] K.J. Laidler, J.H. Meiser, Physical Chemistry, Benjamin/Cummings Publishing Co. Ltd. (1982)

[3] L.J.M.J. Blomen, J. Sukkeland W. Lansink in 'Proc. 2nd European Solid Oxide Fuel Cell Forum', ed. B. Thorstensen, (1996)

[4] Handbook of Fuel Cell Technology, eds Carl Berger, Prentice-Hall, Inc/Engelwood Cliffs N.J. (1969)

[5] W.R. Groves, Philos. Mag. 14 (1839) 127-130

[6] W. Nernst, Z. Elektrochem 6 (1899) 41-43

[7] B.C.H. Steele, MRS Bull. 14[6] (1989) 19-23

[8] Proc. 1st. Intl. Symp. on Solid Oxide Fuel Cells, ed. S.C. Singhal (The Electrochemical Society, Pennington, New Jersey 1989)

[9] Proc. 2nd. Intl. Symp. Solid Oxide Fuel Cells, eds. F. Grosz, P. Zegers, S.C. Singhal and O. Yamamoto (CEC Publ. EUR 13546 EN, Brussels, Belgium 1991)

[10] Proc. 3rd. Intl. Symp. on Solid Oxide Fuel Cells, 1993, 93-94

[11] K. Ledjeff, T. Rohrbach, G. Schaumburg in Proc. 2nd Int. Symp. On SOFC. eds F. Gross, P. Zegers, S.C. Singhal and O. Yamamoto. Commission of the European Communities, Luxembourg (1991) 324

[12] M. Mogensen in 14th Riso Int. Symp. On Materials Science, eds. F.W. Poulsen, J.J. Bentzen, T. Jacobson, E. Skou and M.J.L. Ostergard (1993) 117

[13] W.J. Dollard in Proc. Int. Symp. On SOFC, eds. O. Yamamoto, M. Dokiya and H. Tagawa, Nagoya, Japan, (1989) 1

[14] N.H. Minh, J. Am. Ceram. Soc. 76 (1993) 563 No. 3

[15] N.Q. Minh, High Temperature Fuel Cells Part II. The solid oxide fuel cell. CHEMTECH 21 (1991) 120

[16] Westinghouse Electric Corp. SOFC power generation system. The status of the cell technology. A topical report. Rept no. DOE/ET/17089-15, U.S. Dept. of energy, Washington D.C. 1984

[17] S.C. Singhal in Proc. 2nd Int. Symp. On SOFC. eds. F. Gross, P. Zegers, S.C. Singhal and O. Yamamoto. Commission of the European Communities, Luxembourg (1991) 25

[18] A.O. Isenburg in Fuel Cell seminar abstracts (Tuscon) AZ) Courtesy Associates, Washington D.C. (1985) 102

[19] B.C.H. Steele. in Int. Symp. On SOFC. eds. O. Yamamoto, M. Dokiya and H. Tagawa. Nagoya, Japan. (1989) 135

[20] Y.S. Lin, L.G.J. de Haart, K.J. Vries and A.J. Burggraaf in Pro. Int. Symp. on SOFC eds. O. Yamamoto, M. Dokiya and H. Tagawa, Nagoya, Japan (1981) 67.

[21] K.J. de Vries, R.A. Kuipers and L.G.J. de Hart, in Proc. 2nd Int. Symp. on SOFC. eds. F. Gross, P. Zegers, S.C. Singhal and O. Yamamoto. Commission of the European Communities Luxembourg (1991) 135

[22] L.W. Tai and P.A. Lessing, Plasma Spraying of porous electrodes for a planar solid oxide fuel cell, J.Am.Ceram.Soc. 74 (1991) 501

[23] H. Nagagawa, S. Kosuge, H. Tsuneizumi, E. Matsuda, H. Milhara and Y. Sato in Proc. Int. Symp. on SOFC eds. O. Yamamoto, M. Dokiya and H. Tagawa, Nagoya, Japan (1981) 207

[24] D.C. Fee, P.E. Blackburn, D.E. Busch, T.D. Claar, D.W. Dees, J. Dusek, T.E. Easler, W.A. Ellingson, B.K. Flandermeyer, R.J. Fousek, J.J. Piccaolo, R.B. Poeppel and S.A. Zwick, in: 1986 Fuel Cell Abstracts (Courtesy Associates, Washington DC 1986) 40-43

[25] W. Schäfer, H. Geier, G. Lindemann and D. Stolten in 14th Risø Int. Symp. on Materials Science. Eds. F.W. Poulson, J.J. Bentzen, T. Jacobsen, E. Skou and M.J.L. Ostergard, Roskilde, Denmark (1993) 409-416

[26] McCullough, J.D. and Trueblood, K.N., Acta Crystallogr., 12 (1959) 507-511

[27] G. Teuffer, Acta Cryst. 15[11] (1962) 1187-1188

[28] D.K. Smith and C.F. Cline, J. Am. Ceram. Soc. 45[5] (1962) 249-250

[29] H.G. Scott, J. Mat. Sci. 10[9] (1975) 1527-1535

[30] M. Yoshimura, Ceram. Bull. 67[12] (1988) 1950-1955

[31] R.C. Garvie, J. Phys. Chem. 69[1] (1965) 1238-1243

[32] T. Okubo and H. Nagamoto, J. Mat. Sci., 30[3] (1995) 749-757

[33] F.A. Kroger and H.J. Vink, Sol. State Phys. 3 (1956) 307

[34] B.C.H. Steele in Proc. 1st European SOFC forum, Lucerne, Switzerland ed. U.Bossel. 1 (1994) 375

[35] B. Cales and J.F. Baumard, J. Electrochemical. Soc. 131 (1984) 2407 No.10

[36] H. Yahiro, Y. Baba, K. Eguchi and H. Arai, Solid State Ionics 35 (1989) 2077

[37] T. Inoue, T. Setoguchi, K. Eguchi and H. Arai, Solid State Ionics 35 (1989) 285

[38] Yahiro, H., Eguchi, Y., Eguchi, K. and Arai. H. J. Appl. Electrochem. 18 1988 527

[39] P. Kurek, J.R. Dygas, M.W. Breiter, J. Electroanalytical. Chem. 378, 1994, No.1-2, pp.77-83

[40] Ishihara T., Matsuda H., and Takita Y., J. Am. Chem. Soc. 116, 1994, 3801-3803

[41] P. Slater, J.T.S. Irvine, T. Ishihara and Y. Takita, Solid State Ionics 107 (1998) 319-323

[42] P. Slater, J.T.S. Irvine, T. Ishihara and Y. Takita, J. Solid. State. Chem. 139[1] (1998) 135-143

[43] N.Q. Minh, J. Am. Ceram. Soc. 76[3] (1993) 563-588

[44] D.W. Dees, T.D. Claar and B. Flandermeyer, J. Am. Ceram. Soc. 69[8] 628-633 (1986)

[45] S. Majumdar, T.D. Claar and B. Flandermeyer, J. Am. Ceram. Soc. 69[8] 628-633 (1986)

[46] N.Q. Minh, in: Science and Technology of Zirconia V, eds. S.P.S. Badwal, M.J. Bannister and R.H.J. Hannink (Technomic Publishing Co. Inc., Lancaster USA 1993) 652-663

[47] N.Q. Minh, J. Am. Ceram. Soc. 76[3] (1993) 563-588

[48] N. S. Jacobson, W. L. Worrell, Proc. High Temp. Mater. 2 (1983) 217

[49] F. P. F. van Berkel, F. H. van Hueveln, J. P. P. Huijsmans, Solid State Ionics 72 (1993) 636

[50] B. C. H. Steele, I. Kelly, H. Middleton, F. Rudkin, Solid State Ionics, 28-30 (1988) 1547

[51] S. H. Clarke, A. L. Dicks, K. Pointon, T. A. Smith and A. Swann, Catalysis Today 38 (1997) 411-423

[52] Catalysis Letters 49 (1997), 189-192

[53] M. Suzuki, H. Sasaki, S. Otoshi and M. Ippommatsu in Proc. 2nd Int. Symp. On SOFC. eds. F. Gross, P. Zegers, S.C. Singhal and O. Yamamoto. Commission of the European Communities Luxembourg (1991) 585

[54] T.L. Markin, R.J. Bones and R.M. Dell in conference on superionic conductors eds. G.D. Mahou and W.L. Roth, Plenum Press N.Y. (1976) 15

[55] H.J. Steiner, P.H. Middleton and B.C.H. Steele, J. Alloys and Compounds 190 (1993) 279

[56] M. Mogensen in 14th Riso Int. Symp. On Materials Science. Eds. F.W. Poulson, J.J. Bentzen, T. Jacobsen, E. Skou and M.J.L. Ostergard (1993) 117

[57] H. Naito and H. Arashi, Solid State Ionics 53-56 (1992) 436-441

[58] T. Lindegaard, C. Clausen and M. Mogensen, Proc. 14th Mater. Sci: High Temperature Behaviour of Fast Ion and Mixed Conductors, eds. F.W. Poulsen, J.J. Bentzen, T. Jacobsen, E. Skou and M.J. Ostergard, Riso Nat. Lab., Denmark, 1993

[59] C. Heremans and B.J. Wuensch, J. Sol. State Chem. 117 (1995) 108-121

[60] L.S.M. Traqueia, T. Pagnier and F.M.B. Marques, J. Eur. Cer. Soc. 17 (1997) 1019-1026

[61] K.E. Swider and W.L. Worrell, J. Electrochem. Soc. 143(11) (1996) 3706-3711

[62] W.L. Worell, Solid State Ionics 52 (1992) 147-151

[63] H. Arashi and H. Naito, Solid State Ionics 53-56 (1992) 431-435

[64] J.T.S Irvine, D.P. Fagg, J. Labrincha and F.M.B. Marques; Catalysis Today, 38 (1997) 467-472

[63] M. Kertesz, I. Reiss, D.S. Tannhauser, R. Langpape and F.J. Rohr, J. Sol. State Chem. 42 (1982) 125-129

[66] H. Lauret, E. Caignol and A. Hammou, in: Proc. 2nd. Intl. Symp. Solid Oxide Fuel Cells, ed. S.C. Singhal (The Electrochemical Society, Pennington, New Jersey 1989) 242-253

[67] A. Hammouche, E.L. Schouler and M. Henault, Solid State Ionics 28-30 (1988) 1205-1207

[68] B. Goodenough, Phys. Rev. 100 (1955) 564-573].

[69] N.Q. Minh, in: Science and Technology of Zirconia V, eds. S.P.S. Badwal, M.J. Bannister and R.H.J. Hannink (Technomic Publishing Co. Inc., Lancaster USA 1993) 652-663

[70] S. Srilomask, D.P. Schilling and H.U. Anderson, in: Proc. 1st. Intl. Symp. on Solid Oxide Fuel Cells, ed. S.C. Singhal (The Electrochemical Society, Pennington, New Jersey 1989) 129-140

[71] O Yamamoto, Y. Takeda, R. Kanno and M. Noda, Solid State Ionics 22 (1987) 241-246

[72] O Yamamoto, Y. Takeda, R. Kanno and T. Kojima, in: Proc. 1st. Intl. Symp. On Solid Oxide Fuel Cells, ed. S.C. Singhal (The Electrochemical Society, Pennington, New Jersey 1989) 242-253

[73] H. Yokokawa, N. Sakai, T. Kawada and M, Dokiya, Solid State Ionics 40/41 (1990) 398-401

[74] H. Taimatsu, K. Wada and H. Kaneko, J. Am. Ceram. Soc. 75[2] (1992) 401-405

[75] D. Stolten, M. Kurbjuhn and W. Wagner, Int. Conf. Ceramic Processing Science and Technology, (1994), Germany

[76] G.H. Jonker, Physica C (1954) 1118-1122

[77] R. Berjoan, C. Romand and J.P. Coutures, High Temp. Sci. 13 (1980) 173-188

[78] A.M. Anthony, G. Benezech, F. Cabannes, M. Faucher, M Foëx, V. Loc and D. Yerouchalmi, in: Proc. 3rd Intl. Symp. On High Temperature Technology (Butterworths, London, UK 1967) 215-233

[79] H.U. Anderson, in: Processing of Crystalline Ceramics, eds. H. Palmour III, R.F. Davis and T.M. Hare (Plenum Press, New York 1978) 469-477

[80] L.A. Chick, J.L. Bates, L.R. Pederson and H.E. Kissinger, in; Proc. 1st Intl. Symp. on Solid Oxide Fuel Cells, ed. S.C. Singhal (The Electrochemical Society, Pennington, New Jersey 1989) 170-187

[81] G. L. Messing, S.C. Zhang and G. Jayanthi, J. Am. Ceram. Soc. 76 (1993) 2707-2726

CHAPTER 2

Experimental

2.1. Sample Preparation

The properties of electroceramic materials such as YSZ are highly dependent on the nature of the starting materials e.g. particle size and impurity content. The processing of the starting materials is thus very important when producing high quality ceramics.

2.1.1. Powder Preparation

2.1.1.1. Solid State Synthesis

Binary and Ternary Zirconia based compositions were prepared by conventional solid state mixing. Stoichiometric amounts of the pre-dried oxide powders were ground together, under acetone, in an agate mortar and pestle for 20 minutes.

2.1.1.2. Ball Milling

For improved mixing, homogenisation and reducing particle size, a Fritsch planetary micro mill "pulverisette 7" was used. Powders were placed into Zirconia grinding bowls (25 ml volume) with seven Zirconia balls (12 mm diameter). Acetone was used as a suspension liquid for the powder, with a typical liquid to powder ratio of 1 mlg^{-1}. Individual processing conditions will be discussed in more detail in the relevant results chapters.

2.1.1.3. Coated Yttria-stabilised Zirconia

Tioxide Specialities Ltd supplied 8 and 15 mol% Yttria-coated Zirconia powder. The powder was produced by a novel route, which involved intimately coating ultra fine Zirconia crystallites with the desired level of Yttria. The process is summarised schematically in Figure 2.1. Zirconium tetrachloride was decomposed with oxygen in a D.C. plasma at 1200°C producing an ultra fine, high purity, Zirconia powder. The resultant powder was suspended as an aqueous slurry, and the Yttria dopant added. By careful control of pH, the Zirconia crystallites were coated with Yttria. The coating

process could be repeated until all of the Yttria coating had been applied to the Zirconia. The Yttria-coated Zirconia was then filtered and ball-milled to reduce particle size. The powder was used as received.

2.1.1.4. Co-precipitated Yttria-stabilised Zirconia (TZ-8Y)

A commercially available 8 mol% Yttria-stabilised Zirconia (TZ-8Y), produced by the Tosoh Corporation (Japan), was used. Tosoh prepared the powder by the co-precipitation of yttrium and zirconium salts. The process is summarised schematically in Figure 2.2. This powder is the material generally used in SOFC research and has been well characterised by other workers [1,2]. Typical properties are listed in Table 2.1. The powder was used as received.

Table 2.1. Typical properties of as-received Tosoh co-precipitated 8 mol% YSZ.

Crystallite size	250 Å
Surface area	16 m^2g^{-1}
Average particle size	0.06 μm
Bulk density	5.90 gcm^{-3}

2.1.2. Powder Compaction

Powders were uniaxially pressed using cylindrical steel dies of 13mm diameter. The dies were regularly cleaned with a light oil in order to prevent lamination/cracking of the pellets when removed from the die. A typical pressing pressure was 2000 $kgcm^{-2}$.

2.1.3. Sintering

Sintering is the general name for the process of densification of a polycrystalline body, with or without the presence of a liquid phase to aid the transport of matter.. The driving force for sintering is reduction in the surface free energy associated with a decrease of surface area in powder compacts due to removal of solid-vapour interfaces. Sintering is most usually carried out using a finely powdered material in the form of a compact at temperatures close to and below the solidus. During the initial stages of sintering at subsolidus temperatures, an increase in the areas of interparticle contact

occurs with time. 'Necks' form between grains which grow thicker and have the effect of pulling the crystals closer together, thereby increasing the density of the body. With increasing time or temperature, the body continues to shrink and the pores between the particles become smaller and lose their connectivity. If the pores can shrink to zero size or be 'swept out' to the surface of the body by grain growth, then the bulk density of the body approaches the true or theoretical crystal density. The presence of a small amount of liquid usually speeds up the sintering process greatly and the onset of sintering may occur at much lower temperatures than in the absence of a liquid. The presence of an excessive amount of liquid is obviously undesirable if the body is to maintain its shape and strength.

The possible paths for material transport which may occur during three stages of sintering are summarised in Table 2.2.

Table 2.2. Alternative pathways for material transfer during sintering [3].

Transport Path	Sink of Material	Source of Material
Surface Diffusion	Surface	Neck
Lattice Diffusion	Surface	Neck
Vapour Pressure	Surface	Neck
Boundary Diffusion	Grain Boundary	Neck
Lattice Diffusion	Grain Boundary	Neck

In the case of the ZrO_2-Y_2O_3 system, the melting point is well above 2500°C over the entire composition range. This means that reaction of these two oxides has to occur by purely solid state diffusion at high temperatures i.e. 1500-1700°C. The driving force for such ceramic powders with low vapour pressures is the difference in free energy between the neck region and the surface of the particles.

It is possible to add impurities which lower the melting point of the system but these impurities generally have a detrimental effect on conductivity and high temperature mechanical properties. Thus, recent materials research has focussed on producing ultrafine grained powders prepared by advanced processing techniques [4-7]. In a previous study the differences in sintering characteristics of YSZ produced by different routes was studied in detail by Gibson et al [8].

The process of solid state sintering involves densification by the reshaping of compacted powder through materials transfer by solid state diffusion of ions. The sintering process involves several stages [9, 10]:

(1) Neck formation between adjacent grains.

(2) Subsequent neck growth and densification producing a decrease in pore size. The microstructure consists of a 3D array of channel like pores. Some grain growth may be observed at this stage.

(3) A closed pore stage, where a small amount of porosity exists surrounded by grains. Grain growth can occur at this stage.

Linear shrinkage is approximately proportional to the inverse of the particle radius but is not greatly affected by sintering time so that small particles (~ 1μm) with short diffusion distances are suitable for densification. The need for very fine particle sizes can be removed by using hot uniaxial pressing which utilises heat and pressure during sintering. This method produces higher density and smaller grain sizesat lower temperatures compared with uniaxial pressing and is particularly suited for the fabrication of thin plates.

In this study, the effect of TiO_2 additions and Al_2O_3 additions on the sintered density of the YSZ system are studied in chapters 3 and 5 respectively. The effect of density on conductivity is also discussed in chapter 3.

Pellets, which were prepared by uniaxial pressing, were sintered in a Carbolite RHF 1600°C muffle furnace with a 13% Rh/Pt - Pt thermocouple. Temperature variation was less than ± 5°C. For controlled cooling and heating regimes, a Eurotherm 818P programmable controller was used. A typical sintering regime involved a pre-sinter dwell at 1000°C for 1 hour, a heating rate of 10°C/min, a sintering dwell of 1500°C for 24 hours and a cooling rate of 10°C/min to 1000°C.

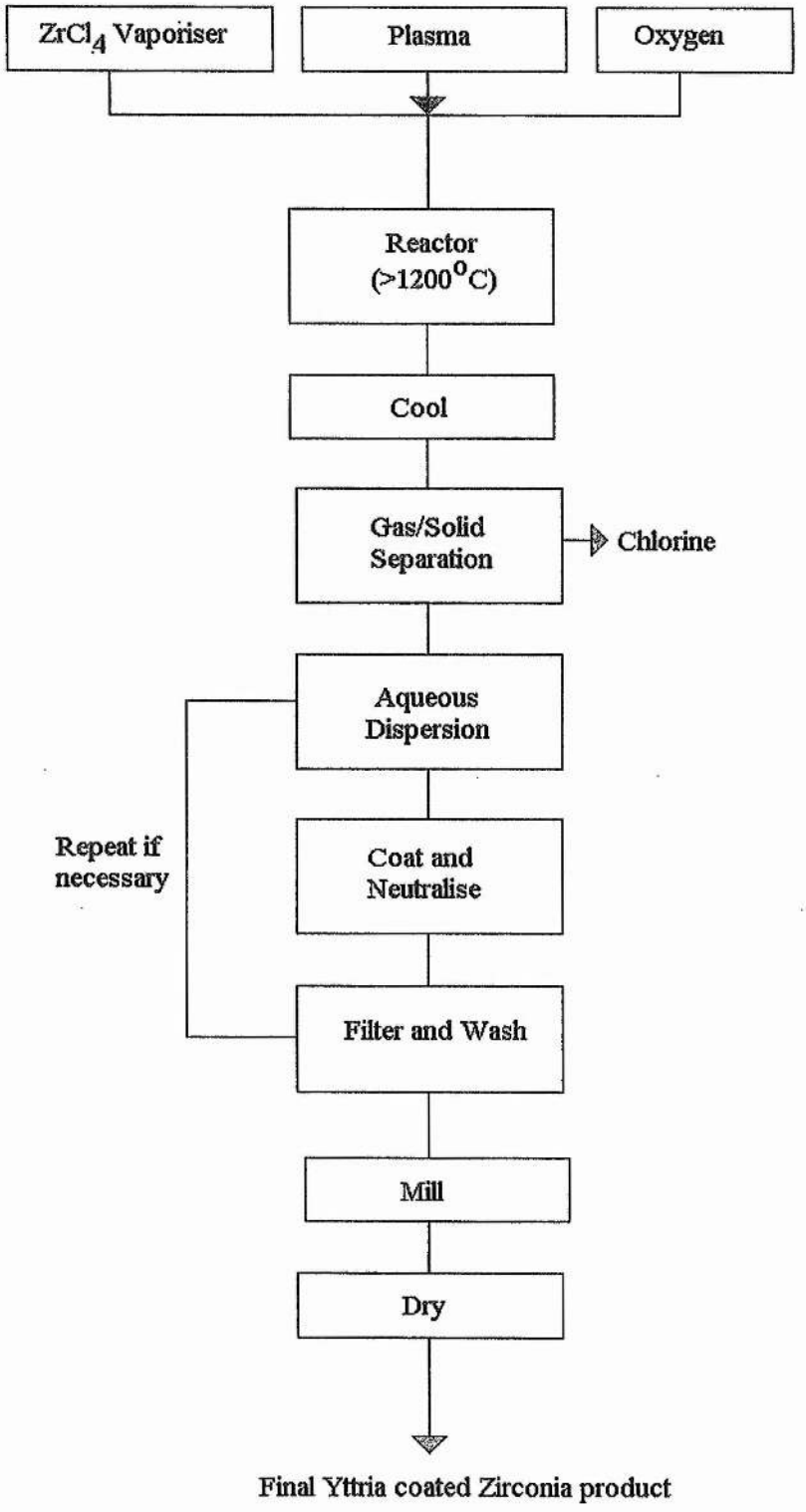

Figure 2.1. Production route for Tioxide Yttria-coated Zirconia.

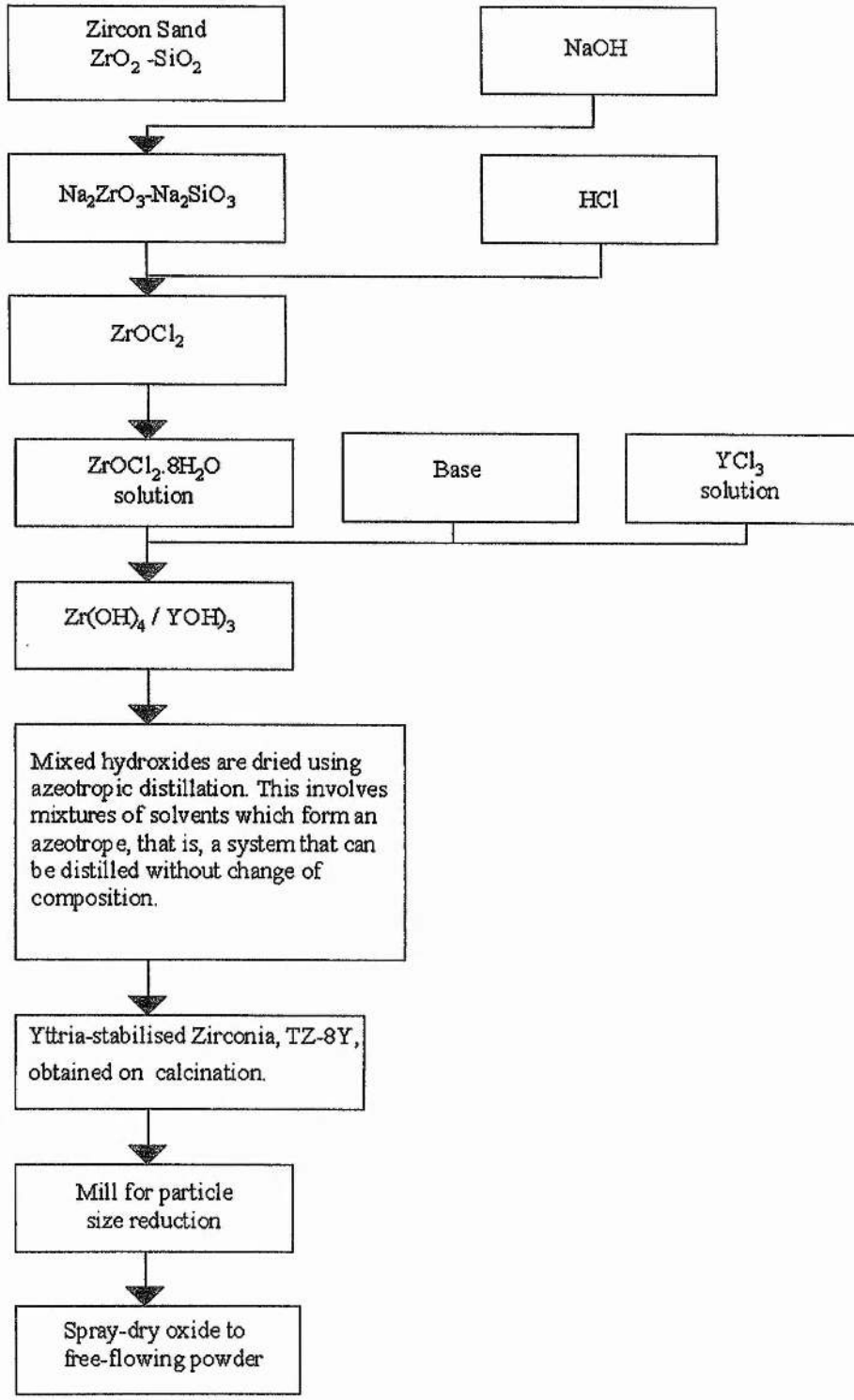

Figure 2.2. Production route for Tosoh co-precipitated Yttria-stabilised Zirconia, TZ-8Y (Tosoh Corporation, Japan).

2.2. Phase Diagrams

Phase diagrams summarise in graphical form the ranges of temperature and composition over which certain phases or mixtures of phases exist under conditions of thermodynamic equilibrium. The fundamental rule on which phase diagrams are based is the phase rule. The phase rule applies strictly only to conditions of thermodynamic equilibrium but in practice it also has great value in some non-equilibrium situations.

The phase rule is given by the equation $P + F = C + 2$, where P is the number of phases present in equilibrium, C is the number of components needed to describe the system and F is the number of degrees of freedom or independent variables taken from temperature, pressure and composition of the phases present.

The number of phases is the number of physically distinct and mechanically separable (in principle) portions of a system, each phase itself being homogeneous. The distinction between different crystalline phases is usually clear. The distinction between different crystalline phases made from the same components but of different composition is usually clear . It is also possible to get different crystalline phases having the same chemical composition. This is known as polymorphism. For example, TiO_2 can exist as Anatase or Rutile, which have different crystal structures.

The number of components of a system is rather more difficult to visualise. It is the number of constituents of the system that can undergo independent variation in the different phases; alternatively it is the number of constituents needed in order to describe completely the compositions of the phases present in the particular system. For example all of the Yttria stabilised Zirconia compounds can be considered to be made from ZrO_2 and Y_2O_3 in varying proportions. ZrO_2-Y_2O_3 is therefore a two-component system even though there are three elements present, Zr, Y and O.

The number of degrees of freedom of a system is the number of independently variable factors taken from temperature, pressure and composition of phases, i.e. it is the number of these variables that must be specified in order that the system be completely defined.

In refractory systems with very high melting temperatures, such as Y_2O_3 - ZrO_2, the vapour pressure of the solid phases and even that of the liquid phase is negligible in comparison with atmospheric pressure. The vapour phase is effectively non-existent, and need not be regarded as a possible phase for work at atmospheric pressure. Such systems are called condensed systems and the phase rule is modified accordingly to give the condensed phase rule, P + F = C +1 (instead of +2). Ternary systems have four independent variables: pressure, temperature and the composition of two of the components. If the composition or concentration of two of the components in a phase is fixed, the third is automatically fixed by difference. As the systems described in this study are not volatile, the ternary system can be described by the condensed phase rule, i.e. $P + F = C + 1 = 4$.

Ternary systems are represented by equilateral triangles and the three components form the three corners of the triangle. Temperature is represented by the vertical axis, perpendicular to the plane of the triangle. A three dimensional prism is needed to fully display the effects of varying composition and temperature. In order to display ternary equilibria on paper it is normal practice either to project the melting relations on to the composition triangle, in much the same way that a geographical contour map is a projection of altitude, or to construct isothermal sections.

Ternary compositions within equilateral triangles are given by reference to a grid, Figure 2.3. Each of the two binary edges is divided into a hundred divisions (only ten are shown for clarity). Point A corresponds to 100% A; the edge BC corresponds to 0% A and the line XY to 10% A. Thus the A content of any ternary composition is given by drawing a line through that composition and parallel to the BC edge. The A content is then read off from the intersection of this line with either the AB or AC edges, respectively. Point P has a composition 30% A, 30% B and 40% C. Compositions can be in either atom per cent or mol per cent or in weight percent. In practice, it is usually preferable to use mol per cent for inorganic systems because the formulae of binary and ternary phases are then clearly related to the composition.

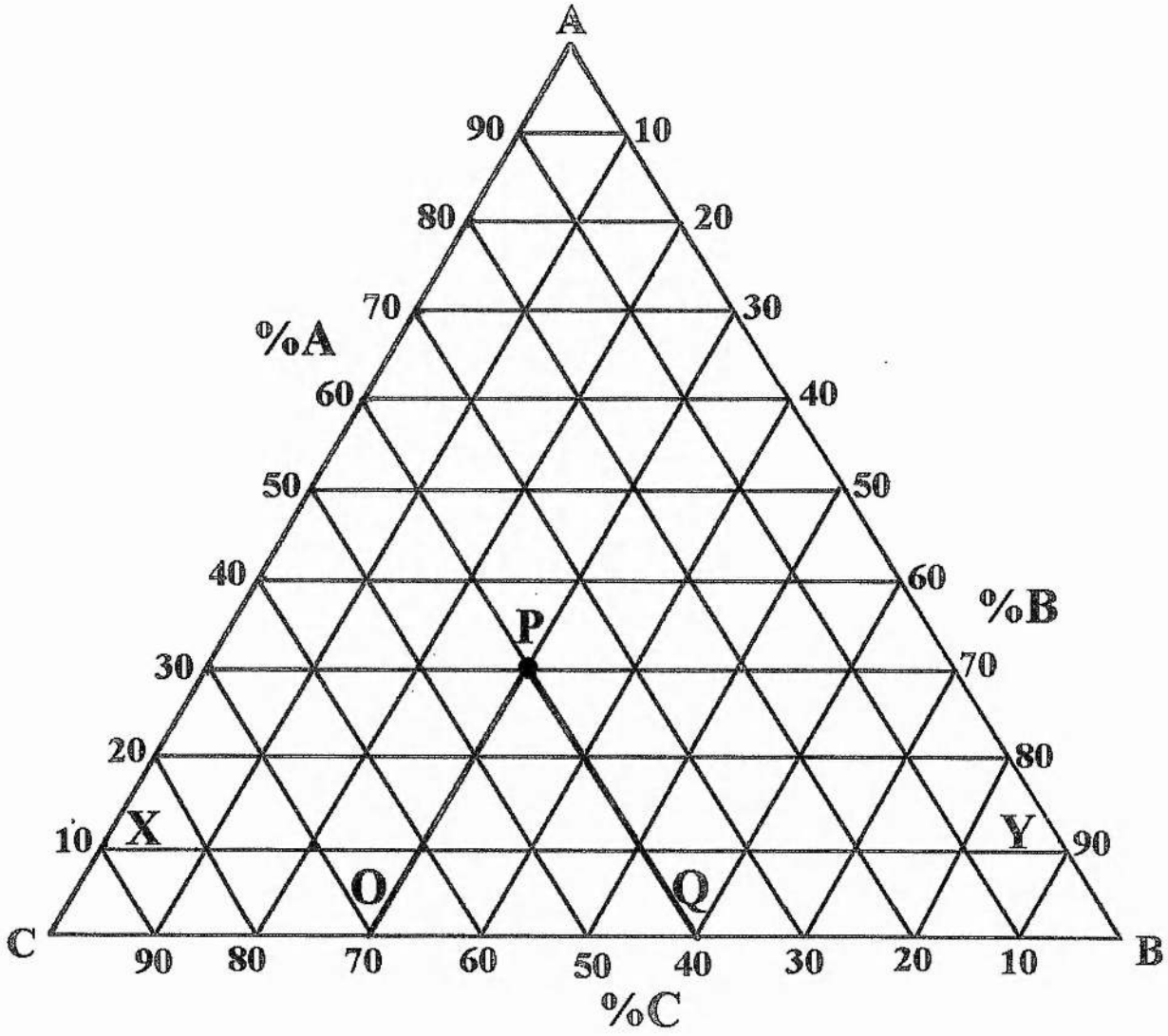

Figure 2.x. Triangular grid for representing compositions of three component systems.

2.3. Sample Characterisation

2.3.1. Density measurements

The conductivity of ceramic bodies is maximised when the density of the body is 100% of theoretical density, therefore it has been important to prepare samples which have densities as close to the theoretical value as possible. The theoretical densities of compounds with the cubic fluorite crystal structure were calculated using the unit cell parameter, a in the equation below [11], in which FW is the formula weight in $gmol^{-1}$ and Z is the unit cell content (formula units).

$$\text{Theoretical Density, } \rho_0 = \frac{1.66 \times FW \times Z}{a^3} = \frac{6.64 \times FW}{a^3} \ gcm^{-3}$$

Sintered densities were obtained from the mass and geometric dimensions of the pellets. Sample mass was measured to $\pm$ 0.1 mg and sample radius (r) and thickness (t) to $\pm$ 0.001mm. The density (gcm^{-3}) was calculated from the equation

$$\rho = \frac{\text{mass}}{\pi r^2 t}$$

The densities were expressed as a percentage of the theoretical density, which for 8 mol% YSZ (Hafnia free) was calculated to be 5.959 gcm^{-3} [12].

Correction of conductivity data for porous samples was achieved by multiplying the measured conductivity by ρ/ρ_0. A more detailed study of correcting conductivity for density is given in Chapter 3.

2.3.2. X-Ray Diffraction

X-ray diffraction was carried out using a Stoe Stadi P automated diffractometer, operating in transmission mode. A germanium monochromator was used to select Cu

$K\alpha_1$ radiation and X-Rays of wavelength 1.54056 Å were used. Lattice parameters, and relative phase contents were determined using the associated software.

Measurement of the diffracted X-Rays was made using a small linear position sensitive detector (PSD) which had a range of approximately 7° 2θ. The detector could move through 10 - 140° 2θ in small increments, the step width, which could be determined by the user.

Samples were prepared by lightly smearing an acetate foil with Vaseline, on to which approximately 1mg of powdered sample was applied. The acetate foil was held in a circular holder. The holder was placed into the diffractometer and rotated continuously to minimise preferred orientation.

For lattice parameter determination, X-Rays were collected over a range of 10-110° 2θ, typically with a step width of 0.5° for the PSD. Data analysis was performed using the associated Stoe software. The collected raw data was stored in the file user.stoe. An output file listing peak positions (2θ and d-spacing), the peak widths (full width at half maximum, FWHM) and relative peak intensity (I/I_0) of all reflections were obtained from the raw data. This was done by using the peak searching program PKS, and by selecting the average peak width and the significant intensity to background ratio.

Lattice parameters were obtained using the lattice refinement program LATREF. The refinement required the input of the approximate unit cell dimensions. Alternatively, the Miller indices for some or all of the reflections could be input using the peak editing program PEAKED prior to refinement. From the symmetry chosen by the user, the LATREF program generates all the possible reflections and, using the least squares procedure, the lattice parameters were refined. The quality of the refinement could be determined by the error in the lattice parameters and the values of the maximum and average differences in $2\theta_{obs}$ and $2\theta_{calc}$.

2.3.3. Neutron Diffraction

Powder neutron diffraction was carried out at the UK spallation neutron source ISIS at the Rutherford Appleton Laboratory. Spallation is the process of creating a continuous spectrum of neutron energies by bombardment of a heavy metal target (depleted uranium or tantalum) by high energy protons. The protons are initially accelerated to 70keV using a linear accelerator (LINAC). They are then injected into a synchrotron storage ring, where they are accelerated to approximately 600 GeV. At fixed intervals, these highly energetic protons are released from the storage ring and allowed to fall on the heavy metal target. The neutron beam is thus similar to a neutron beam from a reactor, the difference being that the neutrons produced by the synchrotron source have a well defined pulse structure. The number of neutrons diffracted can be analysed as a function of time to reach the detector. More energetic neutrons arrive quickly at the detectors and hence have shorter "times of flight" and vice versa. The time of flight can be converted to the equivalent d-spacing using the de Broglie's wave/particle duality relationship and the Bragg diffraction law as follows:

$$\lambda_n = h/m_n v_n = ht/m_n l$$

(λ_n, m_n and v_n are the de Broglie wavelength, mass and velocity of the neutron, respectively; t is the time of flight and l is the distance between neutron chopper and detector.)

$$\therefore \quad \lambda_n = ht/m_n l = 2d\sin\theta$$
$$d = ht/2m_n l\sin\theta$$

(θ is the angle between beam and detector, d is the lattice plane spacing for the diffraction condition). Bragg reflections are measured at fixed scattering angles, by monitoring the 'time-of-flight' and so the wavelength (λ) and d-spacing are obtained.

Data were collected using the Polaris diffractometer. Polaris is a medium resolution, high intensity instrument, allowing data to be obtained in a relatively short time. Samples were contained in cylindrical vanadium cans and a vanadium wound

furnace was used between 20 and 900°C. A thermocouple was attached next to the sample can, ensuring accurate temperature control of ± 1°C. The sample space was evacuated to 10^{-5} Torr. The detector configuration consists of back scattering, 90° and low angle detector banks. Back scattering detectors produce the highest resolution, while low angle detectors allow very large d-spacings to be obtained. The 90° bank of detectors was used as this allows a broad range of d-spacings with good resolution. Data were collected over the time-of-flight range 2500-19500 microseconds. The obtained data were converted to a data file suitable for refinement using the program GENIE.

Data analysis was performed on the in-house software on the ISISE VAX mainframe situated at the Rutherford Appleton Laboratory. The peak shape was modelled using a Voigt function, with double exponential decay. Crystal structures were refined using the Reitveld method with the program TF14LS [13, 14]. Refinements were carried out in a similar approach to Argyriou [15] and were carried out in the space group Fm3m, with the occupancies and positions of Zr/Y and O fixed. Firstly, the scale factor, background and lattice parameters were refined. Finally, the isotropic temperature factors and a peak shape and peak centring function were refined. The quality of the refinement was determined by the value of the weighted profile R-factor, R_{wp}.

2.3.4. 2-Probe AC Impedance Spectroscopy

AC impedance spectroscopy is a well-defined technique used to investigate and characterise the electrical properties and microstructure of a variety of ceramic materials [16]. The technique has been extensively used to measure the ionic conductivity of Yttria-stabilised Zirconia [17], the effects of sintering [18], segregation of impurities [19], defect interactions [20, 21] and ageing phenomenon [22]. The electrical properties of a variety of materials are often studied using D.C. techniques, however, it is difficult to determine which of the different electrical components in the material and the electrodes dominates the response. AC impedance spectroscopy has the advantage that individual components of the material can be separated e.g. bulk, grain boundary, sample/electrode interface, allowing detailed characterisation.

2.3.4.1. Theory

A comprehensive study of AC impedance spectroscopy and its applications has been made by MacDonald [23]. The technique involves applying an AC voltage (V) of varying frequency across the sample

$$V(t) = V_o \sin \omega t$$

The resultant AC current (I) leads the voltage by ϕ, the phase shift of the transfer function, therefore

$$I(t) = I_o \sin (\omega t + \phi)$$

The transfer function can be defined as $H(\omega) = |H(\omega)| e^{j\phi}$ where

$|H(\omega)| = V_o/I_o$ and $|H|$ is the modulus of the transfer function.

$H(\omega)$ is an impedance value and is denoted as $Z(\omega)$ or Z^*.

The complex impedance, Z^*, of the electrochemical cell is a vector quantity and it is a complex number in which the magnitude and direction of the complex impedance can be represented either in polar or Cartesian co-ordinates:

$$Z(\omega) = |Z|e^{j\phi}$$

$$Z(\omega) = Z' - jZ''$$

where Z' is the real part of the impedance and Z'' is the imaginary part.

The relationships between these quantities are :

$$|Z|^2 = Z'^2 - Z''^2$$

$$\phi = \text{Arc tan } (Z''/ Z')$$

$$Z' = |Z| \cos \phi$$

$$Z'' = |Z| \sin \phi$$

The complex impedance can be plotted by Cartesian (Z" vs. Z') or polar co-ordinates (|Z| vs. ϕ), as shown in Figure 2.3.

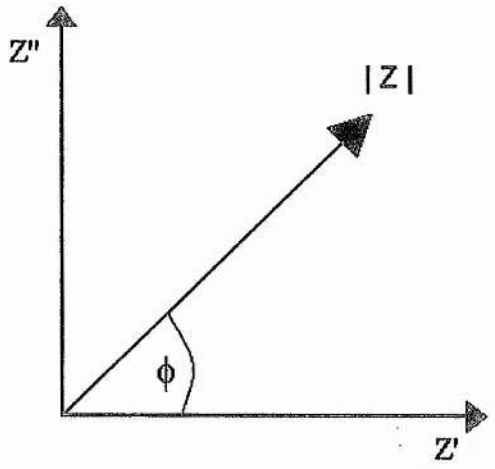

Figure 2.3. The complex impedance plane, which may be plotted as Cartesian (Z" vs. Z') or polar co-ordinates (|Z| , ϕ).

By measuring the amplitude and phase shift (ϕ) of the current for any frequency (ω), with a fixed applied voltage (V), the impedance Z is calculated and the real and imaginary components can be determined. By varying the frequency from 100mHz to 10MHz, a complex impedance plot such as Figure 2.4. can be obtained.

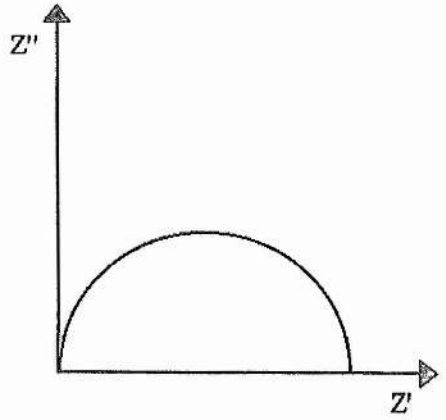

Figure 2.4. A typical complex impedance plot, obtained over a wide frequency range.

2.3.4.2. Equivalent Circuits Analysis

Polycrystalline ceramic materials can obtain many components (e.g. bulk, grain boundary, pores) which can be identified by AC impedance spectroscopy. Each component can be considered as consisting of a combination of resistive and capacitive elements. This combination of resistive and capacitive elements is called an equivalent circuit and, depending on the properties of the material, different combinations will apply. The simplest equivalent circuit is obtained for either an individual ideal resistor or an individual ideal capacitor. For an ideal resistor, current and voltage are in phase, thus

$$R = V_o / I_o$$

where R is the resistance (Ω); therefore

$$Z = R$$

So, for a phase shift $\phi = 0$, Figure 2.5. is obtained.

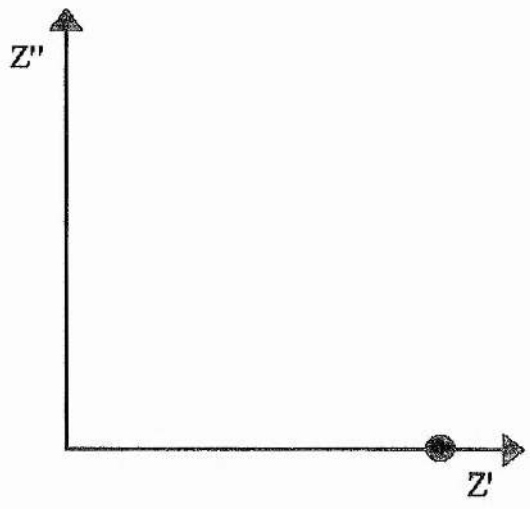

Figure 2.5. Complex impedance plane plot for an ideal resistor.

An alternative formalism is the complex admittance, Y*, which is equal to the inverse of the complex impedance $(Z^*)^{-1}$, so for an ideal resistor

$$Y^* = R^{-1}$$

For an ideal capacitor, the capacitance (F) is given by

$$C = q / V$$

where q is the charge stored (C) and V is the voltage (V) across the capacitor.

$$I = dq / dt = C\,(dV / dt)$$

For a capacitor, the current leads the voltage by 90° - out of phase -, therefore,

$$I = \omega C V_o \sin(\omega t + \pi / 2)$$

therefore

$$Io = \omega C V_o$$

An ideal capacitor allows the flow of an AC current but blocks a D.C. current (i.e. Z'=0), therefore

$$Z^* = 1 / j\omega C$$

and

$$Y^* = j\omega C$$

producing the complex plane in Figure 2.6.

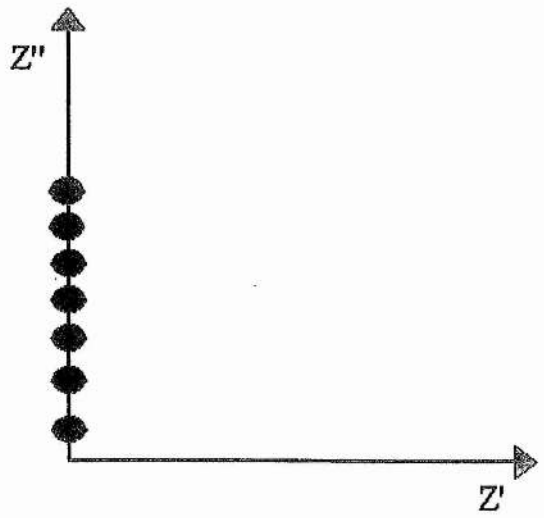

Figure 2.6. Complex impedance plane plot for an ideal capacitor.

Most components e.g. bulk, can be modelled by a resistive element and a capacitive element in parallel. the complex impedance of the parallel RC element is defined as

$$1 / Z^*_T = 1 / Z^*_1 + 1 / Z^*_2$$

or $$Y^*_T = Y^*_1 + Y^*_2$$

and therefore $$Y^*_T = 1 / R + j\omega C$$

i.e. $$Y' = 1 / R \quad \text{and} \quad Y'' = \omega C$$

The total complex impedance is given by

$$Z^*_T = (Y^*_T)^{-1} = (1/R + j\omega C)^{-1}$$

$$= \frac{R}{1 + j\omega RC} \cdot \frac{(1 - j\omega RC)}{(1 - j\omega RC)}$$

$$= \frac{R(1 - j\omega RC)}{1 + (\omega RC)^2}$$

$$= \frac{R}{1 + (\omega RC)^2} - j\,\frac{R(\omega RC)}{1 + (\omega RC)^2}$$

$$= Z' - jZ''$$

i.e. $$Z' = \frac{R}{1 + (\omega RC)^2} \quad \text{and} \quad Z'' = \frac{R(\omega RC)}{1 + (\omega RC)^2}$$

By varying the frequency from 0.1 to 10^7 Hz a complex plane plot, illustrated in Figure 2.4. is obtained. When $\omega RC = 1$, a maximum in Z" is obtained and at this point $Z' = Z'' = R/2$.

From this simple derivation, the resistance and capacitance of an unknown component can be determined by obtaining the real and the imaginary impedances over a wide range of frequencies. From Figure 2.4. the resistance equals the real impedance when the frequency equals zero i.e. at the intercept on the x-axis. The capacitance is calculated from the equation

$$2\pi\omega RC = 1$$

using the frequency (ω) when Z" is a maximum.

The equivalent circuit is described by parallel RC elements, connected in series. The impedance diagrams of such materials are thus generally composed of several capacitive arcs. The equivalent circuit for Yttria-stabilised Zirconia ceramics, Figure 2.7. typically can be modelled by three parallel RC elements and a diffusion element connected in series. The semicircle at high frequency is assigned to the bulk component and the adjacent semicircle at lower frequency is assigned to the grain boundary component. The low frequency semicircle is not associated purely with the YSZ ceramic but with the charge transfer reaction $2O^{2-} \leftrightarrow O_2 + 2e^-$ and the low frequency spike, or Warburg spike, is due to oxygen diffusion at the electrode surface. A typical impedance spectrum is shown in Figure 2.8.

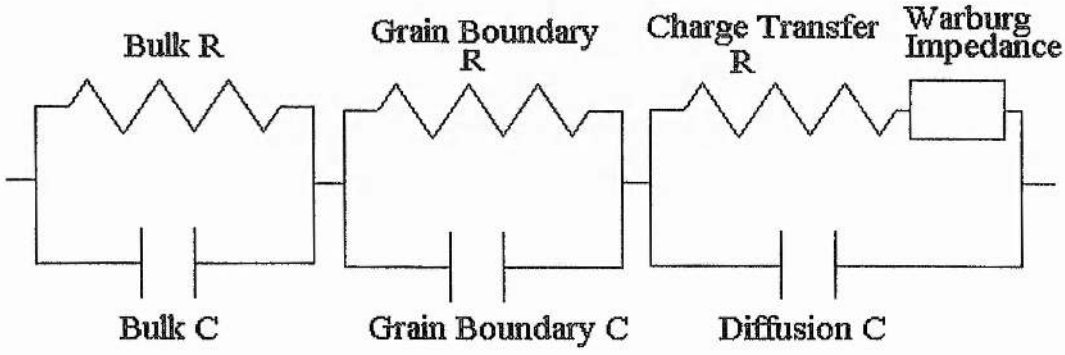

Figure 2.7. The Equivalent circuit for a polycrystalline YSZ ceramic.

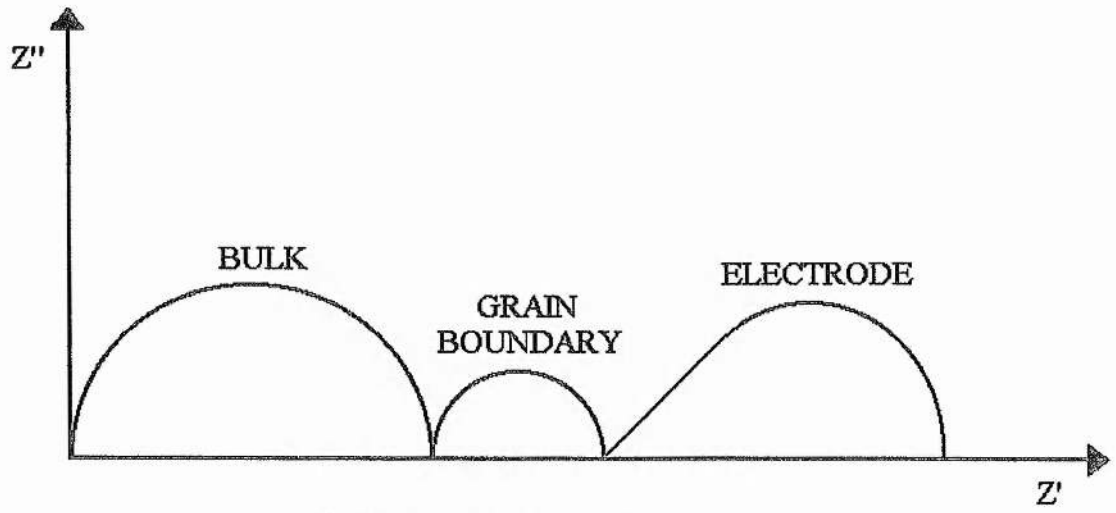

Figure 2.8. Typical complex impedance plane plot for 8 mol% YSZ.

As the bulk and grain boundary components are the only components of interest in this study, a short description of two parallel RC circuits in series follows. From the equations describing Z' and Z'' above and using $Z = Z_1 + Z_2$, the real and imaginary contributions from each RC element are simply summed.

So, $$Z' = R_1[\ 1/(1+(\omega R_1 C_1)^2] + R_2[1/(1+(\omega R_2 C_2)^2]$$

$$Z'' = R_1[\ (R_1 C_1)/(1+(\omega R_1 C_1)^2 + [(R_2 C_2)/(1+(\omega R_2 C_2)^2]$$

The combination of RC elements in series is a simplified model and it has been shown that more complicated equivalent circuits can describe experimental data more accurately [15,16,17]. The simplified model describes exact semicircles for each RC element; however, semicircles often appear compressed, with their centres appearing below the real Z' axis. This non-ideal behaviour may be due to a distribution in relaxation times within each component and models using a constant phase element (CPE) have been used to describe such behaviour.

In addition to a complex plane plot, a bode plot of the imaginary impedance (Z'') versus log (frequency) is extremely useful. The resistance value obtained from this type

of Bode plot is usually different from the value obtained from a complex impedance plot due to the non ideal behaviour of the sample being measured.

2.3.4.3. Capacitance Values

The capacitance values can be calculated for any RC element and can give an indication of what component of the material is being measured. Capacitance values and their possible interpretation are shown in Table 2.2. Similarly, the magnitude of the capacitance of a bulk or grain boundary component can give an indication as to the degree of sintering of the ceramic.

Table 2.2. Capacitance values and their possible interpretation.

Capacitance (Fcm^{-1})	Phenomenon Responsible
10^{-12}	Bulk
10^{-11}	second phase/porosity
10^{-11} - 10^{-9}	grain boundary
10^{-7} - 10^{-5}	Sample-electrode interface
10^{-4}	Electrochemical reaction

Poor interfacial contact between the ceramic and the Pt electrode can also give rise to a response with a capacitance of the order of 10^{-11} Fcm^{-1} [16]. This is brought about due to the contact area between the ceramic and Pt electrode being 10^{-3} % lower than it should be. The capacitance value is thus 10^{-5} times lower than the response obtained from a good contact.

2.3.4.4. Modulus

As AC impedance is a spectroscopic technique, there is a limit on the resolution which can be achieved. The value of the time constant τ for each RC element in a polycrystalline sample, must be separated by at least two orders of magnitude for the independent semicircles in the complex impedance plot to be convoluted.

The detection of an RC element therefore depends on the relative magnitude of its components. The use of the complex modulus formalism changes the dependence

and weighting of the response with frequency and is, therefore used to observe RC elements that maybe masked in the basic complex impedance plot.

The magnitude of the Z" term is proportional to the magnitude of R, whilst the magnitude of the M" term is proportional to the inverse of the capacitance 1/C. For this reason, the size of the Debye peaks differ depending on which formalism is used. The modulus plots highlight the RC element with the smallest capacitance whilst the impedance plots are dominated by the RC element with the maximum resistance. For a single element, both the Z" and M" peaks should be coincident. At the peak maximum in the Z" and M" spectroscopic plots,

$$2\pi fRC = 1$$

which results in

$$M''_{max} = C_0/2C$$

where

$$C_o = e_o A_o/l$$

C_o is the capacitance of the empty measuring cell of electrode area A_o and electrode separation l in a a vacuum and e_o is the dielectric permittivity of free space 8.854×10^{-14} Fcm^{-1}.

The resistance correspondong to this element can be calculated from the M" spectroscopic plot by,

$$R = (1/\omega) \times (1/C) = (2/\omega) \times (1/2C) = (2/\omega) \times (M''_{max}/C_o)$$

Therefore, two methods exist for determining the resistance of an element.

1) From the intercept with the real axis in the comple impedance plot

2) From the frequency and value of M" at the peak maximum in the M" spectroscopic plot.

For ideal elements, the value of the resistance obtained by the two methods should be equal. It is, however, more usual for materials to give non-ideal responses. The semi-circles produced in the complex impedance plot are often depressed, and have centres which are located at an angle θ below the real axis, Figure x.x. This can be attributed to a distribution in relaxation times within the bulk or other relaxations with time constants within two orders of magnitude of the bulk. The simple combination of RC elements having single time constants are insufficient to model this type of behaviour. They must instead be combined with a constant phase element (CPE). This is an element devised to account for the frequency dependence of the conductivity. It is not an ideal lumped constant element but a correction factor calculated from complex non-linear least squares analysis, which describes the behaviour of an element whose nature deviates from that of a pure resistor or capacitor. The fractional exponent φ shown in Figure 2.9. is a frequency independent parameter, which is used to explain a non-ideal response. This factor can take the values $0<\varphi<1$. The ideal Debye response, which has a single value for the relaxation time constant, can be described by $\varphi = 1$ and $\theta = 0$. For a non ideal response, however, the inclusion of a CPE is necessary in order to model the system. The term φ now takes a fixed value between 0 and 1, where the inductance of the constant phase element can be described as:

$$Z^* = A(j\omega)^{-\varphi}$$

Where φ and A are fixed frequency independent parameters.

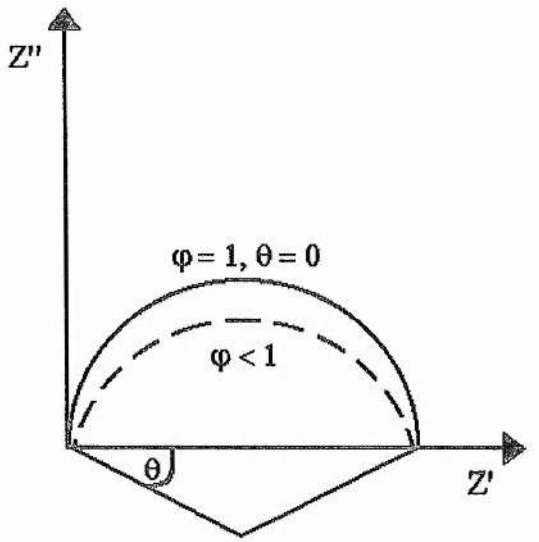

Figure 2.9. Complex impedance planes for an ideal Debye response $\varphi=1$, $\theta=0$ and a depressed semi-circle with its centre below the Z' axis described by θ and $1>\varphi>0$.

2.3.4.5. Conductivity and the Arrhenius Equation

Ionic conductivity in electroceramics, occurs by a process of activated hopping, just as in other crystalline solids, glasses or melts. This mechanism is represented graphically in Figure 2.10a. for an O^{2-} ion in a crystalline electroceramic as it moves along one direction in the ceramic. The potential energy is lowest at sites A and B which correspond to the energetically equivalent sites that may normally be occupied by O^{2-} ions. Between A and B, the potential energy passes through a maximum which represents the saddle point for an ion that is hopping from site to the next.

All ions in a solid vibrate due to their thermal energy, at a frequency, ν, that is around 10^{12} to 10^{13} Hz (i.e. cycles per second). In the absence of an applied electrical field, the vibrating ions have a distribution of energies. At temperature TK the probability that an ion has vibrational energy greater than E and could therefore hop between sites A and B in, or vice versa, is proportional to exp (-E/kT) where k is Boltzmann's constant. The number of jumps per second that each ion makes, on average, is proportional to ν exp (-E/kT). Thus, provided vacant sites are available for ions to hop into, some cations are able to hop, at random, even without an applied

electric field. Since the hops occur in all directions, at random, there is no net current flow.

On application of an electric field across the ceramic, the potential energy diagram is slightly modified, Figure 2.10b. For O^{2-} ions that are jumping towards the anode, the effective energy barrier is slightly reduced and for O^{2-} ions jumping towards the cathode, the energy barrier is slightly greater. The magnitude of these energy differences may be quantified as follows.

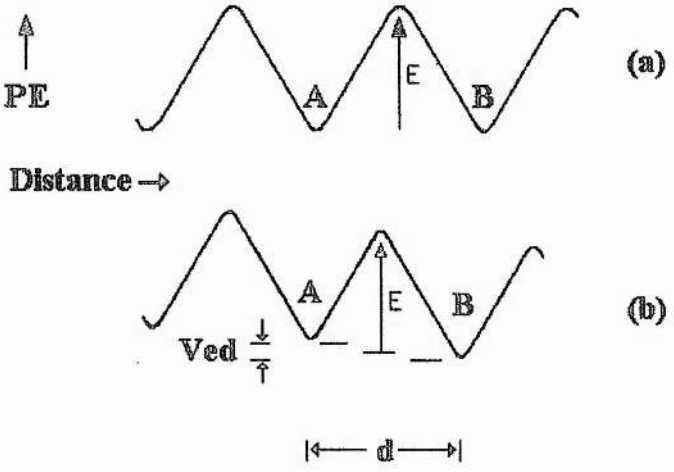

Figure 2.10. Motion of an ion in a solid.

For an applied field V, the work done by the field in moving an ion of charge e by a distance d in the direction of the field is equal to Ved. This work done corresponds to the difference in potential energy between sites A and B. The energy barrier to migration in the two directions A → B and B → A is given by (E - ½Ved) and (E + ½Ved), respectively, and hence it is more probable that an ion will jump from A to B than vice versa.

The net probability, P, of an ion jumping from A to B is given by

$$P \propto \nu \exp [-(E - \tfrac{1}{2}Ved)/kT] - \nu \exp [-(E + \tfrac{1}{2}Ved)/kT]$$

$$\propto \nu \exp (-E/kT)[\exp(eVd/2kT) - \exp(-eVd/2kT)]$$

The term in square brackets may be expanded as a power series and it may be shown that, for eVd <<<< kT, it reduces to eVd/kT, i.e.

$$P \propto eVd\nu/kT \exp(-E/kT)$$

The mean velocity of the ions, u, is given by $u = Pd$

The mobility, μ, of the ions is given by

$$\mu = u/V$$

and the conductivity, σ, is given by

$$\sigma = Ne\mu$$

where N is the number of mobile ions. Therefore,

$$\sigma = Ne^2d^2\nu/gkT \exp(\Delta S/k) \exp(-E/kT)$$

where $\exp(\Delta S/k)$ is a constant of proportionality, ΔS is the entropy of activation and g is the geometric factor that includes the possibility that, for a given ion, several jump directions are possible. The equation is often rewritten as

$$\sigma T = Ne^2d^2\nu/gk \exp(\Delta S/k) \exp(-E/kT)$$

On taking logs and plotting log σT against T^{-1}, a straight line should be obtained of slope equal to -E/k and intercept of $(Ne^2d^2\nu/gk) \exp(\Delta S/k)$. Sometimes the concentration, N, of mobile ions is also thermally activated with a temperature dependence given by

$$N = N_o \exp(\Delta S_f/k) \exp(-E_f/kT)$$

where N_o is the total number of potentially mobile ions in the structure and E_f, ΔS_f are the activation energy and entropy for the creation of mobile ions.

Combining the last two equations:

$$\sigma T = (e^2 d^2 \nu / gk)\, N_o \exp(\Delta S + \Delta S_f/k) \exp(-E + E_f)/kT)$$

The pre-exponential term can be further simplified to

$$\sigma T = A \exp^{(-Ea/kT)}$$

and is usually plotted as $\log \sigma T = \log A - Ea/kT$, which is generally a straight line for conducting materials.

The conductivity of the bulk or grain boundary component, usually quoted in Sm^{-1} is determined from the inverse of the geometrically corrected resistivity of the sample, i.e.

$$\rho = 1 / \sigma = R\, A/t$$

where A is the surface area, t is the thickness and R is the resistance.

The activation energy of any component is determined by measuring the change in conductivity with temperature. The slope of the Arrhenius plot, $\log \sigma T$ vs. 1/T, allows the activation energy to be calculated from the equation:

$$E_A = \frac{2.303 \times \text{slope} \times 1.38 \times 10^{-23}}{1.6 \times 10^{-19}} \quad (eV)$$

which reduces to

$$E_A = 0.1968 \times \text{slope}.$$

2.3.4.6. AC Impedance Sample Preparation

A platinum electrode was attached to one face of a sintered disc using platinum paste (Engelhard). The platinum paste was dried at 140°C for 15 minutes and this procedure was repeated for the other face of the disc. The disc was then sintered at 850°C in air for 30 minutes.

2.3.4.7. Experimental Procedure

The sintered disc was connected to a platinum wire jig using a compressive force applied by a spring. The jig consisted of a 30cm rod of alumina with narrow longitudinal holes through it attached to a larger rod of alumina that contained the pellet. Platinum wire was threaded through the inner rod and another platinum wire and a chromel/alumel thermocouple were threaded through the outer rod, Figure 2.11. The sample end of the jig was placed in a Carbolite horizontal tube furnace, fitted with a Eurotherm temperature controller. The temperature was accurately measured (± 1°C) using the chromel/alumel thermocouple, which was attached to a digital multimeter. Two terminal AC impedance measurements were performed using a Solartron 1260 Impedance Analyser, which was linked to the computer program Zview. An AC voltage of 100mV was applied, over a frequency range of 10MHz to 100mHz, with ten measurements being made for every decade in frequency. An integration time of 1 second per measurement was used with a delay time of 0.2 seconds between each measurement. Measurements were made, in air, over a temperature range of 250°C to 1000°C. Data were corrected for sample geometry and complex impedance plots allowed conductivities (Sm^{-1}) and capacitance (Fcm^{-1}) to be calculated.

2.3.4.8. Jig Correction

To correct for the resistance of the platinum wires in the measuring jig, the wires were connected to make a short-circuit, and the resistance was measured from the inductive response obtained between 300 and 1000°C. The jig resistance was found to increase slightly with temperature and a second order polynomial was derived which

was then applied to each sample impedance value obtained. The resistance of the jig was only significant with respect to the sample resistance at temperatures above 650°C for materials with a conductivity of ~10 Sm^{-1} at 1000°C. The stray capacitance of the jig was determined by measuring the impedance of the open circuit i.e. without the platinum electrodes in contact and was found to be 5 x 10^{-12} F; this low value would only affect the bulk capacitance. All presented data have been corrected for jig resistance and capacitance, where jig contributions were significant (≥0.1%).

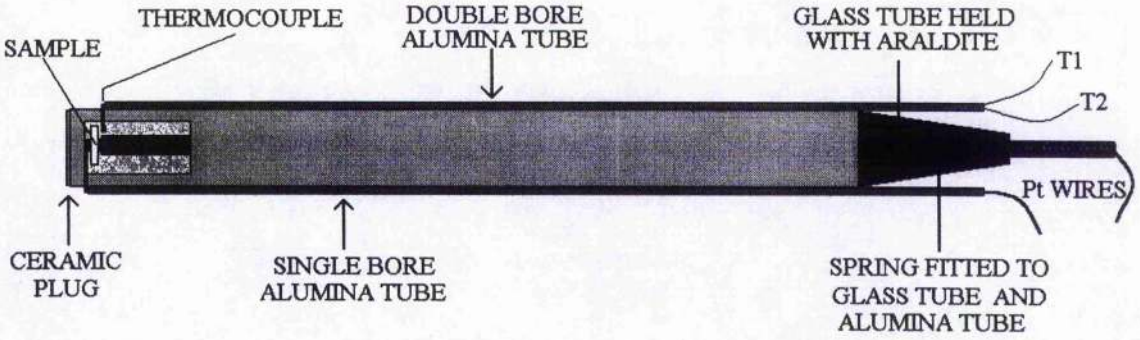

Figure 2.11. The compressive Pt wire jig used for 2-probe A.C. impedance analysis.

2.3.5. 4-Probe D.C. Conductivity Measurements

To measure the effect of reduced oxygen partial pressure on the conductivity of samples, a controlled atmosphere, Kanthal wound furnace was used. The oxygen partial pressure was determined using a Zirconia sensor. The operation of the sensor can be described by the Nernst equation:

$$V_0 = \frac{RT}{4F} \ln \frac{pO_2}{pO_{2,ref}}$$

where V_0 is the E.M.F. of the electrochemical cell, pO_2 is the partial pressure of oxygen in the gas to be measured, $pO_{2,ref}$ is the partial pressure of oxygen in equilibrium with the reference electrode and R,T and F have their usual meanings. Inside the YSZ tube is a reference gas such as air. The tube is coated with porous Pt electrodes to allow absorption and liberation of oxygen gas. If the partial pressure of oxygen that is to be

measured, PO_2, is less than the reference pressure $PO_{2,ref}$ oxide ions migrate through the solid electrolyte. By measuring the potential difference across the cell the oxygen partial pressure inside the furnace can be calculated.

2.3.7.1. Sample Preparation

Platinum foil electrodes were applied to the same face of the sample pellets (~10mm x 3mm) using organo Platinum paste in the configuration shown in Figure 2.13. The electrodes were dried of organic binder and then sintered at 900°C for 1 hour and attached to the sample holder by wrapping the Platinum foil electrodes around Platinum wires. The sample holder was placed inside the furnace which was sealed, heated up to 930°C and purged with 5% H_2 /Argon gas, which displaced the oxygen form the furnace and lowered the oxygen partial pressure. The reduction procedure took a few hours at most and then oxidation of the sample followed by turning off the reducing gas mixture and allowing air to naturally leak back into the furnace. The re-oxidation usually required several hours to approach equilibrium and so was carried out overnight.

The resistivity of the sample is calculated from the equation Rl/dt but renormalised to the two terminal resistance obtained from A.C. impedance in air to correct for any errors that may have been introduced by the difficult sample geometry. The current is applied to the outer edge of the pellet surface using a Keithley 220 Programmable Current Source and the voltage drop across distance l is measured using a Solartron 7065 Voltmeter. The oxygen partial pressure is measured by monitoring the voltage of the Zirconia sensor with a Solartron 7150 Digital Multimeter.

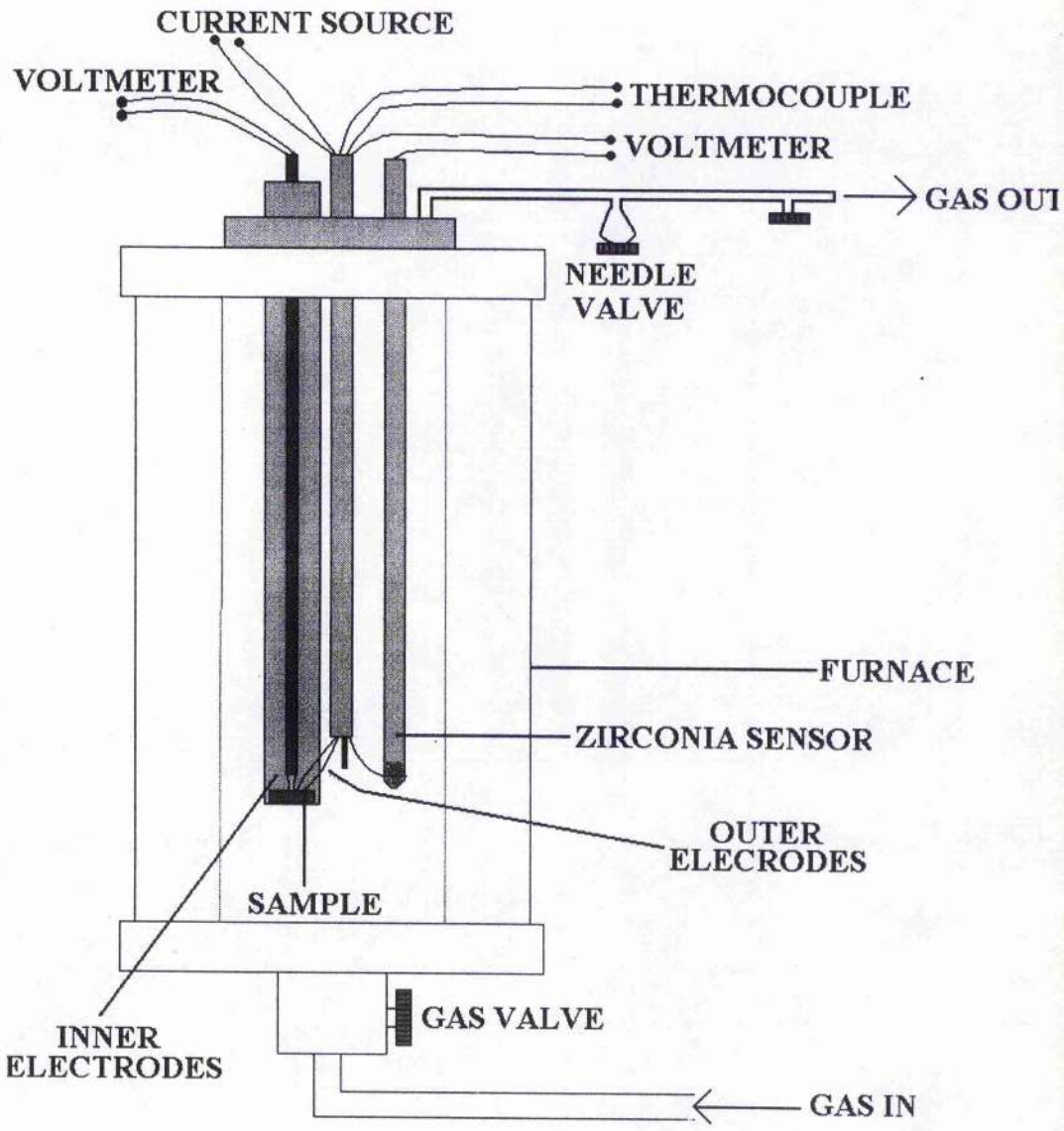

Figure 2.12. Pt wire jig for 4-probe D.C. conductivity measurements in a controlled atmosphere vertical furnace.

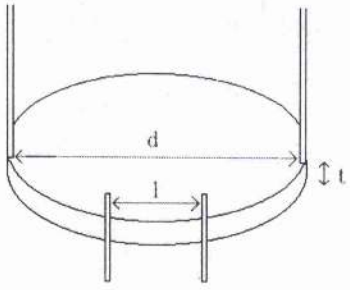

Figure 2.13. Electrode configuration for 4-probe D.C. Electrical Measurements.

2.3.6. Extended X-Ray Absorption Fine Structure Spectroscopy

Extended X-ray Absorption Fine Structure, generally referred to as EXAFS, was carried out at station 9.3 (Materials Science) at the UK Synchrotron Radiation source at the Daresbury Laboratory.

2.3.6.1. Synchrotron Radiation

Synchrotrons are particle accelerators, which were developed to study the basic structure of matter. In essence a synchrotron is an evacuated stainless steel ring in which charged particles are accelerated to very high energies. 'Pumping' in radio frequency radiation provides the energy and the particles are kept on a circular path by magnetic fields. The magnetic fields are produced by very powerful dipole electromagnets, referred to as bending magnets. Thus a synchrotron is not really a circle but straight portions linked by curved portions where the bending magnets are positioned.

Particles in a synchrotron can reach very high energies (in the GeV range; 1GeV = 10^9 eV ~ 10^{11} kJmol^{-1}). For light particles, like electrons and positrons these energies correspond to velocities approaching the speed of light and relativistic effects come into play. A property of a charged particle travelling in a curved path at relativistic speeds is that it emits electromagnetic radiation. This radiation is emitted tangentially to the orbit in front of the particle. This radiation is 'white' and covers all frequencies up to some cut-off determined by the energy of the particle. In addition, the radiation is emitted in a very thin, weakly divergent, pencil of light (i.e. highly collimated) which is polarised with the electric vector in the plane of the orbit.

Most synchrotrons are electron accelerators and usually several 'packets' or 'bunches' of electrons are orbiting at any one time. Clearly, the more electrons in orbit the higher will be the intensity of the radiation. Thus the current in the ring is a measure of the effective light intensity. In order to use the radiation it is 'taken off' at the bending magnets and travels down evacuated tubes to instruments. The light coming down these tubes is not continuous as it appears in pulses every time a bunch of electrons go through the bending magnets.

2.3.6.2. Daresbury SRS

Electrons are accelerated in a linear accelerator, injected into a small 'booster' synchrotron where they are collected, accelerated and then injected into the storage ring. Once in the storage ring they are accelerated to 2 GeV. Injection and steering (ensuring the electrons are in a stable orbit and the radiation is along the centre of the beam lines) takes about 1 hour. Immediately after injection the current is about 300 mA. The current dies away (due to electrons colliding with gas molecules - even at 10^{-12} torr) and after 24 hours the current will be around 100 mA. There are also 'insertion devices' which are arrays of magnets to perturb the electron orbit and affect the radiation spectrum. These include 'wigglers', which push the cut-off energy to higher values and produce a higher intensity of hard X-rays and 'undulators' which produce high intensities at certain pre-determined frequencies.

In summary the properties of synchrotron radiation are as follows:-

1. White light
2. High intensity
3. Naturally collimated
4. Polarised
5. Periodic time-structure
6. High stability over long periods

2.3.6.3. Transmission EXAFS Experiments

Transmission EXAFS is the simplest type of EXAFS experiment. The major components of the system are the monochromator, the incident (or reference) ion chamber to measure I_o, the sample and the signal ion chamber to measure I_t. The monochromator consists of double crystal harmonic rejecting Si crystals cut to expose the same crystal planes (220) which are aligned in parallel. When the X-rays strike the

lower crystal, only those with the wavelength corresponding to the Bragg condition will be diffracted. This diffracted beam will then be diffracted from the second crystal and exit into the experimental area. Rotation of the crystals i.e. changing θ will alter the selected wavelength of the monochromatic beam. Thus a beam of wavelength is made by moving the crystals precisely (in steps of 0.001°) with a computer controlled stepping motor. The monochromated beam contains some harmonics as well as the fundamental wave but rejection of the harmonics is allowed by 'order-sorting' monochromators. The beam leaving the monochromator is typically 1mm high and 5 mm wide.

2.3.6.4. Ion Chambers

The ion chambers are simple metal boxes with very thin mylar windows at each end where the X-Rays enter and exit. A high voltage is set up across two plates in the box. When ionising radiation passes between the two plates a current will flow and is recorded on a counter. Both ionisation chambers are identical except in the gases with which they are filled. The reference chamber must be only weakly absorbing i.e. they must let at most 90% of the radiation through to the sample. The signal ionisation chamber must be highly absorbing. This can be achieved for different X-Ray wavelengths by filling 1 atmosphere with mixtures of He and other rare gases (the higher the atomic number of the gas the higher will be its absorption).

2.3.6.5. Sample Preparation

The preparation of the sample is crucial to obtaining a good EXAFS spectrum. The sample had to be thick enough to produce an EXAFS sample but thin enough to allow sufficient X-Rays through. The thickness was calculated from known X-Ray absorption data for the elements and their concentrations in the sample, and was found to be a few microns. The sample was mixed with silica (a weak X-Ray absorber) and pressed into a pellet.

2.3.6.6. Description of the EXAFS Spectrum

The basic EXAFS experiment involves measuring the X-ray absorption spectrum of a thin sample as a function of X-ray energy. Thus the experiment is simple and involves the measurement of the incident X-ray intensity, I_o and the transmitted intensity, I_t, and evaluating the absorption coefficient, μ, from

$$\mu = \ln I_o / I_t$$

At low energies the X-rays will pass through the sample and μ will be close to zero. As the energy is increased a point will be reached where the X-ray has sufficient energy to 'eject' an inner core electron (a photoelectron) from the K or L shell of the atoms of one of the elements in the sample. The X-ray will be in the energy range 1 to 40 keV. At this point, there is a very steep rise in μ, and this is the absorption edge. The X-ray energy, $h\nu$, will be equal to the binding energy, E_b, of the electron in its initial state. Increasing the X-ray energy further is not expected to change μ as the extra energy should simply be transformed into kinetic energy of the photoelectron. Thus the absorption spectrum would be predicted to be a simple step-function and the final energy state, E_f, of the photoelectron in the energy balance equation, i.e.

$$E_f = h\nu - E_b$$

would simply be the kinetic energy and have a linear dependence on $h\nu$.

However, real absorption spectra for condensed systems, Figure 2.14., usually show three regions; the pre-edge features; the near-edge structure (which extends over about 50eV) and the EXAFS, which are oscillations extending out about 1 keV beyond the edge. The absorption coefficient in the EXAFS region shows oscillations (typically with an amplitude about 10% of the edge step) which extend with decreasing amplitude to about 1keV beyond the edge.

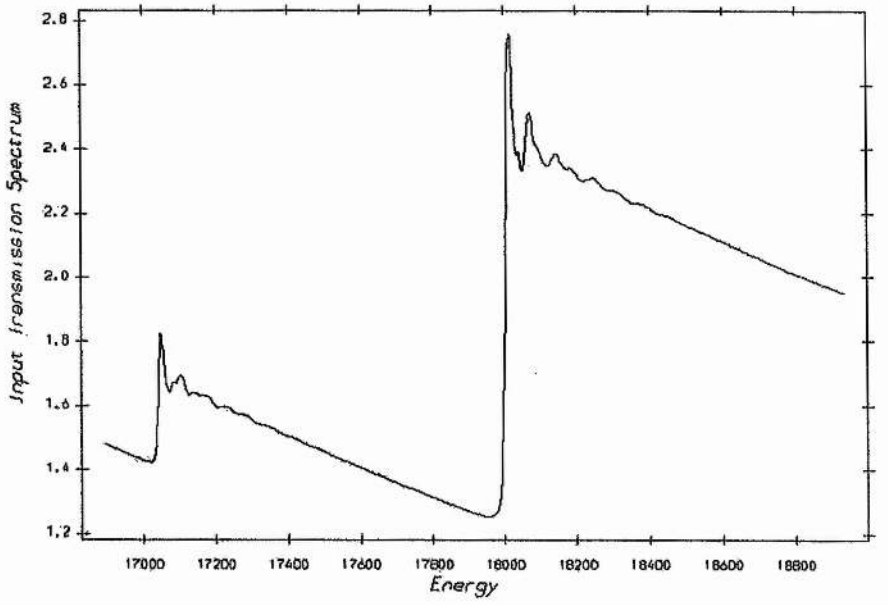

Figure 2.14. The real X-ray absorption spectrum from a condensed phase sample containing Zr and Y.

2.3.6.7. The Advantages and Disadvantages of using EXAFS

EXAFS provides local structural information and unlike diffraction methods does not rely on long range order in the sample. This is a distinct advantage over X-Ray or neutron diffraction. EXAFS is also atom specific. The X-Ray edges of atoms adjacent in the Periodic Table are well separated and the separate EXAFS can be investigated. In contrast X-Ray diffraction will not distinguish between atoms which are isoelectronic or very similar in atomic number e.g. Zr^{4+} and Y^{3+} are isoelectronic but can be studied separately despite the fact that they occupy the same site in the fluorite structure.

Although the co-ordination distances can be precisely determined there are fundamental problems of obtaining precise co-ordination numbers. This is because of the limited range of the region of k-space used for the Fourier transform. The typical errors in co-ordination number of $\pm$ 1 are not very helpful in distinguishing between

small changes in co-ordination number with temperature. However the relative errors between similar samples are likely to be much less.

2.3.7. Flexural Strength Testing

Biaxial flexure testing of 8YSZ-Al_2O_3 samples were carried out using an Ingstron 4644 Universal Testing Machine with a 2 kN load cell. The diameter of the support ring was 15mm and the diameter of the load ring was 4mm. The cross-head speed used was 0.5mm/min. The equation used to calculate the flexural strength was the ISO standard for testing alumina.

2.4. References

[1] R. Maenner, E. Ivers-Tiffée, W. Wersing and W. Kleinlein, Comm. Eur. `Communities [Rep.] EUR 1991, EUR 1991, EUR 113564, Proc. Int. Symp. Solid Oxide Fuel Cells, 2nd (1991) 712-725

[2] F. T. Ciacchi, K. M. Crane ans S.P.S. Badwal, Solid State Ionics 73 (1994) 49-61

[3] W. D. Kingery, H. K. Bowena and D. R. Uhlmann (1976), Introduction to Ceramics, 2nd Edition. New York: John Wiley & Sons

[4] X. R. Wang, O. Y. Wang, J. H. Gu, W. L. Tan, X. Y. Jiang, Z. Y. Wu, European J. Solid State and Inorganic Chem., 1991,Vol.28, No.S, pp.605-609

[5] A. Kato, K. Inoue, Y. Katatae, Mat. Res. Bull., 1987, Vol.22, No.9, pp.1275-1281

[6] G. Gongyi, N. Z. Fang, C. Yuli, Journal of Materials Science, 1991, Vol.26, No.13, pp.3511-3516

[7] T. Okubo, H. Nagamoto, J. Mat. Sci., 1995, Vol.30, No.3, pp.749-757

[8] I. R. Gibson, PhD Thesis, University of Aberdeen, 1995

[9] W. D. Kingery and M. Berg, J. Appl. Phys. 26[10] (1955) 1205-1212

[10] R. L. Coble, J. Appl. Phys. 32[5] (1961) 787-792

[11] A.R. West, Solid State Chemistry and its Applications, John Wiley and Sons, Chichester, 1983

[12] PDF card no. 30-1468, ICDD, Newton Square, Pennsylvania, U.S.A.

[13] R.I. Smith and S. Hull, Report RAL-94-115, Rutherford Appleton Laboratory 1994

[14] W.I.F. David, R.M. Ibberson and J.C. Mathewman, Report RAL-2-032, RAL 1992

[15] D.N. Argyriou, J. Appl. Cryst. 27 (1994) 155-158

[16] J.T.S. Irvine, D.C. Sinclair and A.R. West, Adv. Mater. 2[3] (1990) 132-138

[17] M. Kleitz, H. Bernard, E. Fernandez and E. Schouler, in : Advances in Ceramics, Vol. 3, eds. A. H. Heuer and L. W. Hobbs (The American Ceramic Society, Columbus, OH, 1981), 310-336

[18] E.J.L. Schouler, N. Mesbahi and G. Vitter, Solid State Ionics 9/10 (1983) 989-996

[19] S.P.S. Badwal, Solid State Ionics 76 (1995) 67-80

[20] J.A. Kilner and C.D. Waters, Solid State Ionics 6 (1982) 253-259

[21] A.K. Jonscher, J. Mat. Sci. 19[6] (1984) 1767-1776

[22] F.T. Ciacchi , K.M. Crane and S.P.S. Badwal, Solid State Ionics 3 (1994) 49-61

[23] J. Ross, MacDonald, Impedance Spectroscopy (Wiley, Chichester, UK, 1987)

[24] P.G. Bruce, A. West, D.P. Almond, Solid State Ionics 7 (1982) 57- 60

[25] A.K. Jonscher, J. Mat. Sci. 13[3] (1978) 553-562

CHAPTER 3

Phase Relations and Electrical Conductivity in the Ternary System ZrO_2 - Y_2O_3 - TiO_2

3.1. Introduction

The ZrO_2-Y_2O_3 system has high oxide ion conductivity and the composition 8 mol% Yttria stabilised Zirconia is currently the material of choice for the electrolyte in solid oxide fuel cells. In the search for new SOFC anode materials which are compatible with the electrolyte material and have high electronic and ionic conductivity, the binary ZrO_2-Y_2O_3 system has been doped with TiO_2 in order to introduce reducible Ti^{4+} into the cubic fluorite structure. This chapter describes the phase relations at 1500°C and the electrical properties of the ternary system ZrO_2-Y_2O_3-TiO_2.

3.2. Previous Phase Diagram Studies of the Ternary System ZrO_2-Y_2O_3-TiO_2

3.2.1. The Binary System ZrO_2-Y_2O_3

The widely accepted phase diagram of the ZrO_2-Y_2O_3 system was reported by Scott [1]. The Zirconia-rich region (0-10 mol% Y_2O_3) is presented in Figure 3.1 and the entire phase diagram is shown in Figure 3.2. The precise positions of the equilibrium and metastable phase boundaries have been questioned in the literature and many studies have been carried out since the work of Scott to try and quantify them [2-4]. Comparison of these papers shows that there are large discrepancies in the position of the phase boundaries, Figure 3.3 [5]. These differences are due to different methods of preparation and starting powders, different measurement techniques and different thermal treatments used throughout the studies. It is within the Zirconia rich region, with 0-10 mol% Yttria, that compositions with commercially interesting properties are obtained.

The only equilibrium single phases which appear to be stable at room temperature are a monoclinic phase containing 0 to 2.5 mol% Yttria and a cubic phase containing >9.5 mol% Yttria. According to Scott's diagram, a tetragonal single phase cannot be stabilised to room temperature for any Yttria content and a transformation to a monoclinic phase should always occur.

A number of metastable non-equilibrium phases have, however, been observed; it is the metastable phases, which have interesting properties and find commercial applications. Careful control of the microstructure can produce very small grained materials and the tetragonal phase can be stabilised to room temperature; a maximum grain size of 0.25-0.5 μm is required to stabilise the tetragonal phase to room temperature [6]. Small grain sizes can be achieved by utilising ultrafine powders and using low temperature sintering regimes. Thus, a composition containing ~2.5 mol% Yttria sintered at 1300°C will produce, upon cooling to room temperature, a metastable tetragonal phase, provided that a small grain size has been retained.

Similarly, compositions prepared in the two-phase (cubic and tetragonal) region of the phase diagram will produce a mixture of tetragonal and cubic phases upon cooling if the tetragonal phase grain size is sufficiently small. If the tetragonal grains are allowed to grow above the critical size due to prolonged heating or due to high temperatures, then a mixture of monoclinic and cubic phases will be obtained upon cooling to room temperature.

Scott's phase diagram predicts that a minimum Yttria content of 9 mol% should be required to stabilise a cubic single phase to room temperature. However, cubic single phases have been stabilised to room temperature for compositions containing 7.5 to 9 mol% Yttria, after cooling from a reaction temperature of ~1500°C [7-11]. The phase diagram of Scott would therefore suggest that cubic single phases containing 7.5-9 mol% Yttria were metastable. The kinetic stability of these cubic phases probably arises from the slow diffusion rates of the cations below 1200°C which prevents the thermodynamically stable, equilibrium phases from forming during cooling to room temperature [1]. Analysis of an 8 mol% Yttria-stabilised Zirconia, prepared at 1500°C then annealed in the two-phase region at 1000°C showed evidence of the equilibrium cubic and low-Yttria tetragonal phases [12].

In addition to the metastable phases discussed, Scott [1] observed a metastable 'non-transformable' tetragonal phase, with a higher Yttria content than any equilibrium tetragonal phase. This was produced by quenching samples with a composition of between 3 and 7 mol% Yttria from the cubic region, T>2000°C, to room temperature.

This metastable tetragonal phase formed the equilibrium, cubic and low-Yttria tetragonal phases when annealed at ~1400°C and is discussed in more detail in another study [13].

A more recent study appeared to indicate that the Fluorite to Fluorite + Tetragonal phase transition temperature of 10 mol% YSZ by analysing the electrical conductivity and was found to be 1015 ± 5°C [14]. This temperature is about 70°C higher than the transition data produced by Stubican et al. [15]. The Fluorite to Fluorite + $Zr_3Y_4O_{12}$ phase transition reported by Pascual et al [16] was reported to be at 1205 ± 5°C at 30 mol% Yttria according to electrical measurements [14]. However these phase relations are not in agreement with the more widely accepted phase diagram by Scott [1].

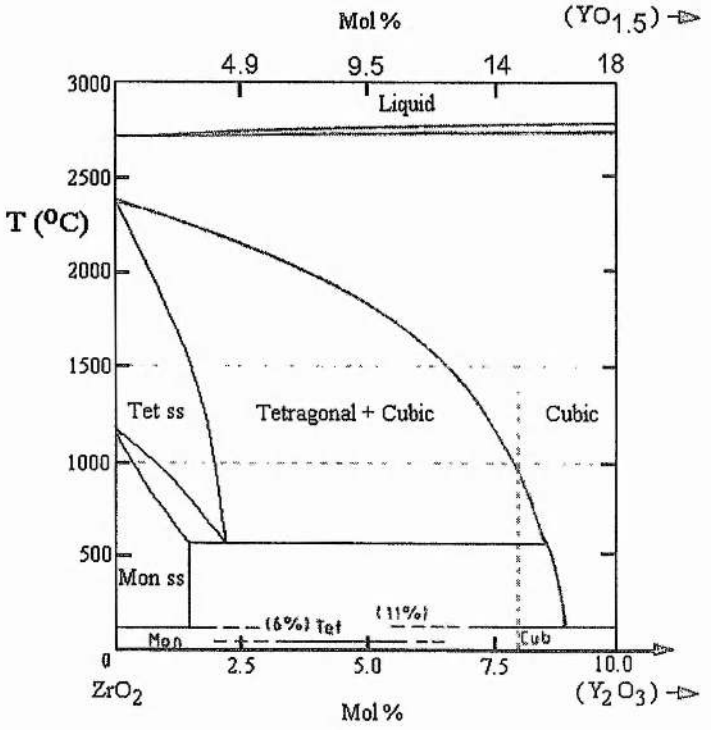

Figure 3.1. The phase diagram of the Zirconia rich binary system ZrO_2-Y_2O_3 [1]. The dashed line indicates the composition containing 8 mol% Y_2O_3.

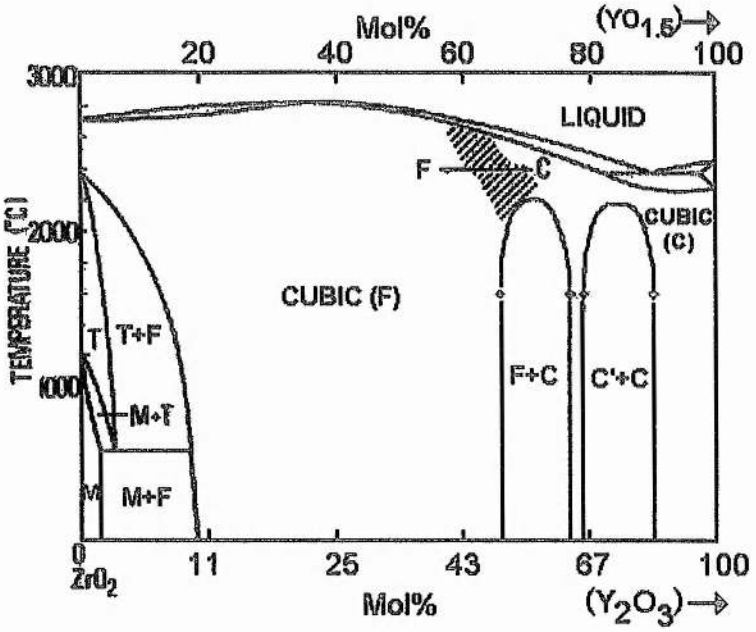

Figure 3.2. The entire phase diagram of the binary ZrO_2-Y_2O_3 system [1].

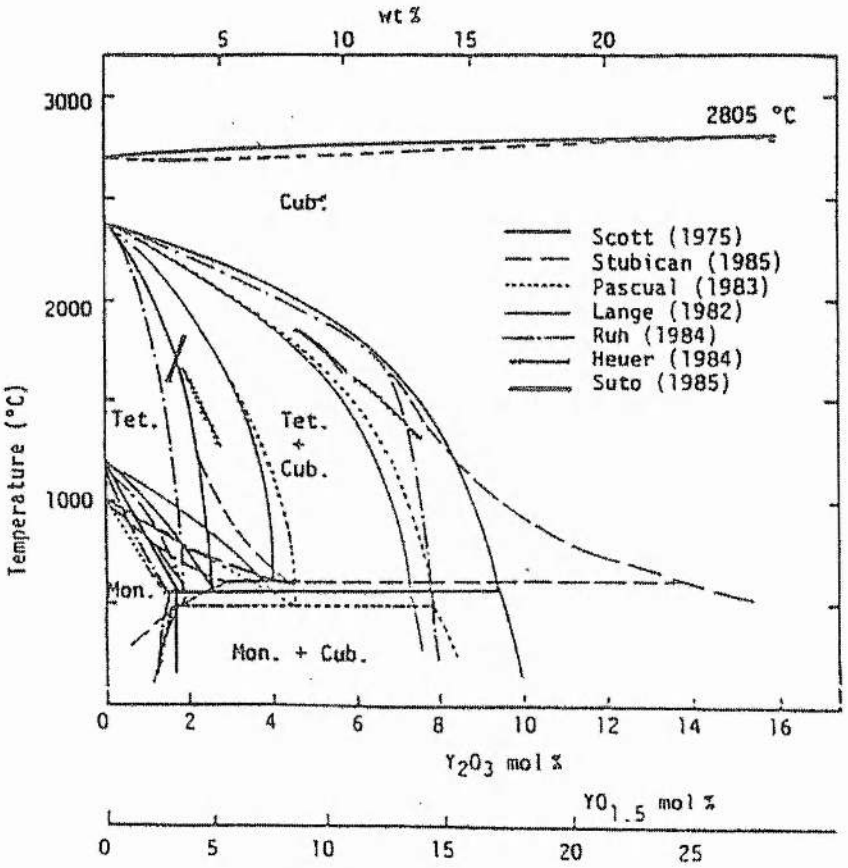

Figure 3.3. The high discrepancies found in the position of the phase boundaries in the Zirconia-rich region of the ZrO_2-Y_2O_3 phase diagram [5].

3.1.2. The Binary System ZrO_2 - TiO_2

Several phase diagram studies have been reported in the literature [17-24]. The most recent study was done by McHale et al [17], Figure 3.4. Shevchenko et al [24] determined that at 1700°C a single phase tetragonal Zirconia region exists to about 17.5 mol% TiO_2, single phase $ZrTiO_4$ solid solution from ~40 to 52 mol% TiO_2 and TiO_2 rutile solid solution from about 82.5 mol%. An earlier study by Noguchi and Mizuno agreed with previous investigators on the solid solution of the end members and on one intermediate compound with a solid solution, however, the details of the equilibrium were still in doubt [21].

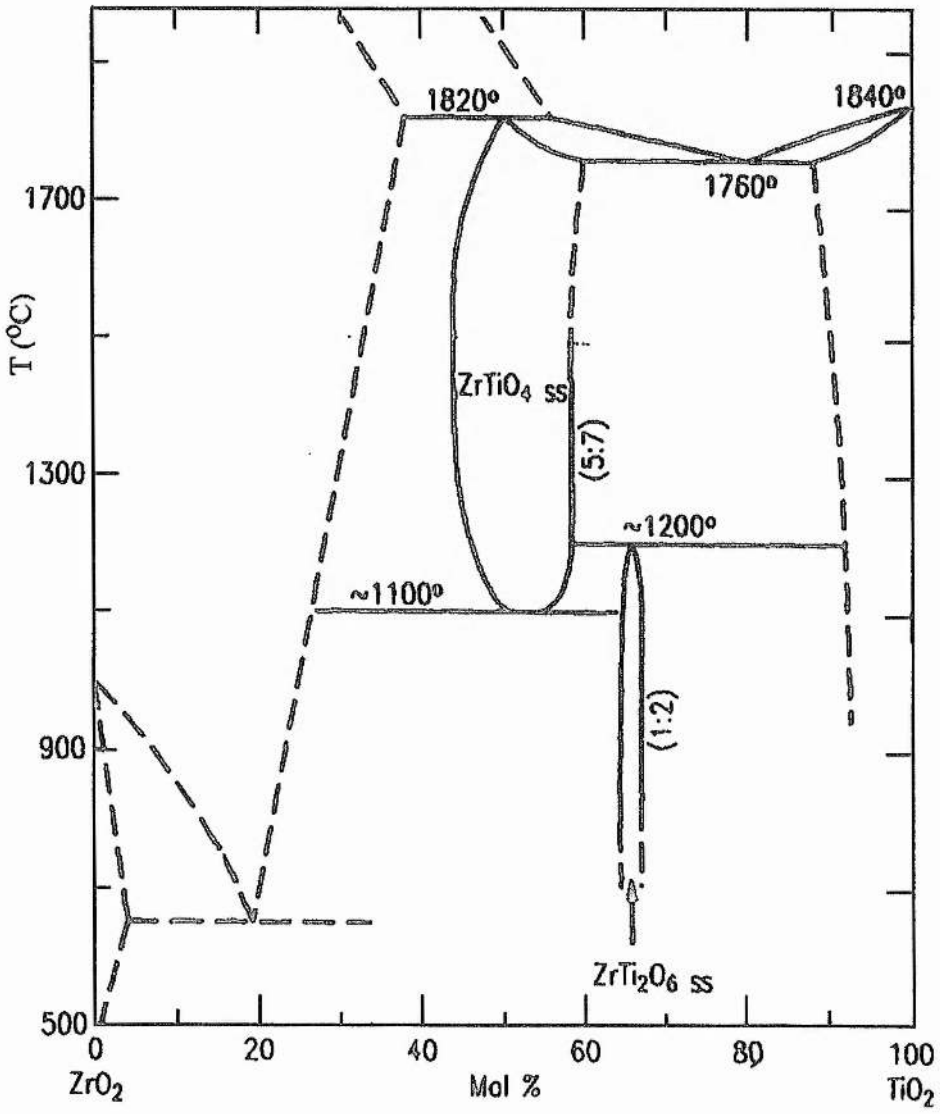

Figure 3.4. The Binary System ZrO_2-TiO_2 proposed by McHale and Roth [17]

3.2.3. The Binary System Y_2O_3 - TiO_2

The Y_2O_3 – TiO_2 system was reported by Mizutani et al [24], Figure 3.5. In this study of the system Y_2O_3 – TiO_2, the regions in which phase formation was detected were at 50 mol% TiO_2 and between 65 – 66.67 mol% TiO_2 , i.e. the Y_2TiO_5 phase is formed and a solid solution with the $Y_2Ti_2O_7$ pyrochlore structure exists, in agreement with the phase diagram by Mizutani et al [25]. The Y_2TiO_5 phase has unit cell parameters a=10.333, b=11.181 and c=3.699 Å. The pyrochlore material, $Y_2Ti_2O_7$, with 33.33 mol% (50 atom%) Y_2O_3 has unit cell parameter a = 10.0947 Å.

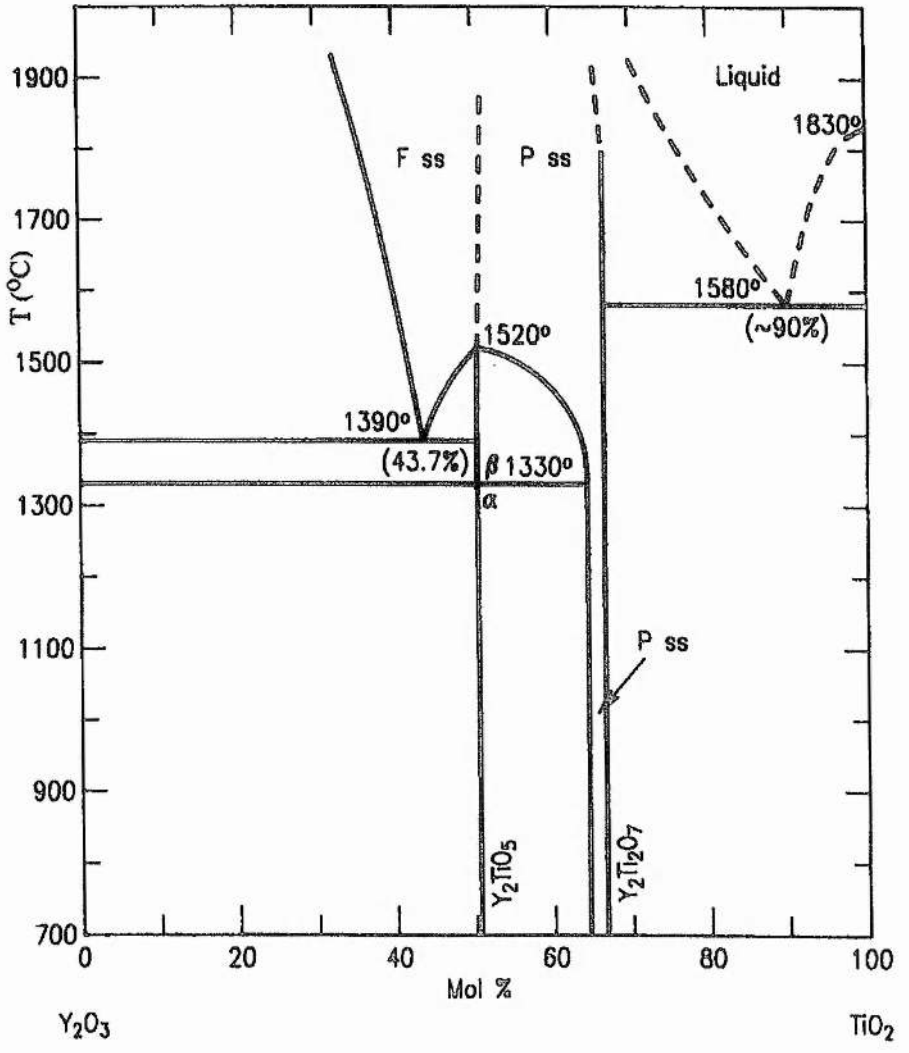

Figure 3.5. The Binary System Y_2O_3 - TiO_2 reported by Mizutani et al [25].

3.2.4. Previous Investigations of The Ternary System ZrO_2 - Y_2O_3 - TiO_2

A previous study determined that for ZrO_2 stabilised with ~15 atom% Y^{3+}, only 4.5 to 8.5 atom% Ti^{4+} dissolved into the cubic YSZ structure [26]. Above this level, peaks attributable to lower symmetry structures of ZrO_2 were detected by X-ray diffraction. Naito and Arashi have reported that for YSZ containing 18 atom% Y^{3+}, specimens containing more than 10.9 atom% Ti^{4+} consisted of 2 phases [27]. Liou and Worrell reported that up to 11-14 atom% Ti^{4+} could be dissolved into YSZ with retention of the cubic fluorite phase [28]. Yokokawa et al calculated the maximum solubility of Ti^{4+} in $Zr_{0.85}Y_{0.15}O_{1.925}$ to be 14 atom% at 1573 K [29]; this is in good agreement with the experimental value obtained at 1873 K [28]. The calculated phase diagram is shown in Figure 3.6 [29].

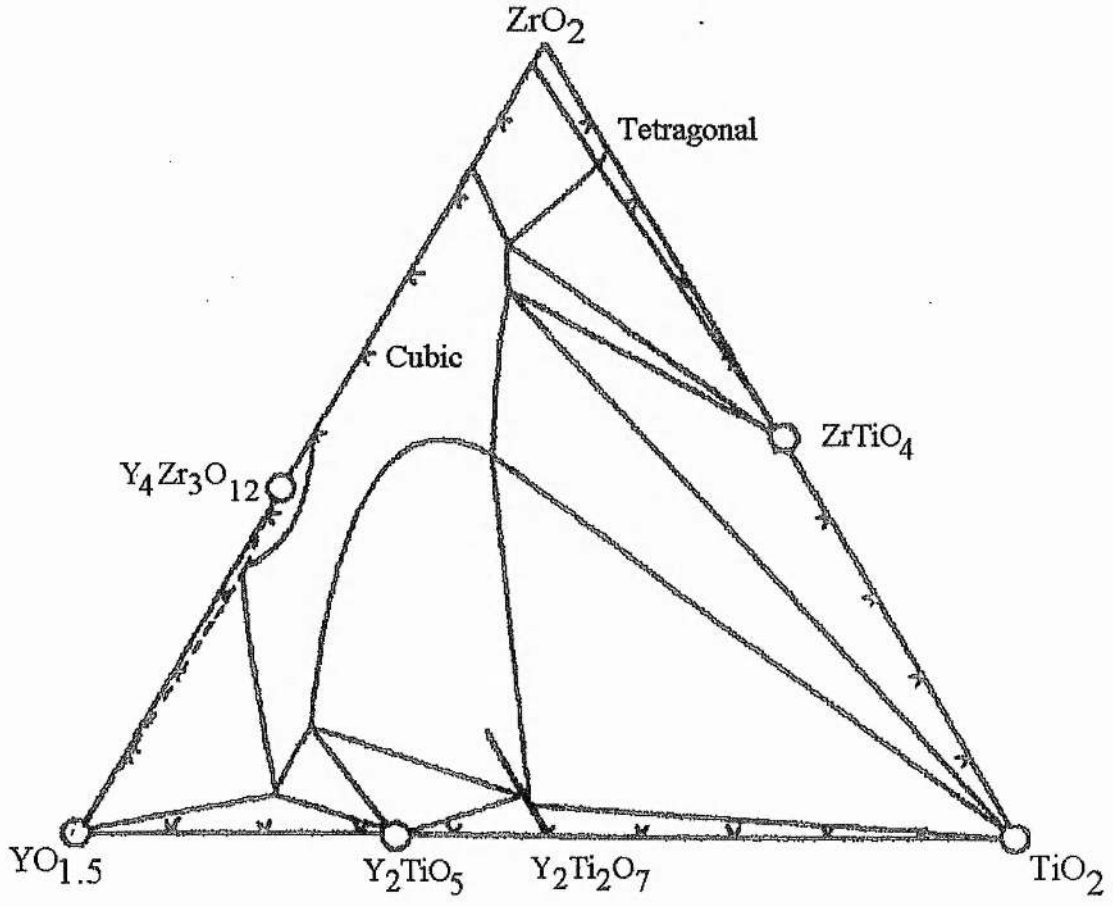

Figure 3.6. The theoretical phase diagram for the system ZrO_2-Y_2O_3-TiO_2 [29].

3.3. Phase Diagram Studies of the Ternary System ZrO_2-Y_2O_3-TiO_2.

3.3.1. The Binary System ZrO_2-Y_2O_3

In this study, ZrO_2-Y_2O_3 binary system phase limits are in reasonable accord with the published phase diagram of Scott [1] i.e. the fluorite phase exists between 8 mol% Y_2O_3 and 40 mol% Y_2O_3. The unit cell increases from 5.1390 Å for 8 mol% Y_2O_3 to 5.2447 Å for 40 mol% Y_2O_3. The increase in unit cell size is due to the Y^{3+} dissolving substitutionally into the ZrO_2 structure. The solubility limit of Y_2O_3 in ZrO_2 is reached at about 40 mol% Y_2O_3, and above this composition, lines characteristic of the C-type structure of Y_2O_3 appear in the X-ray powder pattern. Between 82 and 100 mol% Y_2O_3, only the C-type structure of the Y_2O_3 solid solution is detected. The unit cell parameter of these high Y_2O_3 phases decreases from 10.6040 Å to 10.5652 Å by decreasing the Y_2O_3 content from 100 to 82 mol%. The variation in unit cell parameter with composition in the binary ZrO_2 - Y_2O_3 system is shown in Figure 3.7.

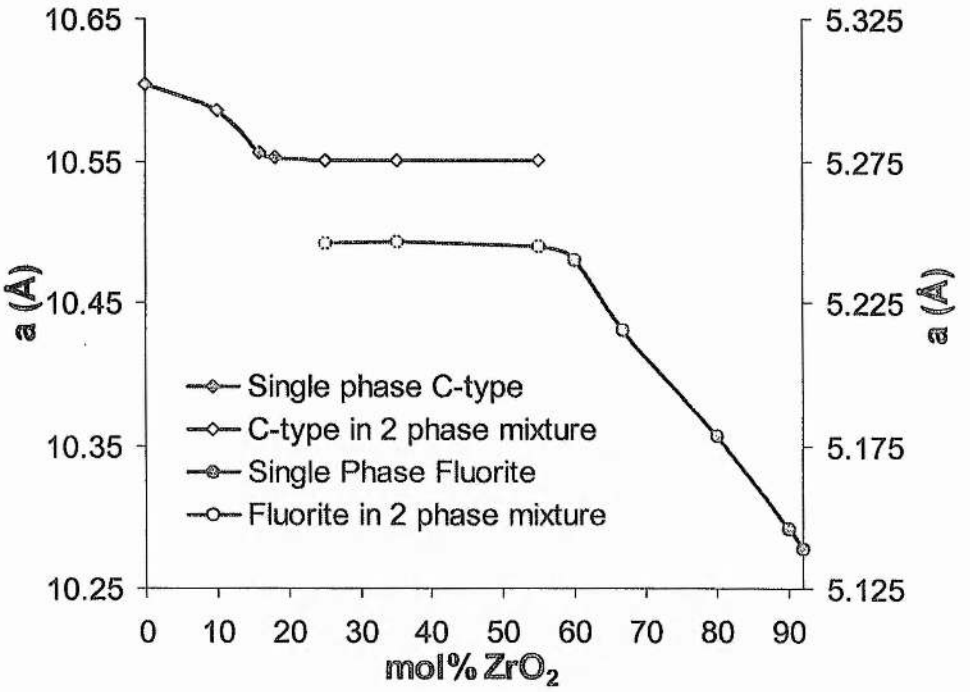

Figure 3.7. The binary system ZrO_2 - Y_2O_3. Plot of the cubic unit cell parameters for the C-type and defect fluorite compositions vs. mol% ZrO_2.

3.3.2. The Binary System ZrO_2-TiO_2

In this study of the ZT system, a limited solid solution region, with the tetragonal TiO_2 (rutile) structure at 1500°C, was found to exist for 0 to 10 atom% Zr^{4+}. The $ZrTiO_4$ solid solution, exhibiting an orthorhombic structure was single phase between 40 and 55 mol% ZrO_2 in agreement with McHale and Roth [17]. Thus a two-phase mixture containing $ZrTiO_4$ and TiO_2 (rutile) exists between 10 and 40 atom% ZrO_2. Up to 22 atom% of Ti^{4+} is soluble in tetragonal ZrO_2 at 1500°C. On cooling these samples to room temperature and grinding for X-ray investigation, 100% conversion from tetragonal to monoclinic occurred. The temperature of the monoclinic to tetragonal transition decreases from 1170°C for ZrO_2 to below 900°C for $Zr_{0.85}Ti_{0.15}O_2$, as determined from DTA studies. On replacing Zr^{4+} with Ti^{4+}, the unit cell size changes from a = 5.3129 Å, b = 5.2125 Å, c = 5.1471 Å, β = 99.218° for ZrO_2 to a =5.3157 Å, b = 5.1403 Å, c = 5.1030 Å, β = 98.908° for $Zr_{0.85}Ti_{0.15}O_2$. This decrease in unit cell is in accord with the smaller ionic radius of Ti^{4+} (0.65Å) compared to that of Zr^{4+} (0.78Å). No evidence was seen for stabilisation of the cubic fluorite structure at 1500°C by Ti^{4+} substitution on its own. The variation in unit cell volume with composition in the ZT system is shown in Figure 3.8.

3.3.3. The Binary System Y_2O_3-TiO_2

In this study of the system Y_2O_3 – TiO_2, the regions in which phase formation was detected were at 50 mol% TiO_2 and between 65 – 66.67 mol% TiO_2, i.e. the Y_2TiO_5 phase is formed and a solid solution with the $Y_2Ti_2O_7$ pyrochlore structure exists, in agreement with the phase diagram by Mizutani et al [25]. The Y_2TiO_5 phase has unit cell parameters a=10.333, b=11.181 and c=3.699 Å. The pyrochlore material, $Y_2Ti_2O_7$, with 33.33 mol% (50 atom%) Y_2O_3 has unit cell parameter a = 10.0947 Å.

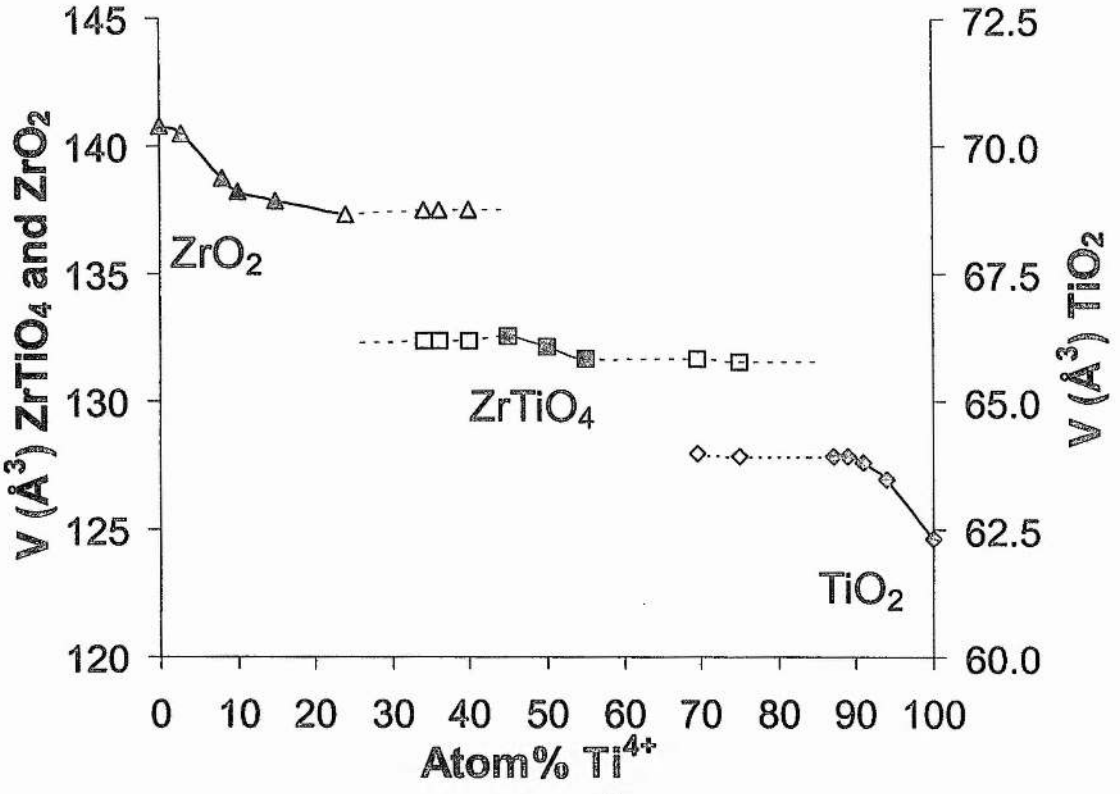

Figure 3.8. The binary system TiO_2 - ZrO_2. Plot of unit cell volume of the tetragonal Rutile phase, the monoclinic ZrO_2 phase and the $ZrTiO_4$ phase vs. atom% Ti^{4+}.

3.3.4. Phase Diagram Studies of the Ternary System ZrO_2-Y_2O_3-TiO_2

The ternary phase diagram is shown in Figure 3.9. The cubic fluorite region in the experimental phase diagram is similar to the cubic region in the calculated phase diagram at 1300°C shown in Figure 3.10. However, there are differences in the extent of the cubic phase and also in the composition of the multi phase regions. The single phase, two phase and three phase regions of the experimental phase diagram are indicated in Figure 3.9. No new phases are observed in the ternary system, and apart from the defect fluorite system, none of the binary systems extend significantly into the ternary system. This cubic defect fluorite region extends from the binary ZrO_2 - $YO_{1.5}$ join from between 15 and 57 atom% Y^{3+} almost 20 atom% Ti^{4+} in to the ternary system. It was determined that for low levels of Y_2O_3 dopant, very little TiO_2 dissolves into the cubic fluorite structure and e.g. ZrO_2 stabilised with 16.5 atom% Y^{3+} dissolves less than

7 atom% Ti^{4+}. As the amount of Y^{3+} is increased, the solubility of Ti^{4+} increases. With increasing Y^{3+} content, the stabilised cubic fluorite phase can incorporate much more Ti^{4+}. This is probably because the highly defective fluorite structure contains a large number of vacancies thus enabling the Ti^{4+} to assume its preferred 6-fold co-ordination. In stabilised Zirconias the vacancies, which usually associate with Zr^{4+}, also associate with the dopant cation when it is undersized leading to the formation of MO_6 polyhedra [30].

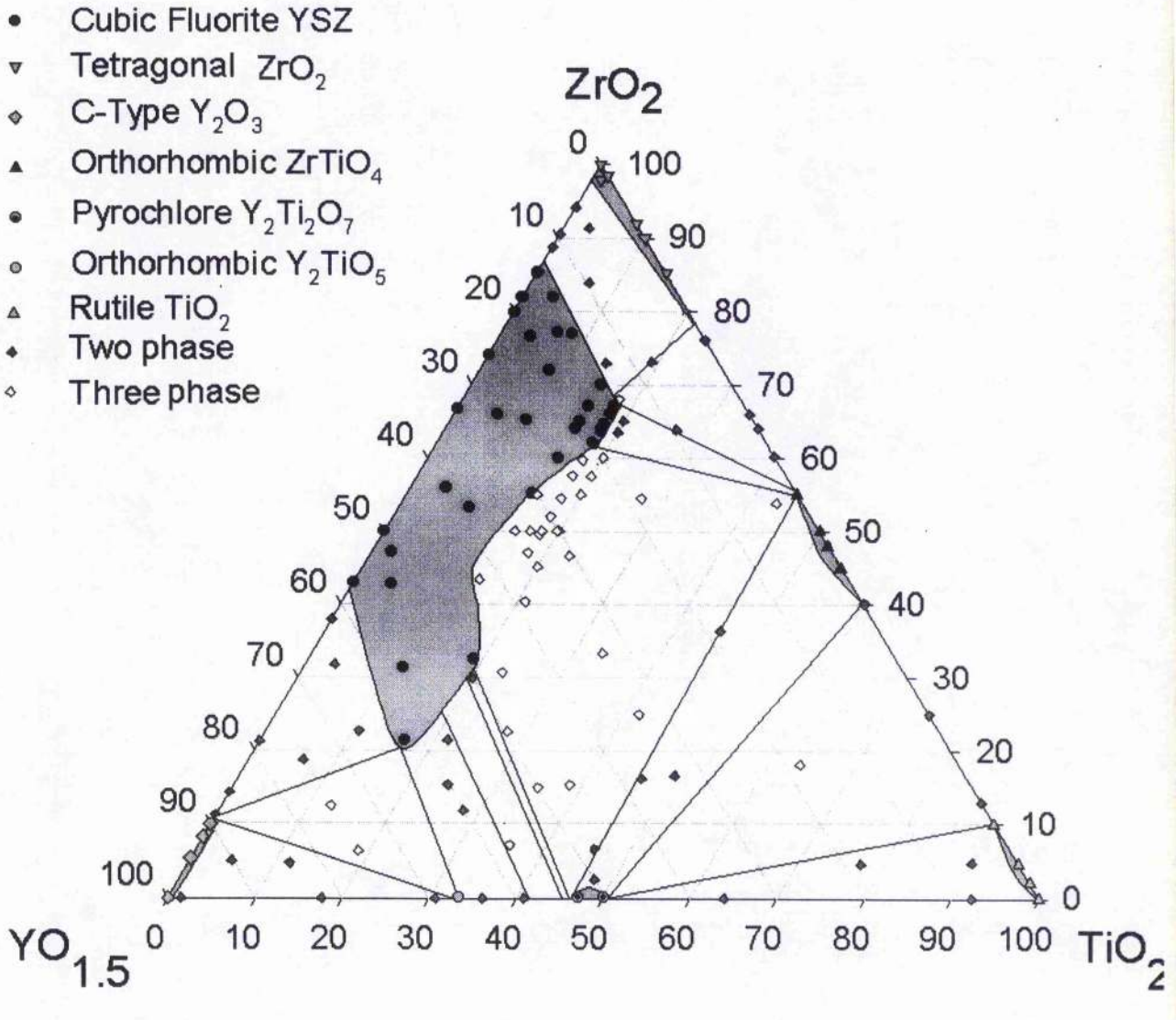

Figure 3.9. The experimentally determined ternary phase diagram of the system ZrO_2 - Y_2O_3 - TiO_2 at 1500°C.

The maximum extent of this single-phase region in the direction of increasing $YO_{1.5}$ is shown to encompass the composition $Zr_{0.21}Y_{0.62}Ti_{0.17}O_{1.69}$, which has 15.5% of the anion sites vacant. It is surprising that in this direction the defect fluorite region approaches the composition $Y_3TiO_{6.5}$ (a two phase mixture of Y_2O_3 and Y_2TiO_5) instead of the structurally related pyrochlore composition $Y_2Ti_2O_7$. In contrast, in the ternary system Gd_2O_3-TiO_2-ZrO_2 the fluorite and pyrochlore regions coalesce along the $GdO_{1.5}$-ZrO_2 join. Indeed, in the Gd_2O_3 analogue a smooth transition between the pyrochlore and fluorite structures is observed with increasing deviation from $Gd_2M_2O_7$ stoichiometry. This is not surprising as the pyrochlore structure can be viewed as an ordered superstructure of the fluorite structure, as is described in chapter 4. This obviously shows the significance of the stabilising dopant size on the resultant structure.

The unit cell parameters in the ternary system were found to increase with Y^{3+} content, as expected from the binary ZY system, and to decrease with increasing Ti^{4+} content. The general trend in unit cell parameter with Y^{3+} is shown in Figure 3.10. For the compositions with no Ti^{4+}, all the points are directly comparable and the plot is linear as expected. For the other data ranges, the data are not comparable due to varying amounts of Ti^{4+}, however the linear nature of the data is obvious, i.e. the unit cell parameter increases with Y^{3+} content, regardless of the Ti^{4+} content. The effect of Ti^{4+} content on the unit cell parameter is shown in Figure 3.11. The plot clearly shows that as the Ti^{4+} content is increased, the unit cell parameter decreases.

The maximum extent of the fluorite phase in the ternary system for lower levels of aliovalent stabilising dopant, where the ionic conducting properties are of considerable interest, has been very accurately determined. The maximum limit of the fluorite phase in this low defect region contains compositions with 18 atom% of reducible Ti^{4+} and with between 14 and 20 atom% of stabilising Y^{3+} i.e. compositions with formula $Zr_{1-x}Y_xTi_{0.18}O_{2-(x/2)}$ for $0.14 \leq x \leq 0.20$. Figure 3.12. shows the variation in unit cell parameter with increasing Ti^{4+} for single phase fluorite compositions containing 15 and 20 atom% Y^{3+}. A typical X-ray diffraction pattern for a composition at the Titanium rich limit of the cubic fluorite solid solution is shown in Figure 3.13.

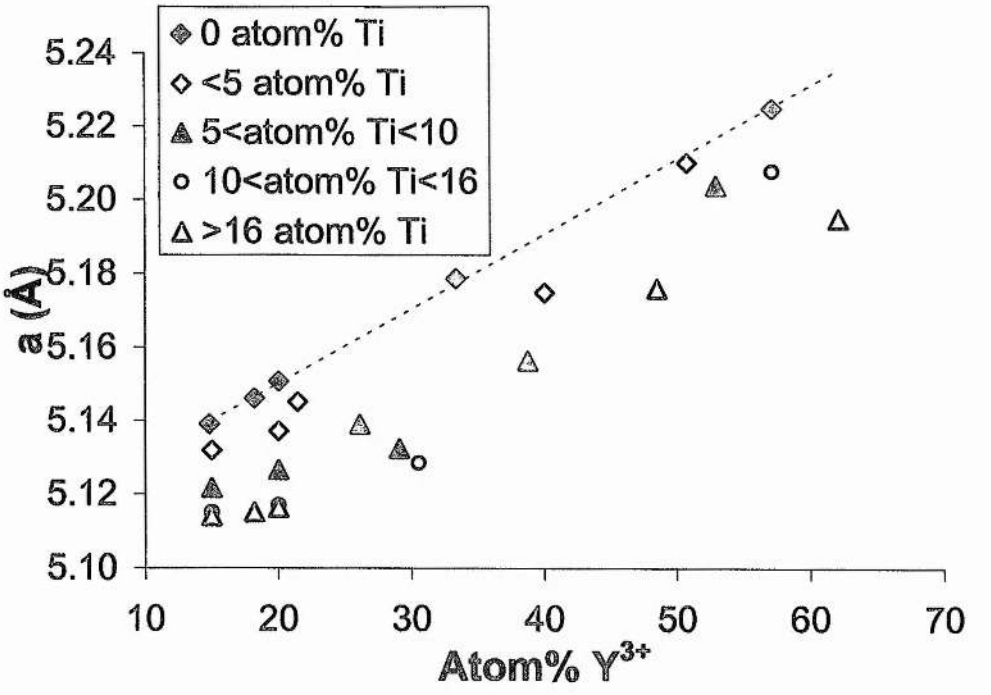

Figure 3.10. The general trend in unit cell parameter with increasing Y^{3+} for the ternary system ZrO_2 -Y_2O_3 -TiO_2.

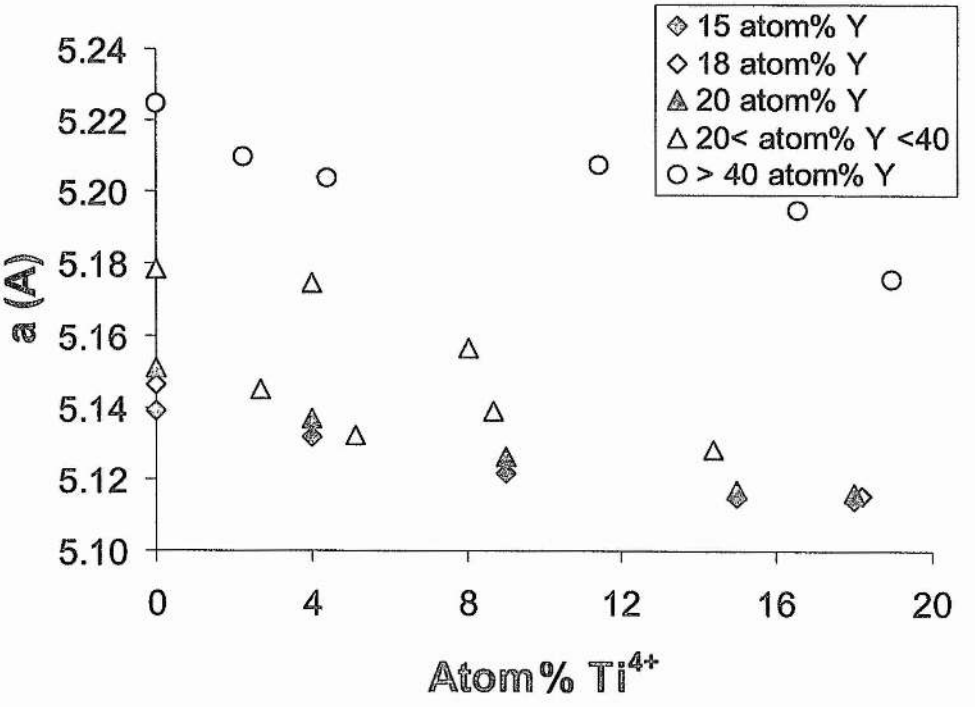

Figure 3.11. The general trend in unit cell parameter with increasing Ti^{4+} for the ternary system ZrO_2 -Y_2O_3 -TiO_2.

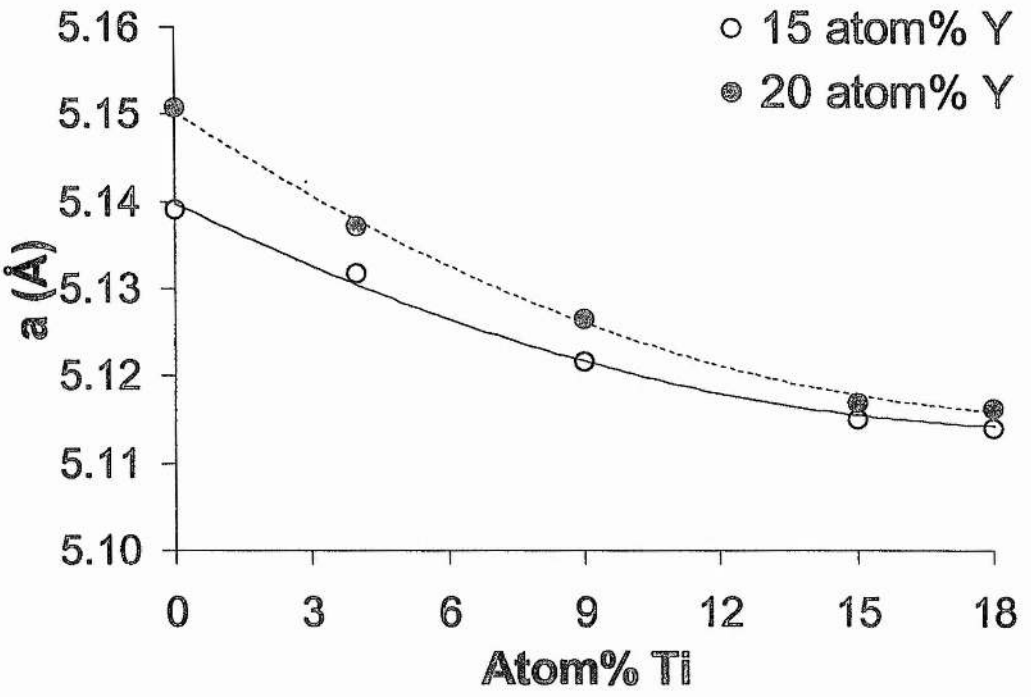

Figure 3.12. Comparison of unit cell parameters as a function of Ti^{4+} content for single phase compositions of formula $Zr_{0.85-x}Y_{0.15}Ti_xO_{1.925}$ and $Zr_{0.80-x}Y_{0.20}Ti_xO_{1.9}$ ($0 < x < 0.18$). All data were obtained at 20°C.

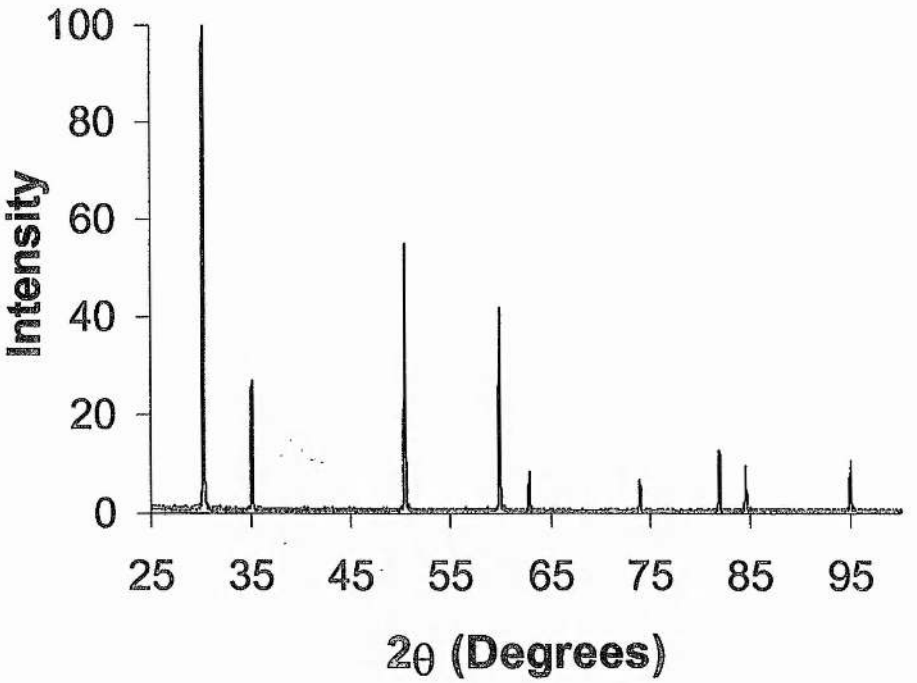

Figure 3.13. The X-ray diffraction pattern for cubic fluorite materials containing 18 atom% Ti^{4+} stabilised by 20 atom% Y^{3+}.

In conclusion, a large defect fluorite solid solution exists in the ternary ZrO_2 - Y_2O_3 - TiO_2 system. The amount of TiO_2 which dissolves into ZrO_2 is highly dependent upon the quantity of stabilising aliovalent dopant. The aliovalent dopant introduces vacancies into the fluorite lattice, thus enabling the smaller Ti^{4+} ion to assume a 6-fold co-ordination environment. A maximum of 18 atom% Ti^{4+} can be dissolved into YSZ stabilised in the fluorite structure by 14-20 atom% Y^{3+}, with vacancy concentrations of 2.9 and 6.25% respectively.

3.4. Electrical Properties of the Ternary System ZrO_2 - Y_2O_3 - TiO_2 in Air

3.4.1. Previous Studies of the Binary System ZrO_2-Y_2O_3

Compositions within this system have attracted considerable academic and commercial interest. Compositions with low levels of Yttria addition, 1-5 to 2.5 mol%, which were prepared so as to maintain a small grain size, may form Yttria-doped Tetragonal Zirconia Polycrystals, Y-TZP. These materials are composed of 100% metastable tetragonal phase, which is stabilised by the small grain size [31]. Y-TZP is used as an engineering ceramic due to it's high fracture strength, 2GPa [32], and toughness, 20 $MPam^{½}$ [33]. The excellent mechanical properties are attributed to transformation toughening [34, 35]; this is the stress induced tetragonal-to-monoclinic transformation which follows the application of an external stress. The transformation to a monoclinic phase is accompanied by a volume increase of 3-5%, which is recognised as opposing crack opening. Larger applied stresses are therefore required to achieve complete fracture of the ceramic body, improving the fracture toughness. The applications of Y-TZP have been limited due to a decrease in the mechanical properties at high temperatures and the instability of the metastable tetragonal phase in moist environments leading to physical degradation and mechanical failure [36].

Intermediate compositions containing 3-7 mol% Yttria contain a mixture of cubic and tetragonal grains and are defined as Yttria partially stabilised Zirconia, Y-PSZ [37]. The mechanical strength of Y-PSZ decreases as the Yttria content and volume fraction of cubic phase increases [38]. Y-PSZ has an average ionic conductivity of 5-10 Sm^{-1} at 1000°C [39-41] and finds application as the solid electrolyte in gas sensors [42].

The low thermal conductivity of Y-PSZ also makes it an excellent thermal barrier coating [43].

Compositions containing 8-10 mol% Yttria, prepared at high temperatures, retain the cubic fluorite structure to room temperature and are known as Yttria Fully-stabilised Zirconia, or more commonly YSZ. YSZ has excellent oxide ion conducting properties. Values quoted in the literature for 8 mol% YSZ vary significantly from 10 to as high as 18 Sm^{-1} due to small differences in impurities, density and Yttria content. Processing and thermal history are also extremely important in achieving a high conductivity. The high ionic conductivity and good thermal stability of YSZ lead to its application as the oxide electrolyte in SOFCs [44-46].

The ionic conductivity of 3 mol% Y-PSZ is greater than that of 8 mol% Yttria content, however, immediate conclusions regarding this increase in conductivity can not be made as compositions containing less than 8 mol% Yttria consist of a mixture of two or more phases [47]. Increasing the Yttria content above 8 mol% produces a decrease in the conductivity. This decrease has been explained in terms of an increase in cation-oxygen vacancy interaction/association (Chapter 6), which causes a reduction in the number and mobility of the oxygen vacancies that are free to migrate.

Compositions containing less than 8 mol% Yttria produce lower values of conductivity at 1000°C but their suitability as fuel cell electrolytes has been investigated [48] because of their high mechanical strength. However, these compositions undergo a tetragonal to monoclinic phase transformation [49, 50] under fuel cell operating conditions i.e. high temperatures and in moist environments, which can lead to the complete disintegration of the ceramic. This phase instability makes the possible application of these compositions in SOFC devices limited.

The bulk resistances of a low Yttria sample e.g. 3 mol% Y-TZP and an 8 mol% YSZ are of similar magnitude at low temperatures. The grain boundary resistances, however, are very different. The grain boundary resistance of 8 mol% YSZ was reported to be approximately one-fifth of 3mol% Y-TZP at 350°C [51].

A potential problem relating to the use of 8 mol% YSZ as the electrolyte material in SOFC's is the decrease in conductivity with time. A decrease in the conductivity of samples in the Zirconia-Yttria system is not restricted to 8 mol% YSZ. The conductivities of Y-TZP and P-PSZ are known to decrease with annealing at low temperatures [49]; annealing temperatures of 200-300°C [50] and 400-1000°C [51] both produced a decrease in conductivity. The decrease in conductivity due to annealing was reported to be time dependent [51]. Annealing Y-TZP and Y-PSZ at low temperatures, 200-300°C, is known to produce hydrothermal degradation [49, 52, 53], causing microcracking of samples. Higher annealing temperatures are thought to cause the transformation of the metastable tetragonal phase observed in Y-TZP and Y-PSZ to the equilibrium, less conductive phases [51]. Low temperature annealing of cubic YSZ has also been examined. The conductivity of 7 mol % YSZ has been found to decrease after annealing at 1600°C for 70 hours [54]. The decrease in conductivity was attributed to a gradual phase decomposition of cubic to cubic and tetragonal. A decrease in conductivity was also observed for higher Yttria cubic samples after annealing below ~800°C. Vlasov et al reported decreases in the conductivity of 7.5 to 10 mol% YSZ annealed at 1050-850°C, with lower Yttria contents producing larger decrease in conductivity [55]. The precipitation and growth of a less conductive second phase was, again, suggested as the cause of the drop in conductivity after annealing. At the recognised SOFC operating temperature, 1000°C, 8 mol% YSZ appears in the two-phase region of the equilibrium phase diagram [1]. This suggests that the cubic symmetry commonly observed at room temperature in samples of this composition, which have been prepared in the single phase region (>1200°C), is metastable. Annealing 8 mol% YSZ at 1000°C should produce a two-phase mixture of cubic and tetragonal phases. The equilibrium phase diagram predicts that a minimum of ~8.5 mol% Yttria would be required to produce a single cubic phase at 1000°C [1].

3.4.2. Observed Ageing Effects In This Study

In this study ageing has been identified by slow cooling samples from the sintering temperature, by ageing in air and by hydrothermal ageing. The slow cooling of 8 mol% YSZ from the sintering temperature of 1500°C can have a serious deleterious effect on the high temperature conductivity, Figure 3.14. The graph clearly shows that

slow cooling increases the susceptibility of 8YSZ to hydrothermal ageing. The conductivity at 1000°C for a sample cooled at 10°C/min from the sintering temperature decreases by 29% when hydrothermally aged in an autoclave at 180°C for 100 hours. The decrease in conductivity increases to 65% when the sample is cooled at 1°C/min.

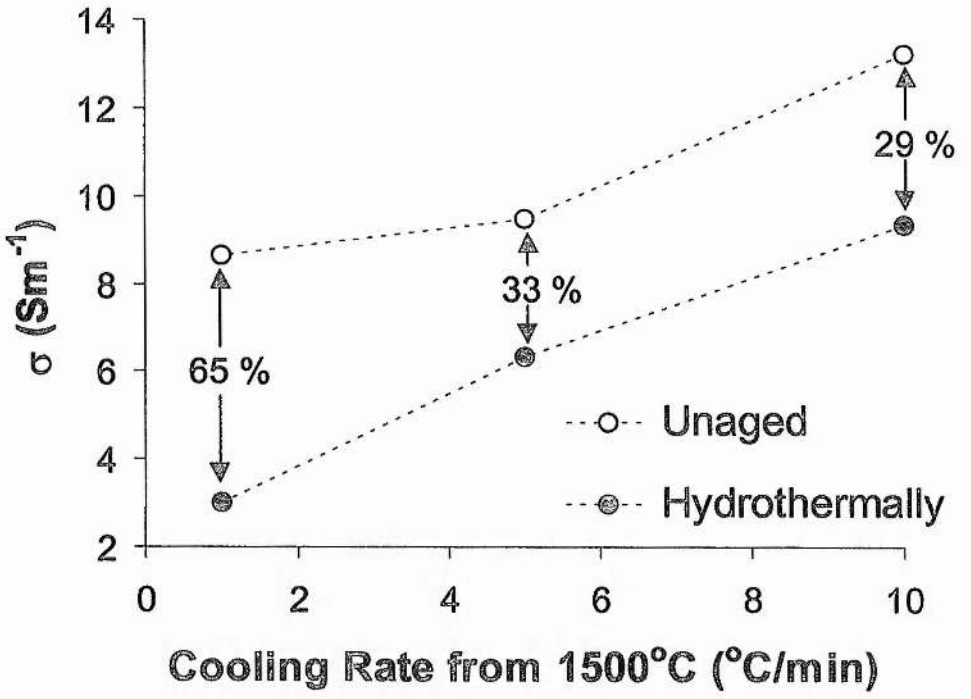

Figure 3.14. Conductivity of 8YSZ at 1000°C versus cooling rate from 1500°C.

The low temperature conductivity shows the opposite effect to the high temperature conductivity in aged samples, i.e. the low temperature conductivity increases with hydrothermal ageing time. Figure 3.15 clearly shows that the conductivity at 300°C increases by half an order of magnitude when aged in an autoclave for 1000 hours. As the temperature is increased, the deleterious effect of hydrothermal ageing on the high temperature conductivity can be seen. The 500°C data for samples aged for 100 and 1000 hours is lower than for samples which have been aged for shorted times, i.e. the decrease in high temperature conductivity can be detected at temperatures as low as 500°C.

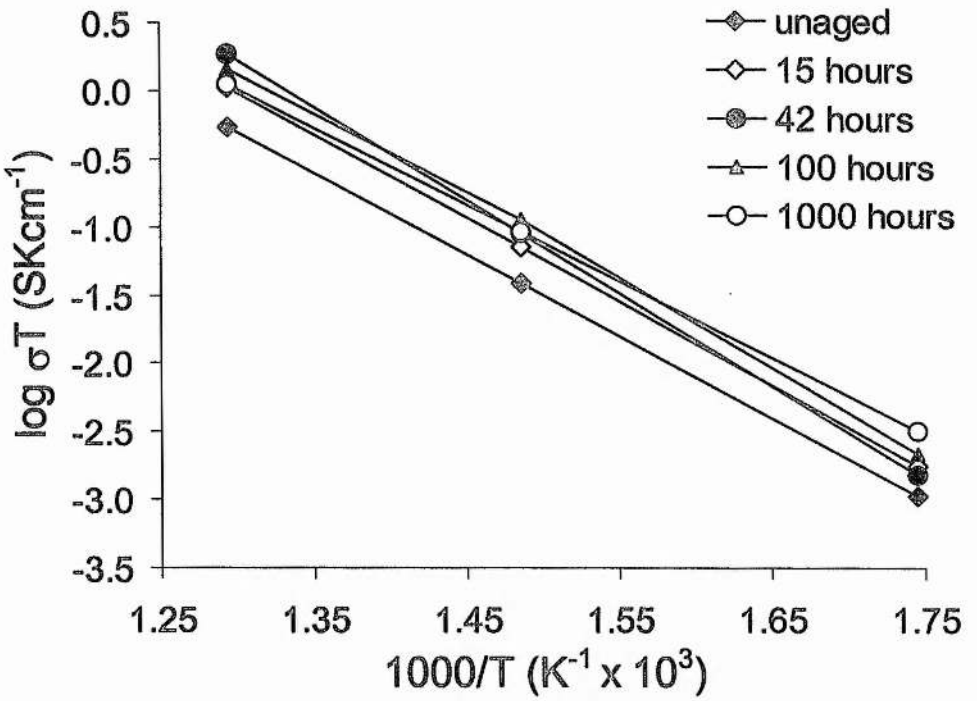

Figure 3.15. Plot of conductivity between 300 and 500°C for 8YSZ which has been hydrothermally aged for between 0 and 1000 hours.

3.4.3. Theoretical Effect of TiO_2 on the Ionic Conductivity of YSZ

As Ti^{4+} is smaller than Zr^{4+} and Y^{3+}, it prefers a co-ordination environment of 6 oxygens [56]. If one considers the possible implications of this preferred co-ordination by calculating the number of vacancies introduced into the cubic fluorite structure by doping with Yttria, (i.e. number of vacancies = 2-(x/2) where x = atom% Y^{3+}) and subtracting 2 x [Ti^{4+}], in order to assume that all Ti^{4+} are co-ordinated by 2 oxygen vacancies, Figure 3.16, we can see whether there is an oxygen vacancy deficiency or excess in the structure, relative to the Ti^{4+}, Figure 3.17. When there is no excess or deficiency of oxide vacancies i.e. zero on the y-axis, we can calculate the maximum amount of Ti^{4+} required to 'trap' all of the available oxygen vacancies, Figure 3.17. Thus we can plot the amount of Ti^{4+} required to trap all of the vacancies for different concentrations of vacancies and therefore Y^{3+} content, Figure 3.18.

It can be seen that even for the composition stabilised in the cubic fluorite structure by 20 atom% Y^{3+}, only 5 atom% Ti^{4+} is required to 'trap' all of the available oxygen vacancies to form a Bevan type 6-fold oxygen arrangement. Thus one would

expect the conductivity to rapidly decrease with an increase in [Ti^{4+}] and remain essentially constant above the vacancy saturated Ti^{4+} concentration. Thus any more Ti^{4+} that dissolves into the fluorite structure will be forced to assume a co-ordination number higher than the preferred 6 oxygens and the vacancies will have to associate with the Zr^{4+} which prefers a co-ordination environment of 7 oxygens [57].

The addition of further Y^{3+} (and resulting decrease in Zr^{4+} content) creates more vacancies, which in theory should result in more Ti^{4+} being able to assume 6-fold co-ordination. However for compositions containing high levels of Ti^{4+} and as much as 20 atom% Y^{3+} there is obviously a problem with the lattice size because a 2-phase mixture forms. It is clearly not a problem with the average cation co-ordination number which restricts the extent of the cubic fluorite region because the binary ZY system can have a co-ordination environment of less than 7 oxygens before phase separation occurs e.g. $Zr_{0.43}Y_{0.57}O_{6.86}$ is single phase fluorite. There is also a large region of the single phase ternary system which also has co-ordination numbers of less than 7, e.g. $Zr_{0.21}Y_{0.62}Ti_{0.17}O_{1.69}$.

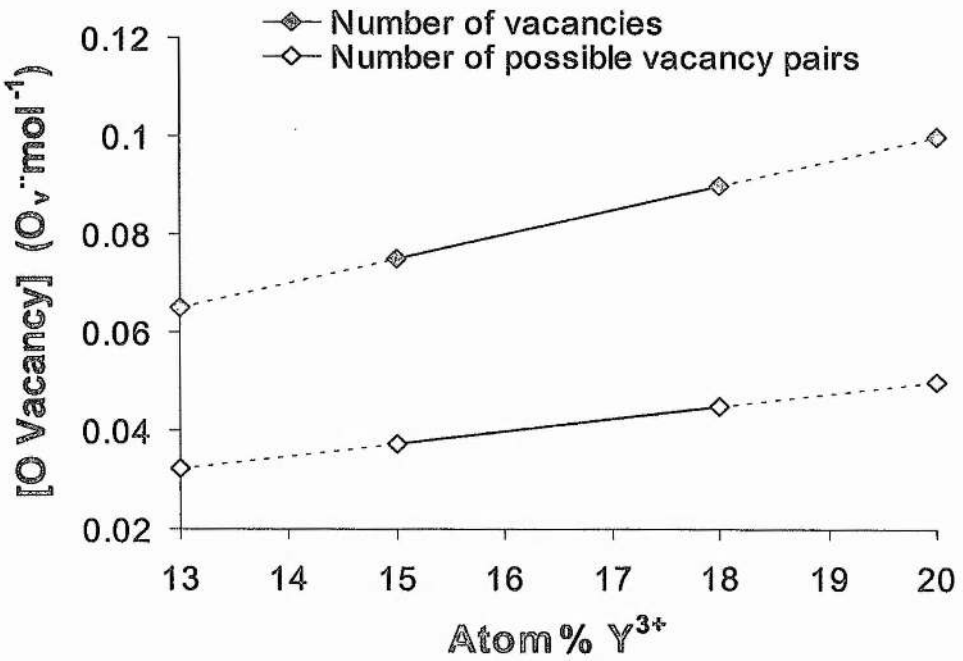

Figure 3.16. Plot of Vacancy Concentration in Cubic fluorite ZYT compositions vs. atom% Y^{3+} for Ti^{4+} 6-fold co-ordination environment.

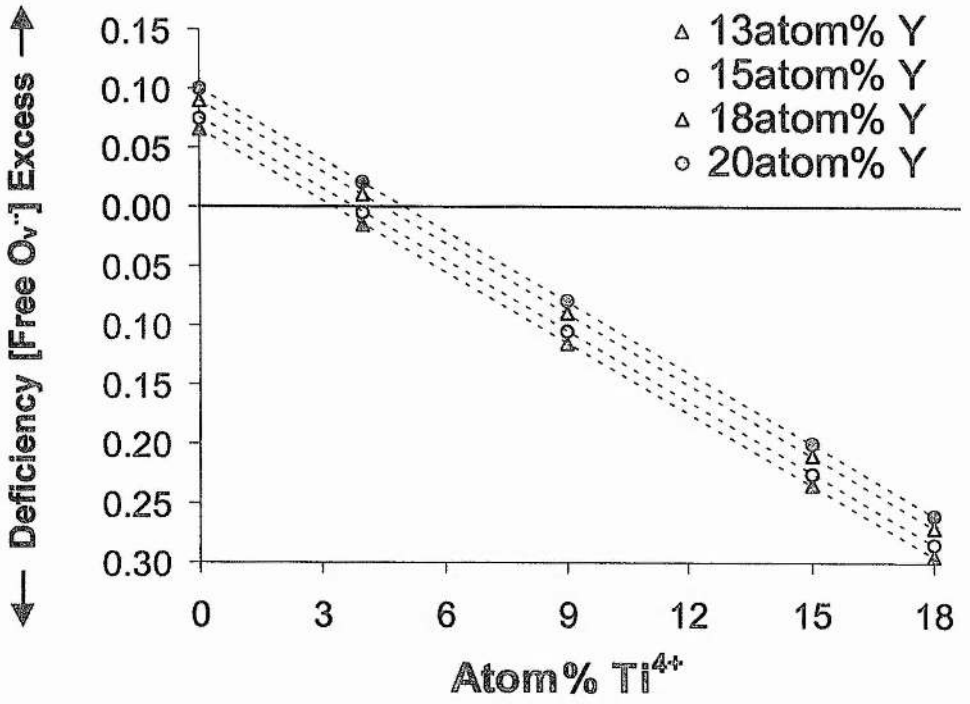

Figure 3.17. Plot of Oxygen vacancy deficiency or excess assuming that all Ti^{4+} ions assume a 6-fold co-ordination for compositions containing between 13 and 20 atom% Y^{3+}.

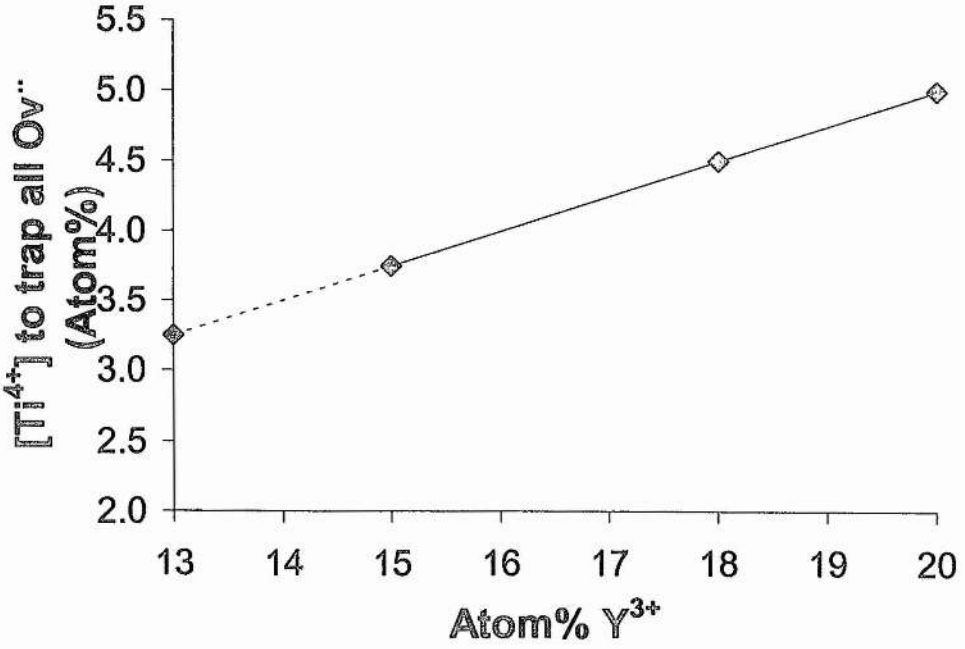

Figure 3.18. Plot of $[Ti^{4+}]$ required to trap all oxygen vacancies introduced by the stabilising dopant vs. Atom% Y^{3+}.

3.4.4. Observed Effect of TiO_2 on Ionic Conductivity in Air

The conductivity of TiO_2 doped YSZ was found to decrease with increasing Y^{3+} and increasing Ti^{4+}. The general effect of Y^{3+} and Ti^{4+} on the ionic conductivity of the ternary system ZrO_2 - Y_2O_3 - TiO_2 can be seen in Figure 3.19. This very general diagram has been divided into 4 regions of similar conductivity. There are, however, different trends within those regions. For example, compositions containing high Y^{3+} content show little change in conductivity with Ti^{4+} addition. In contrast, compositions with low Y^{3+} and low Ti^{4+} content have high ionic conductivity, which upon addition of Ti^{4+}, rapidly decreases. The highest values of ionic conduction are found in compositions containing very little Ti^{4+} and the lowest possible amount of Y^{3+} required to stabilise the cubic phase.

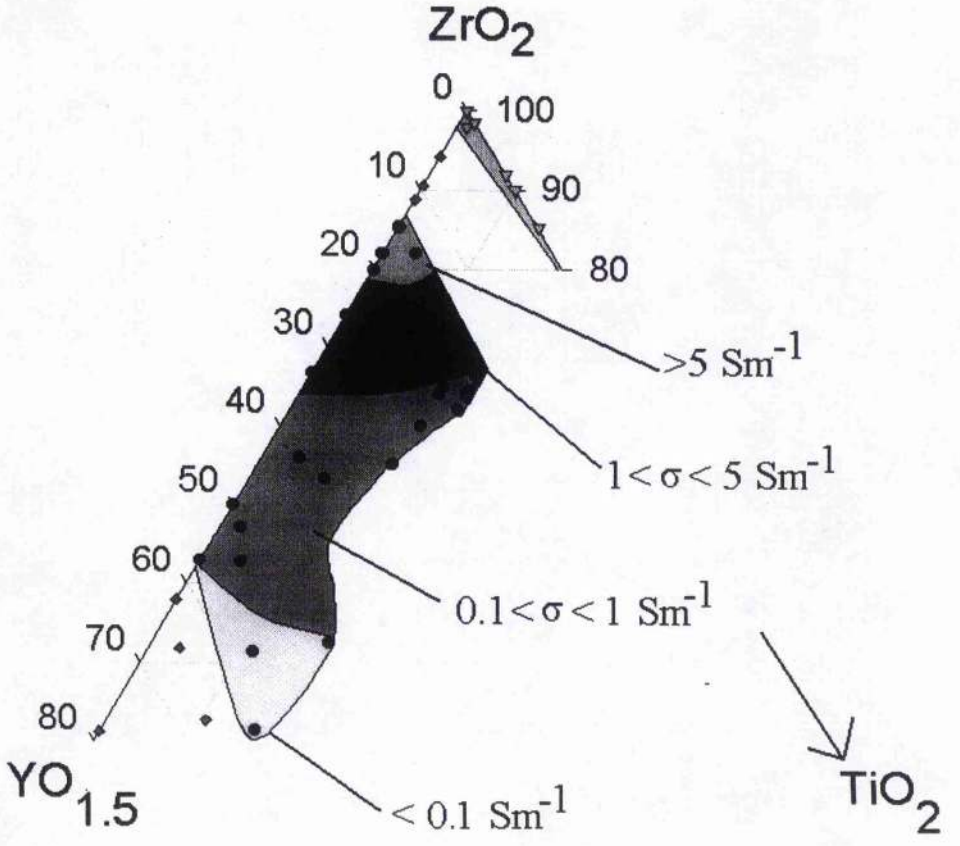

Figure 3.19. The ternary phase diagram of the system ZrO_2 - Y_2O_3 -TiO_2 exhibiting the general trend in ionic conductivity with increasing Y_2O_3 and TiO_2 at 1000°C.

In the region of interest for optimum mixed ionic and electronic conductivity, i.e. low Y^{3+} and high Ti^{4+}, the trend in conductivity with Ti^{4+} content was examined for defect fluorite compositions containing 15 and 20 atom% Y^{3+}. The trend in ionic conductivity is shown in Figure 3.20. Clearly the conductivity decreases substantially on substitution, even for small quantities of Ti^{4+}. The conductivities of $Zr_{0.85}Y_{0.15}O_{1.926}$ and $Zr_{0.80}Y_{0.20}O_{1.90}$ were determined to be 10 Sm^{-1} and 7.7 Sm^{-1} respectively. Replacing 18 atom% Zr^{4+} with Ti^{4+} reduced the conductivity to 1.14 and 0.77 Sm^{-1} for the 15 and 20 atom% Y^{3+} compositions respectively. The conductivity of the undoped YSZ decreased by almost 50% upon addition of only 4 atom% Ti^{4+} indicating that Ti^{4+} has a strong 'trapping' effect on the oxygen vacancies, as outlined earlier.

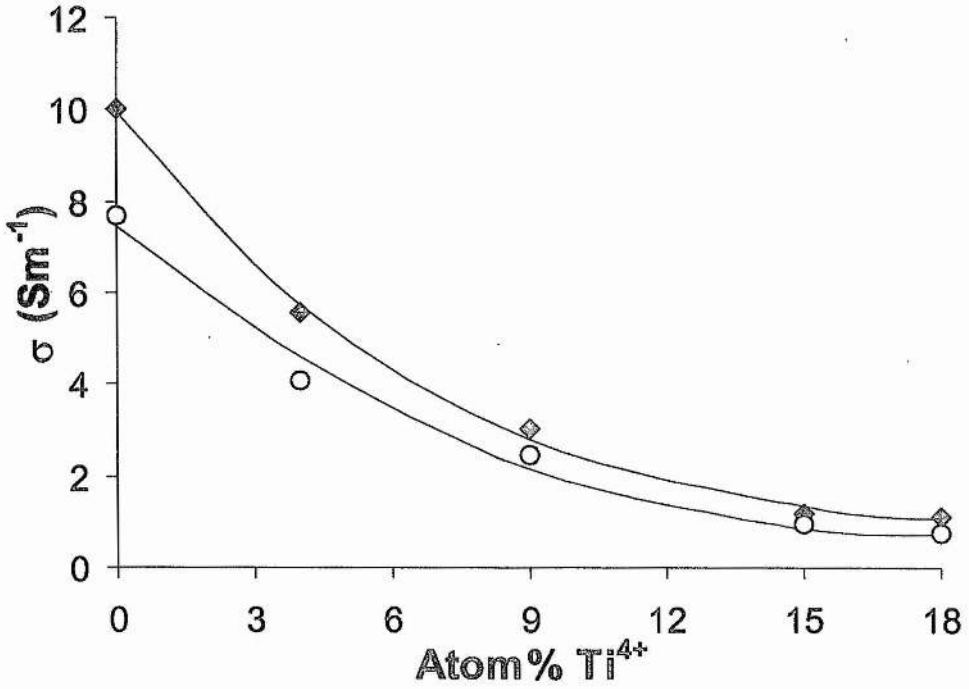

Figure 3.20. Ionic conductivity versus atom% Ti^{4+} for $Zr_{0.85-x}Y_{0.15}Ti_xO_{1.926}$ and $Zr_{0.85-x}Y_{0.20}Ti_xO_{1.90}$.

Curvature in the Arrhenius plots of Zirconia based defect fluorites due to breakdown of vacancy-cation associates is well known [58]. Due to its small size a co-ordination number of 6 is the most usual for Ti^{4+} but co-ordination numbers of 7 and even 8 are possible, indicating that a reasonably high solubility of Ti^{4+} in the fluorite structure is possible. Figure 3.21 shows that in this ternary system the curvature in the

Arrhenius plots in the temperature range 300-1000°C is only observed for Ti^{4+} concentrations below 9 atom%. The decrease in the curvature of the Arrhenius plots is reflected in the activation energies for conduction. The sample with no dissolved Titanium has an activation energy of 1.17eV between 300 and 400°C. As the temperature is increased and the cation-vacancy associates breakdown the activation energy decreases to 0.93eV between the temperatures of 800 and 900°C. As the Ti^{4+} content is increased the difference between the high and low temperature activation energies gradually decreases until the concentration of 15 atom% Ti^{4+} is reached when the Arrhenius plot is no longer curved and the activation energy over the entire temperature range measured is constant at 1.17eV.

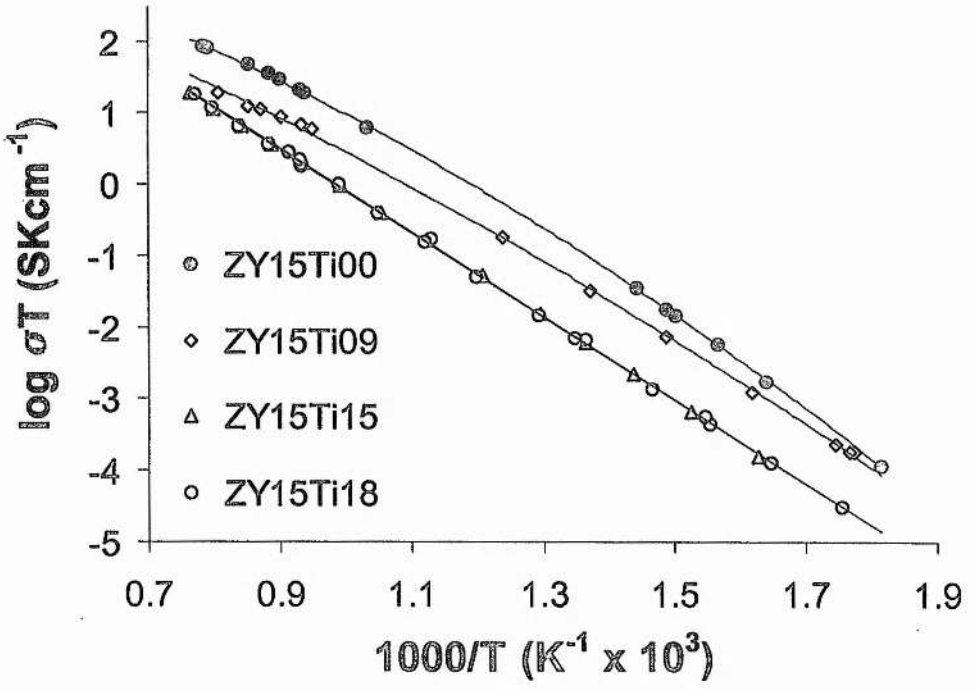

Figure 3.21. Arrhenius conductivity plots for 8 mol% YSZ (15atom% Y^{3+}) doped with 0, 9, 15 and 18 atom% Ti^{4+}.

The effect of Ti^{4+} on conductivity is different from the effect of Y^{3+} in that the activation energy of YSZ is essentially unchanged by addition of Ti^{4+} and it is the pre-exponential factor that decreases due to the decrease in the number of free carriers. This contrasts with Y^{3+} addition which lowers the conductivity of YSZ by increasing the activation energy and decreasing the pre-exponential factor. The two dopants are

similar, however, in that the Arrhenius conductivity plots become linear for both high levels of Ti^{4+} and high levels of Y^{3+}, within the temperature range studied. The fact that the activation energy in YSZ is unaffected by Ti^{4+} doping means that the smaller dopant cation radius is not the dominant factor in reducing the conductivity. The rapid decrease in conductivity can be attributed to the creation of microdomains of order within the oxygen sublattice in which the Ti^{4+} has CN=6. The simplest explanation is that oxygen vacancy migration occurs in the disordered regions. As the Ti^{4+} content increases these regions rapidly decrease in size or disappear and the electrical conductivity decreases. It is also possible that a percolation phenomenon exaggerates this volume effect. Samples below 15-18atom% Ti^{4+} can be seen as essentially continuous network of conductive, disordered domains, with small regions of non conducting domains with ordered sublattices. Above this level of Ti^{4+} the conductive domains are in the minority and essentially form 'islands' in a more insulating matrix. The electrical conductivity would thus be that of the ordered domains. As the activation energy for electrical conduction is almost independent of the Ti^{4+} content, the oxygen migration process is expected to be unaltered. Thus ordering causes a decrease in the pre-exponential factor of the ionic conductivity, which is linked to the number of free charge carriers. A previous study by Traqueia et al used Raman Spectroscopy to show that the amount of ordered microdomains did not change with temperature [59]. Thus for high Ti^{4+} a constant activation energy is expected over a wide range of temperature. The role of Titanium in the electrical behaviour of YSZ is believed to be determined mostly by local lattice distortion in the neighbourhood of Ti^{4+} ions , creating regions of ordered microdomains and thus non-equivalent anion sublattice positions.

Naito et al found that the addition of TiO_2 to YSZ resulted in a decrease in the grain boundary conductivity [60]. In contrast, Liou and Worell added silica and alumina as sintering aids to their TiO_2 doped YSZ and found that the grain boundary conductivity decreased with increasing Ti^{4+} concentration [61]. The same results were found by Matsui who also used sintering aids [62]. The results of Worell et al and Matsui are not surprising because aluminium titanates would probably appear at the grain boundary. From a previous study of 8YSZ to which Al_2O_3 had been added, Al_2O_3 was found to act as a 'getter' for Silica, which is well known to be detrimental to oxygen ion conductivity [63]. This was confirmed in the study of Alumina additioned YSZ in

Chapter 5 which found a large increase in grain boundary conductivity of 8YSZ when Alumina was added. It is likely that a similar phenomenon occurred in the work of Liou et al and Matsui. In this work, a general decrease in the grain boundary conductivity is observed with increasing Ti^{4+} content, however the actual grain boundary content is dependent on the sintering characteristics and the resulting density of the sample thus studies of the sintering of TiO_2 doped YSZ are described in Section 3.6.5. and studies of the effect of density upon conductivity are described in section 3.6.6.

3.5. Mixed Conductivity in the Ternary System ZrO_2 - Y_2O_3 - TiO_2

In Figure 3.22 the dependence of the total conductivity σ_T on oxygen partial pressure at 930°C is given for the sample $Zr_{0.62}Y_{0.2}Ti_{0.18}O_{1.9}$. The electronic contribution σ_e has been calculated according to the equation $\sigma_e = \sigma_T - \sigma_i$ assuming that the concentration of oxygen vacancies is effectively constant over the investigated pO_2 range and that the value for σ_T gives the value of the ionic conductivity σ_i at high pO_2. The electronic contribution of the conductivity σ_e for the re-oxidation range between 10^{-14}-10^{-20} atm is shown in Figure 3.21 as open circles, fitted to a straight dotted line. The calculated slope for this $\log(\sigma_e)$ vs. $\log(pO_2)$ plot and the plots for all other measured samples follow a $pO_2^{-1/4}$ dependence in the pO_2 range from 10^{-13} to 10^{-20} atm. Substantial electronic conductivity is introduced into the system at oxygen partial pressures below 10^{-13} atm via reduction of Ti^{4+} ions to Ti^{3+}. The reason for the hysteresis between the reduction and oxidation curve in Figure 3.21 is the relatively high density of the sample (80% ρ), which did not allow this sample to reach equilibrium (complete reduction or reoxidation), at each measured point. Additionally a bend in all $\log \sigma$ - $\log pO_2$ plots have been observed at very low oxygen partial pressures ($pO_2 = 10^{-18}$ to 10^{-22} atm), indicating that the reduction kinetics were too slow to achieve complete reduction of the samples. This uncompleted (slow) adjustment of the electronic conductivity at 10^{-20} atm leads to relative high deviations in the reading of σ_e.

Figure 3.23 shows the dependence of the electronic and the ionic conductivity on Yttrium content for three compositions containing 15 atom% Ti^{4+} and three compositions containing 18 atom% Ti^{4+}. The electronic conductivity for all

compositions containing 18 atom% Ti^{4+} is higher than for the compositions containing only 15 atom% Ti^{4+}, because σ_e increases with the concentration of Ti^{4+}/Ti^{3+} sites. The electronic conductivity remains the same regardless of Yttrium content.

The ionic conductivity decreases slightly with the higher Ti^{4+} concentration of 18 atom%, whereas σ_i is reduced significantly with Yttrium content. The total conductivity of highly Titania doped YSZ is also dependent on the density of the measured pellets, as will be discussed later in section 3.6.6. With densities near to the theoretical density (i.e. 96%) a maximum electronic conductivity as high as 0.2 Scm^{-1} at 930°C can be achieved for compositions containing 18 mol% Titania. The composition containing 25 atom% Y^{3+} and 18 atom% Ti^{4+} is not phase pure but was included for comparison purposes.

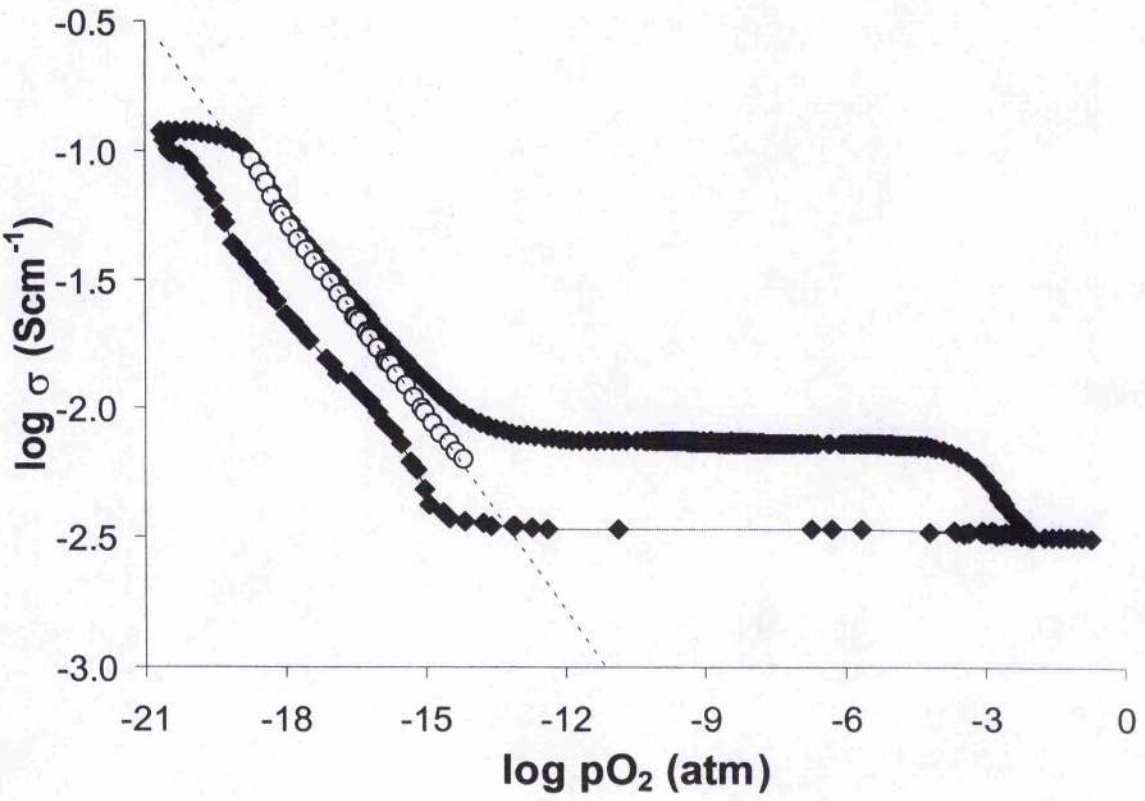

Fig. 3.22. The oxygen partial pressure dependence of $Y_{0.2}Ti_{0.18}Zr_{0.62}O_{1.9}$.

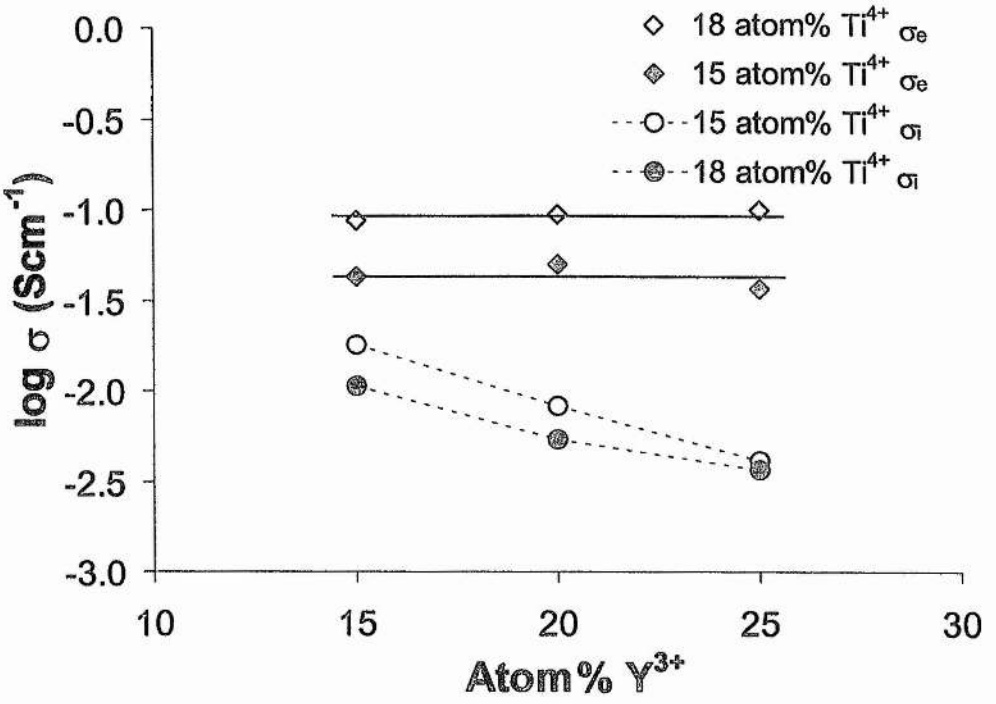

Fig. 3.22. Dependence of ionic and electronic conductivity on Yttrium content in different $Zr_{1-(x+y)}Y_xTi_yO_{2-x/2}$ compositions.

The correspondence between the measured conductivity and theory can easily be derived from the following defect model using the notation of Kröger and Vink. According to the reaction shown by equation (1) below, n-type electronic conductivity is introduced into the ZrO_2-Y_2O_3-TiO_2 compositions with the defect fluorite structure at low pO_2 by the reduction of Ti^{4+} to Ti^{3+}:

$$O_O^x + 2Ti_{Zr}^x \leftrightharpoons V_O^{\bullet\bullet} + 1/2O_2\,(g) + 2Ti_{Zr}' \qquad (1)$$

with Ti_{Zr}^x: representing a Ti^{4+}-ion on a Zr site

and Ti_{Zr}' representing a Ti^{4+} plus trapped electron=Ti^{3+} on Zr site

Applying the law of mass action the following equation can be obtained:

$$K = \frac{[Ti_{Zr}']^2[V_O^{\bullet\bullet}]P_{O2}^{1/2}}{[O_o^x][Ti_{Zr}^x]^2} \qquad (2)$$

Assuming $[Ti_{Zr}^{x}]$ is constant, i.e., $[Ti_{Zr}^{x}] >> [Ti_{Zr}']$

The electrical neutrality is given by:

$$[Ti_{Zr}'] + [Y_{zr}'] = 2[V_O^{\bullet\bullet}] \cong [Y_{Zr}'] \qquad (3)$$

As the number of reduced Ti sites $[Ti_{Zr}']$ is much less than the number of Y dopant sites, the oxygen vacancy concentration is effectively constant, thus combining equation (2) and (3) means that the dependence of oxygen partial pressure on Ti^{3+} concentration can be expressed as :

$$[Ti_{Zr}'] \propto P_{O_2}^{-1/4} \qquad (4)$$

Therefore it is concluded, in accordance with investigations in low Titania doped YSZ [64], that the n-type electronic conduction in highly Titania doped YSZ-compositions is due to a small polaron-hopping mechanism resulting from electrons hopping between Ti^{3+} and Ti^{4+} ions. Thus the highest electronic conductivity achieved in the ternary system ZrO_2-Y_2O_3-TiO_2 was 0.2 Scm^{-1} for 18 atom% Ti^{4+} samples at 10^{-20} atm with a simultaneous ionic conductivity of ~0.01 Scm^{-1} at 930°C.

3.6. Effect of TiO_2 on the sintering of $Z_{1-(x+y)}Y_yTi_xO_{2-(x/2)}$ for $0 < x < 0.18$ and $0.15 < y < 0.18$

To determine the effect of TiO_2 on the sintering of these ternary compositions, the synthesis of 15 and 20 atom% Yttria-stabilised Zirconia compositions containing up to 18atom% Ti^{4+} was achieved by ball milling the three dried oxides for one hour using Zirconia containers and balls with 1ml acetone for each gram of powder. Larger liquid to powder ratios did not result in phase pure compositions, even with milling times of up to 8 hours. For comparative purposes all compositions were prepared in an identical manner, i.e. by ball milling for 1 hour using 5g of powder and 5ml of acetone at the same rotation speed. The acetone was removed from the resulting suspended mixture by warming the Zirconia containers. The powder was then pressed into pellets and fired for 24 hours at 1500°C, followed by rapid cooling in air.

The theoretical density of compositions in the ternary system ZrO_2-Y_2O_3-TiO_2 system, containing 15 atom% Y^{3+}, decreases with increasing dissolved TiO_2 due to the decrease in formula weight and unit cell size with increasing Ti^{4+} e.g. the theoretical density for $Zr_{0.85}Y_{0.15}O_{1.925}$ calculated by X-Ray diffraction is 5.96 gcm^{-3} compared to 5.65 gcm^{-3} for $Zr_{0.67}Y_{0.15}Ti_{0.18}O_{1.925}$, Figure 3.24. For the compositions containing 15 atom% Y^{3+}, the measured geometric density increases from 4.88 gcm^{-3} to 5.14gcm^{-3} on changing from 0 to 9 atom% Ti^{4+}, Figure 3.24. The geometric density then decreases with increasing dissolved Ti^{4+} in the defect fluorite matrix. However, the $\%\rho_0$ calculated from X-ray diffraction still increases above 9 atom% Ti and reaches a limiting density of 91% i.e. The $\%\rho_0$ is approximately 9% higher than the $\%\rho_0$ obtained for compositions containing 15 atom% Y^{3+} and no Ti^{4+}, Figure 3.25. This is in general agreement with a previous study of ball milled ZrO_2, Y_2O_3 and TiO_2 where 5 mol% TiO_2 (4.6 atom% Ti) increased the density of YSZ by 7% [65].

Compositions containing 20 atom% Y^{3+} showed the same trend in density with increased TiO_2 as the compositions containing 15 atom% Y^{3+}, Figure 3.24. The $\%\rho_0$ was slightly lower than for the compositions with 15 atom% Y^{3+}, indicating that the higher Y^{3+} content has a detrimental effect on the density of compositions in this ternary system. However, despite the $\%\rho_0$ being lower than for the 15 atom% Y^{3+} compositions, the measured density for the 20 atom% Y^{3+} compositions increased by 11.55% with 18 atom% Ti^{4+} dopant compared to an increase of only 11.1% for the 15 atom% Y^{3+} compositions. The $\%\rho_0$ for all of the 20 atom% Y^{3+} compositions was greater than for all of the 15 atom% Y^{3+} compositions but the difference between them decreased steadily with increasing TiO_2, Figure 3.26.

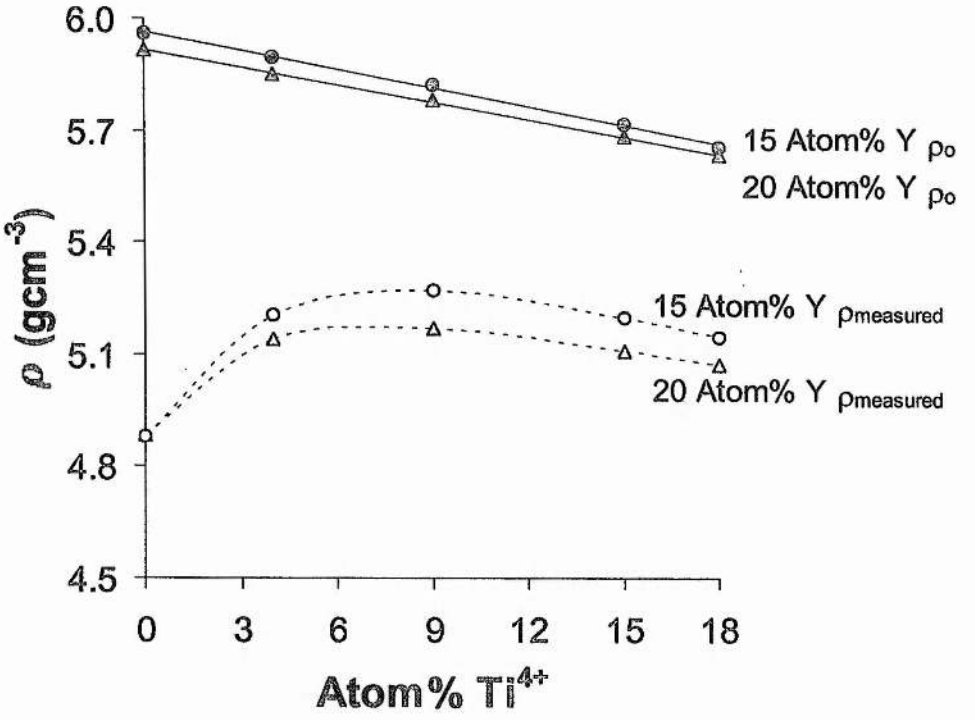

Figure 3.23. Plot of density vs. atom% Ti for $Zr_{1-(x+y)}Y_yTi_xO_{2-(x/2)}$.

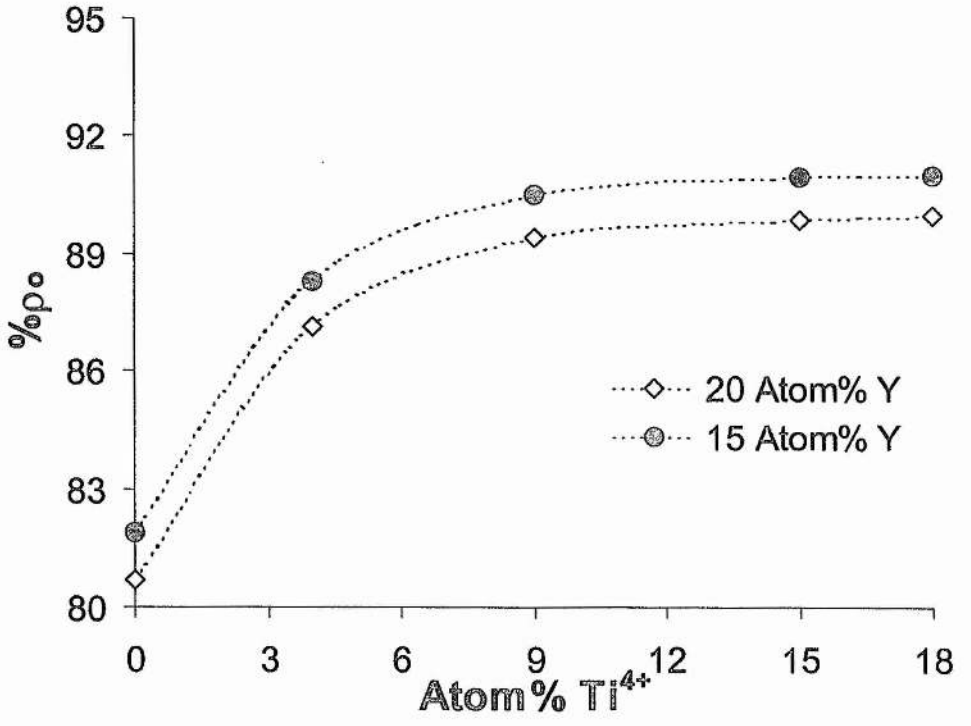

Figure 3.24. Plot of Increase in $\%\rho_0$ for compositions containing 15 and 20 atom% Y^{3+} vs. Atom% Ti^{4+}.

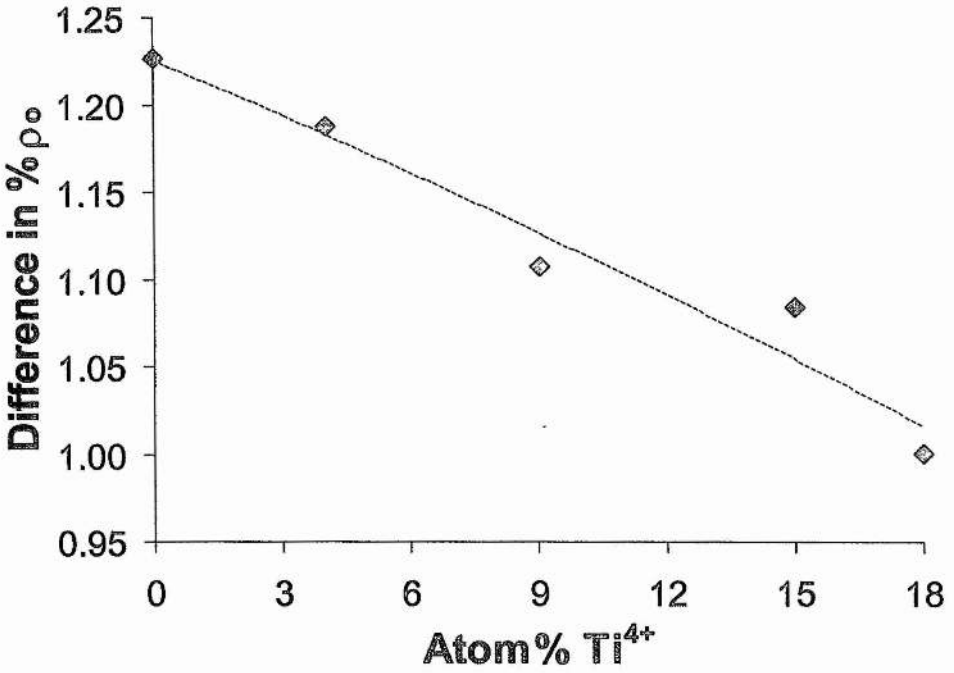

Figure 3.25. Difference in $\%\rho_0$ between 15 and 20 atom% Y^{3+} compositions versus atom% Ti^{4+}.

3.7. Density Effects on the Conductivity of $Zr_{0.62}Y_{0.20}Ti_{0.1.8}O_{1.9}$

In SOFCs the anode materials need to be highly porous in order to allow the reaction of the fuel gas with the oxygen ions to occur over as much surface area of the mixed conducting anode area as possible [66]. However, the porosity has a large effect on the conducting properties of materials and needs to be quantified so that conductivities reported by different researchers can be compared more easily. This section seeks to show the effect of a wide range of densities on the bulk and grain boundary conductivities and capacitances of a near optimum mixed ionic and electronic conducting composition in the ternary system ZrO_2-Y_2O_3-TiO_2. This section also highlights the effect of density on the hysteresis effect obtained when the sample is cycled between reducing and oxidising conditions. High density samples show a large degree of hysteresis because the ionic transport properties are poor due to the strong interaction between vacancies and Titanium thus limiting the rate at which oxygen can penetrate the sample and oxidise the Ti^{3+}. Samples of low porosity show much less

hysteresis because the samples are more readily oxidised by O_2, which is able to penetrate the sample more easily.

There is very little information available in the literature on the density correction of porous polycrystalline electroceramic properties. As solid oxide fuel cell anode materials need to be porous in order to be efficient, it is important to determine just how much of an effect the porosity of an anodic material has on its mixed conducting electrical properties in air and at low oxygen partial pressures.

The well established procedure used to correct conducting materials for porosity is to multiply the measured conductivity by the actual density divided by the theoretical density [67]. This procedure might be expected to give values which are slightly lower than the conductivity which would be obtained for a fully dense sample; however, a previous study by Brugner and Bluementhal [68] reported a comparison of conductivity values for a single crystal CeO_2 and sintered CeO_2 samples of 70 and 85% density, and found excellent agreement using the simple correction procedure.

A previous study by Mizusaki et al attempted to model the electrical resistivity of porous conducting media mathematically, but the proposed model focussed on the thickness of the bottleneck between grains in green bodies with the progress of densification, thus requiring analysis of the microstructure. The derived equations remained dependant on a parameter related to the green density of the material. However, comparison with experimental data on highly porous materials showed discrepancies at relative densities ~70% [69]. Another theoretical study by Boccaccini et al derived a relationship between density and conductivity based on the pore to grain size ratio. However, this still requires quantitative microstructural analysis [70]. Microstructural analysis takes a major effort and probably only changes the conductivity values by a few percent. It has been reported that porous materials may exhibit large additional semicircles on their impedance diagrams [71-73]. In this respect, the pores behave like any other microstructural defect such as grain boundaries, cracks or insulating inclusions [74-77]. In this study, however, no such arc was observed.

Ball milling of starting powders resulted in densities greater than 90%. In order to obtain lower densities, samples were reground and fired at temperatures between 1200 and 1400°C. The measured densities, $\rho_{measured}$, were calculated from the pellet dimensions and mass. The theoretical density was calculated using $\rho_{theoretical} = FW.Z / Na^3$,where FW is the formula weight, Z is the unit cell contents, N is Avogadro's Number $6.28x10^{-23}$ and a is the lattice parameter. The porosity, $\alpha = 1-(\rho_{measured}/\rho_{theoretical})$, was used to compare samples of different density.

3.7.1. Impedance Spectra

The contribution of porosity to impedance spectra has been proposed to consist of a small semicircle positioned between the high frequency bulk semicircle and the lower frequency grain boundary semicircle [75, 77]. In this study there are very clear differences in the impedance plots of highly porous, dense and very dense samples, however, no additional semicircles are obtained. The absence of an additional semicircle indicates that the effect of the high porosity was manifested in the bulk and/or the grain boundary semicircles and did not contribute separately to the impedance plot. Figure 3.27 shows the as measured impedance spectra for samples of varying porosity at 450°C. For porous materials with a density of approximately 60%, the bulk and grain boundary responses are poorly resolved and the 'grain boundary' response, with an associated capacitance of ~3 x 10^{-10} Fcm^{-1}, dominates the impedance plot, Figure 3.28. No bulk response is observed in the modulus plot either, Figure 3.29. For samples with a density of around 80%, the impedance plots show clearly resolved bulk and grain boundary arcs and the capacitance for the 'grain boundary' response has increased by more than 1 order of magnitude. Increasing the density to above 90% results in only a bulk response and no visible grain boundary arc, indicating that the sample is well sintered.

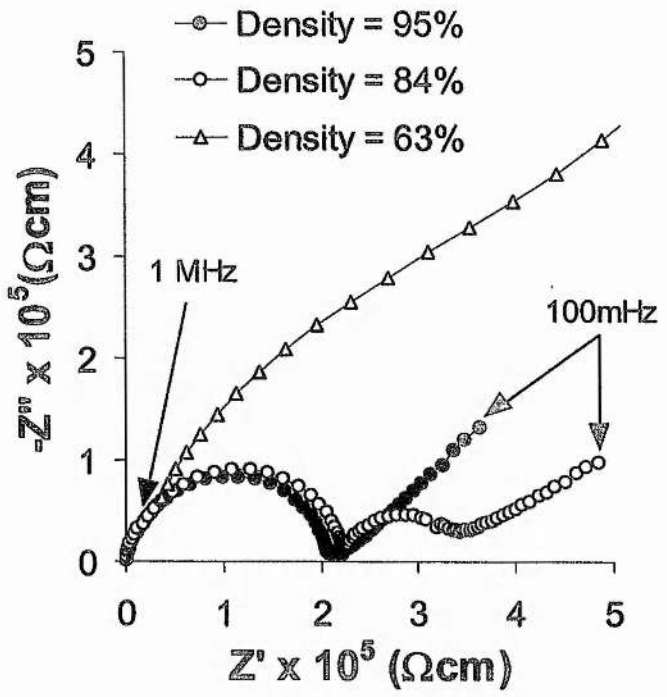

Figure 3.27. Comparison of impedance spectra taken at 455°C for samples with 63, 84 and 95% density at 452°C.

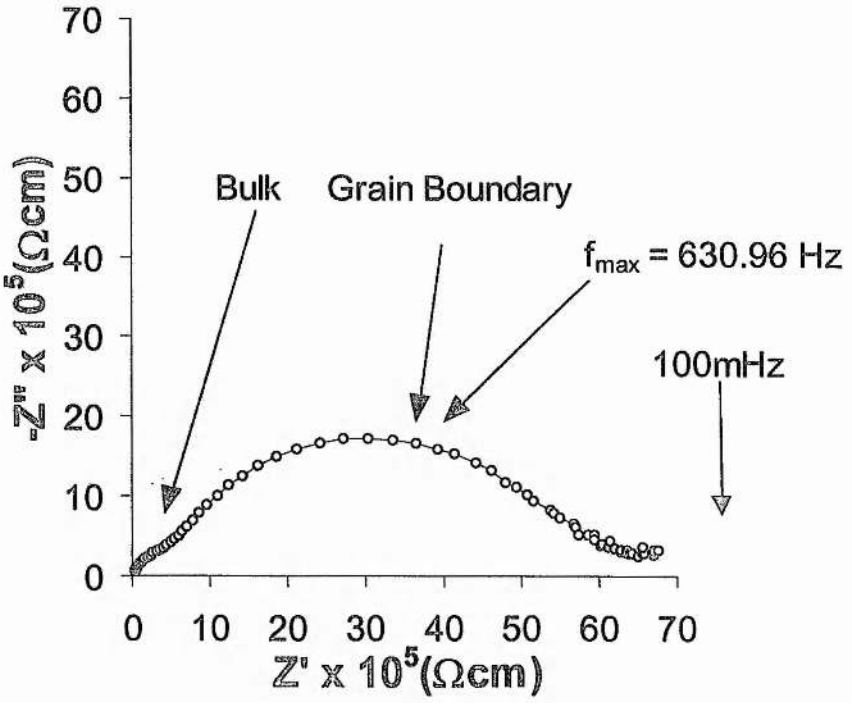

Figure 3.28. Complex plane plot of real versus imaginary impedance for $Zr_{0.62}Y_{0.20}Ti_{0.18}O_{1.90}$ with a density of 63%, obtained at 452.5°C

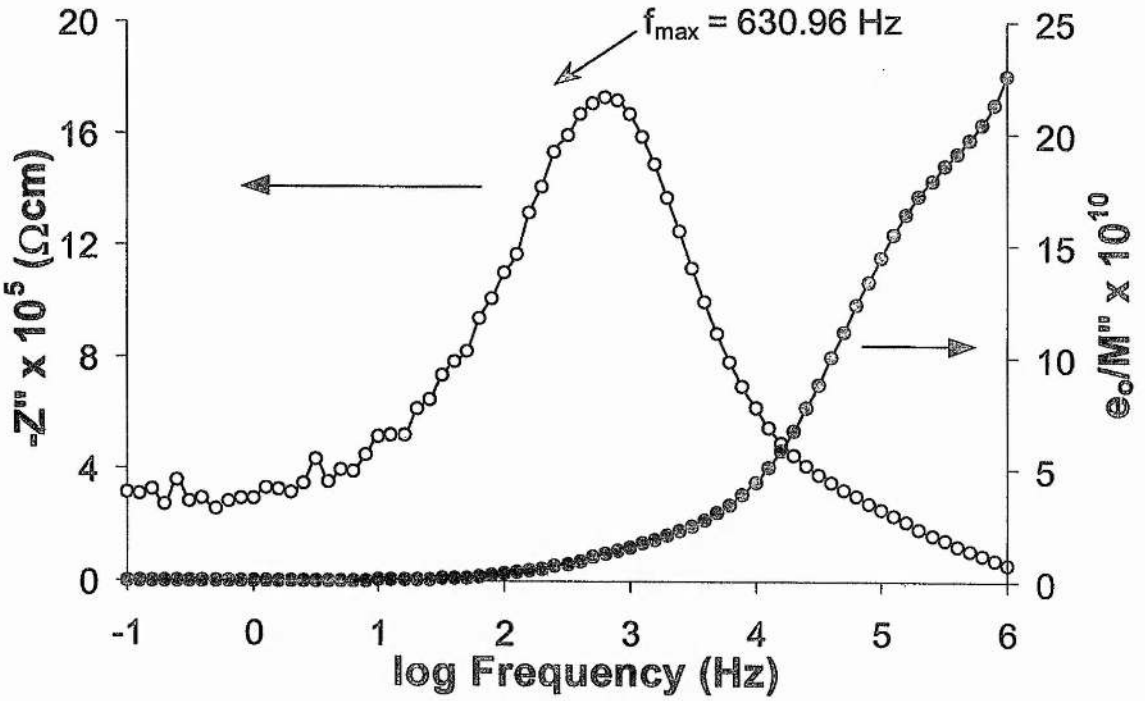

Figure 3.29. Modulus plot of imaginary impedance versus frequency for $Zr_{0.62}Y_{0.20}Ti_{0.18}O_{1.90}$ with a density of 63%, obtained at 452.5°C

3.7.2. Bulk and Grain Boundary Conductivity

The low temperature bulk and grain boundary conductivities of samples with varying density were extracted from linear Arrhenius conductivity plots constructed from the impedance plots. A typical Arrhenius plot for bulk and grain boundary components of a reasonably dense sample is shown in Figure 3.30.

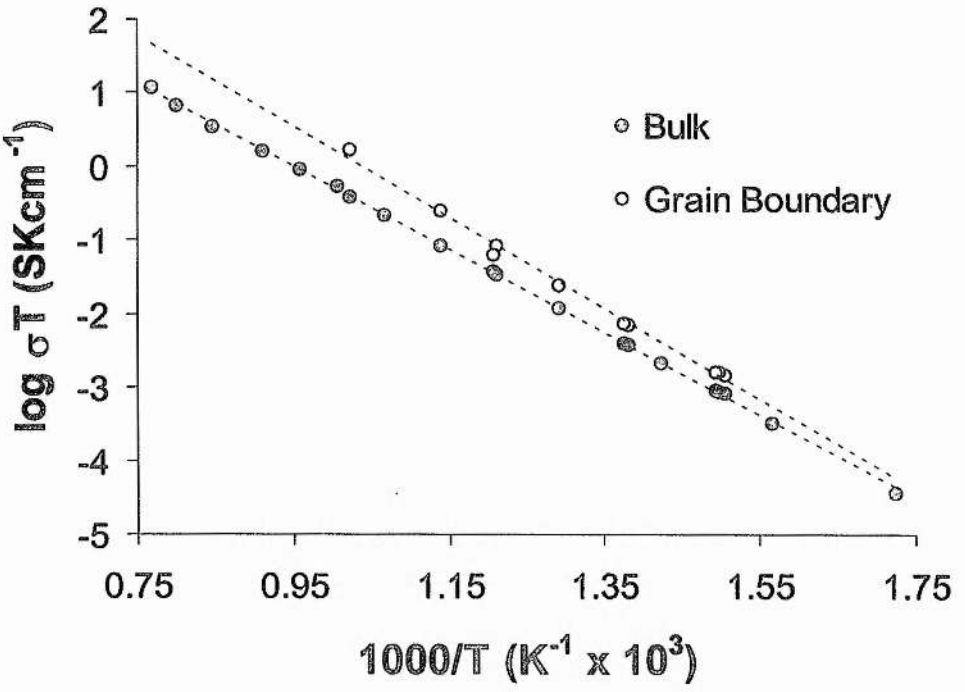

Figure 3.30. Typical Arrhenius Conductivity Plot for $Zr_{0.62}Y_{0.20}Ti_{0.18}O_{1.90}$, exhibiting grain boundary and bulk conductivities. The pellet density was 84.3 % ρ_o. (The conductivity plots were corrected for density by multiplying by $100/\%\rho_o$).

The as measured bulk resistivity at 1000°C is plotted against $\%\rho_0$ in Figure 3.31. The decrease in resistivity with increasing density follows a power law and can be seen to obey the equation $\sigma_{measured} = \sigma(1-\alpha)^n$. By plotting the log of the bulk resistivity at 1000°C versus $1-\alpha$, it is possible to determine the value of n, Figure 3.32.

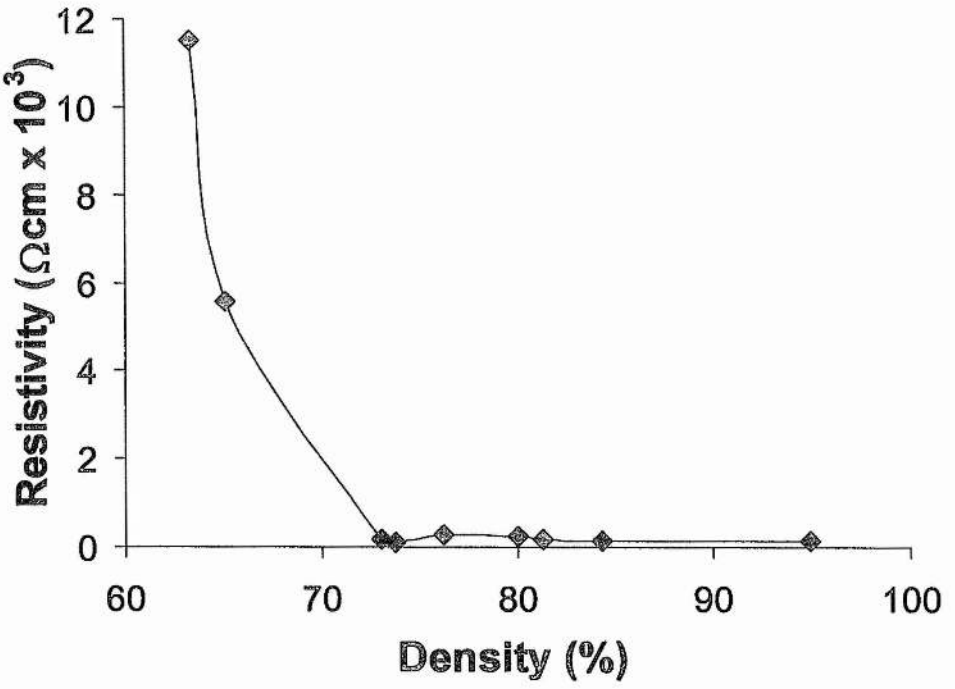

Figure 3.31. Plot of as measured resistivity at 1000°C versus $\%\rho_o$.

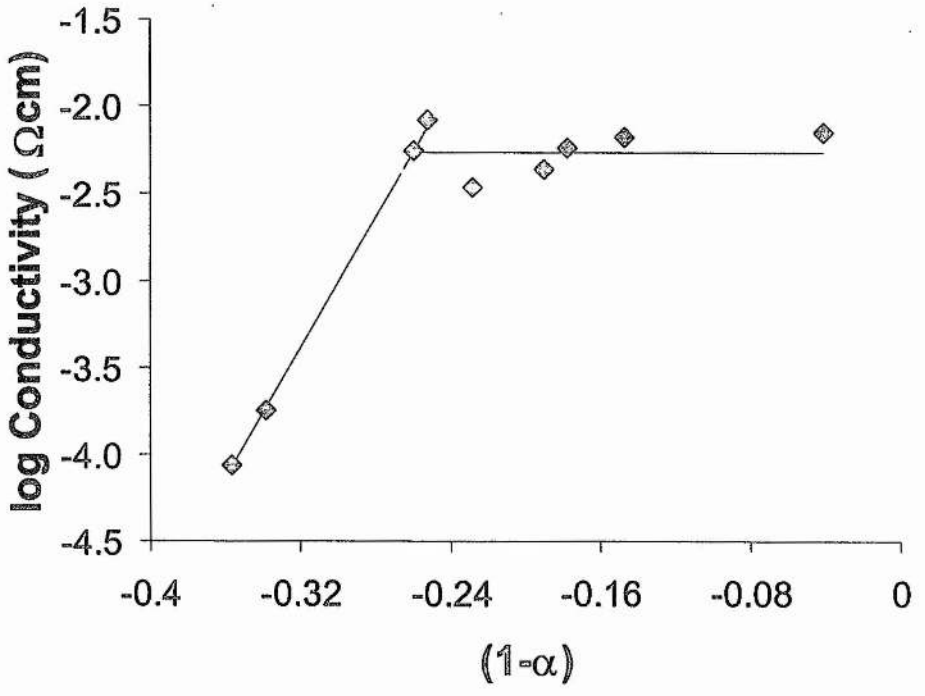

Figure 3.32. Plot of log bulk resistivity at 1000°C versus 1-α (1-porosity).

The value of n for the bulk resistivity is 0 between 27% and 0% porosity, i.e. despite the scatter in the data, the slope is 0, which means that n is 0. The scatter in the data results in the intercept of -2.26 at $1-\alpha=0$ being a little lower than expected, i.e. σ_0 is 0.55 Sm^{-1}. For porosities greater than 27% the slope, n increases to -18.7 and the intercept at $1-\alpha=0$ is 2.60, i.e. $4 \times 10^4 Sm^{-1}$.

The plot of log bulk resistivity at 300°C versus $1-\alpha$ is shown in Figure 3.33. There is a major difference from the 1000°C data in that, apart from one erroneous point, the data do not flatten out until the porosity is less than 15%. The slope, n, for the higher porosity data is 8.5 and the intercept at -6.1 corresponds to a value of 8.3×10^{-5} Sm^{-1} for σ_0.

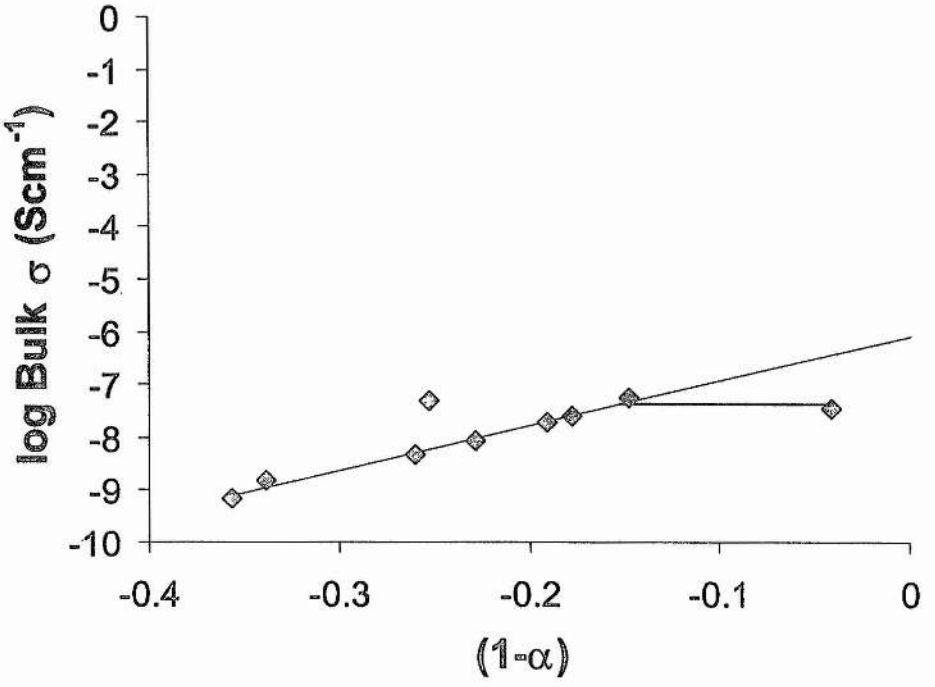

Figure 3.33. Log Plot of As measured bulk conductivity at 300°C versus $1-\alpha$.

The grain boundary conductivity at 300°C can also be seen to obey the equation $\sigma_{measured} = \sigma(1-\alpha)^n$. The as measured grain boundary resistivity is plotted against density in Figure 3.34 and the log conductivity is plotted against 1-α in Figure 3.35. The intercept at -3.40 gives σ_o a value of 0.04 Sm^{-1} at 300°C and the slope, n was ~10.

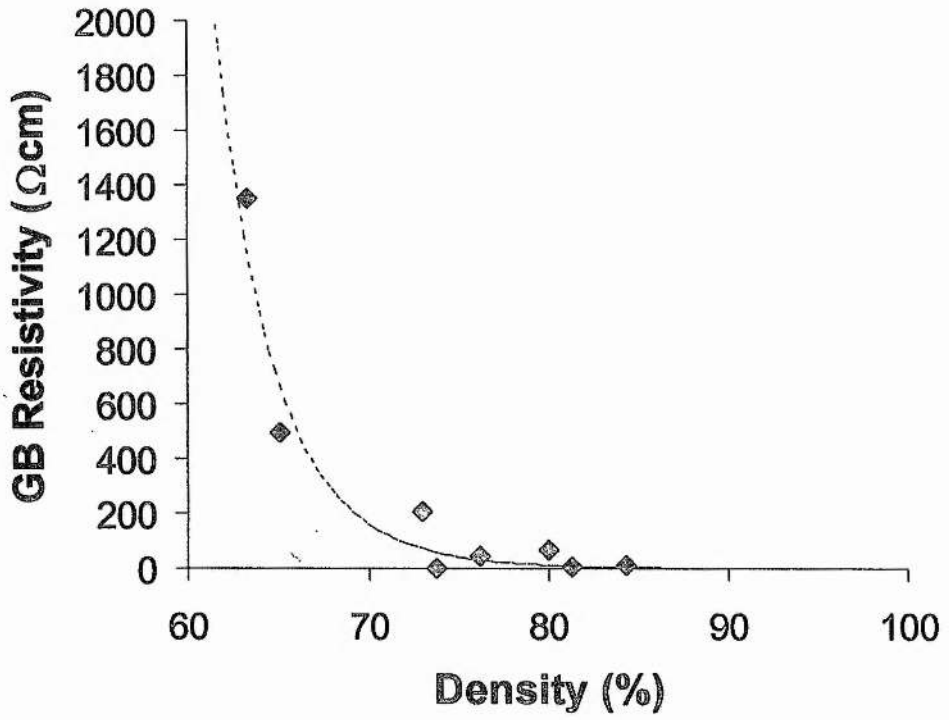

Figure 3.34. As measured grain boundary resistivity at 300°C versus density.

The contribution of the grain boundary resistance to the total resistance, i.e. R_{GB}/R_{TOTAL}, was found to decrease approximately linearly with density, Figure 3.35. This ratio can be parameterised as α_R, or the blocking effect where $\alpha_R = 1/(R_{GB}/R_{TOTAL})$, Figure 3.36 [75, 79]. Low porosity yields high values of α_R and increasing porosity produces a steady decrease in α_R.

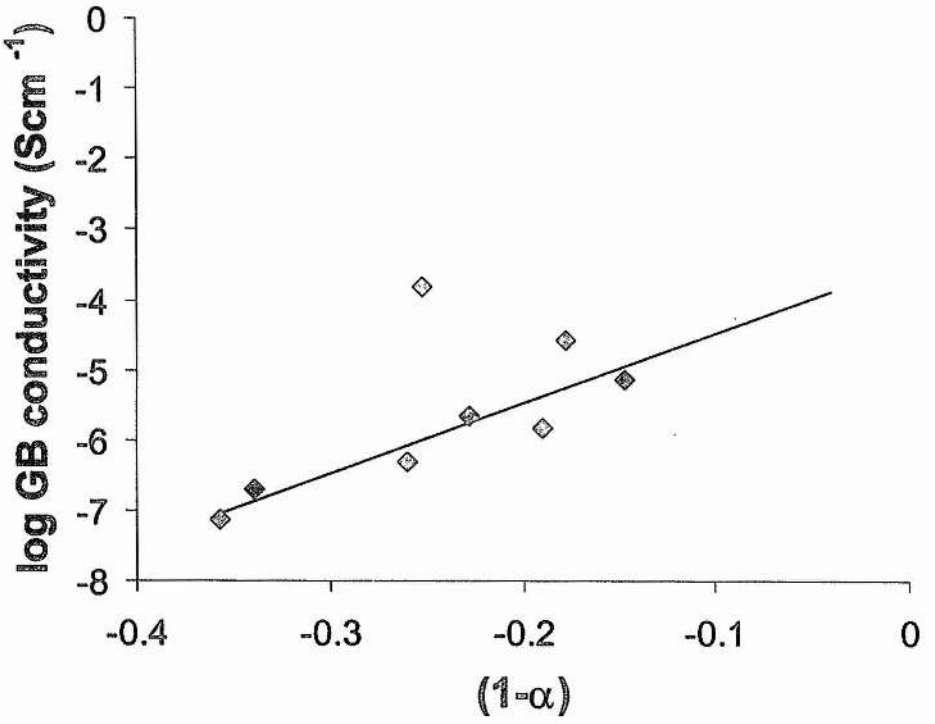

Figure 3.35. Plot of log Grain boundary conductivity at 300°C versus 1-α.

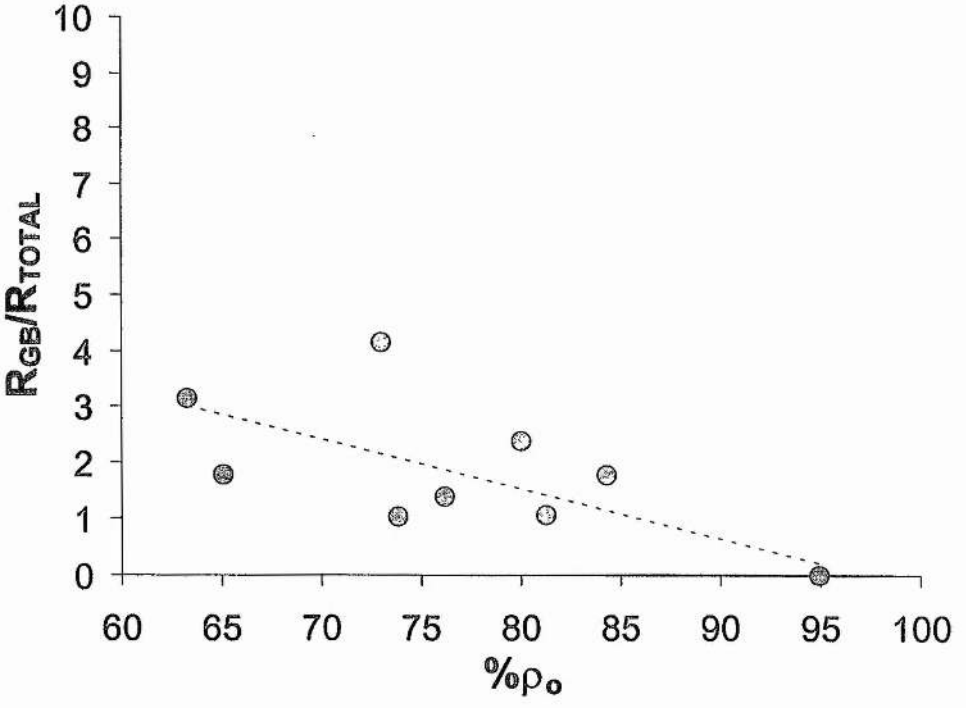

Figure 3.36. Ratio of the Grain Boundary Resistivity to Total Resistivity at 300°C for $Zr_{0.62}Y_{0.20}Ti_{0.18}O_{1.90}$.

As the plots of log bulk conductivity show that the conductivity at 1000°C for densities >73% and the conductivity at 300°C for densities >85% can be corrected for density. Thus above these critical densities the standard correction procedure used to correct for porosity can be used, i.e. the measured conductivities are multiplied by the measured density and divided by the percentage theoretical density i.e. Density corrected σ = measured σ x $100/\%\rho_0$. The grain boundary conductivities divided by 1-α at 300°C and the activation energies obtained from the linear Arrhenius conductivity plots are plotted together in Figure 3.37. The observed activation energy for ionic conduction in the grain boundaries is independent of density, lying in the range 1.3 ± 0.06 eV. The grain boundary conductivity shows the same trend with density as the grain boundary capacitance, Figure 3.39, i.e. the corrected conductivity increases linearly with density, indicating that the porosity is not manifested in the grain boundary impedance response.

The corrected bulk ionic conductivity at 1000°C and activation energy for ionic conduction in the grains are plotted against density in Figure 3.38. The corrected bulk conductivity clearly shows that the density correction procedure only becomes valid for samples with less than 27% porosity, in good agreement with the work of Brugner and Blumenthal [68]. Figure 3.38. shows that the maximum conductivity at 1000°C is 0.74 ± 0.22 Sm^{-1}.

The activation energy for bulk ionic conduction is, as with the grain boundary activation energy, essentially independent of density. The activation energy is 1.17 ± 0.04 eV. There is a difference of almost 2 orders of magnitude between the conductivity of 63 and 73% density samples.. A similar trend was found for Alumina additioned Zirconias, which showed a two order of magnitude decrease in conductivity for an increase of ~29 volume% insulating Al_2O_3 inclusions and pores (Section 5.4).

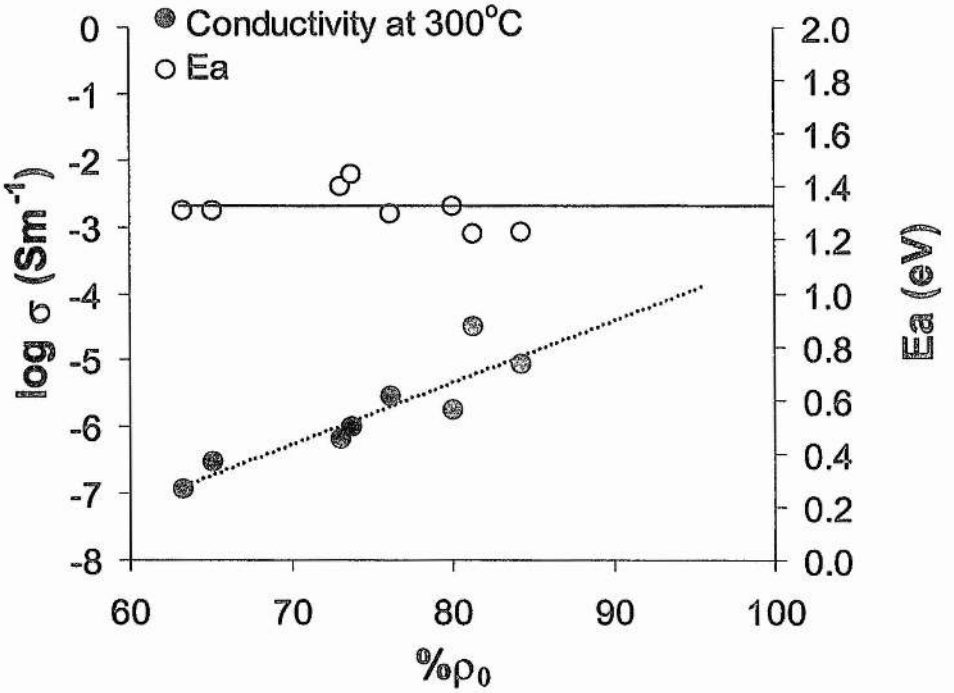

Figure 3.37. Plot of Activation Energy and Corrected Grain Boundary Conductivity at 300°C vs. $\%\rho_0$.

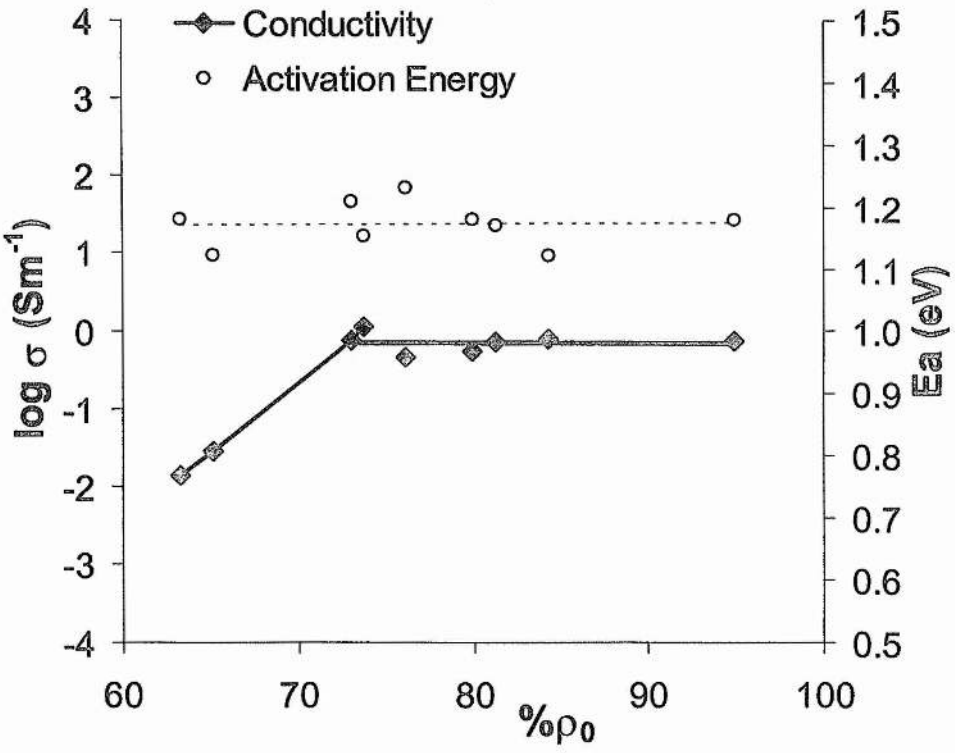

Figure 3.38. Plot of Bulk Ea and Corrected Bulk Conductivity at 1000°C vs. $\%\rho_0$.

3.7.3. Bulk and Grain Boundary Capacitance of Polycrystalline $Zr_{0.62}Y_{0.20}Ti_{0.18}O_{1.90}$

The capacitance of the bulk and grain boundary components of $Zr_{0.62}Y_{0.20}Ti_{0.18}O_{1.90}$ were compared for samples with different density, in order to investigate the dependence of capacitance upon density. The capacitance values plotted in Figure 3.38 were corrected for porosity using the equation

Porosity Corrected Capacitance = Measured Capacitance x $(\rho_{theo}/\rho_{meas})$

For this correction procedure to be valid for these polycrystalline materials, the value of n should become equal to zero above the critical level of porosity, giving the true capacitance of a fully dense ceramic.

The Bulk capacitance for the most porous sample, with 63% density, could not be determined from impedance plots because the bulk arc was not well resolved from the grain boundary arc in the impedance plots, Figures 3.27 and 3.28; however, a frequency maximum was obtained from a plot of phase angle versus frequency, which corresponded to a capacitance of 1.6×10^{-12} Fcm^{-1}, Figure 3.39. Samples of greater than 70% density showed clearly resolved bulk and grain boundary arcs in the impedance plots, e.g. Figure 3.26. The capacitance for the bulk component in the sample with 76% density was below 5×10^{-12} Fcm^{-1}. Increasing the density to 73% caused an increase in capacitance of 1.6×10^{-12} Fcm^{-1}. The corrected capacitance then remained constant for higher density samples, indicating that the density correction procedure outlined above is only valid for samples with less than 27% porosity i.e. The bulk capacitance can be corrected for density when the sample porosity accounts for less than 27% of the sample volume, as with the bulk conductivity at 1000°C, Figure 3.39.

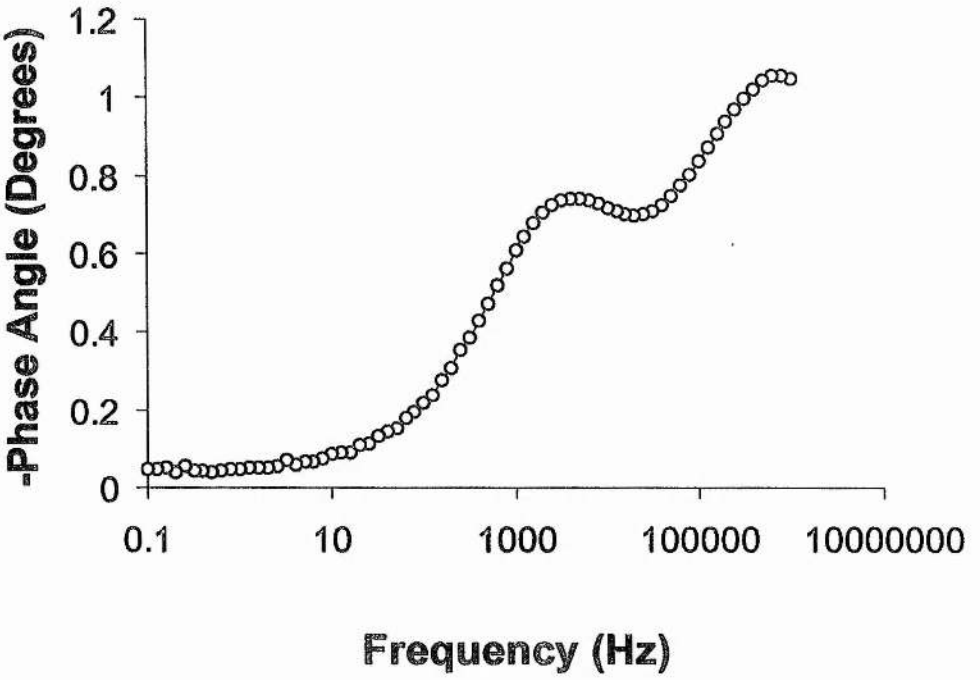

Figure 3.38. Bode plot of Phase Angle (θ) versus Frequency (Hz) for $Zr_{0.62}Y_{0.20}Ti_{0.18}O_{1.90}$ with a density of 63%, obtained at 452.5°C.

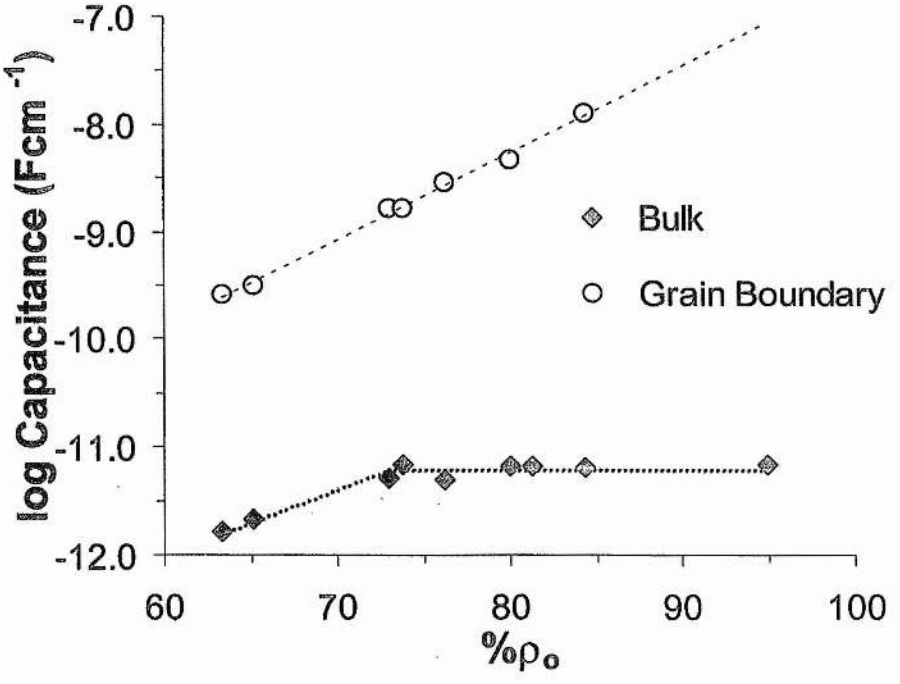

Figure 3.39. Plot of Bulk and Grain Boundary Capacitance x 100/%$D_{X\text{-}ray}$ vs. %$D_{X\text{-}Ray}$ of $Zr_{0.62}Y_{0.20}Ti_{0.18}O_{1.9}$.

The Grain Boundary capacitance for the most porous sample (63%) was calculated to be 2.6 x 10^{-10} Fcm^{-1}. The capacitance then increases linearly with density to 1.3 x 10^{-8} Fcm^{-1} for the sample with 84% density, i.e. the capacitance increases by almost 2 orders of magnitude for an increase in $\%\rho_o$ of 20%. The fact that the grain boundary capacitance increases linearly with density suggests that the pores in these polycrystalline samples are located within the grains of the ceramic, and not at the grain boundaries. Thus the grain boundary conductivity should not be corrected for density. For the highly dense sample, with a density of 95%, no grain boundary component is observed in the Cole-Cole plots, indicating that the sample is well sintered.

The time constants of the grain boundary and bulk components are shown in Figure 3.40. The time constant ($2\pi RC$) of the grain boundary component remained essentially unchanged with density. The time constant was 7.88 x 10^{-3} ± 3.24 x 10^{-3} seconds. The time constant of the bulk component decreased approximately linearly with density, however all values of τ were within 1 order of magnitude of each other in the range 5 x 10^{-6} - 6 x 10^{-5} seconds.

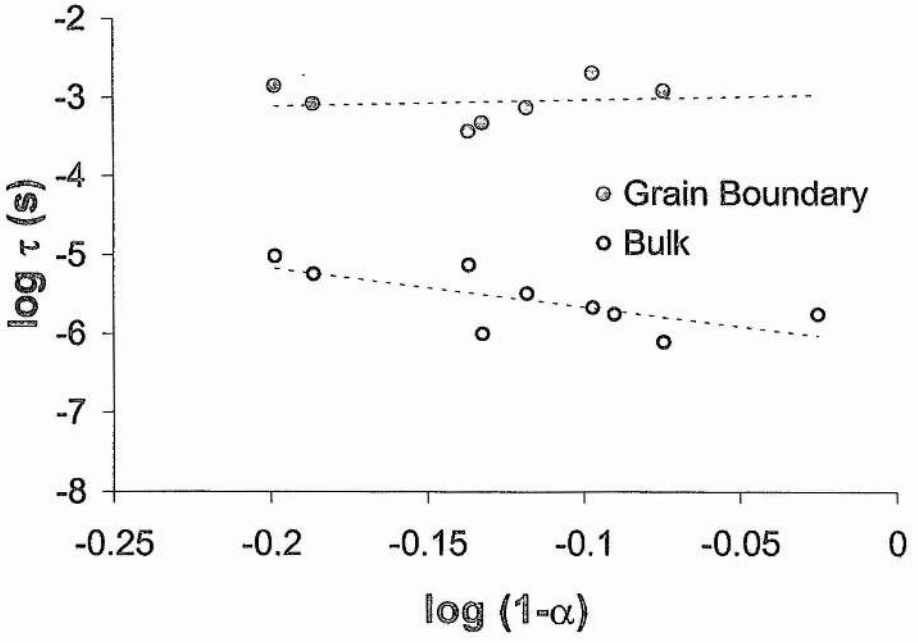

Figure 3.40. Time constants of the grain boundary and bulk components versus 1-α.

Figure 3.38 above shows that below 73% density the standard correction procedure of multiplying the conductivity at 1000°C by $100/\%\rho_0$ gives values which are too low. Thus for conductivity measurements at 1000°C, densities greater than 73% of the theoretical density should always be used in order to get an 'ideal' conductivity value. At 300°C a much smaller region shows the $1/\%\rho_o$ dependence. The characterisation of the potential anode material should then be carried out on a porous material of known density, in order to reduce hysteresis as much as possible, and then compared to the 'dense' conductivity value. In this system, below 63% the mechanical integrity of the pellet is extremely poor and so it requires careful handling. In a real fuel cell system, the anode may need to have between 40 and 50% porosity in order for oxidation of the fuel gas to occur over a large surface area. However, anodes of this low density will be mechanically supported by other layers in the ceramic system.

3.7.4. Electrical Conductivity in Reduced Oxygen Partial Pressure Atmospheres

D.C. resistivity measurements were made in reducing conditions characteristic of SOFC anode conditions to determine the effect of Ti^{4+} reduction on the electrical conductivity of $Zr_{0.62}Y_{0.20}Ti_{0.18}O_{1.90}$. Figure 3.41 shows the increase in conductivity for samples of 65 and 80% density with reduced oxygen partial pressure at 930°C. For the sample of 80% density, reduction of the Ti^{4+} begins at log $P(O_2)$ = -14.5 atmospheres. The slope of the electronic component of the reduction curve was calculated to be exactly -¼ between log $P(O_2)$ = -15 and -19 atmospheres, in agreement with a previous study on ZYT compositions [80]. At log $P(O_2)$ = -15 the conductivity, presumably due to only oxide ion conduction, was 0.33 Sm^{-1}. As the oxygen partial pressure decreased further, the conductivity increased by a factor of 28 to 9.3 Sm^{-1} at log $P(O_2)$ = -20.7, due to increased carrier concentration due to partial reduction of Ti^{4+} to Ti^{3+}.

After the initial reduction, oxidation of the sample occurs by allowing air to leak into the system naturally. The relatively high density of the pellet (80%) resulted in some hysteresis, with the conductivity upon oxidation being around one third of an order of magnitude higher than the conductivity obtained during reduction. This is because the oxide transport properties are low thus hindering the transport of oxygen into the sample in order for maximum possible oxidation to occur at each partial

pressure that a measurement is taken. Above log $P(O_2)$ = -4 the oxidation of the sample occurs relatively rapidly and the hysteresis drops to zero at log $P(O_2)$ = -2.

By comparison the sample with 15% lower density shows much less hysteresis because the poor oxygen transport properties are overcome by the oxygen being able to penetrate the sample due to the high porosity. Very little hysteresis occurs, with the greatest difference between the reduction and oxidation curves occurring below log $P(O_2)$ = -19 atmospheres. On increasing the oxygen partial pressure to above log $P(O_2)$ = -12 atmospheres there is no hysteresis.

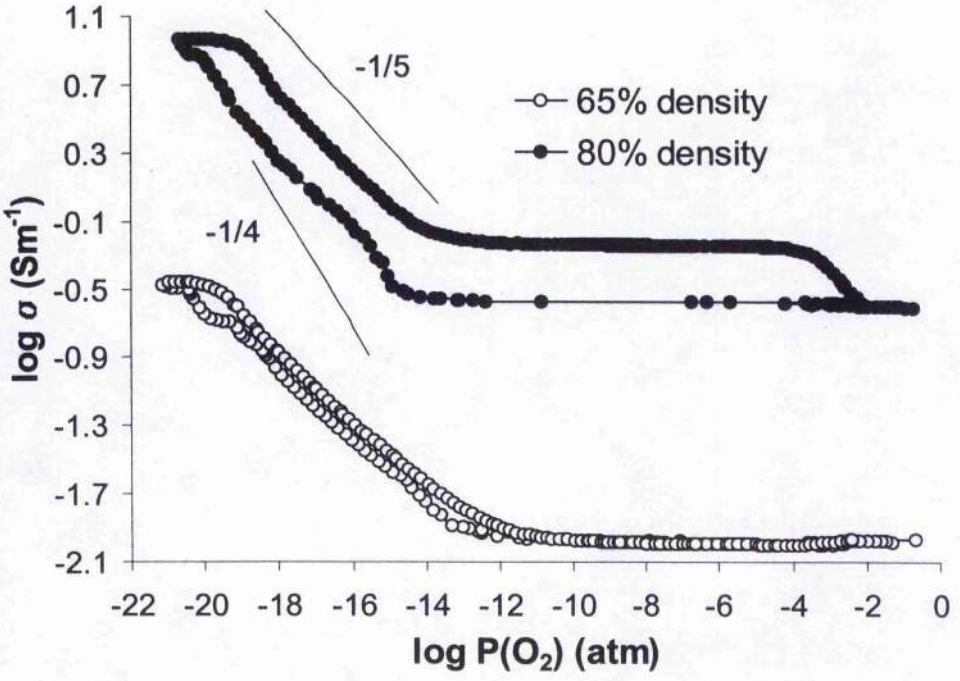

Figure 3.41. Plot of as measured conductivity at 930°C vs. Oxygen Partial Pressure for $Zr_{0.20}Y_{0.20}Ti_{0.18}O_{1.9}$ with density 65 and 80%.

As mentioned, the slope of the porous sample $\log(\sigma_{total} - \sigma_{ionic})$ plot between $P(O_2)$ -15 and -19 is -1/4 for the porous sample. This region excludes any curvature due to the transition from the predominantly ionic to the mixed conducting region and also excludes data below log $P(O_2)$ = -19 atm where density effects cause a decrease in the slope of the reduction curve towards -1/5. The oxidation curve shows a more pronounced difference from the ideal slope of -1/4. However, by subtracting the ionic conductivity from the total conductivity, a slope of -1/4 is obtained for the electronic conductivity, as described in Section 3.5.4.

For the 80% dense sample, the slope of the log $(\sigma_{total} - \sigma_{ionic})$ plot between $P(O_2)$ -15 and -18 is -1/3.4. This is due to the higher density hindering the complete reduction of the Ti^{4+} at each $P(O_2)$. The slope of -1/4 is never quite attained because of the high density of the sample. Below log $P(O_2)$ = -19 atm the density effects cause the slope of the reduction curve to remain between -1/3 and -1/4. The oxidation curve has a slope of almost -1/9 up to log $P(O_2)$ = -19. Increasing the oxygen partial pressure further results in a curve with a slope of -1/4, i.e. the density has little effect on the oxidation of the sample below log $P(O_2)$ = -19.

Thus the density plays a large part in determining the measured conductivity of electroceramic materials. For Compositions with densities of more than 73% of the theoretical density, the conductivity at 1000°C can be corrected for porosity very accurately by multiplying the measured conductivity by ρ_0/ρ_{meas}. At 300°C, the conductivity can only be corrected for a much smaller range of density. For higher levels of porosity, the conductivity is severely hindered by the presence of insulating pores and the porosity increases the resistivity of both the grain boundary and grain contributions to the total resistivity. The conductivity of a 60% dense material at 1000°C is almost 2 orders of magnitude less than the dense conductivity.

3.8. Conclusion

The ternary system ZrO_2 - Y_2O_3 - TiO_2 has been shown to exhibit a large defect cubic fluorite region which exhibits a range of ionic and electronic conducting properties. The optimum mixed conducting compositions containing between 15 and 20 atom% Y^{3+} and 15-18 atom% Ti^{4+} have ionic conductivity values one order of magnitude lower than the Titania free compositions, i.e. ~1 Sm^{-1}. Significant electronic conductivity is introduced at low oxygen partial pressures, however, the highest electronic conductivity of 20 Sm^{-1} obtained for compositions containing 18 atom% Ti^{4+} at 10^{-20} atmospheres is not high enough to be considered as a replacement for the current Ni/YSZ cermet anode materials in SOFCs. One of these optimum compositions could, however, be used to replace the YSZ in the cermet, as the unit cell parameters are similar to YSZ as will be the thermal expansion coefficient and chemical compatibility.

3.9. References

[1] H.G. Scott, J. Mat. Sci. 10[9] (1975) 1527-1535

[2] Y. Du, Z. Jin and P. Huang, J. Am. Ceram. Soc. 74[7] (1991) 1569-14577

[3] R. Ruh, K. S. Mazdiyasni, P. G. Valentine and H. O. Bielstein, J. Am. Ceram. Soc. 67[9] (1984) c-190-c-192

[4] F. F. Lange, J. Mat. Sci. 17[1] (1982) 225-234 (part 1)

[5] M. Yoshimura, Ceram. Bull. 67[12] (1988) 1950-1955

[6] F. F. Lange, J. Mat. Sci. 17[1] (1982) 225-234 (part 1)

[7] T. Okubo and H. Nagamoto, J. Mat. Sci. 30[3] (1995) 749-757

[8] R. Maenner, E. Ivers-Tiffée, W. Wersing and W. Kleinlein, Comm. Eur. Communities [Rep.] EUR 1991, EUR 13564 Proc. Int. Symp. Solid Oxide Fuel Cells, 2nd (1991) 712-725

[9] F.T. Ciacchi, K.M. Crane and S.P.S Badwal, Solid State Ionics, 73 (1994) 49-61

[10] K. Hishinuma, M. Abe, K. Hasegawa, Z. Nakai, T. Akiba and S. Somiya, in: Science and Technology of Zirconia V, eds. S. P. S. Badwal, M. J. Bannister and R. H. J. Hannink (Technomic Publishing Co. Inc., Lancaster USA 1993) 207-214

[11] M Yoshinaka, K. Hirota, O. Yamaguchi, H. Kune, S. Inamira, H. Miyamoto, N. Shiokawa and R. Shikata, Br. Ceram. Trans. 93[6] (1994) 234-238

[12] F. T. Ciacchi, S. P. S. Badwal and J. Drennan, J. Eur. Ceram. Soc. 7 (1991) 185-195

[13] I.R. Gibson, PhD Thesis, University of Aberdeen, 1995

[14] Y. Suzuki, Solid State Ionics 81 (1995) 211-216

[15] V. S. Stubican, G. S. Corman, J. R. Hellmann and G. Senft, in: Advances in Ceramics, Vol. 12, Science and Technology of Zirconia II, eds. N. Claussen, M. Ruhle and A. H. Heuer (Am. Ceram. Soc., Columbus, OH, 1984) pp. 96-106

[16] C. Pascual and P. Duran, J. Am. Ceram. Soc. 66 (1983) 23

[17] A.E. McHale and R.S. Roth, J.Am. Ceram. Soc., 69[11] 827-832 (1986)

[18] L. Domingues, A.E.McHale, R.S. Roth and T. Negas, Extended abstract, 2nd International Conference on the Sciece and Technology of Zirconia, Zirconia-83, Stuttgart, June 21-23, 1983

[19] A.E. McHale and R.S.Roth, J.Am.Ceram.Soc.,66[2] C18-C20 (1983)

[20] Antonio Cocco, Ann. Chim. (Rome) 48 598 (1958)

[21] T. Noguchi and M. Mizuno, Bull. Chem. Soc. Jap., 41 [12] 2898 (1968)

[22] L.W. Coughanour, R.S. Roth and V.A. Deprosse, J.Research Natl. Bur Standards, 52[1] 39 (1954); RP 2470

[23] Frank H. Brown, Jr.,and Pol Duwez, J. Am. Ceram. Soc., 37[3] 132 (1954)

[24] A. V. Shevchenko, L. M. Lopato, I. M. Maister and O. S. Gorbunov, Russ. J. Inorg. Chem., 25[9] 1379-1381 (1980)

[25] N. Mizutani, Y. Tajima and M. Kato, J. Am. Ceram. Soc., 59 [3-4] 168 (1976)

[26] L.S.M. Traqueia, T. Pagnier and F.M.B. Marques, J. Eur. Ceram. Soc. 17, 1019 (1997).

[27] H. Arashi and H. Naito, Solid State Ionics 53-56, 431 (1992)

[28] S.S. Liou and W.L. Worrell, Appl. Phys. A. 49, 25 (1989)

[29] Yokokawa H, Horita T., Sakai N., Dokiya M., Van Herle J. and Kim S. G. , Denki Kagaku, 1996, Vol.64, No.6, pp.690-691

[30] Ping. Li and I-Wei Chen, Denki Kagaku, 64, 690 (1993)

[31] R.C. Garvie, J. Phys. Chem. 69[1] (1965) 1238-1243

[32] T. Masaki, J. Am. Ceram. Soc. 69[7] (1986) 519-522

[33] K. Tsukuma, Y. Kubota and T. Tsukidate, in: Advances in Ceramics, Vol. 12, eds. N. Claussen, M. Rühle and A. H. Heuer (The American Ceramic Society, Columbus, OH, 1984) 555-571

[34] F. F. Lange, J. Mat. Sci. 17[1] (1982) 225-234 (part 1)

[35] F. F. Lange, J. Mat. Sci. 17[1] (1982) 225-262 (parts 2-5)

[36] M. Hirano, Br. Ceram. Trans. J. 91 (1992) 139-147

[37] A. H. Heuer, in: Advances in Ceramics, Vol. 3, eds. A. H. Heuer and L. W. Hobbs (The American Ceramic Society, Columbus, OH, 1981) 98-115

[38] M. Matsui, T. Noma and I. Oda, in: Advances in Ceramics, Vol. 12, eds. N. Claussen, M. Rühle and A. H. Heuer (The American Ceramic Society, Columbus, OH, 1984) 371-381

[39] N. Bonanas, R. K. Slotevenski, B. C. H. Steele and E. P. Butler, J. Mat. Sci. Letts. 3 (1984) 245

[40] F. K. Moghadam and D. A. Stevenson, J. Am. Ceram. Soc. 65[4] (1982) 213-216

[41] M. Kuwabara, T. Murakami, M. Ashizuka, Y. Kubota and T. Tsukidate, J. Mat. Sci. Letts. 4 (1985) 467-471

[42] E. M. Logothetis, in: Advances in Ceramics, Vol. 3, eds. A. H. Heuer and L. W. Hobbs (The American Ceramic Society, Columbus, OH, 1981) 388-405

[43] R. J. Bratton and S. K. Lau,in: Advances in Ceramics, Vol. 3, eds. A. H. Heuer and L. W. Hobbs (The American Ceramic Society, Columbus, OH, 1981) 406-418

[44] Proc. 1st. Intl. Symp. on Solid Oxide Fuel Cells, ed. S. C. Singhal (The Electrochemical Society, Pennington, New Jersey 1989)

[45] Proc. 2nd. Intl. Symp. Solid Oxide Fuel Cells, eds. F. Grosz, P. Zegers, S. C. Singhal and O. Yamamoto (CEC Publ. EUR 13546 EN, Brussels, Belgium 1991)

[46] Proc-Electrochem. Soc. 1993, 93-94, Proc. 3rd Intl. Symp. on Solid Oxide Fuel Cells

[47] S.P.S. Badwal, Solid State Ionics 52 (1992) 23-32

[48] N. Bonanos, R.K. Slotevenski, B.C.H. Steele and E.P. Butler, J. Mat. Sci. Letts. 3 (1984) 245-248

[49] K. Kobayashi, H. Kuwajima and T. Masaki, Solid State Ionics 3/4 (1981) 489-493

[50] M. Kuwabara, M. Ashizuka, Y. Kubota and T. Tsukidate, J. Mat Sci. Letts. 5 (1986) 7-9

[51] F.K. Moghadam, T, Yamashita and D.A. Stevenson, in : Advances in Ceramics, Vol. 3, eds. A.H. Heuer and L.W. Hobbs (The American Ceramic Society, Columbus, OH, 1981) 364-379

[52] K. Nakajima, K. Kobayashi and Y. Murata, in: Advances in Ceramics, Vol. 3, eds. N. Claussen, M. Rühle and A.H. Heuer (The American Ceramic Society, Columbus, OH, 1981) 399-407

[53] T. Sato and M. Shimada, J. Am. Ceram. Soc. 68[6] (1985) 356-359

[54] Y. Suzuki, T.Takahashi and N. Nagae, Solid State Ionics 3/4 (1981) 483-487

[55] A.N. Vlasov and M.V. Perfiliev, Solid State Ionics 25 (1987) 245-253

[56] R. D. Shannon, Acta Crystallogr. A32, 751 (1976)

[57] C. R. A. Catlow, A. V. Chadwick, G. N. Greaves and L. M. Moroney, J. Am. Ceram. Soc., 69[3] 272-77 (1986)

[58] I.R. Gibson and J.T.S. Irvine, J. Mater. Chem. 6 (1996) 895-898

[59] L.S.M. Traqueia, T. Pagnier and F.M.B. Marques, J.Eur.Ceram.Soc. 17 (1997) 1019-1026

[60] H. Naito and H. Arashi, Solid State Ionics 53-56, (1992) 436-441

[61] S.S. Liou and W.L. Worell, Appl. Phys. A 49 (1989) 25

[62] N. Matsui, Denki Kagaku 58 (1990) 716

[63] E.P. Butler and J. Drennan, J. Am. Ceram. Soc. 65 (1982) 474-478

[64] K. E. Swider, W. L. Worrel, J. Electrochem. Soc., 143 (1996) 3706-3711

[65] K.C. Bradford, R.J. Bratton, J Mat. Sci. 14 (1979) 59-65].

[66] M. Mogensen, Proc. 14th Int. Mater. Sci., F.W. Poulsen, J.J. Bentzen, T. Jacobsen, E. Skou, M.J.L. Ostergard (Eds.), High Temp. Electrochem., Behaviour Fast Ion and Mixed Cond.,Riso Nat. Lab., Denmark, 1993, p. 117.

[67] M. Mogensen, T. Lindegaard and U.R. Hansen, J. Electrochem. Soc.141[8] (1994) 2122-2128

[68] F. S. Brugner and R.N. Bluementhal, J. Am. Ceram. Soc., 54 (1971) 57

[69] J. Mizusaki, S. Tsuchiya, K. Waragi, H. Tagawa, Y. Arai and Y. Kuwayama, J. Am. Ceram. Soc. 79 109-13 (1996)

[70] A. R. Boccaccini and Z. Fan, J. Am. Ceram. Soc. 79[11] (1996) 2997-98

[71] E. J. L. Schouler, N. Mesbahi and G. Vitter, Solid State Ionics 9&10 (1983) 989

[72] S.P.S. Badwal and J. Drennan, J. Mater. Sci., 22 (1987) 3231

[73] S.P.S. Badwal, Applied Physics. A, 50 (1990) 449

[74] S.P.S. Badwal, Solid State Ionics, 76 (1995) 67

[75] L. Dessemond, R. Muccillo, M. Henault and M. Kleitz, Appl. Phys. A, 57 (1993) 57

[76] M. Kleitz, C. Pescher and L. Dessemond, in Science and Technology of Zirconia V, S.P.S. Badwal, M.J. Bannister, and R.H.J. Hannink, Editors, p.593, Technomic Publishing Co., Lancaster-Basel (1993)

[77] M.C. Steil and F. Thevenot, J. Electrochem. Soc., 144 (1997) 390-398

[78] L. Dessemond, J. Guindet, A.Hammou and M. Kleitz, Proc. Int. Symp. SOFC's 2nd (1991) 712

[79] M.V. Inozemtsev, M.V. Perfil'ev and A.S. Lipilin, Elektrokhimiya 10 (1974) 1471

[80] K.E. Swider and W.L. Worrell, J. Electrochem. Soc., Vol. 143 (1996) 3706-3711

CHAPTER 4

The Ternary System ZrO_2 - Gd_2O_3 - TiO_2

4.1. Introduction

4.1.1 The Pyrochlore Structure

The pyrochlore structure has the formula $A_2B_2O_7$ and exhibits a wide range of physical properties. This is because the B element can be a transition metal with variable oxidation state or a post transition metal and the A element can be a rare earth or an element with inert lone-pair of electrons. Thus the electrical nature of the pyrochlore varies from highly insulating through semiconducting to metallic behaviour with a few compounds exhibiting a semiconductor to metal transition,

The general formula of the oxide pyrochlores can be written as $A_2B_2O_6O'$ with four crystallographically non-equivalent kinds of atom. The space group of the ideal pyrochlore structure is Fd3m and there are 8 molecular units per cell (z=8). The structure is composed of two types of cation co-ordination polyhedron. The A cation (usually ~1 Å ionic radius) are 8 co-ordinated and are located within scalenohedra (distorted cubes) that contain six equally spaced anions (O' atoms) at a slightly shorter distance from the central cations. The smaller B cations (~0.6 Å ionic radius) are six co-ordinated and are located within trigonal antiprisms with all the six anions at equal distances from the central cations. Apart from the general rules regarding allowed (hkl) x-ray reflections for Fd3m space group, the additional rules for the pyrochlore structure are: h, k and l must be equal to 4n+2 or 4n, or h + k + l must be equal to 2n + 1 or 4n. The lattice parameters are generally ~10 Å whereas the x parameter is found to range from 0.309 to 0.355. The shortest A-O and B-O distances in pyrochlores are usually close to the average bond distances encountered in the A and B binary or ternary oxides with eight and six-fold co-ordination respectively.

Only one parameter, the 48f oxygen x value, needs to be defined in the structure containing 4 different kinds of atoms, A, B, O and O'. However, the 8-fold and 6-fold co-ordination polyhedra of oxygens around the A and B cations respectively in $A_2B_2O_7$ change shape with x and the entire structure can be viewed in several different ways. The (3+, 4+) phases are large in number and the existence of Ln^{3+} ions with a systematic variation in ionic radius enables one to exactly define the stability field of (3+, 4+) pyrochlores in terms of radius ratio. The relative ionic radii, RR = (r_A^{3+}/r_B^{4+})

and the oxygen parameter (x) govern the formation and stability of the oxide pyrochlore. Pyrochlores can form for RR = 1.46 to 1.80 (e.g. $r_{Gd}/r_{Zr} = 1.47$ and $r_{Gd}/r_{Ti} = 1.75$) at atmospheric pressure.

Bystrom and others [1-4] described the pyrochlore as a network structure of corner linked BO_6 octahedra with the A atoms filling the interstices. Aleshin and Roy [5] and Longa et al. [6] described it on the basis of an anion deficient fluorite unit cell. There as several other more generalised descriptions involving penetrating networks of BO_6 octahedra and A_2O' chains [7] or of A_4 and B_4 tetrahedra [8] with oxygens suitably placed inside or outside [9]. However, the fact remains that no single description can explain all the structural characteristics of the pyrochlores.

The preferred description of the pyrochlore structure for this study is that based on a fluorite type cell. As described in Chapter 1, the fluorite structure, with space group Fm3m, consists of a cubic close packed array of zirconium ions, with oxygen occupying all the tetrahedral sites. The pyrochlore structure, which has space group Fd3m, can be considered as an anion deficient superstructure composed of 8 defect fluorite blocks. The oxygen ions occupy the 48f and 8a sites and leave the 8b site systematically vacant. Thus 1/8 of the anion sites in fluorite become empty interstitial sites in pyrochlore. This ordering on the anion and cation sublattices, results in a unit cell twice the size of the equivalent fluorite cell. The larger A cations occupy the 16c sites and the smaller B cations occupy the 16d sites, forming parallel strings of atoms along the <110> directions. This results in 3 kinds of tetrahedral interstices for anions: 48f positions having two A and two B near neighbours, 8a positions having four A near neighbours and 8b positions having four B near neighbours. In the pyrochlore structure, the 8b positions are vacant ($A_2B_2O_7$ vs 4 CaF_2). The four B cations that neighbour such an anion vacancy tend to be electrostatically shielded from one another by a displacement x of each 48f anions from the centre of it's tetrahedral interstice towards its two neighbour B cations [6]. The 48f anions, originally at x = 0.375 are shifted to a position x = 0.3125 where B ions are in perfect octahedra that share corners along the [110] direction. It makes the B-O-B angle increase from 109°28' to about 132°. The 8a anions (O') remain equidistant from the four nearest A cations. The 8b sites are properly viewed as empty interstitial sites rather than oxygen vacancies. As a consequence, ideal pyrochlore oxides are ionic insulators.

Although this description is fairly simple, it is suitable only for pyrochlores with an x value in the vicinity of 0.375 and most of the x values lie well below this region [7]. This type of description is, however, suitable for compounds with higher x, i.e. compounds with large ionic radius such as Zr^{4+} for the B site. Some of these compounds undergo a pyrochlore-defect fluorite type transition. This type of transition never occurs in the pyrochlore structure containing smaller B cations. Three different representations of the pyrochlore structure are shown in Figures 4.1-4.3.

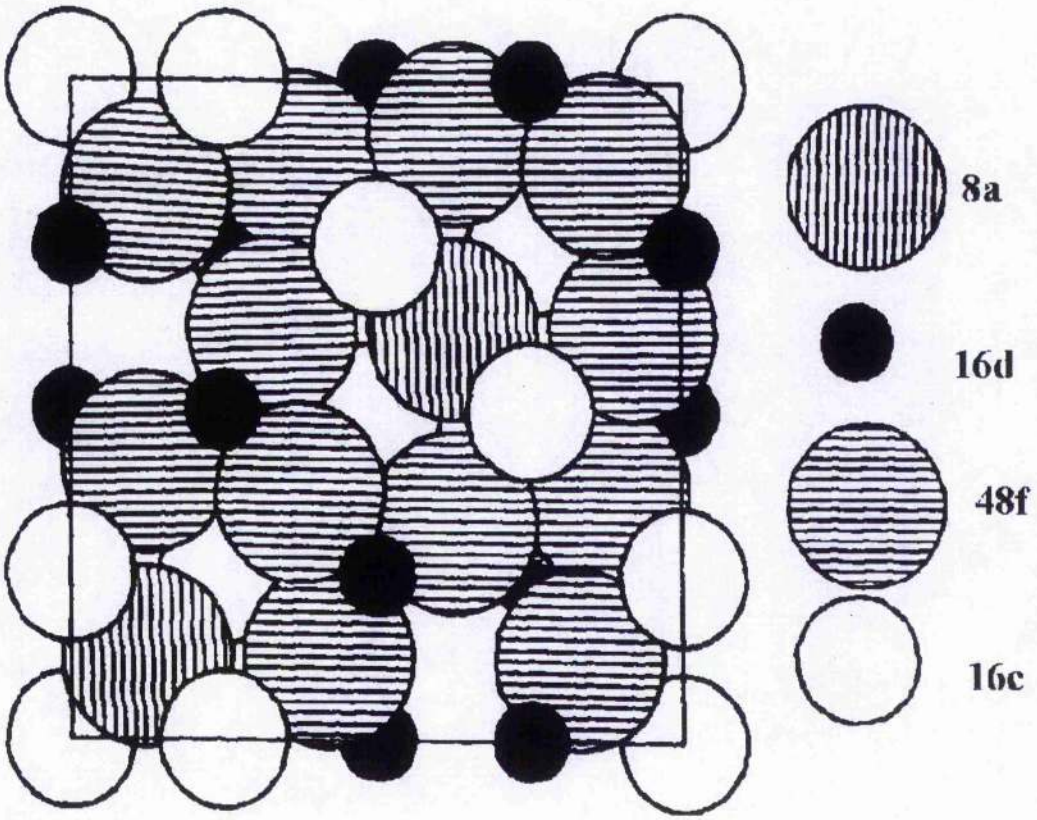

Figure 4.1. (100) projection of a portion of one unit cell of the pyrochlore structure. Ionic radii are based on $Gd_2Ti_2O_7$. The empty space in the lattice represents the vacant 8b site.

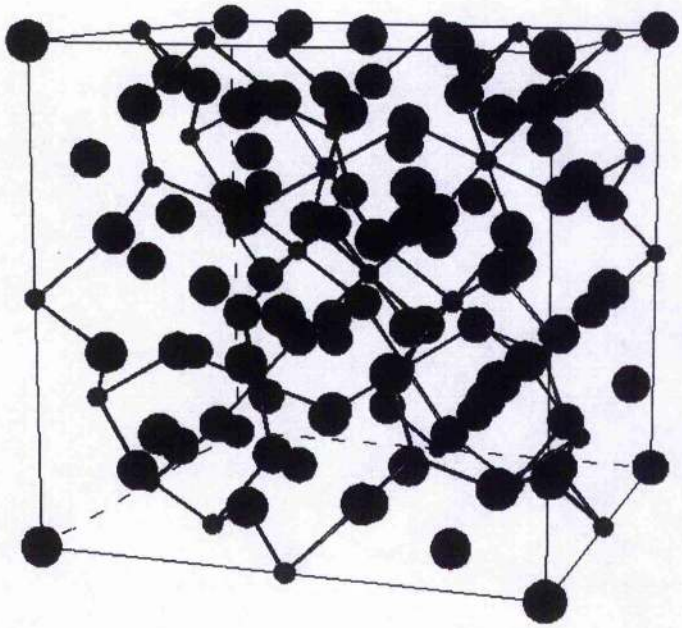

Figure 4.2. The Pyrochlore Unit Cell, composed of 8 defect fluorite blocks.

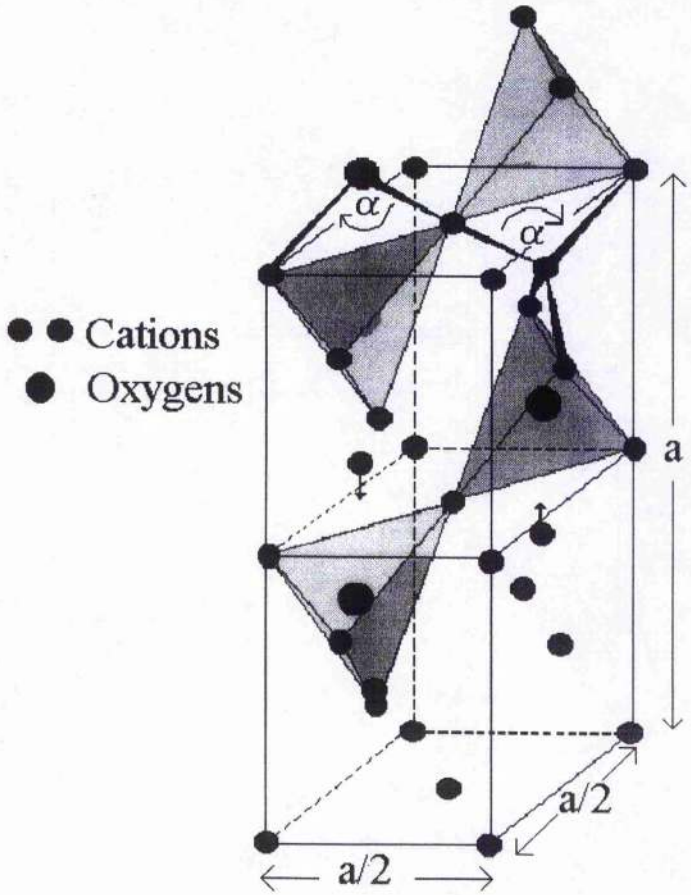

Figure 4.3. One quarter of the pyrochlore unit cell. The Bevan type arrangement of oxygen vacancies can be clearly observed around the central cation.

Among the 3d transition elements only four elements, i.e. B^{4+} = Ti, V, Cr, Mn, yield the (3+, 4+) pyrochlore phases. The titanates and vanadates are formed at ambient pressures whereas high pressures are required for the synthesis when B^{4+} = Cr and Mn. The lattice parameters of $Ln_2Ti_2O_7$ phases systematically decrease with decreasing radius of the Ln^{3+} ion as expected. Titanate pyrochlores are refractory substances with melting points, 1560-2000°C. They are white in colour with densities around ~6.2-7.2 gcm^{-3}. Since there are no d electrons in $Ln_2Ti_2O_7$, (Ti^{4+}:d^0 system) and the f-electrons due to the Ln-ions are localised in the inner 4f levels, no electronic conductivity is expected at ordinary temperatures. However at higher temperatures ~1000°C p-type conduction occurs. Oxygen ion conduction is also exhibited at elevated temperatures in some titanates and capacitance measurements show that their dielectric constants are relatively high.

Among the 4d transition elements, e.g. Zr^{4+}, $Ln_2Zr_2O_7$ compounds (Ln = La to Gd) can easily be prepared and have a cubic pyrochlore structure. These are stable at ordinary temperatures but at high temperatures (>1500°C) an order-disorder transition, i.e. a pyrochlore-defect fluorite transition occurs. The transition temperature depends on the Ln ion (e.g. La, no transition; Nd, 2000°C; Gd, 1550°C). Similar to $Ln_2Ti_2O_7$ phases the $Ln_2Zr_2O_7$ compounds are also expected to be electronic insulators. However ionic conductivity is possible at high temperatures, e.g. $Gd_2Zr_2O_7$.

4.1.2. Phase Relationships and Conductivity in the Ternary System ZrO_2-Gd_2O_3-TiO_2

The phase relationships and properties in the system ZrO_2 - Gd_2O_3 - TiO_2 have been studied previously, especially for the binary systems. The binary system Gd_2O_3 - ZrO_2 has been studied with phase diagram studies of the system ZrO_2 - Gd_2O_3 by Perez y Jorba et al, Rouanet et al and Lefèvre in the 1960s, Figures 4.4, 4.5 and 4.6. [10, 11 and 12]. The phases obtained in the mixed oxide systems are heavily dependent on the methods of preparation due to slow achievement of equilibrium. There is little agreement on the phase relations in this system, however, there are some consistencies between them all. Perez y Jorba reported a ZrO_2 solid solution, a fluorite-pyrochlore-fluorite region, a hexagonal region and a C-type region. Lefèvre reported the same ZrO_2 phase and cubic phase, but did not report on compositions greater than 20 mol% Gd_2O_3. Rouanet et al also reported the tetragonal ZrO_2 solid solution and the face centred cubic

region but the phase diagram cannot be directly compared to the two earlier diagrams as the temperature range studied by Rounanet et al was above 1800°C. Bhattacharyya et al studied ZrO_2 - Gd_2O_3 compositions containing up to 8 mol% Gd_2O_3, prepared by three different methods and the sinterability and extent of stabilisation [13]. It has been reported that only 3 mol% Gd_2O_3 is needed for complete stabilisation of the tetragonal phase [14, 15], although this does not agree with Lefèvre [11]. Single crystals were studied by Kang et al [16]. They reported the unit cell parameters of 10, 12.5 and 15 mol% Gd_2O_3 as 5.164, 5.172 and 5.184 Å respectively and also reported peak broadening in Raman spectra caused by point defects such as anion vacancies and substituted cation ions. This type of peak broadening is typical of disordered phases and has been reported previously [17]. The decrease in the Raman shift is due to the weakening of the bond strength of the nearest-neighbour Gd-O pair or the decrease of the nearest-neighbour oxygen atoms around a Gadolinium ion with increasing Gd_2O_3 content.

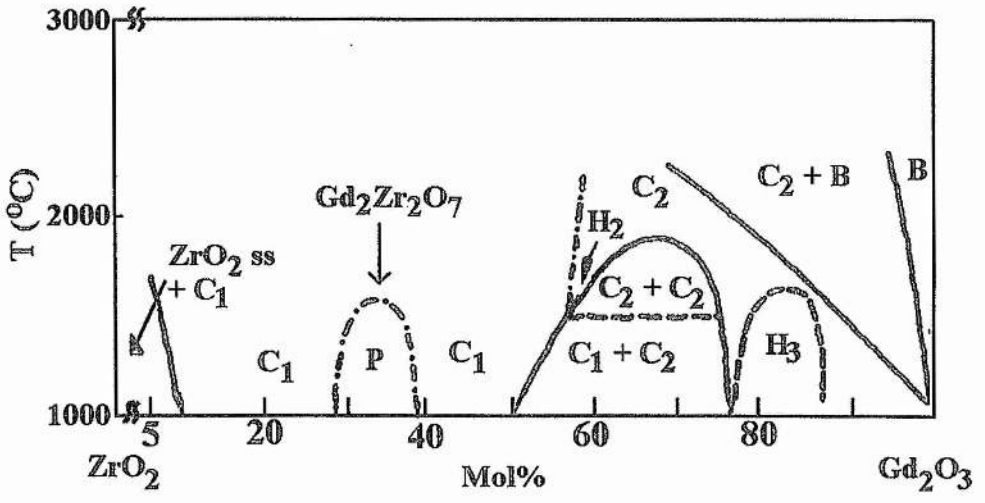

Figure 4.4. The binary system ZrO_2 - Gd_2O_3 proposed by Perez y Jorba [11].

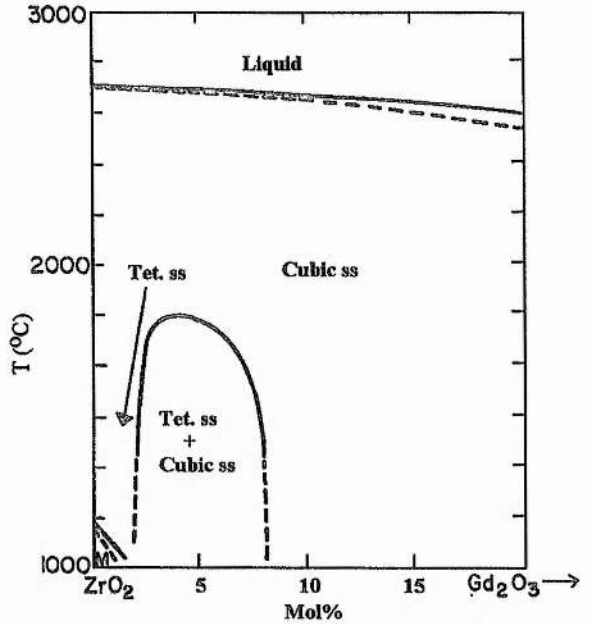

Figure 4.5. The binary system ZrO_2 - Gd_2O_3 proposed by Lefèvre [11].

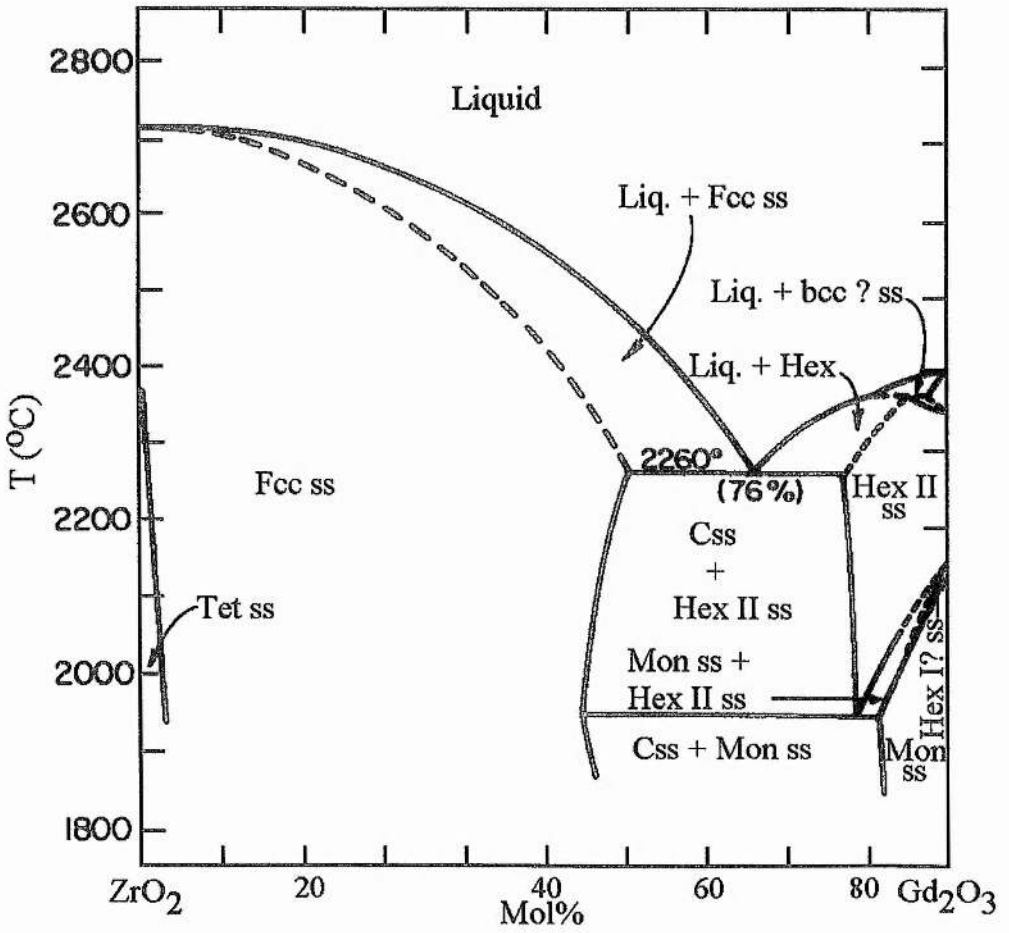

Figure 4.6. The binary system ZrO_2 - Gd_2O_3 proposed by Rouanet and Foex [12].

The electrical properties of the binary system ZrO_2-Gd_2O_3 were studied by Van Dijk et al. Similar studies have been reported by Moztarzadeh [18] and Kang et al [16]. Michel et al. [14] prepared Gd_2O_3 doped tetragonal Zirconia single crystal by Skull melting and Leung et al [15] studied the high temperature phase partitioning in the ZrO_2 - Gd_2O_3 system prepared from aqueous precursors. The decrease in Raman shift with increasing Gd_2O_3 is accompanied by a decrease in the pre-exponential conductivity factor, however, van Dijk et al reported that the pre-exponential factor remains constant in the range 10-20 mol% Gd_2O_3. They also reported that the activation energy increases with Gd_2O_3 content, in agreement with other studies by van Dijk et al [12, 13]. The increase in activation energy has been attributed to passage narrowing (despite the increase in lattice parameter) and associate formation. It has also been attributed to ordering of the disordered phase resulting in an increase in anomalously long jump distances for the conducting ions.

The binary system Gd_2O_3 - TiO_2 has also received little attention in terms of phase relationship studies. Waring and Schneider reported the binary phase diagram in 1965, Figure 4.7 [19]. A line phase and two solid solutions were reported. The line phase Gd_2TiO_5 exhibits two polymorphs with a transformation at 1712°C. One solid solution is based on $Gd_2Ti_2O_7$ pyrochlore and the other, which only exists above 1600°C is based approximately on $Gd_6Ti_2O_{13}$. No other reports have been made since.

In the ternary system ZrO_2 - Gd_2O_3 - TiO_2 the existence of a solid solution between the stoichiometric binary pyrochlores $Gd_2Zr_2O_7$ and $Gd_2Ti_2O_7$ was reported by Tuller et al [20]. The Zirconate end member is highly disordered, i.e. the Gd^{3+} and Zr^{4+} are similar in size and can thus occupy the same 6-fold and 8-fold sites. The Titanate end member is highly ordered because of the large difference in the ionic radii of the Gd^{3+} and the Ti^{4+}. The amount of order within the structure can thus be controlled and hence electronic and ionic conductivities. Tuller et al found it possible to vary both the magnitudes and ratio of ionic and electronic conductivities over wide limits in the pyrochlore solid solutions $Gd_2(Zr_xTi_{1-x})_2O_7$ through systematic changes in x. For large values of x, σ_i increases by orders of magnitude relative to the Titanate end member due to increased structural disorder while σ_e decreases sharply due to increases in reduction enthalpy and narrowing of the Ti 3d band. Similar effects can be achieved by

doping Titanate-rich pyrochlores on the "A" site or "B" site.

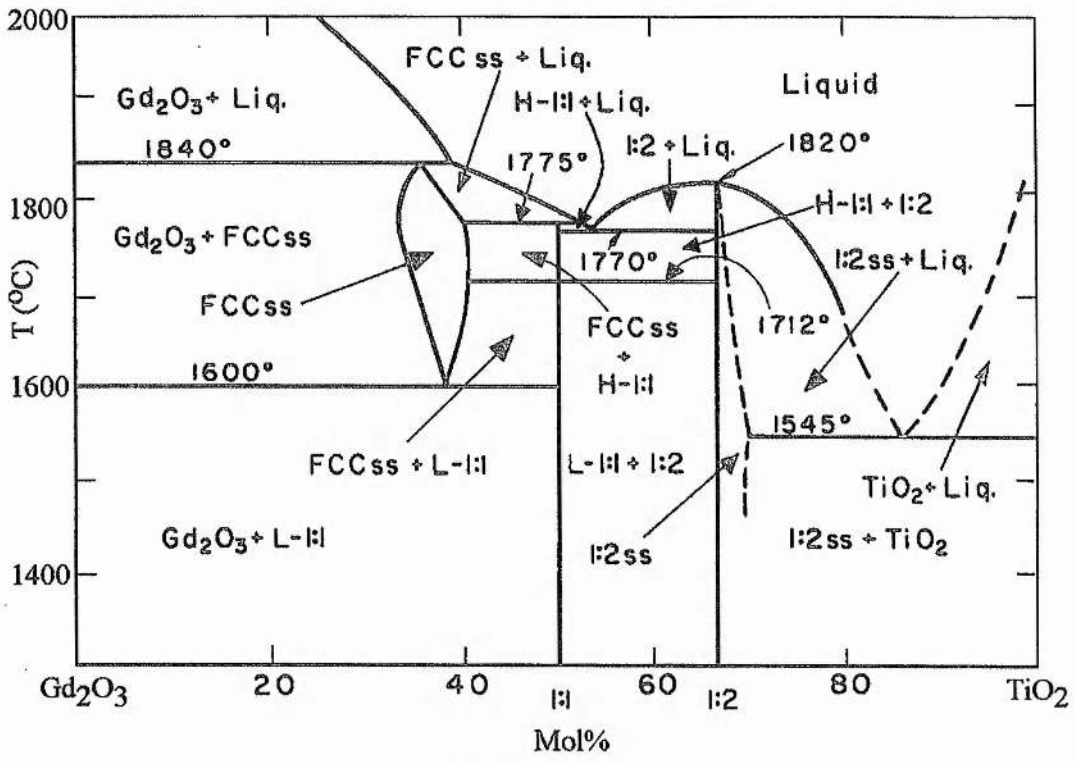

Figure 4.7. The binary system Gd_2O_3-TiO_2 [19].

Two types of order are important in pyrochlores. The first is anti-site disorder on the cation sublattices in which A and B cations switch positions. In the limit of complete randomisation of the A and B cations on the 16c and 16d sites, we revert back to the situation in the fluorite case. The second type of disorder, which is relevant to the analysis of ionic transport, concerns a Frenkel type disorder on the anion sub lattice. In this type of disorder the oxygen ions leave the normally occupied 48f sites and enter the 8b interstitial sites, thereby forming oxygen vacancy-interstitial pairs. It is largely increases in σ_o, the pre-exponential conductivity factor, rather than decreases in E_{ionic}, the activation energy for ionic conduction, that contributes to the increase in σ_{ionic} for x values above 0.25. Acceptor doping of ZGT also showed that it is the increase in oxygen disorder as reflected in σ_o rather than an increase in oxygen mobility that drives the increase of σ_i with x [21].

Significant levels of electronic and ionic conductivity can be achieved in ZGT,

particularly for low values of x. This follows from the ease with which Ti^{4+} reduces to Ti^{3+} at reduced PO_2 and elevated temperatures as observed previously by Rao et al [22]. The electronic and ionic components of the total conductivity can generally be identified by their unique oxygen partial pressure dependencies. In ZGT for values of x where the intrinsic quasi-frenkel equilibrium dominates, the combined effects of anion frenkel equilibrium, electron hole generation and reduction determine the numbers of oxygen vacancies [$V_o^{\circ\circ}$], electrons,n and electron holes,p:

$$[V_{O^{\circ\circ}}] = K_f^{1/2} \qquad (1)$$

$$n = K_f^{-1/4} K_r^{1/2} PO_2^{-1/4} \qquad (2)$$

$$p = K_f^{1/4} K_r^{-1/2} K_e PO_2^{1/4} \qquad (3)$$

where K_f, K_e and K_r represent equilibrium constants from Frenkel, electron-hole and reduction reactions, respectively. The n-type conductivity decreases with increasing substitution of Zr for Ti, as might be expected from equation 2. Increased disorder in GZT at larger x is reflected in an increase in K_f and therefore a decrease in n. Perhaps less obvious are the decrease in K_r and μ_e which accompany the dilution of Ti and thereby the width of the 3d-like conduction band.

4.2. Experimental

High purity Zirconia, Gadolinia and Titania (Aldrich) were used as the starting materials. These powders were dried at 800°C for 18 hours and then intimately mixed in the appropriate ratios under acetone, using an agate mortar and pestle. The powders were pressed into pellets (8 mm diameter x 3 mm) at a pressure of 2000 $kgcm^{-2}$. The pellets were presintered at 1000°C for 1 hour , heated at 10°C/min to 1500°C, sintered at 1500°C for 32-48 hours in air, with intermediate regrinding, and then removed from the furnace to rapidly cool to room temperature. Phase purity and accurate unit cell lattice parameters for single phase fluorite and pyrochlore compositions were determined using X-ray diffraction as described in Chapter 2. Electrical measurements were carried out using 2-probe A.C. and 4-probe D.C. techniques as described in Chapter 2.

4.3. Phase Diagram Studies of the Ternary System ZrO_2 - Gd_2O_3 - TiO_2

The extent of the single phase pyrochlore and fluorite regions in the ternary system ZrO_2-Gd_2O_3-TiO_2 has not been previously reported, other than the stoichiometric join between the two binary pyrochlore compositions $Gd_2Zr_2O_7$ and $Gd_2Ti_2O_7$ [20].

4.3.1. The Binary System ZrO_2 - Gd_2O_3

In the ZG binary system, the phase limits at 1500°C are in reasonable accord with the published phase diagrams, however no evidence of the hexagonal phase, H_3, reported by Perez y Jorba was found [10]. A small tetragonal ZrO_2 solid solution formed with only a few atom% Gd^{3+}. Increasing the Gd_2O_3 content results in a 2 phase mixture of tetragonal ZrO_2 solid solution and a defect cubic fluorite phase. On cooling these samples to room temperature and grinding for X-ray investigation, 100% conversion from tetragonal to monoclinic occurred. A defect fluorite solid solution exists between 8 and 25 mol% Gd_2O_3. This structure gradually orders, leading towards a pyrochlore solid solution above 25 mol% Gd_2O_3, which can be viewed as an ordered superstructure of the fluorite structure and thus has a cubic unit cell parameter double that of the equivalent fluorite composition. This ordered superstructure exists between approximately 30 and 40 mol% Gd_2O_3, i.e. it exists around the stoichiometric compound $Gd_2Zr_2O_7$, which has been reported to disorder to the fluorite structure above ~1550°C [10]. Increasing the Gd^{3+} content introduces more vacancies into the superstructure lattice, resulting in increasing disorder and a decrease in the intensity of the superstructure reflections until only the peaks characteristic of the defect fluorite structure are visible. The fluorite phase exists between 40 mol% and 50 mol% Gd_2O_3. Between 50 and 80 mol% Gd_2O_3, there is a two phase mixture composed of the high temperature, face centred cubic form of Gd_2O_3 (C-type) and the fluorite phase. Increasing the amount of Gd_2O_3 creates a single phase region of the high temperature cubic Gd_2O_3 in the region 80-90 mol% Gd_2O_3. Above 90 mol% Gd^{3+} a two phase region composed of the C-type Gd_2O_3 and the low temperature monoclinic form of Gd_2O_3 occurs. The monoclinic form of Gd_2O_3 was observed for 100 mol% Gd_2O_3.

The unit cell parameters of the monoclinic Gd_2O_3 at 20°C were a = 14.061 Å, b

= 3.566Å, c = 8.76 Å and B = 100.1°. The unit cell parameter, a, of the cubic phases in the ZG system are plotted against mol% Gd_2O_3 in Figure 4.8. The lattice parameters are not a linear function of Gd_2O_3 especially in the region 18-33.33 mol% Gd_2O_3. This curvature has previously been reported in a careful study of the fluorite/pyrochlore region of the ZrO_2 - Gd_2O_3 system [23]. It is likely that the bend occurs due to the onset of oxygen vacancy ordering.

4.3.2. Phase Relationships in the Binary System Gd_2O_3 - TiO_2

For the system Gd_2O_3 - TiO_2 (GT) two distinct regions of phase formation were detected as with the Y_2O_3 - TiO_2 system (Section 3.3). The Gd_2TiO_5 line phase is formed at 50 atom% Ti^{4+} and a small solid solution with the $Gd_2Ti_2O_7$ pyrochlore structure exists between 50 and 53 atom% Ti^{4+}, in agreement with the phase diagram by Waring and Schneider [19]. The Gd_2TiO_5 phase has unit cell parameters a = 10.4788 Å, b = 11.328 Å and c = 3.7547 Å . The pyrochlore material, $Gd_2Ti_2O_7$, at 50 atom% Gd^{3+} has a cubic unit cell parameter a = 10.1860 Å. No other regions of solubility were detected between Gd_2O_3 and TiO_2. The relationship between composition and unit cell parameter is shown in Figure 4.9. The relationship between unit cell volume per anion and composition is shown in Figure 4.10.

4.3.3. Phase Relationships in the Ternary System ZrO_2 - Gd_2O_3 - TiO_2

A large pyrochlore region exists around the known solid solution system $Gd_2Zr_2O_7$ - $Gd_2Ti_2O_7$, Figure 4.11. Outwith the single-phase pyrochlore region, there are 2 separate regions in which compositions exhibit the defect fluorite structure. These defect fluorite regions only exist for compositions which have less than ~30 mol% TiO_2. The maximum extent of non-stoichiometry in the ternary system is attained for compositions containing 20 mol% TiO_2, extending from 20 mol% Gd_2O_3 to almost 45 mol% Gd_2O_3. The single phase, two phase and three phase regions are indicated. No new phases are observed in the ternary system, and apart from the defect fluorite system and the pyrochlore system, none of the binary systems extend significantly into the ternary system.

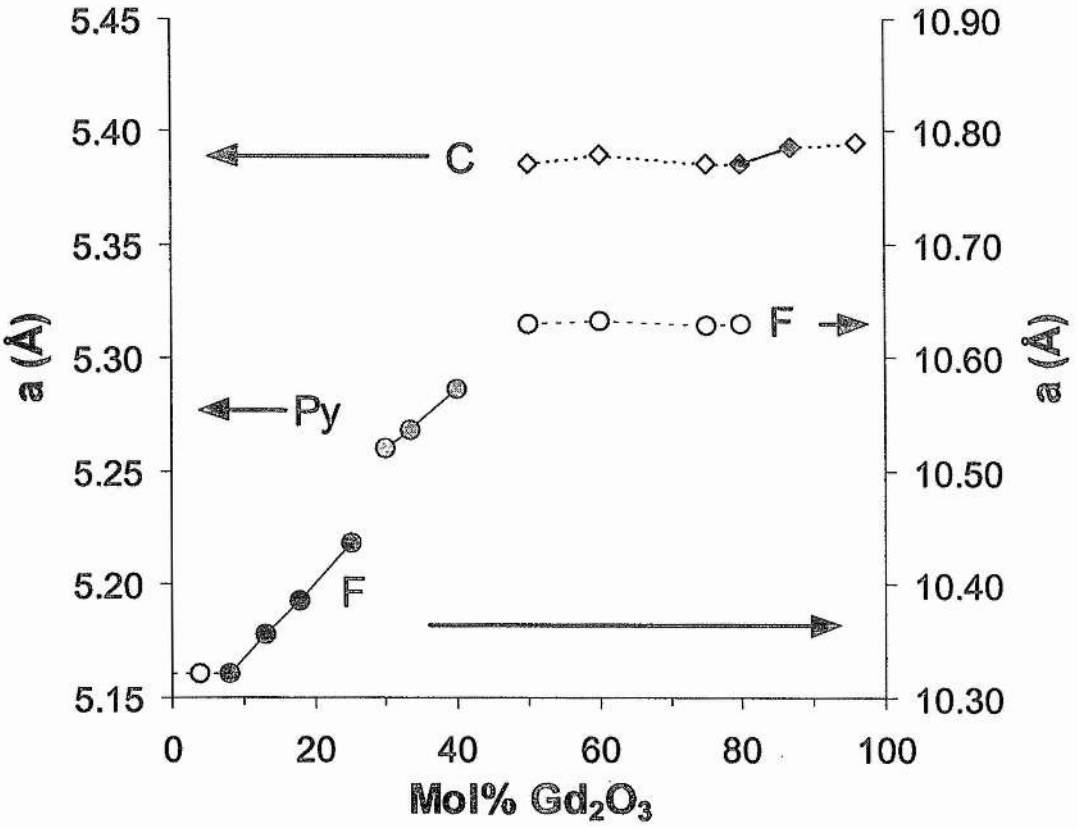

Figure 4.8. The unit cell parameters of the binary system ZrO_2 - Gd_2O_3.

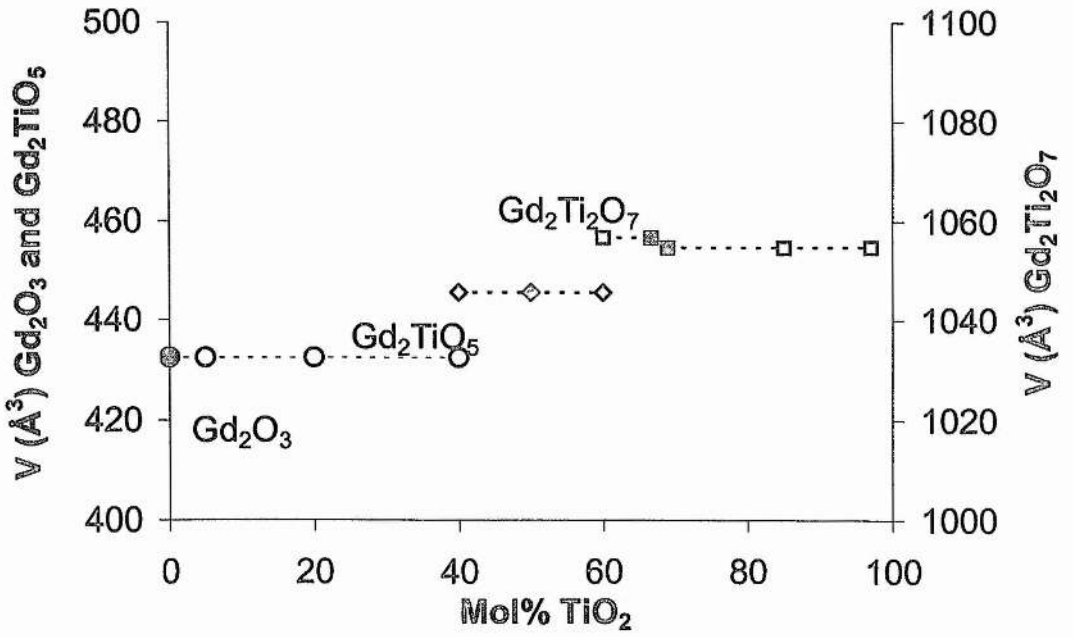

Figure 4.9. Unit cell volume versus mol% TiO_2 for the binary system Gd_2O_3-TiO_2.

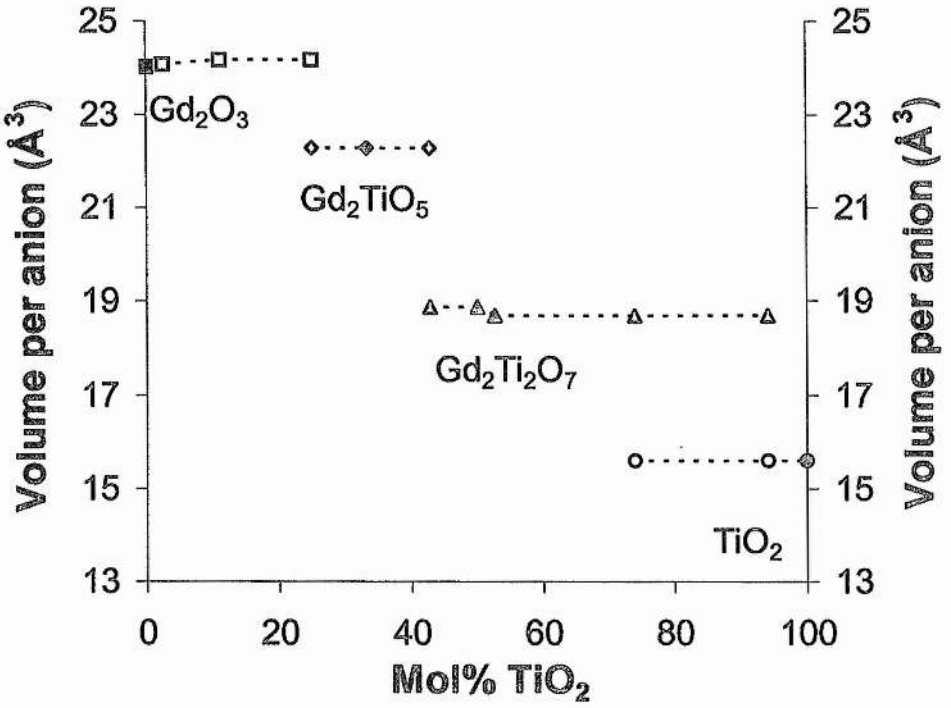

Figure 4.10. The unit cell volume per anion versus atom% TiO_2 for the binary system Gd_2O_3-TiO_2 .

Increasing the non-stoichiometry in the ternary pyrochlore system causes sufficient disordering of the cation and anion sublattices of the pyrochlore structure to result in the disappearance of the superstructure reflections and thus the fluorite average structure appears. As with the binary ZG system, no evidence of a two phase region between the pyrochlore and fluorite regions was found. The transition from the pyrochlore structure to the fluorite structure is a continuous order-disorder transition. Figure 4.12. shows the ratio of the superstructure (311) reflection intensity to the fluorite related (222) reflection intensity for pyrochlore compositions containing 20 mol% TiO_2. The ratio can be seen to increase up to the stoichiometric composition containing 33.33 mol% Gd_2O_3. The ratio of the intensities then decreases rapidly as the amount of disorder caused by the increase in aliovalent Gd^{3+} increases. When the (311) reflection is not visible the structure is no longer pyrochlore and the ratio of the intensities is zero.

The maximum extent of the defect cubic fluorite structure with increasing Gd_2O_3 and thus increasing non-stoichiometry is shown to encompass the defect fluorite

composition $Zr_{0.13}Gd_{0.67}Ti_{0.20}O_{1.67}$. This is close to the limit of the single phase, defect fluorite structure in the ZrO_2 - Y_2O_3 - TiO_2 system, for which the composition $Zr_{0.21}Y_{0.62}Ti_{0.17}O_{1.69}$ was prepared, Section 3.4.

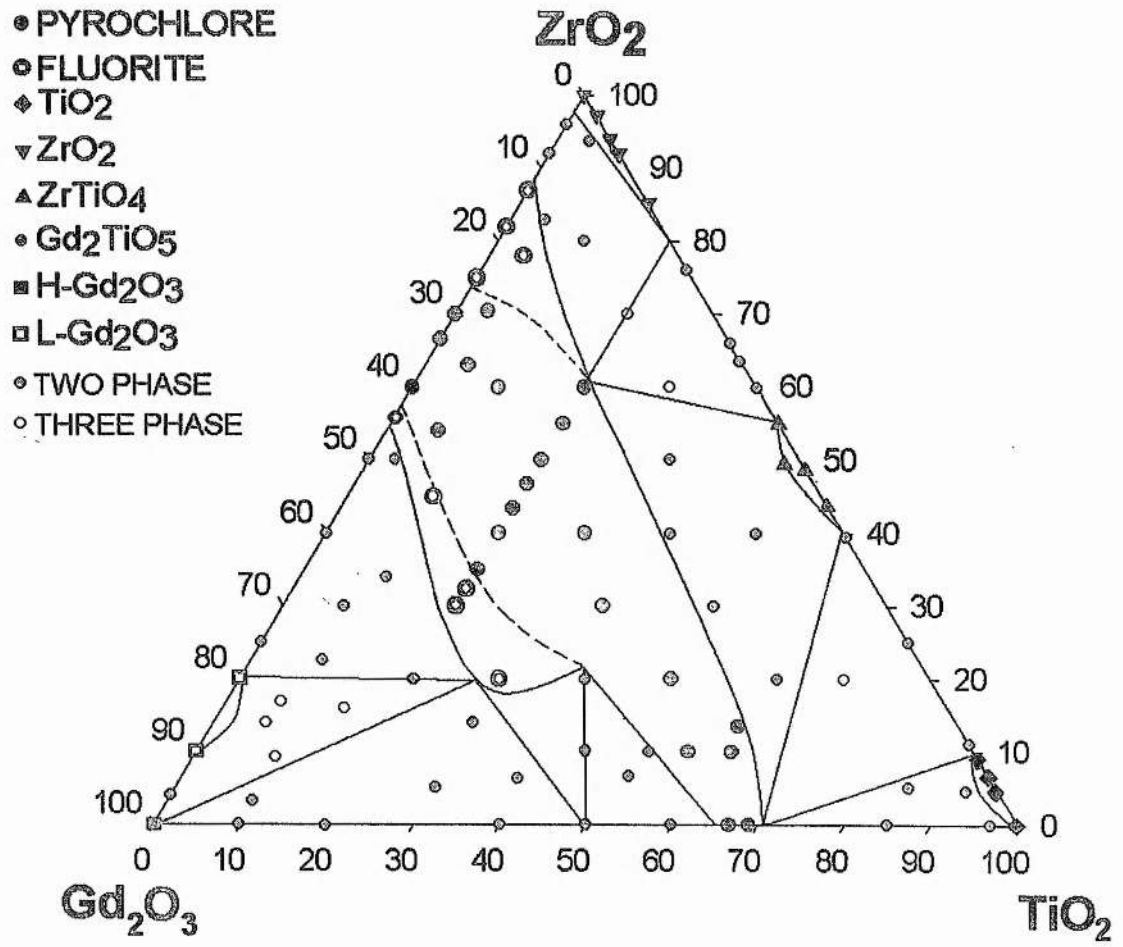

Figure 4.11. The experimentally determined ternary phase diagram for the ternary system ZrO_2 - Gd_2O_3- TiO_2.

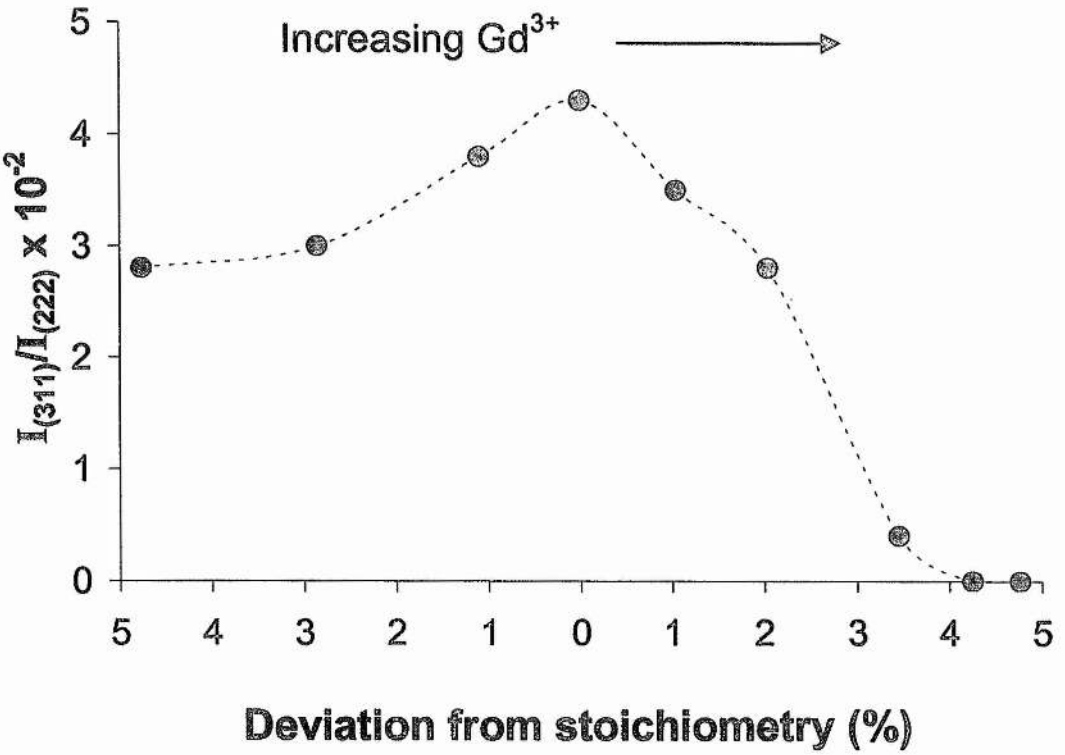

Figure 4.12. Ratio of the (311) peak intensity to the (222) peak intensity at 20°C as a function of deviation from $Gd_2M_2O_7$ stoichiometry for pyrochlore and fluorite compositions containing 20 mol% TiO_2.

Cell parameters for the stoichiometric pyrochlore samples containing 33.33 mol% Gd_2O_3 are shown with the cell parameters for the non-stoichiometric compositions containing 30 and 40 mol% Gd_2O_3 in Figure 4.13. The unit cell parameters for the stoichiometric compositions, along the $Gd_2Zr_2O_7$ - $Gd_2Ti_2O_7$ join, decrease from 10.520 Å to 10.186 Å for the respective solid solution end members. This corresponds to a decrease of 5.01×10^{-3} Å per mol% TiO_2, due to the smaller Ti^{4+} replacing Zr^{4+} (0.605 Å versus 0.84 Å [25]). Cell parameters for the pyrochlore and fluorite samples containing 20 mol% TiO_2 are shown in Figure 4.14. As the amount of Gd_2O_3 increases from 20 to 45 mol%, the unit cell expands from 10.354 Å to 10.543 Å, i.e. the unit cell expands by approximately 7.5×10^{-3} Å per mol% Gd_2O_3. This is due to the larger size of Gd^{3+} versus Zr^{4+} (1.06 Å versus 0.84 Å [25]) as well as due to the introduction of oxygen vacancies into the lattice. Between 45 and 48 mol% Gd_2O_3 the structure becomes more disordered and changes from pyrochlore to defect fluorite. The compositions containing 48 and 50 mol% Gd_2O_3 have the cubic fluorite structure and

unit cell dimension a = 5.2760 Å and 5.2909 Å respectively.

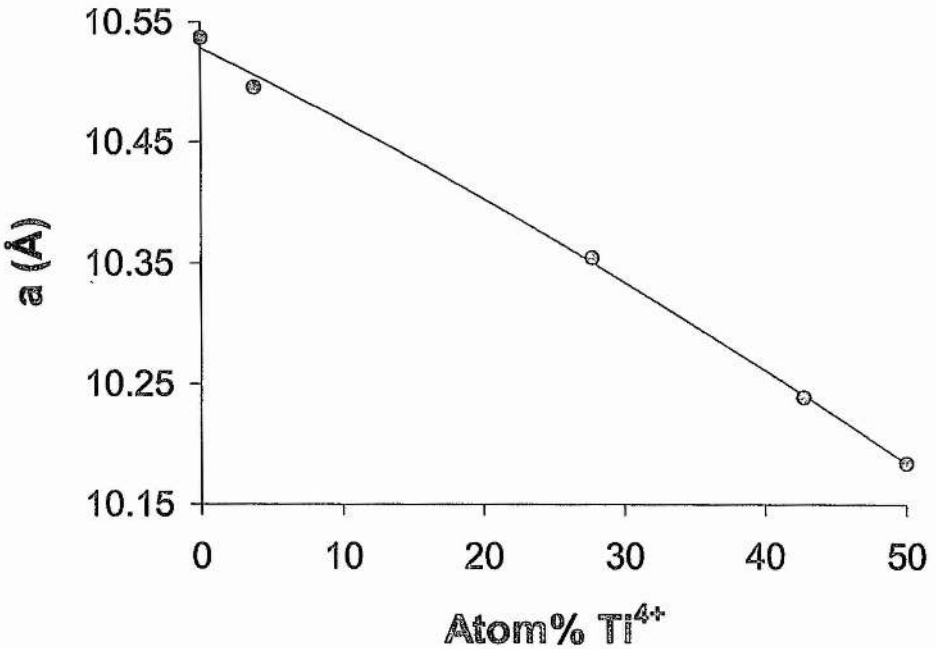

Figure 4.13. Plot of unit cell parameters for compositions containing 30, 33.33 and 40 mol% Gd_2O_3 versus mol% TiO_2.

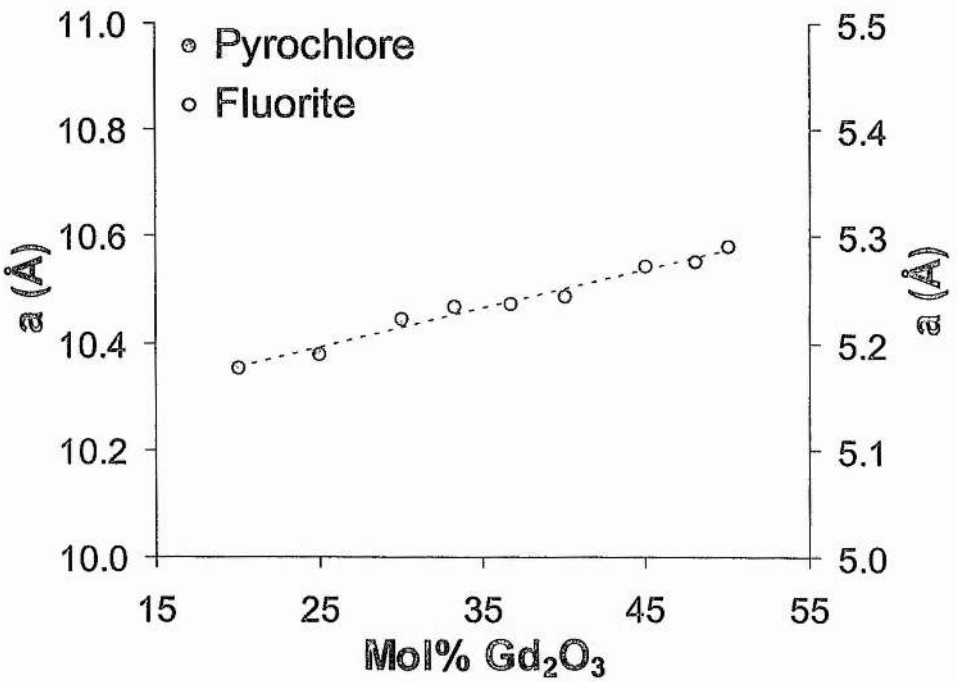

Figure 4.14. Plot of cubic fluorite and pyrochlore lattice parameter versus mol% Gd_2O_3 for compositions containing 20mol% TiO_2.

Typical powder X-ray powder diffraction patterns for samples containing 50 mol% Gd_2O_3 and 45 mol% Gd_2O_3 , exhibiting the defect cubic fluorite and pyrochlore structures respectively , are shown in Figures 4.15. and 4.16, demonstrating the high purity achieved. As 45 mol% Gd_2O_3 is very close to the limit of the pyrochlore domain, the additional peaks due to anion ordering in pyrochlore, which are absent in fluorite, are quite weak. These additional peaks are much stronger in compositions with lower Gd_2O_3 content, Figure 4.17.

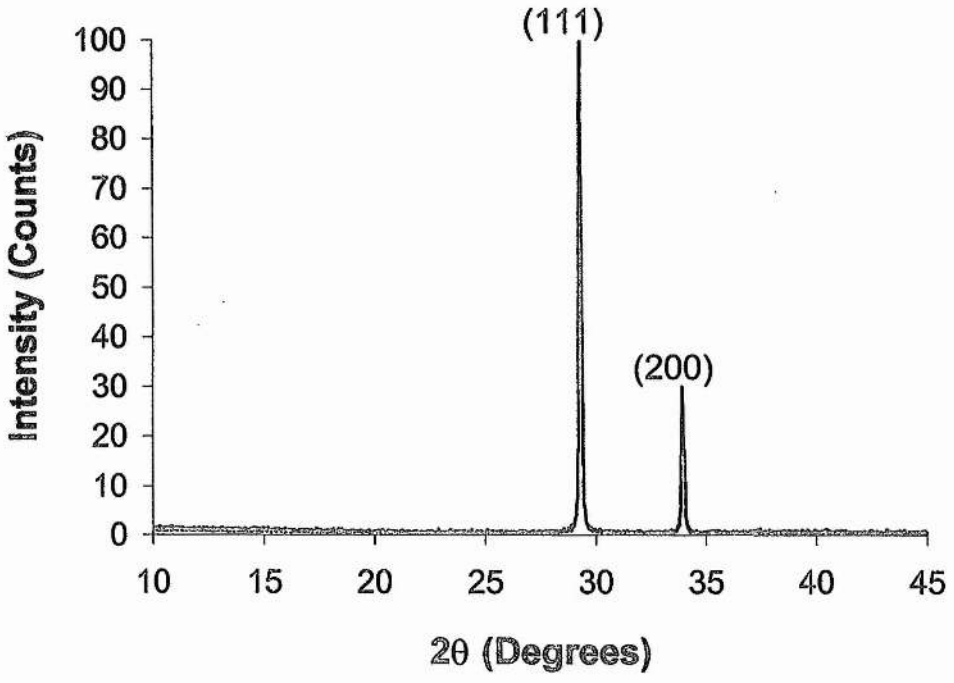

Figure 4.15. Powder X-ray diffraction pattern for $Zr_{0.8}Gd_{2.67}Ti_{0.53}O_{6.67}$ (20 mol% TiO_2 and 50 mol% Gd_2O_3), showing only cubic fluorite peaks.

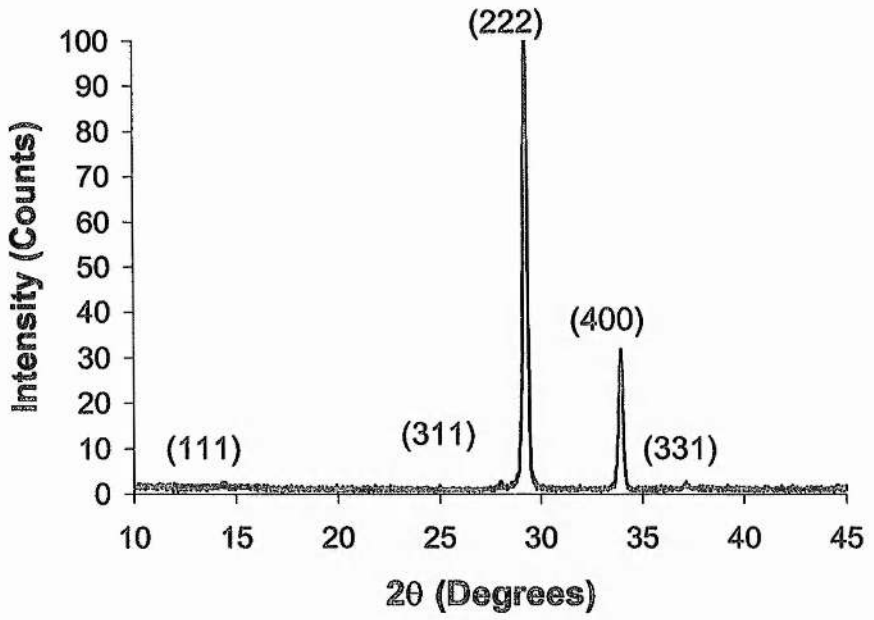

Figure 4.16. Powder X-ray diffraction pattern for $Zr_{0.97}Gd_{2.48}Ti_{0.55}O_{6.76}$ (20 mol% TiO_2 and 45 mol% Gd_2O_3), exhibiting the same characteristic peaks as the defect fluorite structure and the additional superstucture reflections characteristic of the pyrochlore structure.

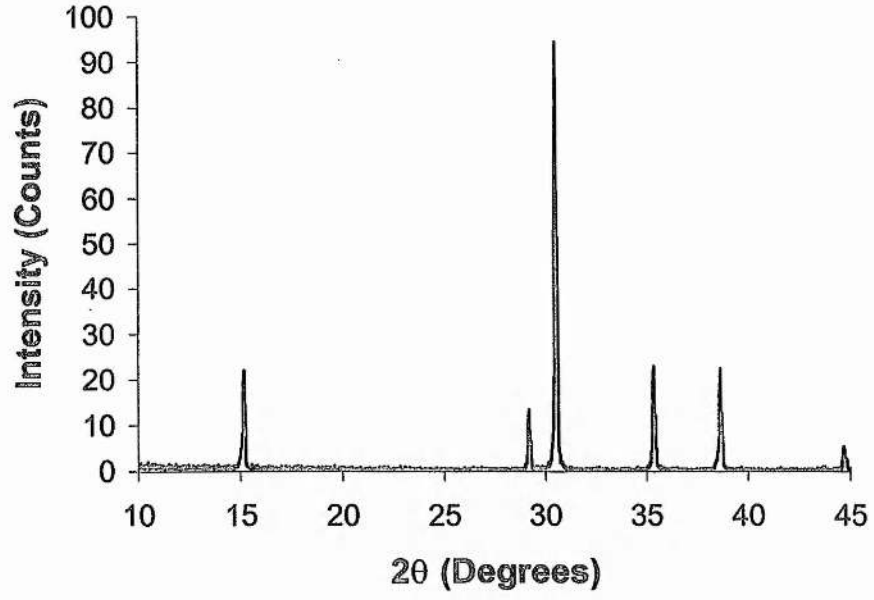

Figure 4.17. Powder X-ray diffraction pattern for $Gd_2Ti_2O_7$ (33.33 mol% Gd_2O_3), exhibiting the same characteristic peaks as the defect fluorite structure and additional high intensity superstructure reflections characteristic of the pyrochlore structure.

4.4. Conductivity Studies of the Ternary System ZrO_2 - Gd_2O_3 -TiO_2

As described in Section 4.1.1. the pyrochlore structure is a superstructure of fluorite with ordering on both the cation and anion sublattices. The pyrochlore structure easily accommodates anion disorder with interstitial oxygen on the 8b sites and oxygen vacancies on some of the normally occupied sites [23]. It is this Frenkel disorder that is the source of oxygen ion conduction in the pyrochlore structure.

$Gd_2Ti_2O_7$ (GT), which has the pyrochlore structure, is highly ordered and thus has poor ionic transport properties but is a good electronic conductor [26]. When mixed with the highly disordered composition $Gd_2Zr_2O_7$ (GZ), a complete solid solution is formed (ZGT) [20]. The isovalent substitution of Zr for Ti in $Gd_2(Zr_xTi_{1-x})_2O_7$ results in an increase in oxide ion conductivity at 600°C of over 4 orders of magnitude [26, 27]. The increase in structural disorder with addition of GZ causes the conductivity to become predominately ionic over wide ranges of oxygen partial pressure and temperature.

Most of the previously published work on these pyrochlore systems has concentrated on doping the highly ordered, electronic conducting Titanium rich end of the solid solution with acceptor cations in order to improve ionic conductivity. For example, the addition of Ca^{2+} to GT can increase the ionic conductivity to greater than that for GZ i.e. to 5 Sm^{-1} for 10 mol% dopant at 1000°C. This value is within a factor of 2 of YSZ and is the highest ionic conductivity reported for a Titanate material [28]. Al^{3+} has a similar effect as Ca^{2+} however the maximum in σ_i is at lower levels than for Ca^{2+} doping [23]. Conversely, doping with donor ions such as Nb^{5+} decreases the ionic conductivity and increases the electronic conductivity [24]. More recently GT has been doped with variable valence impurities such as Mn [24] and Ru [29]. These systems have complicated electrical behaviour but do hold promise for controlling levels of mixed ionic-electronic conduction.

4.4.1. Ionic Conductivity of the Binary System ZrO_2 - Gd_2O_3

The conductivity of pyrochlore and fluorite compositions in the binary ZrO_2-Gd_2O_3 system was measured previously by van Dijk et al [30]. In the present work a comparative study was carried out in order to make direct comparison with the compositions containing 20 mol% TiO_2. Figure 4.18. shows the trends in the pre exponential factor, A, and the activation energy, Ea, with mol% Gd_2O_3. The trends in activation energy and pre-exponential factor are very similar in nature. A maximum in Ea and A clearly occurs in the fluorite region and a minimum in Ea and A clearly occurs for the pyrochlore composition containing 33.33 mol% Gd_2O_3 (50 atom% Gd^{3+}). This same trend was found by van Dijk et al.

The minimum in activation energy for the stoichiometric pyrochlore composition $Gd_2Zr_2O_7$ was 1.06 eV. This is in good agreement with the values found by van Dijk et al, i.e. 112 $kJmol^{-1}$ (1.16 eV) for $Gd_2Zr_2O_7$ with the fluorite structure and 84 $kJmol^{-1}$ (0.87 eV) for $Gd_2Zr_2O_7$ with the pyrochlore structure [30]. The value in this study, i.e. for rapidly cooled samples from 1500°C, is closer to the fluorite value than to the pyrochlore value determined by van Dijk et al because $Gd_2Zr_2O_7$ is known to undergo an order-disorder transition at ~1550°C, hence the fluorite structure is obtained when the sample is quenched from above ~1550°C. Thus with different degrees of order being achieved for different quenching and annealing temperatures, the electrical properties are highly dependent on the thermal history of the samples.

Due to the absolute values of Ea and A, this results in a maximum in the curve of conductivity at 1000°C versus mol% Gd_2O_3, Figure 4.19. The maximum conductivity was found to occur at the pyrochlore composition $Gd_2Zr_2O_7$, with an ionic conductivity of 1 Sm^{-1} at 1000°C. The minimum conductivity was found to be 0.16 Sm^{-1} for the fluorite composition containing 40 mol% Gd_2O_3, which is close to the limit of the face-centred cubic solid solution.

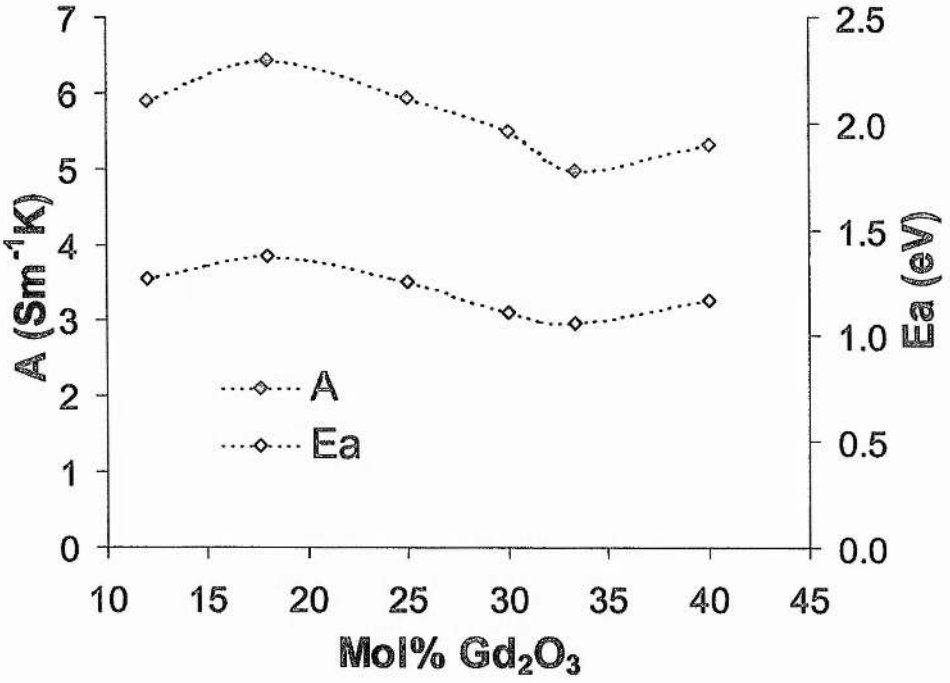

Figure 4.18. Plot of Activation energy, Ea, and pre-exponential factor, A, versus mol% Gd_2O_3 for the binary system ZrO_2 - Gd_2O_3.

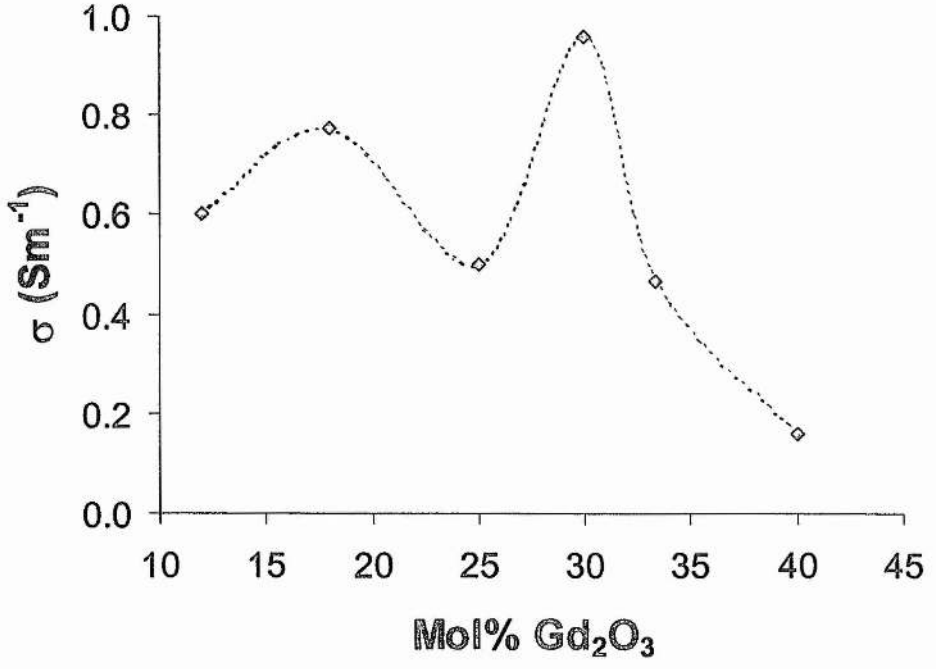

Figure 4.19. Plot of Conductivity at 1000°C versus mol% Gd_2O_3 for the binary system ZrO_2 - Gd_2O_3.

4.4.2. Conductivity in air of the ternary system ZrO_2 - Gd_2O_3 - TiO_2

As Ti^{4+} is a reducible ion, samples containing 20 mol% TiO_2 should be electronically conducting under the reducing, anodic conditions of a solid oxide fuel cell and also have high catalytic activity. In order to be a useful fuel cell material, the material must also have high oxide ion conductivity, and therefore we measured the ionic conductivity of compositions containing 20 mol% TiO_2 in air. AC impedance spectroscopy was used to resolve the bulk, grain boundary and electrode components of the resistivity. The electrode response of all samples containing 20 mol% TiO_2 was consistent with purely ionic conductivity. Indeed, evidence of an electronic contribution was only detectable at 1000°C in air for compositions with around 40 mol% TiO_2.

For the stoichiometric compositions along the main pyrochlore join, i.e. those containing 33.33 mol% Gd_2O_3 (50 atom% Gd^{3+}), the ionic conductivity at 1000°C was found to decrease by more than 2 orders of magnitude, from 1 Sm^{-1} to 0.01 Sm^{-1}, with increasing Ti^{4+} content. The Arrhenius plots for $Gd_2Zr_2O_7$ and $Gd_2Ti_2O_7$ are shown in Figure 4.20. The conductivities of the non-stoichiometric compositions containing 30 and 40 mol% Gd_2O_3 were both lower than for the stoichiometric material and they exhibit the same trend in conductivity as the stoichiometric compositions. i.e. the ionic conductivity at 1000°C decreases by several orders of magnitude with increasing Ti content, Figure 4.22.

For compositions containing 20 mol% TiO_2, the ionic conductivities at 1000°C were plotted against Gd_2O_3 content, Figure 4.21. Initially the conductivity increases with increasing Gd^{3+} content due to the production of oxygen ion vacancies in order to maintain charge balance. The conductivity then reaches a maximum value of 0.7 Sm^{-1} at 1000°C for the stoichiometric composition $Gd_2Zr_{1.4}Ti_{0.6}O_7$,which lies on the $Gd_2Zr_2O_7$ - $Gd_2Ti_2O_7$ pyrochlore join. Further addition of Gd_2O_3 significantly increases the oxygen vacancy/interstitial concentration which in turn increases defect aggregation. This causes the conductivity to decrease sharply. This behaviour is similar to the behaviour observed in the Gd_2O_3 - ZrO_2 binary system. This type of behaviour is somewhat surprising as one might expect ordering to be strongest for the $Gd_2M_2O_7$ composition and hence that conductivity would be lowest for these compositions.

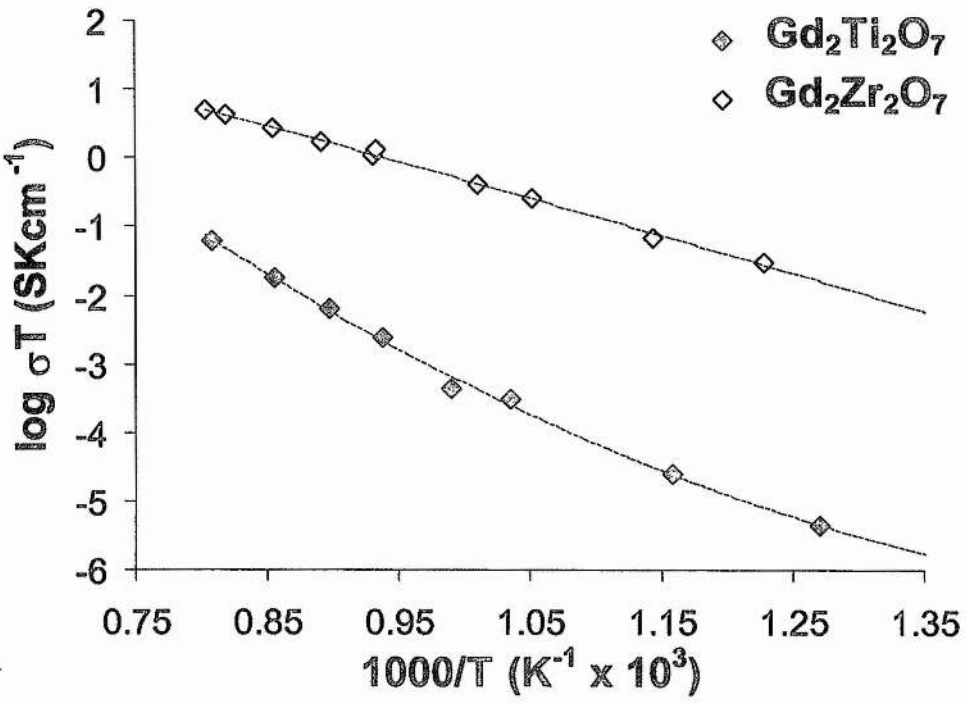

Figure 4.20. Arrhenius conductivity plots for the stoichiometric compounds $Gd_2Ti_2O_7$ and $Gd_2Zr_2O_7$.

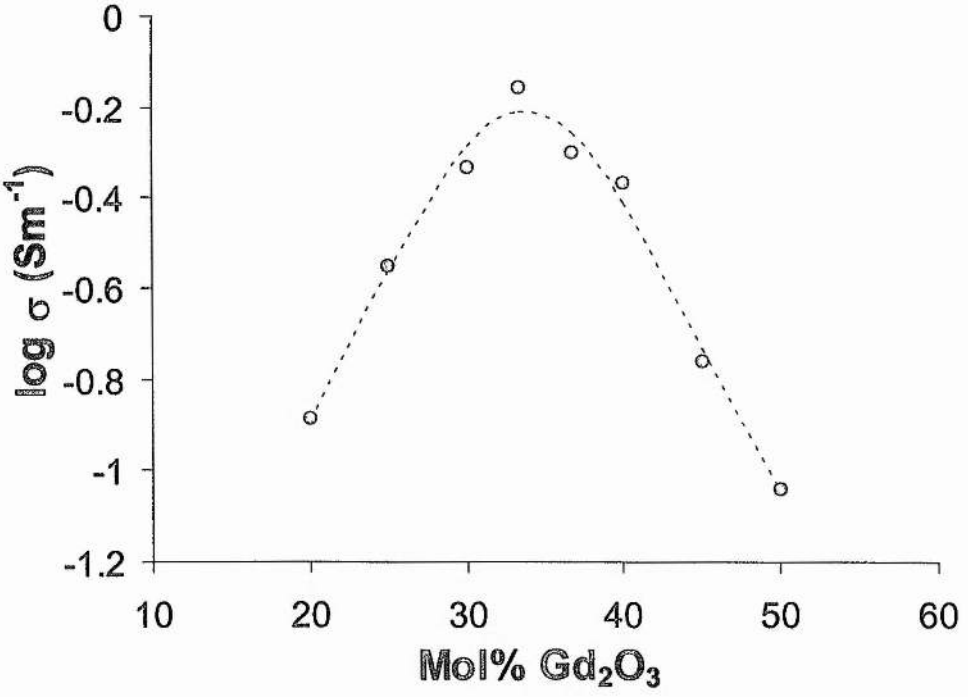

Figure 4.21. Plot of ionic conductivity at 1000°C versus mol% Gd_2O_3 for compositions containing 20mol% TiO_2.

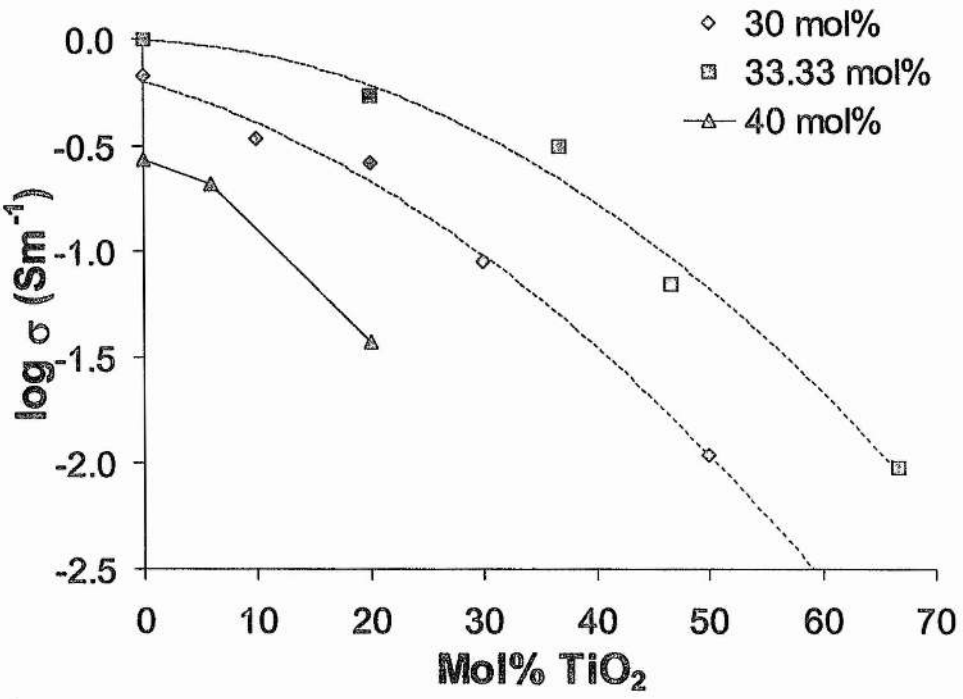

Figure 4.22. Plot of conductivity at 1000°C versus mol% TiO_2 for pyrochlore compositions containing 30, 33.33 and 40 mol% Gd_2O_3.

The GZ–GT system is reported to exhibit a change in activation energies between low and high temperature [14]. $Gd_2(Zr_xTi_{1-x})_2O_7$ materials with x>0.4 typically have activation energies of ~0.8 eV at high temperatures increasing to 1-1.2eV at low temperatures (<600°C), presumably due to defect association. GT is reported to exhibit an activation energy for conduction of 0.94 eV [31].

At high temperatures (800-900°C), the activation energy for conduction in the $Gd_2Zr_2O_7$ - $Gd_2Ti_2O_7$ system increased from 0.9 eV to approximately 1.2 eV for 0 and 40 mol% TiO_2 levels respectively, Figure 4.23. The activation energy rapidly increases above 40 mol% TiO_2 (x=0.4 in $Gd_2(Zr_xTi_{1-x})_2O_7$ reaching 2.1eV for the $Gd_2Ti_2O_7$ material perhaps indicating that the conduction mechanism has changed from being controlled by the population of charge carrying defects determined by the aliovalent dopant concentration to being controlled by the intrinsic Frenkel defects in the crystal. The high impedance of the $Gd_2Ti_2O_7$ material at lower temperatures yields very little conductivity information although the activation energy seems much less than at high temperatures.

For compositions containing 30 mol% Gd_2O_3 the activation energy follows the same trend as the stoichiometric materials, except that for materials with less than 20 mol% TiO_2 , the activation energy is lower than for the materials with 33.33 mol% Gd_2O_3. This might be due to the lower concentration of aliovalent dopant in these materials and thus less dopant/vacancy interactions occurring. For higher levels of TiO_2 the activation energies become equal for these 2 different systems indicating that the TiO_2 concentration is the dominant factor in determining which conduction mechanism predominates at high temperature.

For compositions containing 20 mol% TiO_2 and varying Gd_2O_3 content the low and high temperature activation energies were found to increase with increased aliovalent dopant density due to increased interaction between the aliovalent dopant and oxide vacancies, Figure 4.24. The pyrochlore material with the lowest aliovalent dopant concentration, i.e. 20 mol% Gd_2O_3 and 20 mol% TiO_2 has low and high temperature activation energies of 0.98 and 0.75 eV respectively. For levels of Gd_2O_3 above 50 mol%, the dissociation occurs at temperatures above the temperature range studied. This results in linear Arrhenius conductivity plots over the temperature range studied and a single activation energy of 1.23eV for the material with 20 mol% TiO_2 and 50 mol% Gd_2O_3. From previous work in transition metal doped YSZ, the activation energy for ionic conduction is expected to level out at around 1.3 eV for higher levels of aliovalent dopant [32].

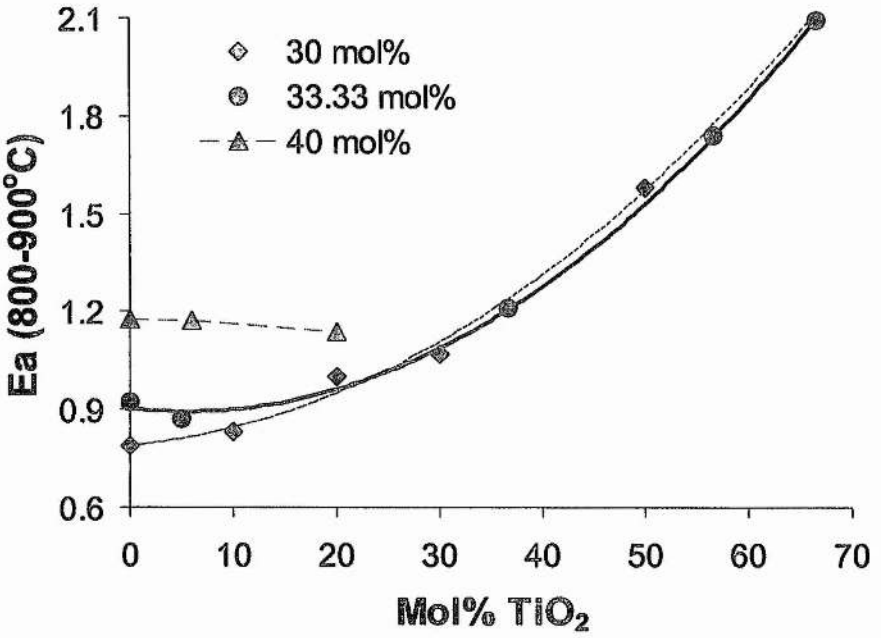

Figure 4.23. Plot of activation energy measured between 800 and 900°C for compositions containing 30, 33.33 and 40 mol% Gd_2O_3.

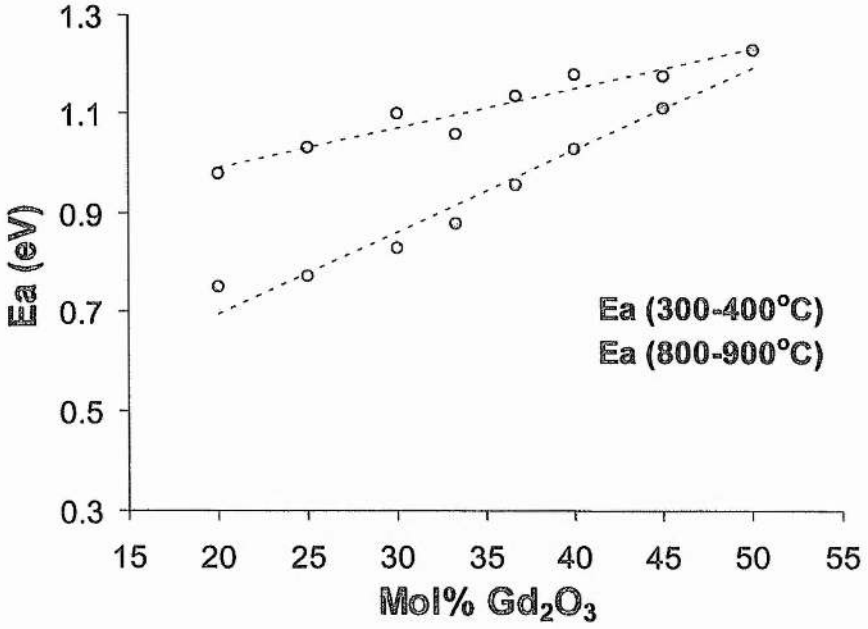

Figure 4.24. Plot of high and low temperature activation energies versus mol% Gd_2O_3 for compositions containing 20 mol% TiO_2.

4.4.3. Mixed Ionic and Electronic Conductivity in ZGT Pyrochlore Compositions

The pyrochlore composition containing 25 mol% Gd_2O_3 and 20 mol% TiO_2, $Zr_{1.76}Gd_{1.6}Ti_{0.64}O_{7.2}$, exhibits a conductivity of 0.175 Sm^{-1} at 950°C (0.28 Sm^{-1} at 1000°C), Figure 4.25. At high oxygen partial pressures, between log $P(O_2)$ = -0.7 and -3.7, the conductivity is almost entirely ionic. It is however, approximately 2.9% higher than the conductivity in the log $P(O_2)$ region -3.7 to -10, due to p-type electronic conduction. Below log $P(O_2)$ = -10, the conductivity increases by 3.5 times from 0.28 Sm^{-1} to 0.98 Sm^{-1} at log $P(O_2)$ = -20. This increase in conductivity with reduced oxygen partial pressure is due to n-type electronic conduction being introduced by the removal of oxygen ions from the sample and the subsequent reduction of the Ti^{4+} to Ti^{3+} according to equation (1) given in Section 3.5.4. The oxidation curve between log $P(O_2)$ = -18 and -20 appears to follow a -1/5 power law. However, by subtracting the ionic conductivity from the total conductivity to calculate the electronic conductivity, the slope follows a -1/4 power law.

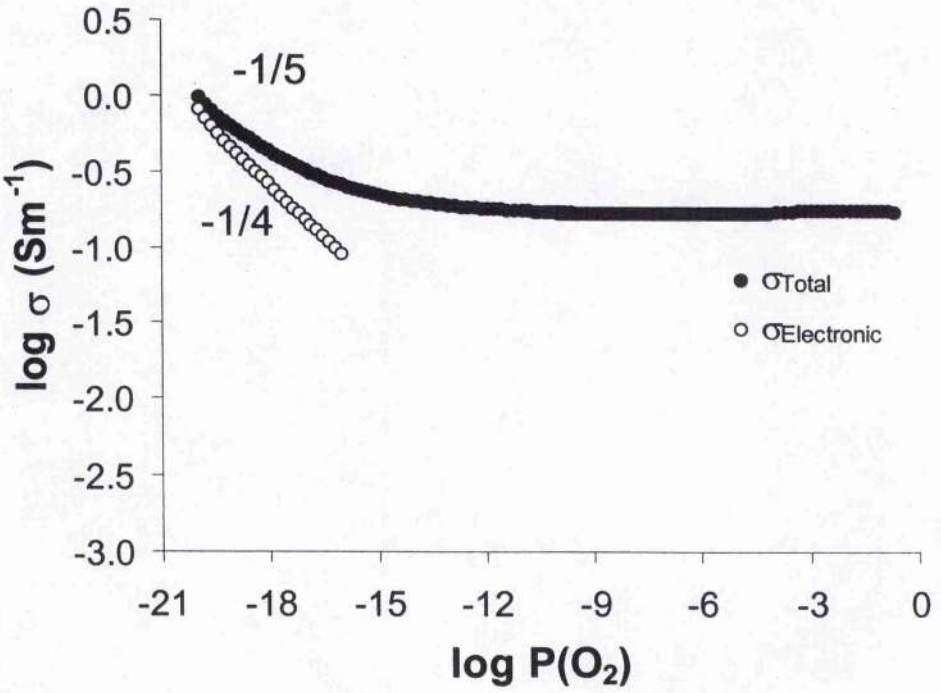

Figure 4.25. Oxidation of $Zr_{1.76}Gd_{1.6}Ti_{0.64}O_{7.2}$ at 950°C.

The conductivity profile of the stoichiometric pyrochlore composition containing 33.33 mol% Gd_2O_3 and 20 mol% TiO_2 is plotted against oxygen partial

pressure in Figure 4.26. The conductivity at 950°C in air is 0.40 Sm^{-1} (0.54 Sm^{-1} at 1000°C) and is only 0.58 Sm^{-1} at log $P(O_2)$ = -20 atmospheres. There is a slight minimum in the conductivity profile centred around log $P(O_2)$ = -9.5 atmospheres, where oxygen fugacity problems may arise.

The stoichiometric pyrochlore $Gd_2Ti_2O_7$ has a conductivity in air of 4.3 x 10^{-3} Sm^{-1}, Figure 4.27. This conductivity is predominantly electronic due to the highly ordered nature of the pyrochlore structure for this particular composition. The conductivity initially rises from 4.3 x 10^{-3} Sm^{-1} in air to 2 x 10^{-2} Sm^{-1} for a two order of magnitude decrease in oxygen partial pressure, with the slope of the conductivity plot = -¼. The conductivity remains essentially constant between log $P(O_2)$ = -4 and -9 atmospheres and then rapidly increases to 1 Sm^{-1} at log $P(O_2)$ = -12 atmospheres. As with the previous composition, this may be due to oxygen fugacity problems. Decreasing the oxygen pressure further results in an increase in conductivity with a slope of -2/15 up to log $P(O_2)$ = -18 atmospheres. This slope is close to -1/6 and indicates that the oxygen vacancies produced on reduction are starting to dominate the conductivity at low oxygen partial pressures. At lower oxygen partial pressures the conductivity slope changes to -1/15, exactly half twice that of the preceding conductivity profile. This flattening of the conductivity at low oxygen partial pressure may not be a real effect and can be eliminated by better sealing of the experimental apparatus.

Comparison of the conductivity profile of the stoichiometric materials $Gd_2Ti_2O_7$ and $Zr_{1.4}Gd_{2.0}Ti_{0.6}O_7$ shows that 15 atom% Ti^{4+} (20 mol% TiO_2) does not significantly alter the conductivity characteristics of Gadolinia stabilised Zirconia and the conductivity remains almost constant over a wide range of oxygen partial pressure. In contrast, the composition containing 50 atom% Ti^{4+} (66.67 mol% TiO_2) has predominantly electronic conductivity, which increases by approximately 3.5 orders of magnitude with decreasing oxygen partial pressure. Comparison of the stoichiometric composition containing 20 mol% TiO_2, $Zr_{1.4}Gd_2Ti_{0.6}O_7$ and the non-stoichiometric composition $Zr_{1.76}Gd_{1.6}Ti_{0.64}O_{7.2}$ clearly shows that for similar levels of reducible Ti^{4+} there is a significant difference in the conductivity profiles. The conductivity in the oxygen excess composition increased by almost an order of magnitude between air and log $P(O_2)$ = -20 atmospheres compared to an almost negligible increase of less than one

tenth of an order of magnitude in the stoichiometric composition. The reason that the electronic contribution seems lower is due to the much higher ionic conductivity of the stoichiometric composition.

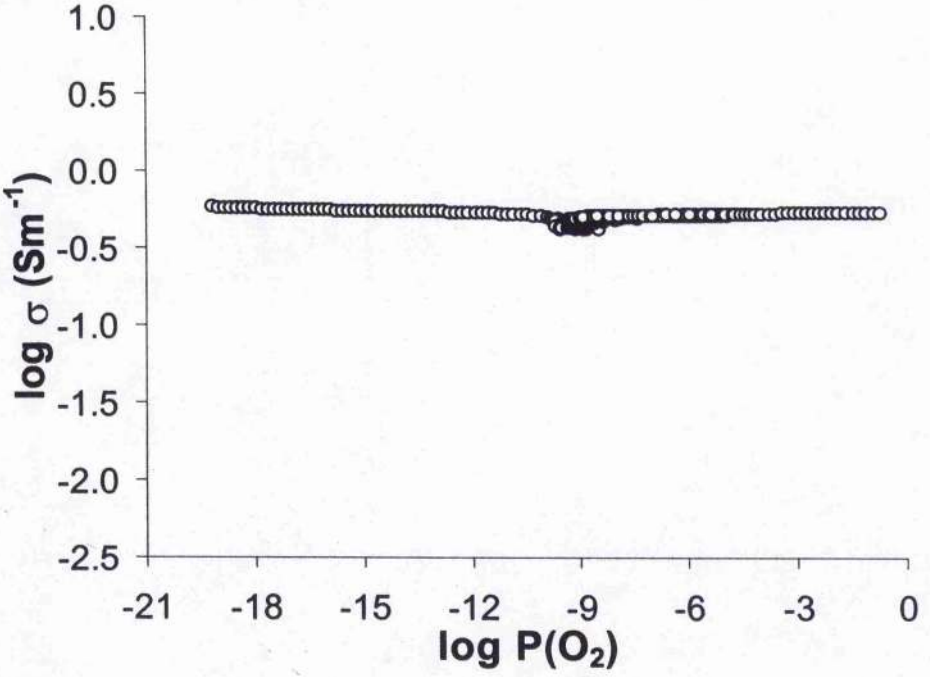

Figure 4.26. Oxidation of $Zr_{1.40}Gd_{2.00}Ti_{0.60}O_7$ at 950°C.

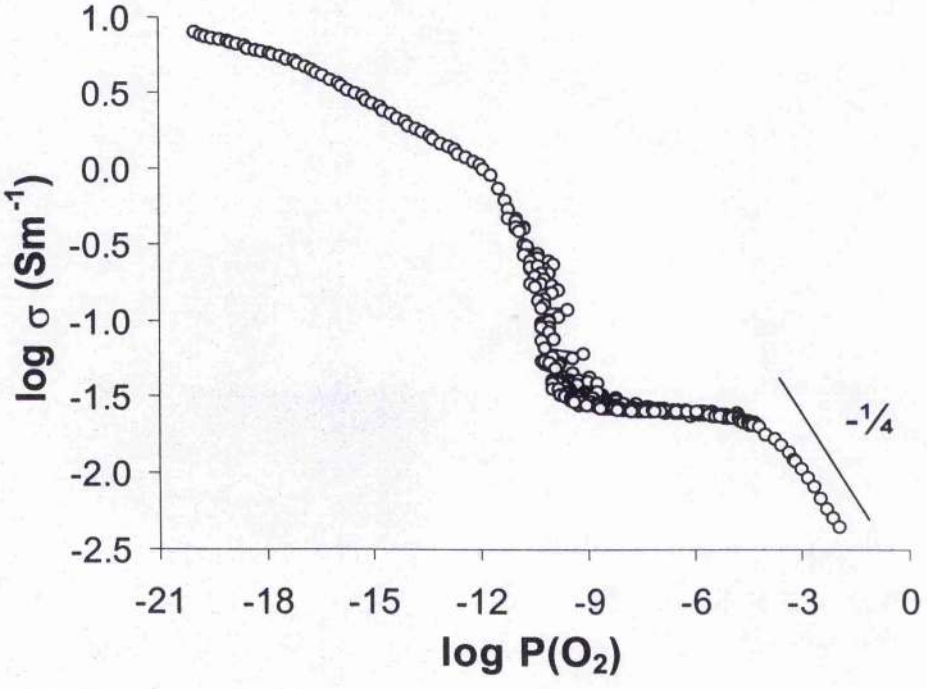

Figure 4.27. Oxidation/Reduction Conductivity profile for $Gd_2Ti_2O_7$ at 950°C.

4.5. Conclusions

The cubic fluorite and pyrochlore structures exist over a wide range of stoichiometry in the solid solution system $ZrO_2 - Gd_2O_3 - TiO_2$. The extent of the cubic region is greatest for compositions containing 20 mol% Ti^{4+} and the transition between the pyrochlore and the fluorite regions is continuos due to an increase in disorder with increasing non-stoichiometry.

The ionic conductivity of materials containing 20 mol% of reducible Ti changes by only an order of magnitude between the lowest and highest conducting compositions, with the highest conductivity being slightly less than 1 Sm^{-1} at 1000°C. Despite this value being an order of magnitude lower than the ionic conductivity in the preferred electrolyte, YSZ, even the lowest ionic conductivity observed, 10^{-1} Sm^{-1}, should impart sufficient oxide ionic mobility to allow fuel oxidation to occur over the electrode surface, not just at three point boundaries as in Ni/YSZ cermets. The electronic conductivity determined in this study for stoichiometric and non-stoichiometric compositions is probably not high enough for these materials to be used without additions as the anode in Solid Oxide Fuel Cells.

In principle, however, because the SOFC presently suffers from fabrication difficulties and from chemical and mechanical instability due to the use of a variety of phases for electrodes, electrolytes and interconnects held in intimate contact at elevated temperatures, the wide variety of ionic and electronic conducting properties of the ZGT system could be used to develop an electrochemical cell based on the electrode and electrolyte materials from the same system.

4.6. References

[1] A. Byström, Ark. Kemi Min. Geol., 18A, 1 (1945)

[2] O. Knop, F. Brisse, L. Castelliz, and sutarno, Can. J. Chem., 43, 2812 (1965)

[3] F. Jona, G. Shirane, and R. Pepinsky, Phys. Rev., 98, 903 (1955)

[4] H. Nyman, S. Andersson, B. G. Hyde and M. O'Keeffe, J. solid state Chem., 26, 123 (1978); M. O'Keefe and B. G. Hyde, Phil. Trans. Roy. Soc., (London), 295, 553 (1980)

[5] E. Aleshin and R. Roy, J. Am. Ceram. Soc., 45 18 (1962)

[6] J.M. Longo, P.M. Raccah and J.B. Goodenough, Mat. Res. Bull., 4, 191 (1969); H.S. Horowitz, J.M. Longo and J.T. Lewandowski, ibid., 16, 489 (1981)

[7] A.W. Sleight, Inorg. Chem., 7, 1704 (1968); 8, 2039 (1969)

[8] J. Pannetier and J. Lucas, Mat. Res. Bull., 5, 797 (1970)

[9] M.A. Subramanian, G. Aravamudan and G.V. Subba Rao, Prog. Solid St. chem, Vol. 15, pp55-143, 1983.

[10] Monique Perez y Jorba, Ann. Chim. (Paris), 7, 509 (1962)

[11] Jean Lefèvre, Ann. Chim. (Paris), 8 [1-2] 128 (1963)

[12] A. Rouanet and M. Foex, C. R. Acad. Sci. Ser. C, 267 [15] 875 (1968)

[13] S. Bhattacharyya and D. C. Agrawal, J. Mat. Sci. 30 (1995) 1495-1499

[14] D. Michel, L. Mazerolles and M. Perez y Jorba, J. Mater. Sci. 18 (1983) 2618

[15] D. K. Leung, C. Chan, M. Ruhle and F. F. Lange, J. Am. Ceram. Soc. 74 (1991) 2786

[16] T. K. Kang, T. Nagasaki, N. Igawa, K. I. Hiun and Ohno, J. Am. Ceram. Soc. 75 (1992) 2297

[17] D. Michel, M. Perez, Y. Jorba, and R. collongues, J. Raman. Spectrosc., 5, 163-80 (1976)

[18] F. Moztarzadeh, pp 901-905 in Advances in Ceramics, Vol. 24, Science and Technology of Zirconia III. Edited by S. Somiya, N. Yamamoto and H. Yanagida, American Ceramic Society, Westerville, OH, 1988

[19] J. L. Waring and S. J. Schneider, J. Res. Natl. Bur. Std., 69A [3] 257 (1965)

[20] O. Porat and H. L. Tuller, J. Am. Ceram. Soc. 79 [12], 3078-82 (1996)

[21] Moon P. K. and Tuller H. L. (1989), Solid State Ionics, (MRS Symp. Proc. Vol. 135), eds. G. Nazri, R. A. Huggins and D.F. Shriver, Pittsburgh, PA, 149-163

[22] Rao C. N. R., Gopalakrishnan J., and Vidyasagor K. (1984), Ind. J. Chem. 23A,

265-284

[23] T. van Dijk, K.J. de Vries and A.J. Burggraaf, Phys. Stat. Sol. (a) **58**, (1980) 115

[24] I. Kosacki and H.L. Tuller, pp703-708 in Solid State Ionics IV Vol. 369. Edited by G.A. Nazri, J.M. Tarascon and M. Schreiber. Materials Research Society Pittsburgh, PA, 1995

[25] R.D. Shannon, Acta Crystallogr. **A32**, (1976) 751

[26] P.K. Moon and H.L. Tuller, in Science and Technology of Fast Ion Conductors, pp307-11. Edited by H.L. Tuller and Balkanski, Plenum Press, New York, 1989

[27] M. Spears, S. Kramer, H.L. Tuller and P.K. Moon, in: Ionic and Mixed Conducting Ceramics, Proc. 91-12,eds. T.A. Ramanarayanan and H.L. Tuller (Electrochem. Soc. Pennington, NJ, 1991) pp 32-45

[28] S.A. Kramer, M.A. Spears and H.L. Tuller, Solid State Ionics 72 (1994) 59-66

[29] M.A. Spears and H.L. Tuller, pp. 94-105 in Ionic and Mixed Conducting Ceramics, Proceedings of the Electrochemical Society Symposium (San Francisco, CA, 1994). Edited by T.A. Ramanarayanan, W.L. Worrell, and H.L. Tuller. The Electrochemical Society, Pennington, NJ, 1994

[30] M.P. van Dijk, K. J. de Vries and A.J. Burggraaf, Solid State Ionics 9&10 (1983) 913-920]

[31] S.A. Kramer and H.L. Tuller, Solid State Ionics 82 (1995) 15-23

[32] D.P. Fagg, PhD Thesis (University of Aberdeen) 1996

CHAPTER 5

Effect of Alumina Additions on the Electrical Properties of 8 mol% Yttria-Stabilised Zirconia

CHAPTER 5

Effect of Alumina Additions on the Electrical Properties of 8 mol% Yttria-Stabilised Zirconia

5.1. Introduction

Solid Oxide Fuel Cells (SOFC's) currently utilise cubic Zirconia, stabilised with 8 mol% Yttria (8YSZ) as the electrolyte material. However, the mechanical strength of 8YSZ is low, hindering the fabrication of self-supported electrolyte plates for use in planar SOFC systems. These planar systems have higher volumetric power density than the alternative tubular SOFC system, which requires the use of a porous support [1].

Tetragonal Zirconia stabilised with 3 mol% Y_2O_3 (Y-TZP) has a high bending strength at room temperature [2] and reasonable conductivity at 1000°C, however the strength decreases remarkably with increasing temperature. The addition of Al_2O_3 improved the strength of Y-TZP [3-7]; however, the conductivity decreases considerably with increasing alumina and Y-TZP is extremely susceptible to hydrothermal ageing, leading to physical degradation [8]. Several authors have reported the effects of Al_2O_3 additions on the sintering [9,10], electrical [9-13,15], microstructure [13, 14] and mechanical properties [13,16,17] of cubic YSZ. These papers have described alumina additions to have both beneficial and detrimental effects on the bulk and grain boundary conductivities of YSZ, depending on the impurity content of the starting materials. The studies of mechanical properties all indicate that alumina addition increases the mechanical strength of YSZ. Ishizaki et al reported that the bending strength could be increased by 1.5 times by adding 30 wt% Al_2O_3 but this caused the conductivity to decrease by 1.5 orders of magnitude [16]. Esper et al increased the mechanical strength of YSZ by 50% by the addition of 20wt% Al_2O_3 [17] and the conductivity was reported to decrease by 25% for this level of alumina addition by Ishizaki [18]. Mori et al also found that 20wt% Al_2O_3 increased the mechanical strength of YSZ but that further addition did not

improve the strength [13]. They also reported that the particle size of the Al_2O_3 affected its distribution in the sintered composite materials but had little effect on the strength, indicating that the homogeneous distribution of Al_2O_3 in the 8YSZ matrix is not the most important factor in determining the strength of the composite.

5.2. Structures

The cubic fluorite structure of 8 mol% Yttria-stabilised Zirconia can be viewed as a simple cubic lattice of 8 oxygen ions, which is surrounded by a cubic close packed arrangement of cations. i.e. the oxygens occupy the tetrahedral interstices of the cubic close packed cation array. The cations have an average co-ordination number of 7.7 due to 3.7% of the anion sites being vacant in order to maintain charge balance. Pure α-Al_2O_3 (Corundum) has a rhombohedral crystal structure comprising a hexagonal close packed array of oxide ions with Al^{3+} ordered symmetrically on two thirds of the octahedral interstices. In the corundum structure the Al^{3+} ions are co-ordinated to 6 oxygen ions. As these 2 oxides have very different unit cell characteristics and the co-ordination environments of the cations in Al_2O_3 and 8YSZ differ, the oxides are structurally dissimilar and therefore are not expected to react together to any great extent.

5.3. Experimental

Tosoh 8 mol% Yttria Stabilised Zirconia (TZ8Y) and Fisons Alumina (Camag 100-250 mesh) were used as the starting materials. The alumina was composed of both (α and γ) forms of anhydrous Al_2O_3 phases. The γ–Al_2O_3 exists only below about 1000°C and underwent an irreversible phase transition to the α–phase above 1000°C. These powders were suspended in ethanol and intimately mixed and ground using zirconium oxide (97%) bowls and balls in a Fritsch Planetary Micro Mill "pulverisette-7". The powders were uniaxially pressed into pellets (13 mm diameter x 3 mm thick) at a pressure of 2000 $kgcm^{-2}$. Varying the pressing pressure between 1000 and 5000 $kgcm^{-2}$ was found not to have any effect on the final sintered density of the composite materials. The

pellets were placed on Pt foil and pre-sintered at 1000°C for 1 hour, heated at 10°C/min to 1500°C, sintered at 1500°C for 24 hours in air, and then cooled to 1000°C at 10°C/min.

5.4. Results and Discussion

For the pressing conditions and sintering regime used the Tosoh 8YSZ had a final sintered density of 95 % of the theoretical, slightly lower than the density obtained for a 2-hour sinter. Densification of alumina additioned samples prepared by solid state mixing in acetone was hindered with increasing alumina content e.g. Samples with 20wt% Al_2O_3 were only 68% of theoretical density. Densification of the composite materials was improved by ball milling in ethanol, with composites containing 20wt% Al_2O_3 having densities 79% of theoretical, 11% higher than for samples prepared by solid state mixing. However, the relative density of the composites still decreased with increasing Al_2O_3 content. Figure 5.1. shows the specimen densities obtained for several different compositions prepared by solid state mixing and ball milling. For all samples the measured conductivities were corrected for porosity by multiplying with the theoretical density and dividing by the actual density. This correction procedure probably gives conductivity values slightly lower than would be expected for fully dense samples but has been successfully used previously [20].

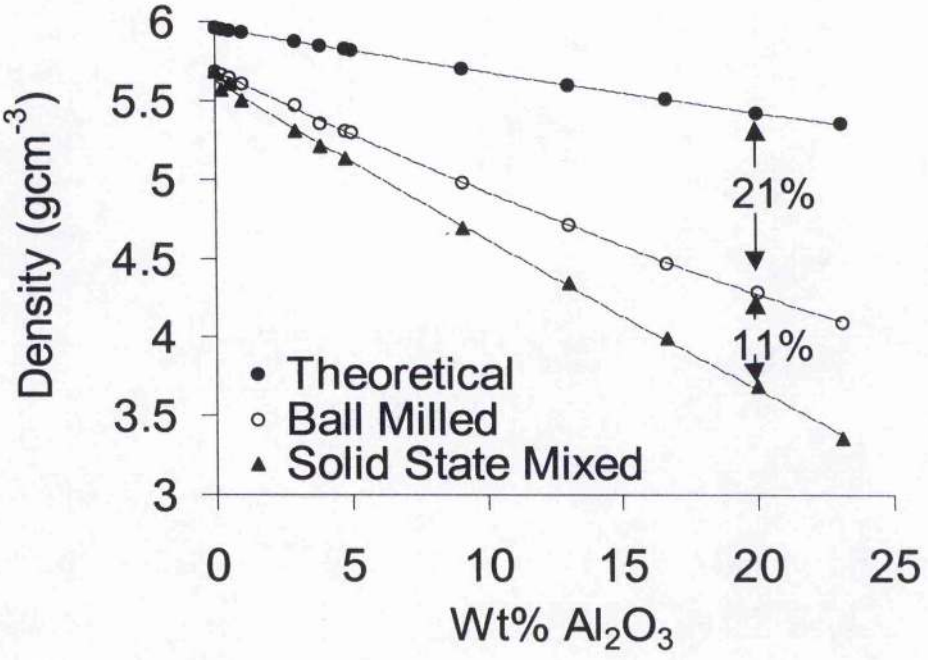

Figure 5.1. Plot of theoretical and sintered densities of alumina additioned Tosoh 8YSZ *vs.* wt% Al_2O_3.

SEM observation indicated that the Alumina phase was concentrated at the grain boundaries in the form of almost perfectly spherical particles of diameter 1.09 - 1.3μm, Figure 5.2. EDS of the YSZ grain boundary regions showed a strong X-ray peak corresponding to the $Zr_{L\alpha}$ line, a small peak corresponding to the $Al_{K\alpha}$ line and a small but significant peak corresponding to the $Si_{K\alpha}$ line, Figure 5.3. Similar spectra were obtained for the YSZ grains but there was no peak attributable to Silicon, Figure 5.4.

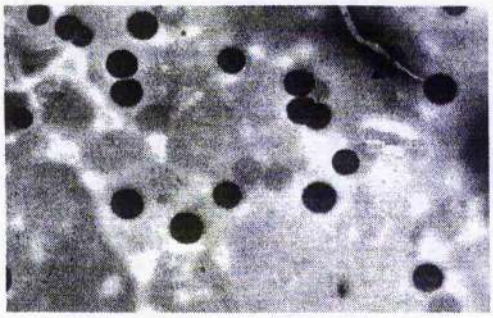

Figure 5.2. SEM photograph of Al_2O_3 (~2wt%) additioned 8 mol% YSZ.

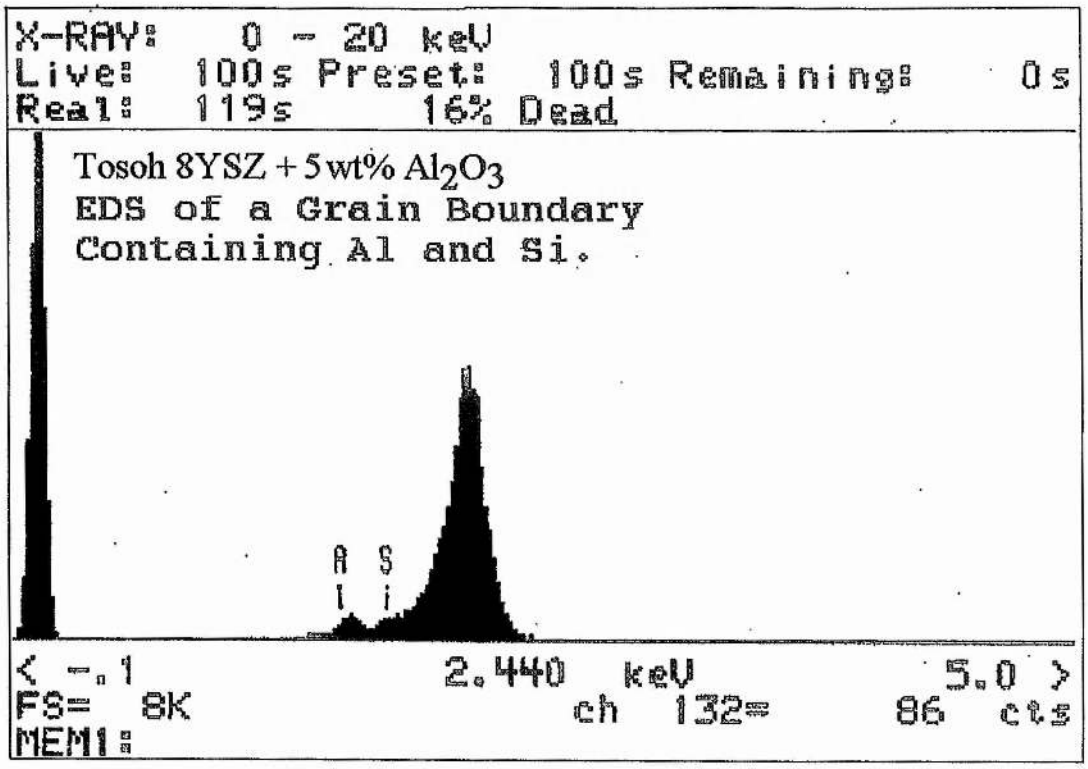

Figure 5.3. EDS of a 8YSZ grain boundary in a sample of Tosoh 8YSZ + 5wt% Al_2O_3.

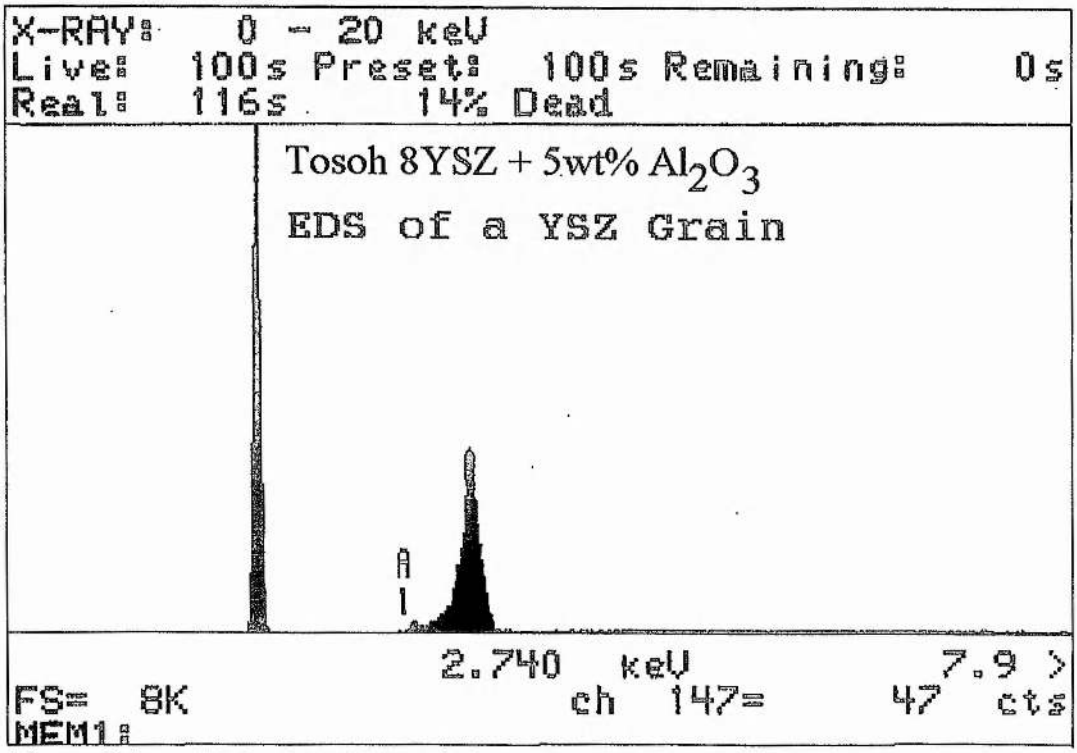

Figure 5.4. EDS of a 8YSZ grain in a sample of Tosoh 8YSZ + 5wt% Al_2O_3.

XRD analysis of the composites containing up to 5wt% Al_2O_3 revealed only

cubic fluorite reflections, Figure 5.5. XRD of materials containing greater than 5wt% Al_2O_3 revealed the fluorite phase and the corundum (α-Al_2O_3) phase, Figure 5.6. No change in the unit cell dimensions of the corundum phase (a=b=4.759 Å and c=12.992 Å) was detected, however there was a very small increase in the 2θ positions of the fluorite phase peaks. This decrease in unit cell size from 5.139 Å to 5.133 Å corresponds to a decrease of 0.12 %. From Figure 5.7 it can be seen that between 0.5 and 1 wt%, i.e. about 0.7 mol%, Al_2O_3 can dissolve into the fluorite structure. It is unlikely that the highly charged Al^{3+} cations could dissolve interstitially into the YSZ fluorite lattice. The decrease in unit cell size is due to the smaller Al^{3+} (0.53 Å) replacing Zr^{4+} and Y^{3+} (0.84 Å and 1.015 Å respectively [21]), as indicated by EDS. The solubility limit of Al_2O_3 in YSZ sintered at 1700°C and cooled at 220°C/hr was previously reported to be only 0.5 mol% [22]. The solubility of Al_2O_3 in YSZ was also reported to be about 0.1 mol% when sintered at 1300°C [23]. The defect chemistry equations for this aliovalent substitution into ZrO_2 can thus be written as

$$Y_2O_3 \rightarrow 2Y'_{Zr} + V_o^{\bullet\bullet} + 3O^x_o \text{ and } Al_2O_3 \rightarrow 2Al'_{Zr} + V_o^{\bullet\bullet} + 3O^x_o$$

i.e. the Al_2O_3 that dissolves into the ZrO_2 creates the same number of vacancies as the addition of Y_2O_3. Increasing the concentration of aliovalent dopants to ZrO_2 is known to result in lower conductivity due to an increase in defect association [24]. The conductivity can be further reduced due to the higher association energy of the Al'_{Zr} - $V_o^{\bullet\bullet}$ defect. Mackrodt and Woodrow calculated that the association energy for a single Al'_{Zr} - $V_o^{\bullet\bullet}$ defect is –143 $kJmol^{-1}$ and that the association energy for a Y'_{Zr} - $V_o^{\bullet\bullet}$ defect is only –39 $kJmol^{-1}$. i.e. The Y'_{Zr} - $V_o^{\bullet\bullet}$ defect is 3.5 times less energetically favourable than the Al'_{Zr} - V''_o defect [25]. This results in the Al'_{Zr} reducing the mobility of $V_o^{\bullet\bullet}$ in YSZ bulk regions and increasing the resistivity. The grain boundary resistivity might also be expected to increase due to the depletion of vacancies in the space-charge layer.

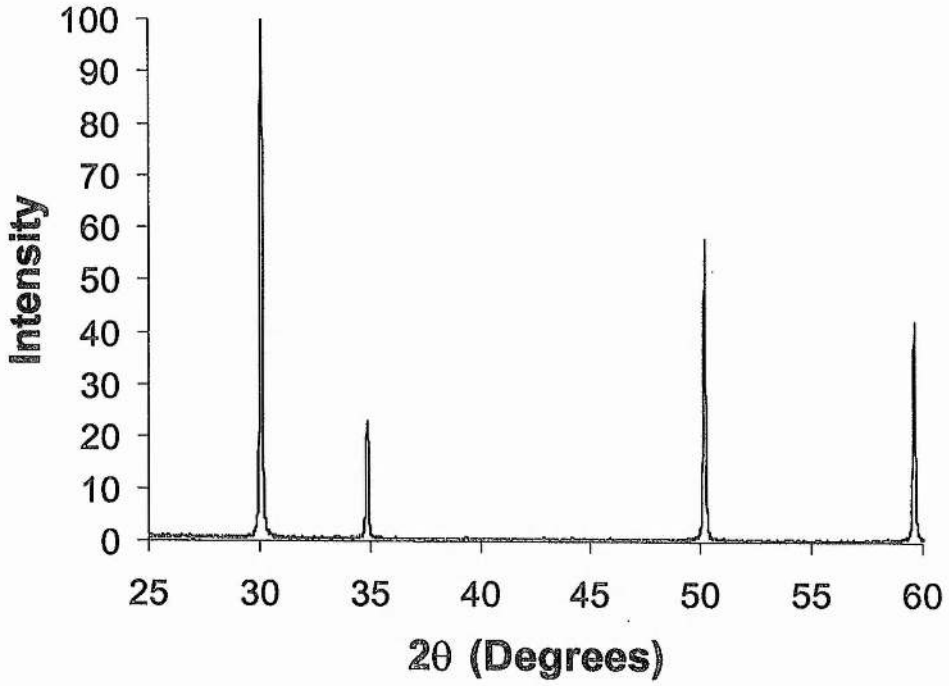

Figure 5.5. Powder XRD of composite materials containing less than 5 wt% Al_2O_3, exhibiting only the (111) and (200) reflections of the cubic fluorite structure.

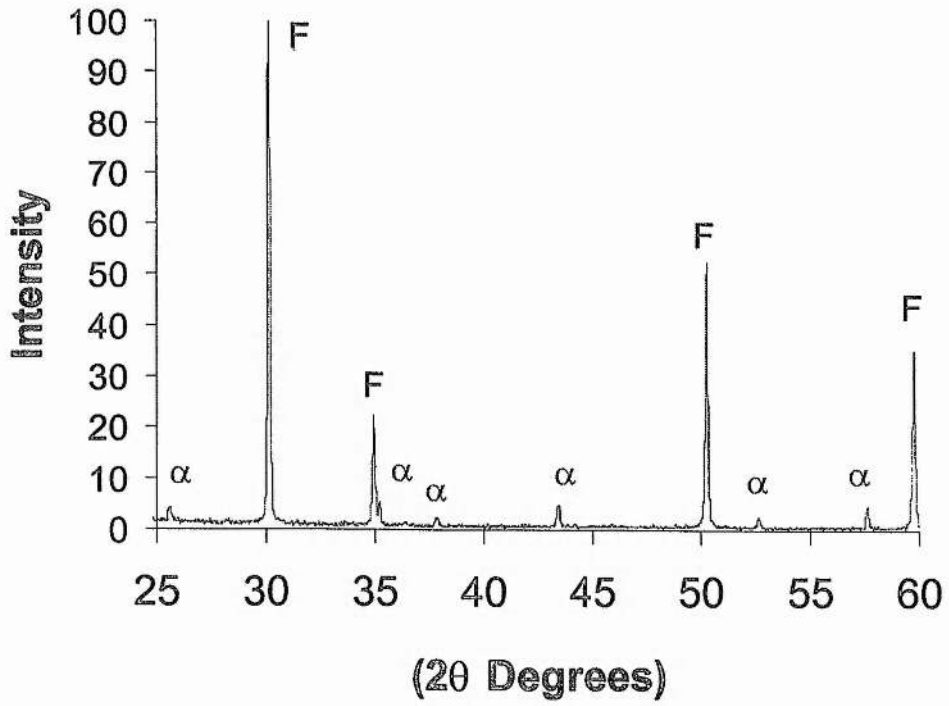

Figure 5.6. Powder XRD of composite material containing 8YSZ + 23 wt% Al_2O exhibiting the fluorite (F) and α-Al_2O_3 (α) peaks.

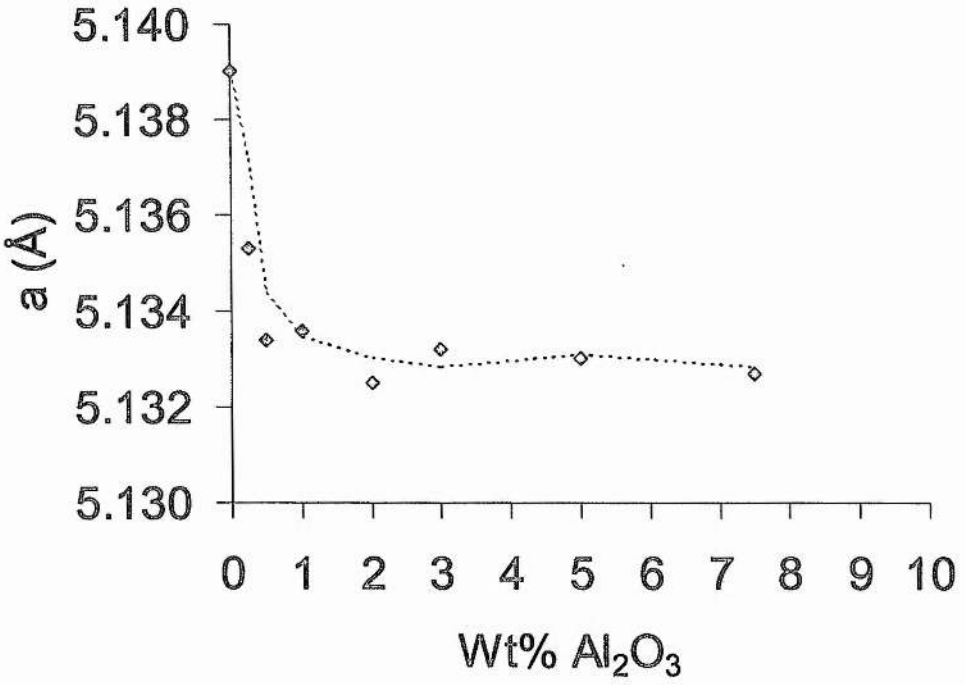

Figure 5.7. Plot of the fluorite phase unit cell parameter, a, vs. wt% Al_2O_3.

Figure 5.8. shows the complex impedance plot obtained for 8YSZ additioned with 0.5 wt% Al_2O_3 at 300°C. The high frequency arc, with a relaxation frequency of 63.1 kHz and an associated capacitance of about 5 x 10^{-12} Fcm^{-1}, is the bulk component of the resistivity. The arc at lower frequency is the grain boundary component, characterised by a capacitance of 10^{-8} Fcm^{-1}.

Figure 5.9. shows the isothermal conductivity at 300°C against wt% Al_2O_3 addition. The bulk conductivity at 300°C decreases from 2.9 x 10^{-4} to 1.8 x 10^{-4} Sm^{-1} for 0 and 1wt% Al_2O_3 addition, a decrease in conductivity of almost 37%, and then remains essentially constant up to 10 wt%. Above 10 wt% Al_2O_3 the bulk conductivity decreases rapidly until 23wt% Al_2O_3, when the conductivity is almost 2.5 orders of magnitude lower than that obtained for 8YSZ. The increase in resistivity at 300°C from 0 to 1 wt% Al_2O_3 is accompanied by a decrease in capacitance of approximately 1 $pFcm^{-1}$, Figure 5.10. This level of alumina addition corresponds to the solubility limit of Al^{3+} into 8YSZ as described earlier by the decrease in unit cell parameter of the fluorite phase.

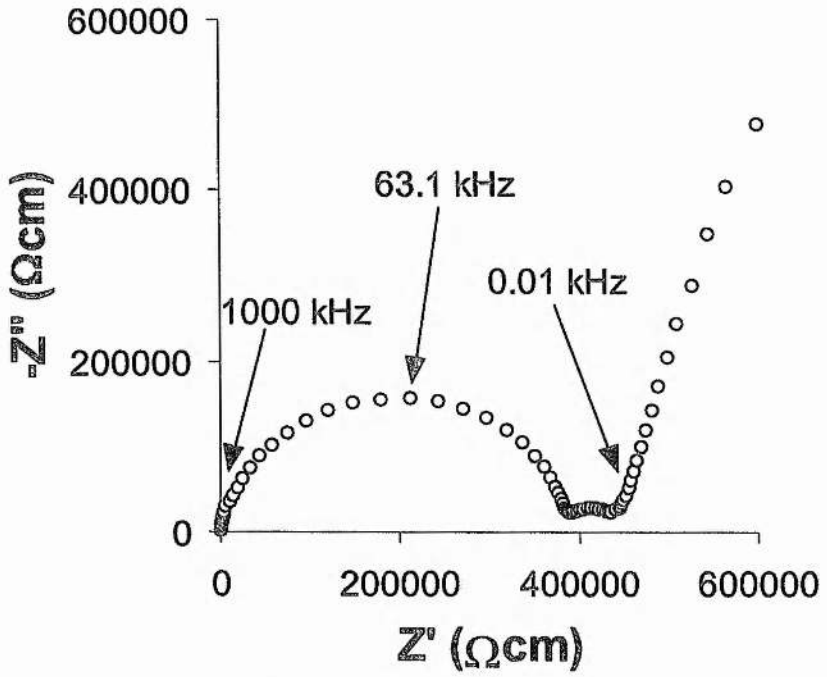

Figure 5.8. The complex impedance plot for Tosoh 8YSZ additioned with 0.5 wt% Al_2O_3 at 300°C.

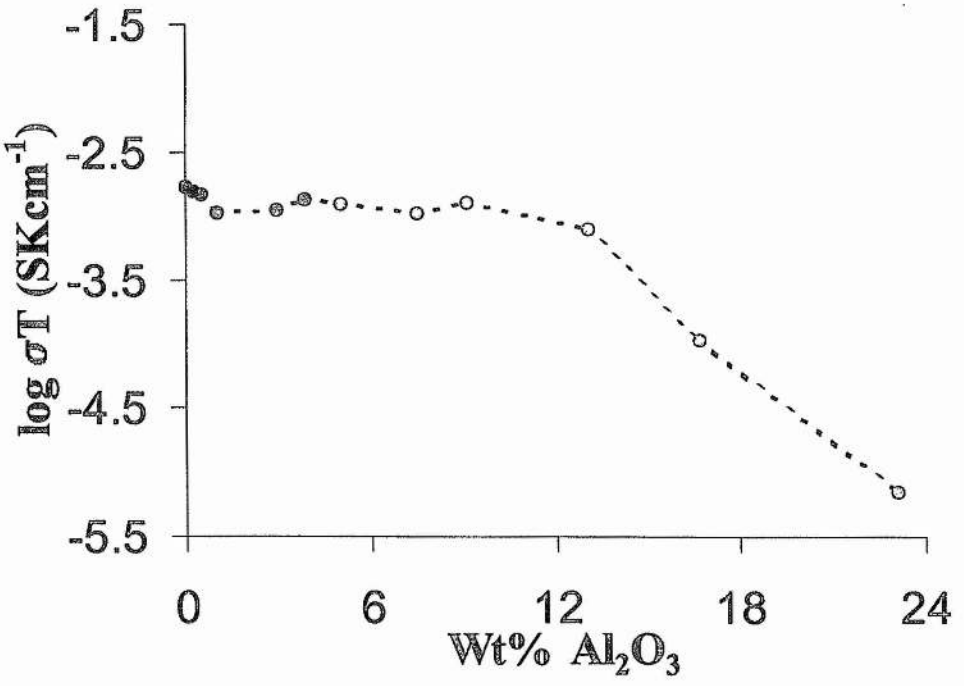

Figure 5.9. Plot of Bulk conductivity at 300°C vs. wt% Al_2O_3.

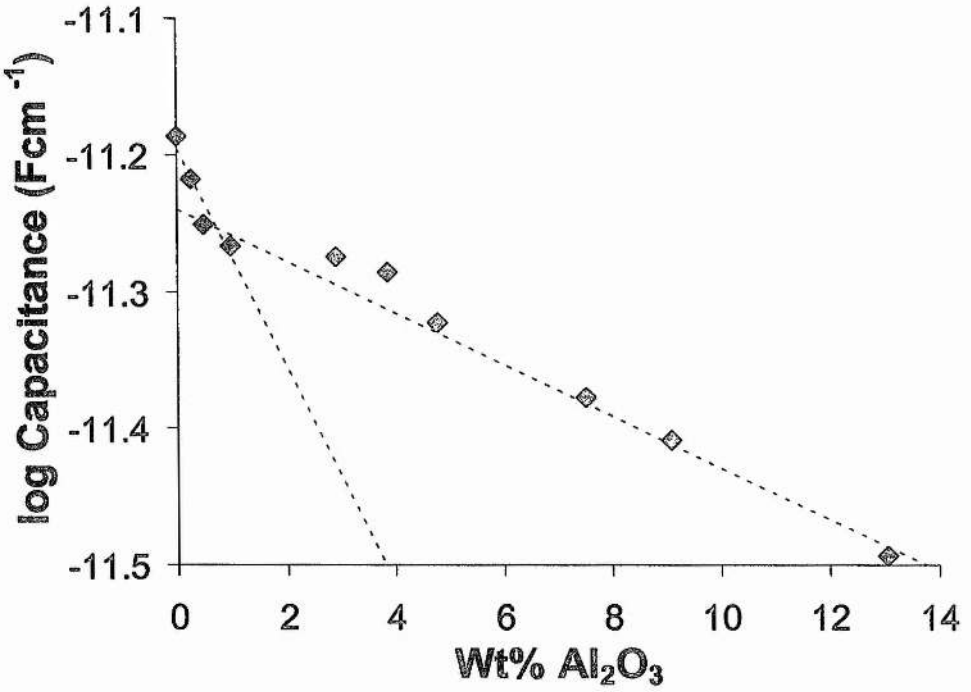

Figure 5.10. Plot of Bulk Capacitance at 300°C vs. wt% Al_2O_3.

The grain boundary response is opposite to that of the bulk for small amounts of alumina addition, indicating that the solubility of Al^{3+} and the resulting higher defect association energy is not the dominant factor in determining the grain boundary conductivity, Figure 5.12. The grain boundary resistivity decreases by almost 1.5 orders of magnitude, from 10^{-4} Ωcm^{-1} to 4.4 x 10^{-3} Ωcm^{-1} on increasing the alumina content from 0 to 1 wt%. The grain boundary conductivity then decreases with increased alumina addition due to the increased concentration of insulating alumina particles at the grain boundaries; however, even when the composite material contains as much as 13 wt% Al_2O_3, the grain boundary conductivity is 1.1 x 10^{-3} Ωcm^{-1}, more than 1 order of magnitude higher than for the 8YSZ to which no alumina had been added. Impedance plots for materials containing more than 13 wt% (18.2 vol%) of Al_2O_3 showed only single asymmetric arcs, for which the bulk and grain boundary components could not be resolved.

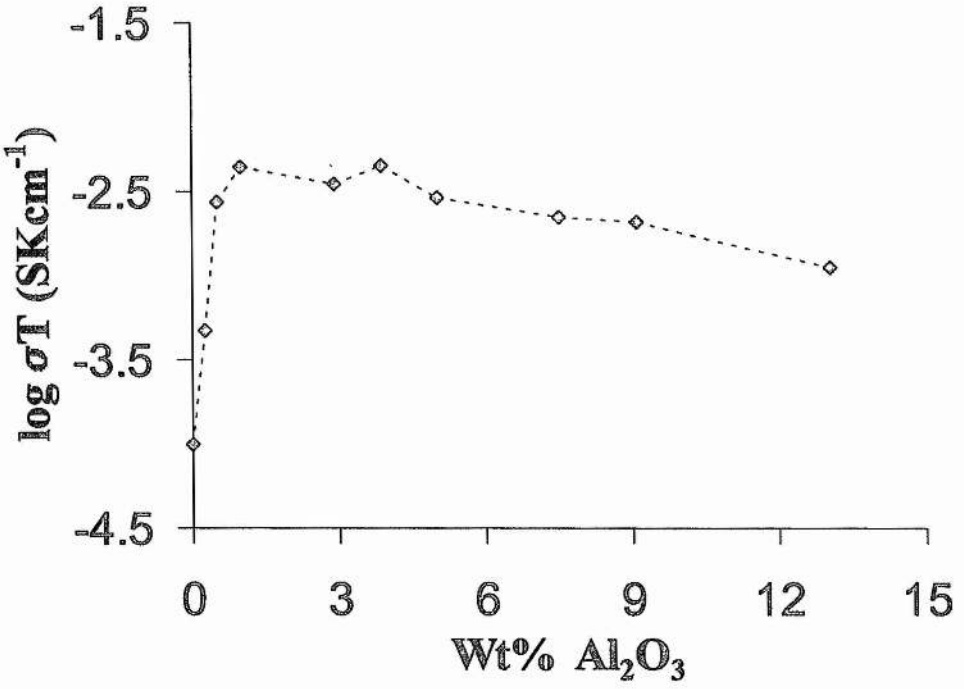

Figure 5.11. Plot of Grain Boundary conductivity at 300°C vs. wt% Al_2O_3.

This increase in grain boundary conductivity has been reported previously [9,11,15]. Butler and Drennan have suggested that Al_2O_3 acts as a scavenger for SiO_2 impurities located at the grain boundaries, resulting in reduced resistivity [14]. i.e. The SiO_2 wets the insulating Al_2O_3 particles instead of the conductive YSZ grains, resulting in easier oxide vacancy migration. Although SiO_2 concentrations have not been determined for the present system, Tosoh TZ8Y is one of the best Si content YSZs available has previously been reported to contain only 0.008 wt% SiO_2. Thus only a very small amount of Silica impurity can have an extremely detrimental effect on the conducting properties of YSZ.

The high temperature impedance was determined from the high frequency intercept of the electrode response with the real axis. The isothermal conductivity plot in Figure 5.12. shows that the conductivity for unadditioned 8YSZ at 1000°C is 8.9 Sm^{-1}.

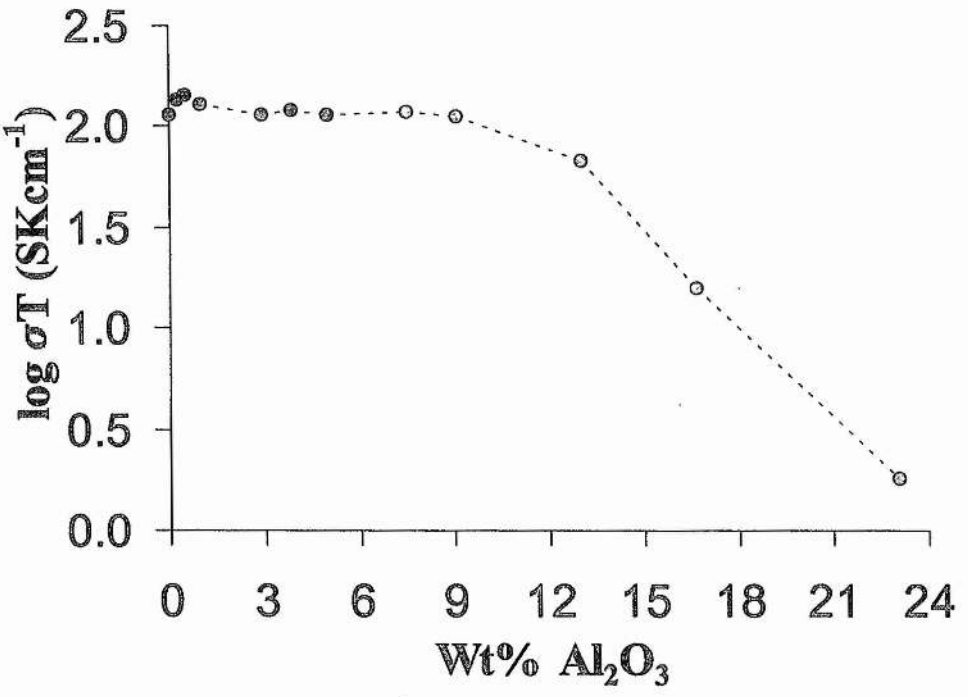

Figure 5.12. Ionic conductivity at 1000°C vs. wt% Al_2O_3.

This value is much lower than the value of 14 Sm^{-1} which is normally obtained for Tosoh 8YSZ which has been sintered for 2 hours. The lower conductivity is thus due to the extended sintering time of 24 hours. A previous study reported that extended sintering produced a small decrease in density an d was possibly due to increased grain growth entrapping porosity within the grains [33]. This is unlikely to be the cause of the large decrease in conductivity found in this study as the measured conductivity has been corrected for density. The conductivity then increases to 11.2 Sm^{-1} on increasing the Al_2O_3 content to 0.5 wt%, an increase of almost 26% in conductivity. The conductivity then decreases to around the value for 8YSZ, i.e. 9 Sm^{-1} and remains essentially constant until around 10 wt% (23.4 vol%) Al_2O_3. Above this quantity of alumina, as is observed in the low temperature conductivity, the high temperature conductivity rapidly decreases. The conductivity at 1000°C for the material containing 23 wt% Al_2O_3 was almost 2 orders of magnitude lower than for 8YSZ, presumably due to increased cracking, porosity and volume fraction of the insulating alumina phase. A recent study by Yuzaki et al found that up to 20wt% Al_2O_3 could be added to

8YSZ without affecting the conductivity. The difference from this study is that they used uniaxial and hydrostatic pressing and used a different heating rate and sintering temperature. The particle size of the Al_2O_3 used in this study (~1μm) was also larger than that used by Yuzaki et al [34].

The activation energy of 8YSZ is known to decrease with increasing temperature due to the breakdown of ordered microdomains as the oxygen vacancies become mobile [26]. The low and high temperature activation energies, measured in the regions 300-400°C and 800-900°C respectively, are plotted in Figure 5.13. The high temperature activation energy can be seen to increase from 1.17 eV to 1.20 eV as up to 1wt% Al^{3+} dissolves into the fluorite phase. Above 1wt% Al_2O_3, the activation energy at low temperatures remains essentially constant from 1 to approximately 5wt% Al_2O_3 addition and then increases steadily to 1.3eV for the composite containing 23wt% Al_2O_3. The activation energy for the 800-900°C follows the same general trend as the activation energy at lower temperatures, increasing from 0.75 to 0.95 eV for 0 to 23wt% Al_2O_3 respectively. This is in agreement with the calculated association energy for a $Al'_{Zr} - V_o^{\bullet\bullet}$ defect being greater than the association enthalpies in non-additioned YSZ.

Several authors have reported the ageing of cubic 8YSZ due to its metastable nature [27-28]. This ageing process, usually represented as a decrease in conductivity at the current solid oxide fuel cell operating temperature of 1000°C, can also be observed with slow cooling of 8YSZ from the sintering temperature of 1500°C, Figure 5.15.. The decrease in cooling rate from 10°C/min to 5°C /min results in the conductivity at 1000°C decreasing from 13.2 to 9.5 Sm^{-1}. Further decrease in the cooling rate to 1°C/min caused the high temperature conductivity to decrease further to 8.7 Sm^{-1}. This ageing process occurs because the equilibrium phases for the 8YSZ composition at temperatures much lower than the sintering temperature, contains tetragonal and cubic phases [29]. As the more quickly cooled materials contain less tetragonal phase than the materials which have been cooled slowly, the susceptibility of 8YSZ to hydrothermal ageing increases with reduced cooling rate because the tetragonal phase can

undergo a martensitic transformation to the monoclinic phase under hydrothermal conditions [30]. The decrease in conductivity at 1000°C for hydrothermally aged materials increases from 29 to 33% for cooling rates of 10 and 5°C/min respectively. Reducing the cooling rate further to 1°C/min has a much larger effect in increasing the susceptibility to ageing, with the high temperature conductivity decreasing by up to 65%. The extended sintering of 8YSZ (24 hours) also increased the susceptibility of the 8YSZ to hydrothermal ageing. The conductivity at 1000°C decreased by 46% on ageing, compared to a decrease of less than 30% for 8YSZ sintered for only 2 hours (the time required to fully sinter this co-precipitated powder).

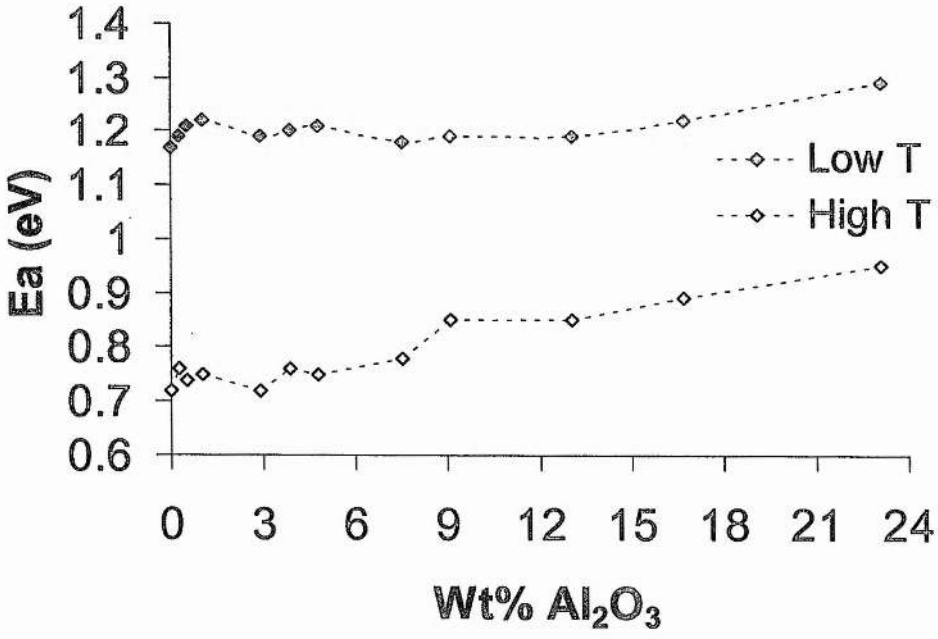

Figure 5.13. Plot of bulk activation energies in the temperature ranges 300-400°C and 800-900°C vs. wt% AL_2O_3.

For the alumina additioned materials, sintered for 24 hours and cooled at 10°C/min, the susceptibility to hydrothermal ageing decreased considerably with increased alumina content. Figure 5.15. shows that the decrease in conductivity between the as prepared composites and hydrothermally aged composite materials is reduced from almost 50% to around 10%.

This improvement in stability has been reported previously for Al_2O_3 addition to Y-TZP and has been attributed to the decrease in grain size and the higher Young's modulus which increases the elastic constraint of the Y-TZP matrix, thereby allowing the t-ZrO_2 to be retained [31]. A Y-TZP pellet would normally only remain mechanically intact for a few hours under the same hydrothermal conditions detailed earlier, resulting in a mixture of tetragonal and monoclinic phases in powder form.

We have found that this catastrophic mechanical failure does not occur in Tosoh materials containing 3 mol% Y_2O_3 and 20wt% Al_2O_3 (TZ3Y20A). Unfortunately, the conductivity of TZ3Y20A is unacceptable for an electrolyte in a practical SOFC [32]; its value at 1000°C is 2.6 Sm^{-1}, compared to 7.5 Sm^{-1} for unadditioned TZ3Y. Hydrothermal ageing of the more resistant TZ3Y20A for 24 hours caused a decrease in the conductivity at 1000°C by a further 30%.

Another possible reason for the stabilisation of 8 mol% YSZ by Al_2O_3 addition may be due to stabilisation of the cubic phase. The small amount of Al^{3+} that dissolves in YSZ will result in increased trivalent dopant and oxygen vacancy concentrations. Small increases in trivalent Yttrium concentration have previously been shown to prevent ageing in YSZ [33].

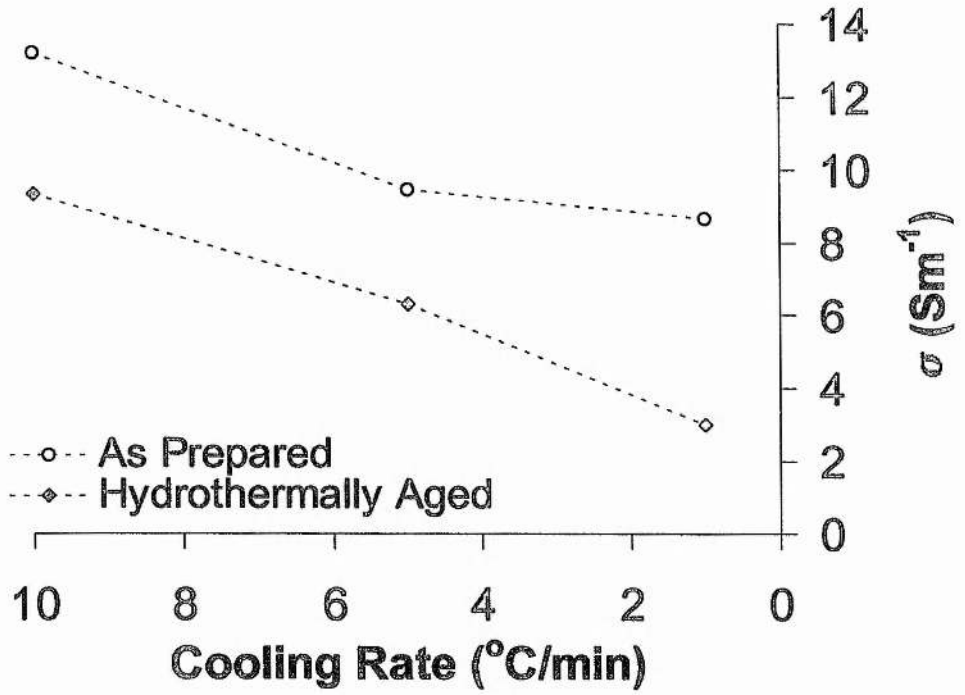

Figure 5.14. Plot of conductivity at 1000°C vs. cooling Rate for as prepared and hydrothermally aged 8YSZ with no alumina addition.

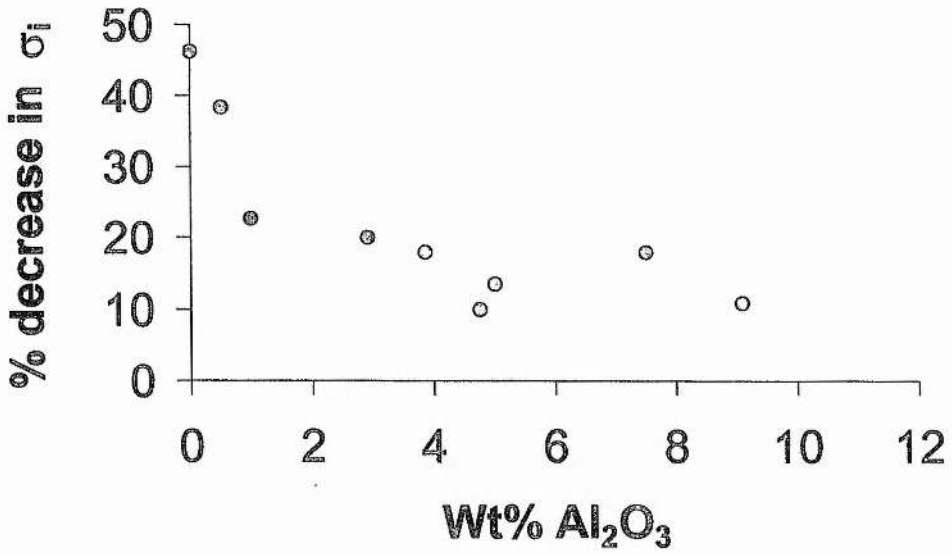

Figure 5.15. Plot of decrease in conductivity at 1000°C vs wt% Al_2O_3 for hydrothermally aged composite materials.

5.5. Mechanical Strength

The flexural strength of the Al_2O_3-YSZ composites prepared from different 8YSZ sources were tested to see what effect the Al_2O_3 had on the strength of 8YSZ. The measured results were opposite to those expected based on the results of other studies, i.e. the strength decreased with Al_2O_3 addition rather than increase. For example in the most recent study of alumina additioned 8YSZ, the bending strength of a 20wt% Al_2O_3 composite was 350 MPa compared to 250Mpa for unadditioned YSZ [34].

The strength of the samples to which no alumina had been added were very low as were the composites containing 5 wt% Al_2O_3, Table 5.2. The reasons for the low strength may be attributed to thermal shock as the samples were not slowly cooled to room temperature from the sintering temperature. Also, the pellets may have been too small for the experimental setup. The pellets were slightly larger than 15mm in diameter and the support ring was only 15mm in diameter. Ideally the pellets should have been around 20mm in diameter.

Table 5.2. Bending strength of Al_2O_3 - 8YSZ composites for 8YSZs prepared by Tosoh, Daiichi and Tioxide. The standard deviations are indicated in brackets.

SAMPLE	STRENGTH NO Al_2O_3((MPa)	STRENGTH 5 WT% Al_2O_3 (MPa)	% INCREASE IN STRENGTH
DAIICHI	98 (26)	93 (27)	-5
TOSOH	81 (32)	62 (18)	-23
TIOXIDE	172 (22)	115 (27)	-33

5.6. Conclusions

Approximately 1wt% of alumina dissolves into the fluorite structure of 8YSZ for a sintering regime of 24 hours at 1500°C and ramp rates of 10°C/min. This solubility limit can be detected for low temperature (~300°C) conductivity studies, where a noticeable decrease in the bulk conductivity and bulk

capacitance is observed. Addition of ~1 wt% Al_2O_3 also substantially increases the grain boundary conductivity, observable at low temperatures, due to the Al_2O_3 interacting with SiO_2 impurities. The high temperature conductivity increases for ~1wt% addition and then decreases to approximately the same conductivity as the non-additioned 8YSZ. The conductivity then remains constant until 10wt% Al_2O_3 has been added to 8YSZ, at which point the conductivity rapidly decreases, and the capacitance increases due to increased cracking and porosity. The susceptibility of 8YSZ to hydrothermal ageing, as detected by the deterioration in high temperature conductivity, can be considerably reduced by the addition of greater than 5 wt% Al_2O_3. Therefore, for the preparation and sintering conditions used in this study, the optimum composition for an improved Tosoh 8YSZ electrolyte material is between 5 and 10 wt% Al_2O_3 content.

5.7. The Effect of $Ca_{12}Al_{14}O_{33}$ Additions on the Electrical and Structural Properties of 8 mol% Yttria-Stabilised Zirconia

5.7.1. Introduction

$Ca_{12}Al_{14}O_{33}$, also known as $C_{12}A_7$ in oxide notation, is a stable, crystalline ceramic material, well known from its occurrence in cement clinkers. It is an oxide ion conductor at high temperatures, whose conductivity is only 8-10 times lower than that of Yttria-stabilised Zirconia [35]. In oxidising or inert atmospheres, it exhibits an ionic transport number of unity [36, 37]. These properties suggest that it could have applications in oxygen sensors and in fuel cells.

Existing oxide ion conductors are essentially confined to a small group of ceramic oxides with structures related to the fluorite structure but $C_{12}A_7$ exhibits an unrelated cubic structure. The reasons for the high conductivity are not well understood but may be associated with the fact that the crystal structure contains a mixture of anions, a 3-dimensional aluminate framework and essentially free oxide ions.

The crystal structure is based on a framework of corner-sharing AlO_4 tetrahedra, arranged in 8 membered rings [38]. Alternate tetrahedra share three and four corners respectively, with other tetrahedra, giving the framework a formula of $(Al_{14}O_{32})^{22-}$. The calcium ions occupy seven-co-ordinate sites within this framework. The co-ordination environment of calcium consists of six oxygens that belong to the aluminate framework and an additional oxygen site (shaded circle, Figure 5.16) that does not belong to the framework. This additional oxygen site is only partially occupied (i.e. the extra oxide ions are disordered over a large number of sites in the crystal structure). For the ideal $Ca_{12}Al_{14}O_{33}$ formula, its occupancy would be 1/6. Thus, oxide ion conductivity in $Ca_{12}Al_{14}O_{33}$ [35, 36] is thought to be related to the presence of these partially occupied oxide ion sites, outwith the aluminate framework. It can thus be regarded as an interstitial oxide ion conductor and its formula represented as $Ca_{12}Al_{14}O_{32}O$.

A significant proportion of fluoride and chloride ions can replace this additional oxide ion, up to the limiting composition $Ca_{12}Al_{14}O_{32}(F,Cl)_2$ [46]. The structure of the fully fluorinated compound has been determined [47].

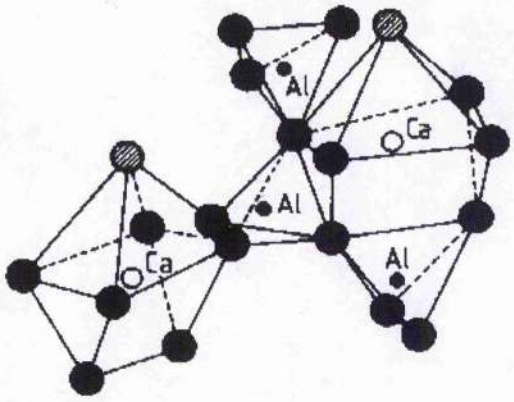

Figure 5.16. The co-ordination environments of Ca and Al in $Ca_{12}Al_{14}O_{33}$.

Other anions that can replace the additional oxide ion include superoxide [45] and immobile hydroxide ions. Low levels of superoxide (0.02 O_2^- per formula unit) are found in samples prepared over a range of conditions [42]. The hydroxide ions are introduced into the structure in the temperature range 930° to 1300°C by $C_{12}A_7$ entering into a reversible equilibrium with atmospheric H_2O.

At 950°C up to one molecule of water per formula unit may be taken up into the structure [40, 41]. Uptake of water can be represented by the equation:

$$Ca_{12}[Al_{14}O_{32}]O + H_2O \leftrightarrow Ca_{12}[Al_{14}O_{33}]OH_2$$

This results in a change in the unit-cell size and the density. The water can be removed by heating at higher temperatures e.g. 1350°C and the original conductivity can be recovered. This indicates that water uptake involves reaction between water and the oxide outwith the aluminate framework.

Although the bulk conductivity is not as high as that of YSZ, $C_{12}A_7$ does offer distinct advantages in its ease of processing. It is possible to sinter the sample to high density and reduce the magnitude of the grain boundary resistance until it is comparable to the bulk crystal resistance. Scanning electron micrographs show that the microstructure of $C_{12}A_7$ changes from that of an open network to a continuous mass as sintering is improved [37].

5.7.2. Preparation of $Ca_{12}Al_{14}O_{33}$

$Ca_{12}Al_{14}O_{33}$ was prepared by solid state reaction of the dried (@600°C) oxides $CaCO_3$ and Al_2O_3 in a Pt crucible. Samples were initially fired at 900°C for several hours to drive off CO_2. The dry, crushed powders were pressed into discs and sintered at 1350°C and 1365°C, just below the melting point of $C_{12}A_7$. Incomplete drying of the starting materials resulted in the more Calcium rich cubic phase $Ca_3Al_2O_6$ (C_3A) forming as an impurity phase, as suggested by the phase diagram, Figure 5.17. The most intense peak (hkl=440) observable for this impurity phase occurs at 33.169 °2θ (d=2.699) [48] and can appear as a peak or a shoulder on the low angle side of the most intense peak (hkl=420) of the $C_{12}Al_{14}O_{33}$ phase. The powder X-ray diffraction patterns of a CaO and Al_2O_3 mixture fired at 900°C and $C_{12}Al_{14}O_{33}$ fired at 1350°C are shown in Figures 5.18. and 5.19.

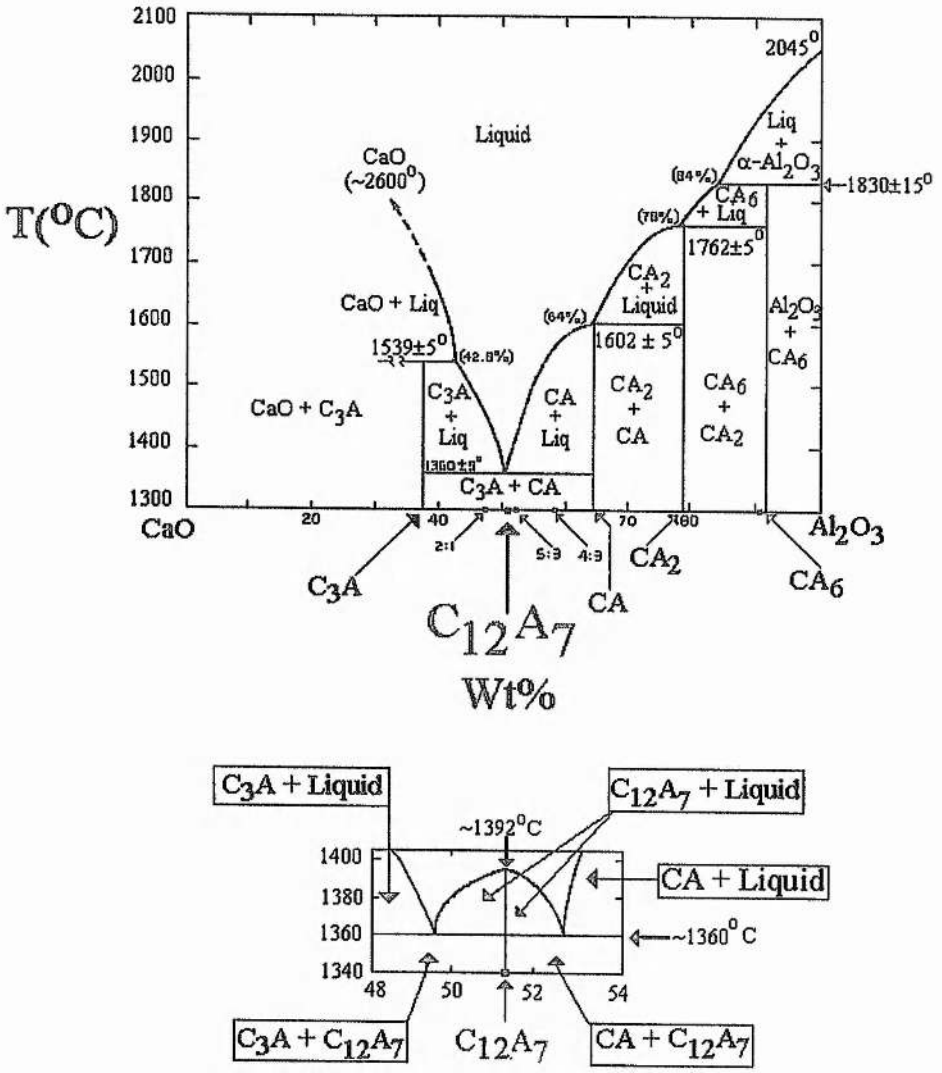

Figure 5.17. The binary system CaO-Al_2O_3 in a moisture-free atmosphere. A = Al_2O_3 and C = CaO [9,10].

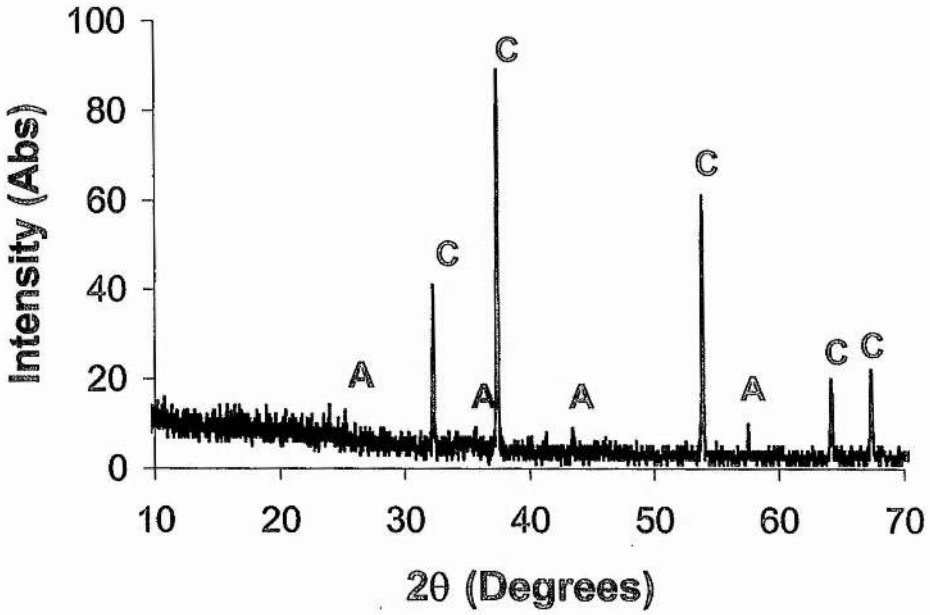

Figure 5.18. The X-ray diffraction pattern of the decarbonated 12:7 CaO/Al_2O_3 mixture fired at 900°C. A = α-Al_2O_3, C = CaO.

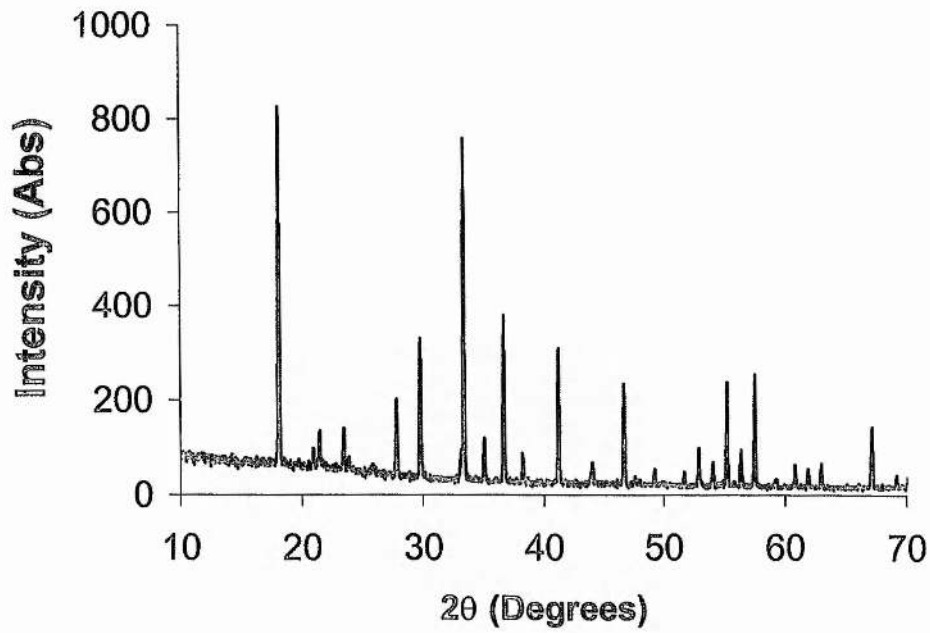

Figure 5.19. The X-ray diffraction pattern of $Ca_{12}Al_{14}O_{33}$ sintered at 1350°C.

The structure of $C_{12}Al_{14}O_{33}$ is cubic, with a unit cell parameter of

11.982Å, and is described by the space group I-43d. A list of the observed peaks and Miller indices is shown in Table 5.3.

Table 5.3. Powder X-ray data for $C_{12}Al_{14}O_{33}$.

2θ (Degrees)	d-spacing	Relative Intensity	hkl	2θ (Degrees)	d-spacing	Relative Intensity	hkl
18.127	4.890	95	211	54.060	1.695	8	710
20.395	4.240	6	220	55.223	1.662	30	640
23.454	3.790	16	310	56.403	1.630	10	721
27.822	3.204	25	321	57.519	1.601	30	642
29.777	2.998	45	400	60.810	1.522	6	651
33.408	2.680	100	420	61.891	1.498	6	800
35.080	2.556	18	332	62.965	1.475	8	741
36.697	2.447	50	422	67.143	1.393	18	750
38.269	2.350	10	510	69.231	1.356	4	752
41.207	2.189	40	521	70.178	1.340	8	840
44.052	2.054	10	530	72.224	1.307	8	842
46.662	1.945	30	611	73.198	1.292	6	761
49.212	1.850	8	541	74.200	1.277	6	664
51.690	1.767	6	631	75.164	1.263	6	930
52.880	1.730	12	444	77.103	1.236	4	932

The theoretical density of $C_{12}Al_{14}O_{33}$ calculated from the unit cell parameter, formula weight and unit cell content is 2.68 gcm^{-3}. The densities of the single phase $C_{12}Al_{14}O_{33}$ samples sintered at 1350°C and 1365°C were 85 and 93 % of the theoretical density respectively.

5.7.3. A.C. Impedance Spectroscopy Studies of $Ca_{12}Al_{14}O_{33}$

For conductivity measurements to be carried out, Pt electrodes were applied by decomposition of organo-platinum paste with a final firing at 900°C for 30 minutes. The initial ac impedance response of $C_{12}A_7$ was not well defined as shown in Figure 5.20. A broad asymmetric arc is seen with a poor response at lower frequencies. The effective resistance of the ceramic was obtained from the low frequency intercept on the real, Z', axis. At this stage the resistivity could not be separated into bulk and grain boundary components although from the distorted shape of the impedance arc, electrical inhomogeneities must be present in the ceramic. Also, the large capacitance value of $12pFcm^{-1}$ associated with the arc is too large to be attributed purely to a homogeneous bulk. Resistivity values extracted from the complex plane impedance plots were used to construct the Arrhenius plot in Figure 5.21. The data is clearly non-linear but was reproducible provided the temperature was not raised above 900°C. On refiring each sample at 1350°C for a short time, the resistivities followed a different path. Linear plots were obtained which were reproducible between heating and cooling, again provided that the temperature was not raised above about 900°C.

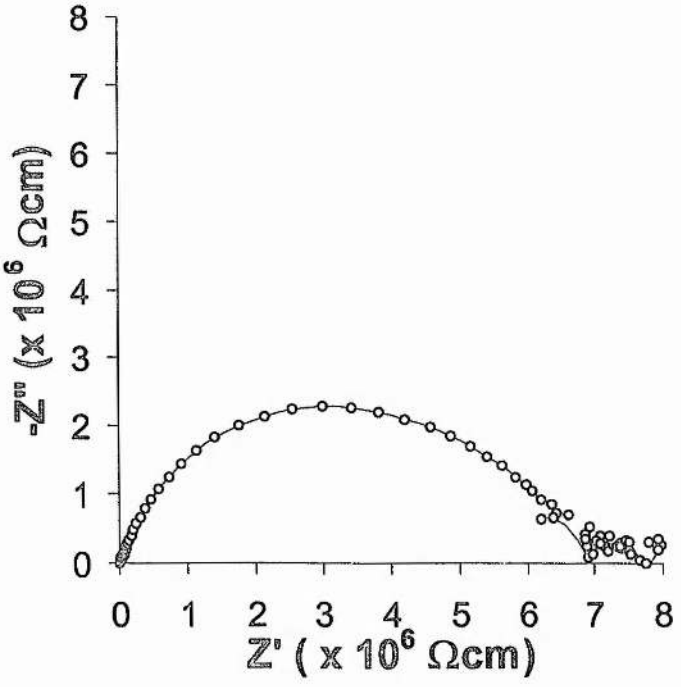

Figure 5.20. The impedance response of $C_{12}A_7$ at 600°C, (after firing at 900°C).

The plot of bulk conductivity for the sample fired at 1350°C (after firing the Pt electrodes at 900°C), Figure 5.21, is linear and the activation energy was calculated to be 0.75eV. However, heating at 1350°C for longer times gave rise to a bulk activation energy of 0.85eV, possibly due to the slower cooling of the sample. The grain boundary activation energy was 1.22 eV for the sample sintered at 1350°C for 1 hour.

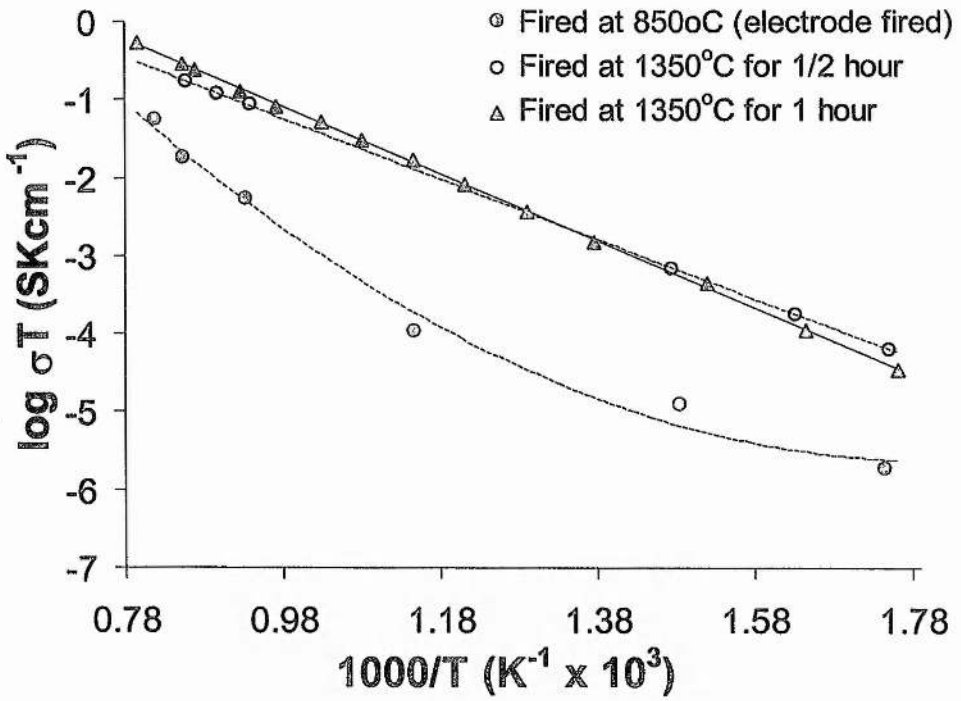

Figure 5.21. Arrhenius conductivity plots for $C_{12}A_7$. The filled circles include grain and grain boundary components. The other points are for the bulk conductivity only.

Reduction of bulk and grain boundary resistance was achieved by sintering at 1365°C, just below the melting point of $C_{12}A_7$. The bulk resistivity at 501°C decreased from 2.09 x 10^5 to 1.47 x 10^4 Ωcm^{-1} and the grain boundary resistivity decreased from 1.82 x 10^5 to 1.90 x 10^4 Ωcm^{-1}. The spectroscopic impedance plot shown in Figure 5.22. clearly shows the decrease in resistivity of each resistive component with increased sintering temperature. The high frequency peaks (1MHz - 10MHz) represent the bulk resistance and the peaks at lower frequency (0.1kHz - 10kHz) represent the grain boundary resistance. The bulk activation energy remained the same as for the sample sintered at 1350°C

(0.85 eV) but the grain boundary activation energy decreased from 1.27 eV to 1.12 eV. The grain boundary conductivity of $C_{12}Al_{14}O_{33}$ fired at 1350 and 1365°C are shown in Figure 5.23. The grain boundary and bulk conductivities of the sample sintered at 1365°C are plotted together in Figure 5.24.

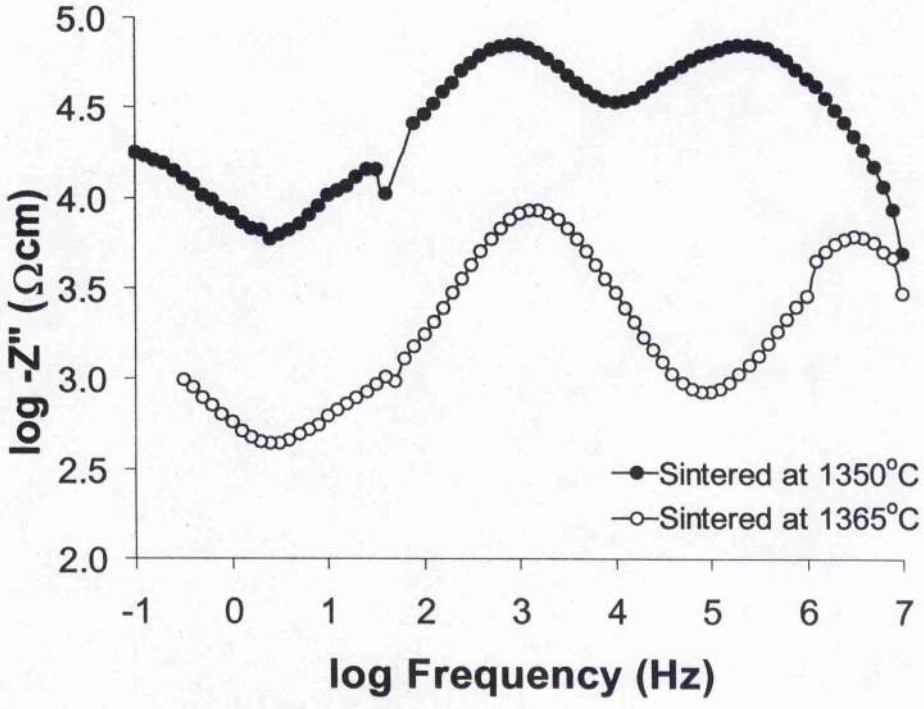

Figure 5.22. Spectroscopic impedance plots obtained at 501°C for $C_{12}A_7$ sintered at 1350°C and 1365°C.

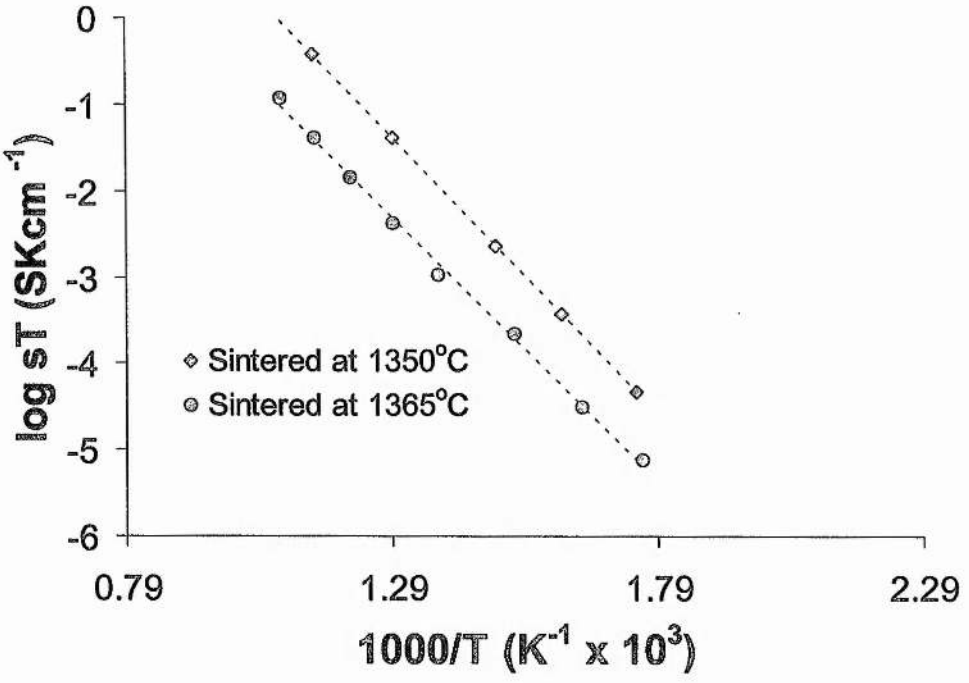

Figure 5.23. Arrhenius plots of grain boundary conductivity for $C_{12}A_7$ sintered at 1350 and 1365°C.

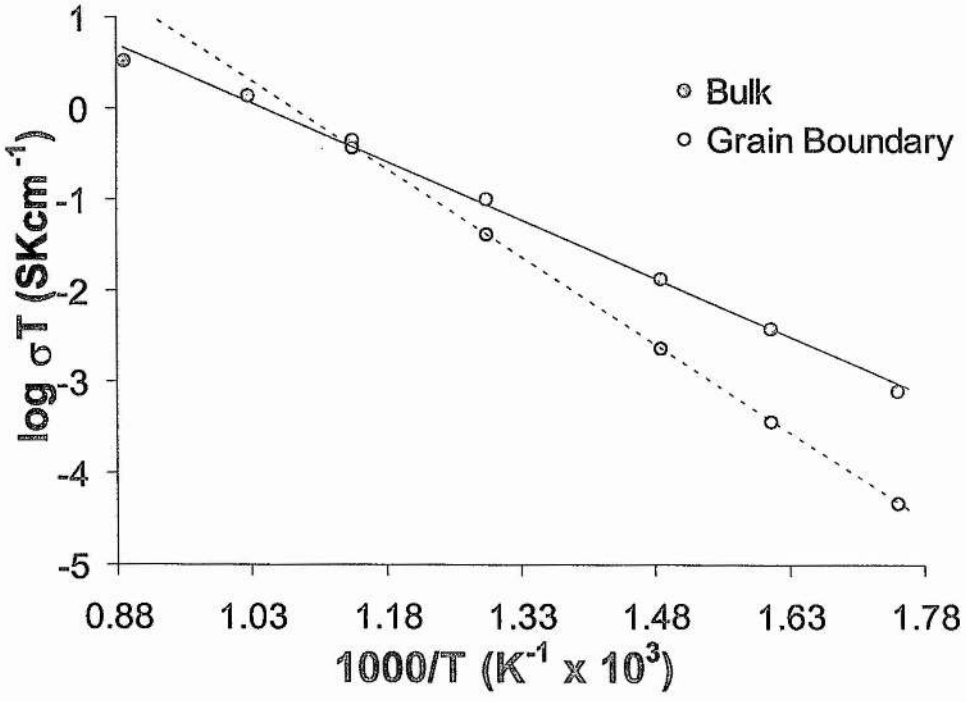

Figure 5.24. Bulk and Grain Boundary Conductivity of $C_{12}A_7$ sintered at 1365°C.

There were also changes in the grain boundary and bulk capacitance's upon sintering at temperatures near the melting point. The bulk capacitance increased slightly, from 2.98 to 3.16 $pFcm^{-1}$. The capacitance of the grain boundary increased by a factor of about 5, from 9.7×10^{-10} Fcm^{-1} to 5.9×10^{-9} Fcm^{-1}. Assuming that capacitance is proportional to 1/thickness, the increase in capacitance would indicate that the grain boundaries become thinner by a factor of ~5. These observations taken together indicate that the resistivity of the grain boundary decreases with sintering temperature.

There are 3 factors which affect the conductivity of $C_{12}A_7$. First the microstructure of the ceramic has a major effect on the nature and the size of the grain boundary impedance. Second, the presence of water in the sample appears to affect the bulk conductivity. Third the nature of the electrodes affects the conductivity. During the initial stages of firing the Pt paste electrodes, oxygen appears to be removed from the sample leading to an increased resistivity. All three of these affect the lower curve in Figure 5.21. and affect the other curves in Figure 5.21. to a lesser extent.

5.7.4. $C_{12}Al_{14}O_{33}$ Additioned Tosoh 8YSZ

As the conductivity of $C_{12}Al_{14}O_{33}$ is within an order of magnitude of the conductivity of 8 mol% YSZ, Ca stabilises Zirconia and Al_2O_3 improves the ceramic properties of YSZ, the effect of adding $C_{12}Al_{14}O_{33}$ to 8YSZ was investigated.

Several compositions between 0 and 17 wt% $C_{12}A_7$ were prepared by ball milling the mixed powders in ethanol for 1 hour using Zirconia containers and grinding balls. The mixtures were dried at 100°C for an hour and pellets were uniaxially pressed at 4000 $kgcm^{-2}$. The samples were sintered at 1500°C for 2 hours with heating and cooling rates of 10°C/min. The theoretical densities were calculated for each composition by assuming that no reaction occurred and that the law of addition holds. Plots of the theoretical and actual densities are shown in Figure 5.25. The plots clearly show that the relative density decreases with addition of $C_{12}A_7$. This is surprising because at 1500°C the $C_{12}A_7$ would have

melted and all compositions should have the same relative % theoretical density.

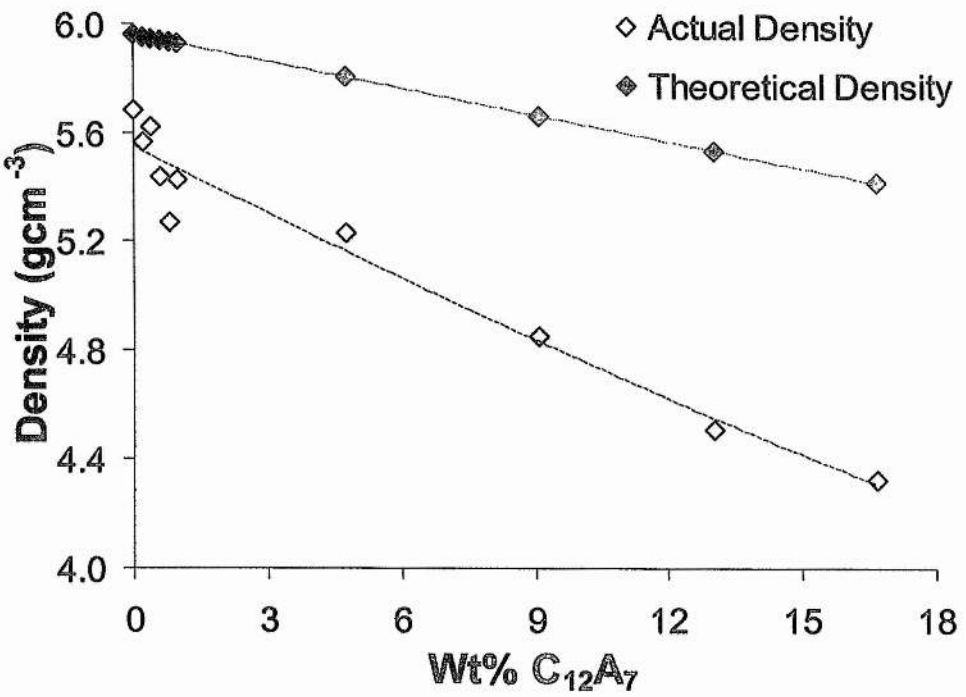

Figure 5.2.5. Plot of theoretical density and actual density for $C_{12}A_7$ additioned Tosoh 8YSZ.

The high and low temperature conductivity of the $C_{12}A_7$ additioned 8 mol% YSZ decreased significantly for all compositions, Figures 5.26. and 5.27. The conductivity at 1000°C decreased from 14 Sm^{-1} for pure 8YSZ (for samples sintered for only 2 hours) to approximately 1 Sm^{-1} for compositions containing 1 wt% $C_{12}A_7$ or more. The bulk conductivity at 300°C shows the same trend as the high temperature data except that for low wt% additions, the conductivity increases before it decreases. The bulk activation energy for conduction increased linearly with $C_{12}A_7$, Figure 5.28. The grain boundary activation energy was relatively high, generally being around 1.3 eV.

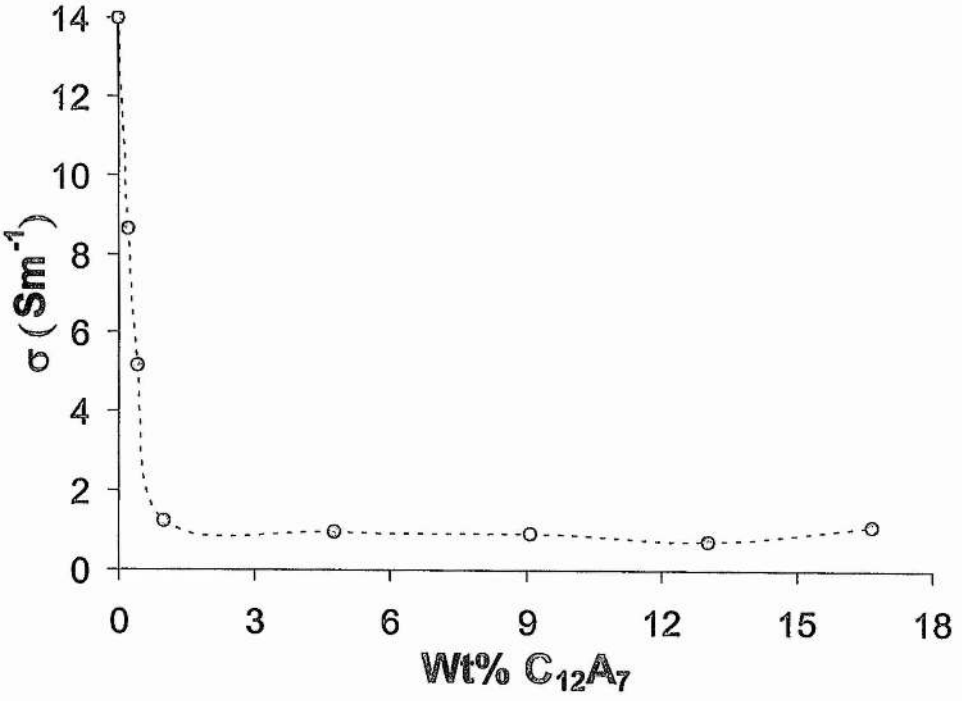

Figure 5.26. Plot of conductivity at 1000°C for $C_{12}A_7$ additioned Tosoh 8YSZ.

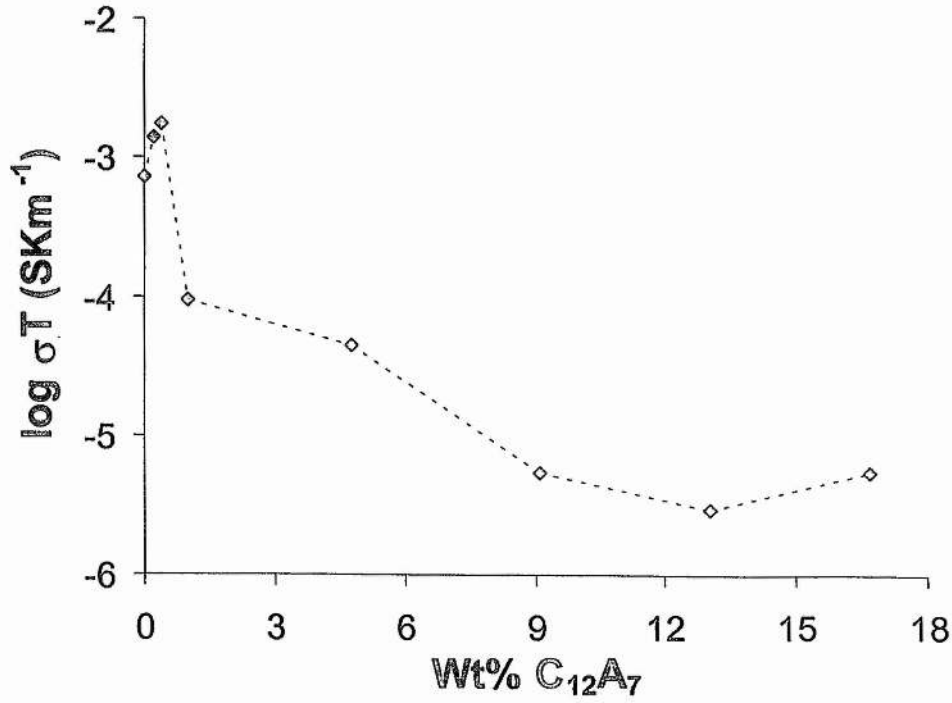

Figure 5.27. Plot of conductivity at 300°C for $C_{12}A_7$ additioned Tosoh 8YSZ.

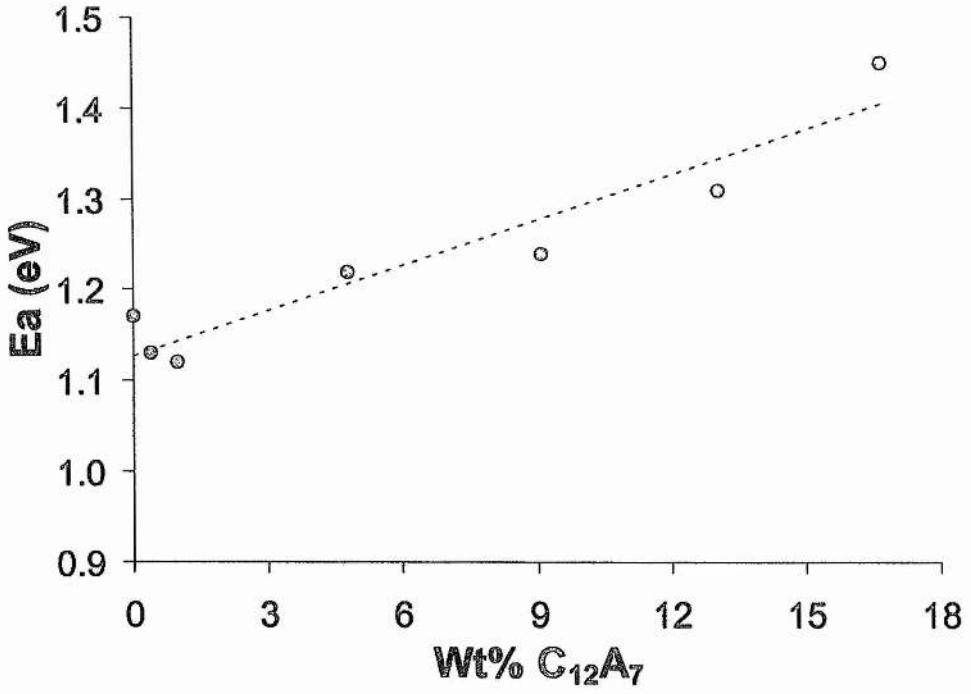

Figure 5.28. Plot of bulk activation energy vs. Wt% $C_{12}A_7$ for additioned Tosoh 8YSZ.

The complex plane impedance plots generally showed asymmetric responses with a very poor electrode response. This was probably due to the firing of the electrodes at 850°C as was the case with the pure $C_{12}A_7$. Therefore it was necessary to refire all pellets used for impedance measurements at 1380°C (above the melting point of $C_{12}A_7$) for 30 minutes in order to remove any water that had been absorbed into the structure and to return oxygen to the sample before the measurements were made.

5.7.5. X-ray diffraction of the $C_{12}A_7$ additioned 8YSZ samples

Only cubic fluorite peaks were observed by X-ray diffraction in samples containing up to 10wt% $C_{12}A_7$. Samples with 10, 13 and 17 wt% $C_{12}A_7$ showed peaks which could not be attributed to the fluorite phase or the $C_{12}A_7$ phase. The peaks could not be assigned to any other calcium aluminate phase either, nor could they be identified by using the 3 most intense peaks as a search criteria.

The unit cell parameter of the fluorite phase remained essentially constant at 5.139 Å. The X-ray diffraction pattern of 8YZ additioned with 17wt% $C_{12}A_7$ is shown below in Figure 5.29.

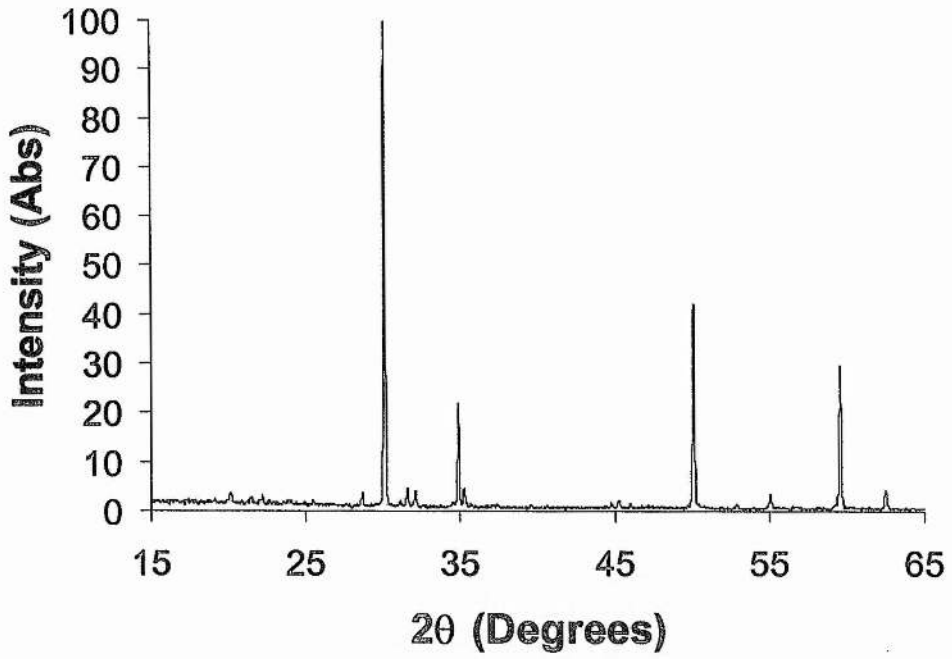

Figure 5.29. X-ray diffraction pattern of Tosoh 8YSZ + 17wt% $Ca_{12}Al_{14}O_{33}$ fired at 1500°C for 24 hours.

5.6.6. Conclusions

$Ca_{12}Al_{14}O_{33}$ additions to 8YSZ have a drastic effect on the conductivity of 8YSZ. The small increase in the low temperature conductivity with low additions of $C_{12}A_7$ and the drastic decrease in the high temperature conductivity of the composites with $C_{12}A_7$ addition suggests that a third poorly conducting phase is formed. Electron Microscopy would be useful to identify this third phase as identification was not possible by X-ray diffraction.

5.8. References

[1] B.C.H. Steele, ed., in: Ceramic Electrochemical Reactors (Ceramionics, 1987)

[2] T.K. Gupta, F.F. Lange and J.H. Betchtold, J. Mater. Sci. 13 (1978) 1464

[3] K. Tsukuma, K. Ueda, and M. Shimada, J. Am. Ceram. Soc., 68 (1985) C-4-C-5

[4] M. Kihara, T. Ogata, K. Nakamura, and K. Kobayashi, J. Ceram. Soc. Jpn., Int. Ed., 96 (1988) 635-42

[5] T. Shimada, K. Nagata, M. Hashiba, E. Miura, T. Ono, and Y. Nu: in Advances in Ceramics, Vol, 24A, Science and Technology of Zirconia III, ed., N. Somiya, O. Yamamoto and H Yanagida, (American Ceramic Society, Westerville, OH, 1988) p. 397-403

[6] F.F. Lange, J. Mater. Sci., 17 (1982) 24-54

[7] S.J. Glass, D.J. Green, J. Am. Ceram. Soc. 79 (1996) 227-36

[8] K.Kobayashi, H. Kuwajima and T. Masaki, Solid State Ionics 3-4 (1981) 389

[9] M.J. Verkerk, A.J.A. Winnubst and A.J. Burggraaf, J. Mater. Sci. 17 (1982) 3113

[10] K.C. Radford and R.J. Bratton, J. Mater. Sci.. 14 (1979) 66-69

[11] H. Bernard, Rep. CEA-R-500, CEN-Saclay, France, 1981

[12] Xin Guo, Run-Zhang Yuan, Solid State Ionics 80 (1995) 159-166

[13] M.Mori, T. Abe, H. Itoh, O. Yamamoto, Y. Takeda, T. Kawahara, Solid State Ionics 74 (1994) 157-164

[14] E.P. Butler and J. Drennan, J. Am. Ceram. Soc. 65 (1982) 474-478

[15] M. Miyayama, H. Yanagida and A. Asada, Am. Ceram. Soc. Bull. 64 660-64 (1985)

[16] F. Ishizaki, T. Yoshida and S. Sakurada, Proc. Int. Symp. SOFCs, Nagoya, Japan, Nov 13-14, 1989, ed., O. Yamamoto, M. Dokiya and H. Tagawa (Science House Co. Ltd, Tokyo, 1989), p. 172-176

[17] F.J. Esper, K.H. Friese and H. Geier, in: Science and Technology of Zirconia, eds. N. Claussen, M.Ruhle and A.H. Heuer (American Ceramic Society, Columbus, OH, 1984) p. 528

[18] F. Ishizaki, T. Yoshida and S. Sakurada, Proc. Electrochem. Soc. Fall

Meeting (1989) p. 3.

[19] Handbook of Chemistry and Physics 76th Edn, Ed in Chief. David R. Lide, (1995-1996) 6-15

[20] M. Mogensen, T. Lindegaard, U.R. Hansen and G. Mogensen, J. Electrochem. Soc., 141 (1994) 2122-2128

[21] R.D. Shannon, Acta Crysta., A32 (1976) 751

[22] X. Guo, C.Q. Tang and R.Z. Yuan, J. Eur. Ceram. Soc. 15 (1995) 25

[23] H. Bernard, Rep. CEA-R-5090, Commissariat à l'Energie Atomique, CEN-Saclay, France, 1981, p. 117.

[24] S.P.S. Badwal, Solid State Ionics 52 (1992) 23-32

[25] W.C. Mackrodt and P.M. Woodrow, J. Am. Ceram. Soc. 69 (1986) 277-280

[26] I.R. Gibson and J.T.S. Irvine, J. Mater. Chem. 6 (1996) 895-898

[27] F.T. Ciacchi, K.M. Crane and S.P.S. Badwal, Solid State Ionics 73 (1994) 49-61

[28] H. Raeder, T. Norby and P.A. Osborg, in: Ceramic Processing Science and Technology, eds H. Hausner, G.L. Messing and S. Hirano, Ceram. Trans. 51 (1995) 719-723

[29] H.G. Scott, J. Mat. Sci. 10 (1975) 1527-1535

[30] M. Yoshimura, T. Noma, K. Kawabata and S. Somiya, J. Mat. Sci. Lett. 6 (1987) 465-467

[31] F. Wakai, S. Sakaguchi and Y. Matsuno, Adv. Ceram. Mater. 1 (1986) 259

[32] O. Yamamoto, T. Kawahara, K. Kohno, Y. Takeda and N. Imanishi, in Solid State Materials, eds. S. Radhakrishna and A. Dand (Narosa, New Delhi, 1991) p. 366

[33] I.R. Gibson, G.P. Dransfield and J.T.S. Irvine, J. Euro. Ceram. Soc, 18 (1998) 661-667

[34] Aya Yuzaki, Akira Kishimoto and Yoshinobu Nakamura, Solid State Ionics 109 (1998) 273-277

[35] M. Lacerda, J.T.S. Irvine, F.P. Glasser and A.R. West, Nature 332 (1988) 525

[36] J.T.S. Irvine, M. Lacerda and A.R. West, Mat. Res. Bull. 23 (1988) 1033

[37] J.T.S. Irvine, M. Lacerda and A.R. West, Proc. Intern. Symp. Solid Oxide

Fuel Cells, Nagoya, Japan (1989) p. 153

[38] H.Bartl and T. Scheller, Neues Jahrb.f. Mineral. Monatsch, (1970) 547

[39] A.N. Christensen, Acta Chem. Scand. A41 (1987) 110

[40] K.V. Singh and F.P. Glasser, Ceram Int., 14 (1988) 59

[41] J.T.S. Irvine and A.R. West, J. Appl. Electrochem., 19 (1989) 410

[42] R. Strosser, M. Nofz, W. Gessner, C.H. Schroter and G. Kranz, J. Solid State Chem. 81 (1989) 152

[43] R.W. Nurse, J.H. Welch and A.J. Majumdar, Trans. Brit. Ceram. Soc. 64 [9] 416 (1965)

[44] R.W. Nurse, J.H. Welch and A.J. Majumdar, Trans. Brit. Ceram. Soc. 64 [9] 413 (1965)

[45] J.A. Imlach, Dent Glasser, L.S. & Glasser, F.P. Cement & Concrete Res. 1, 57-61 (1971)

[46] J. Jeevaratnam, F. P. Glasser & L. S. Dent, J. Am Ceram. Soc. 47 105-106 (1964)

[47] P. P. Williams, Acta Crystallogr. B29, 1550-1551 (1973)

[48] F. Ordway, Symp. Chem. Cement, London 1952, Cem.Conc.Assoc. 1954

6.1. Introduction

The maximum conductivity of YSZ occurs with a Yttria content of 8 mol% (15 atom% Y^{3+}) [1-3]. Increasing the amount of Yttria dopant above 8 mol% results in lower conductivity. This decrease in oxygen ion mobility is due to the increase in oxygen vacancy-cation associations which reduce the number of 'free' oxygen vacancies available to migrate [4-6]. From conductivity measurements of 8 mol% YSZ between 300 and 1000°C, a curved Arrhenius plot is obtained. From this the activation energy for ionic conduction can be determined.

An increase in bulk activation energy with decreasing temperature has been observed by conductivity measurements of both polycrystalline and single crystal YSZ [7,8]. Figure 6.1. illustrates a typical Arrhenius plot of 8 mol% YSZ ($Y_{0.15}Zr_{0.85}O_{1.925}$) and shows a gradual change in the slope in the region of 600°C. At high temperatures the activation energy is lower than at low temperatures.

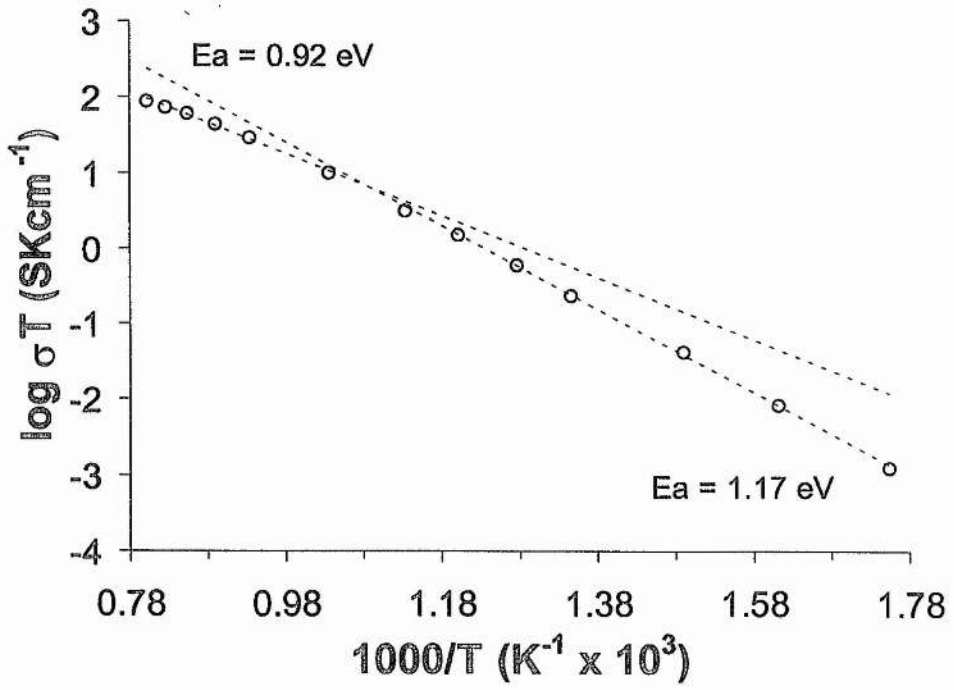

Figure 6.1. Arrhenius plot for Bulk ionic conductivity of 8YSZ.

The low temperature behaviour (below 550°C) has been suggested to arise from the association of Oxygen vacancies and the cations. Two types of association have been proposed [10].

$$Y_{Zr}' + V_o^{\bullet\bullet} \rightarrow (Y_{Zr}' V_o^{\bullet\bullet})^{\bullet}$$

$$\text{and} \quad 2Y_{Zr}' + V_o^{\bullet\bullet} \rightarrow (Y_{Zr}' V_o^{\bullet\bullet} Y_{Zr}')^{x}$$

Nowick et al [11] and Kilner et al [12] have indicated that the charged associate, i.e. $(Y_{Zr}' V_o^{\bullet\bullet})^{\bullet}$, is most likely to form for low concentrations of dopant because the probability of two cations being situated adjacent to one oxygen vacancy is very low. Kilner et al stated that at lower temperatures [12] the bulk activation energy comprised of an oxygen vacancy migration enthalpy (ΔH_m) and an association enthalpy (ΔH_a), corresponding to the enthalpy required for the dissociation of a vacancy-cation associate, i.e.

$$(Y_{Zr}' V_o^{\bullet\bullet})^{\bullet} \rightarrow Y_{Zr}' + V_o^{\bullet\bullet}$$

so that

$$E_a = \Delta H_m + \Delta H_a \quad \text{(low temperature)}$$

At temperatures above ~550°C, all oxygen vacancies are considered to be free i.e. not associated with dopant cations; the bulk activation energy now contains only the migration enthalpy term, so that

$$E_a = \Delta H_m \text{ (high temperature)}$$

The additional association enthalpy, observed at low temperatures for YSZ is typically 0.1-0.3 eV [12]. According to Kilner et al [10] values of 0.1-0.3 eV would produce a change in the bulk activation energy at 700-730°C. Increasing the amount of Yttria dopant produces an increase in the low temperature activation energy [13]. As the high temperature bulk activation energy, ΔH_m, appears to remain constant for increasing Yttria content, the increase in the low temperature activation energy can be attributed to an increase in the association enthalpy, indicating an increase in the number of vacancy-

cation associates. The effect of vacancy-cation complex formation on the conductivity of YSZ at low temperatures has been reviewed in the literature [12,14].

Although it is widely considered that oxygen vacancies form associated complexes with the dopant cation, Y^{3+}, at low temperatures [6, 10, 12, 15-17], an EXAFS study of 10 mol% YSZ by Catlow et al [9] indicated that the Zr^{4+} cation was in 7-fold oxygen co-ordination, with a Zr-O bond length of 2.11Å , which is similar to its environment in monoclinic ZrO_2: 7-fold oxygen co-ordination, with an average Zr-O bond length of 2.16 Å [18,19]. This was confirmed in the study described in Chapter 7, in which the Zr-O bond length was 2.147 Å and the co-ordination number of Zr^{4+} was 6.9. The expected environment of Zr^{4+} in YSZ might be 8-fold oxygen co-ordination with a Zr-O bond length of 2.225 Å. Catlow observed that Y^{3+} had 8-fold co-ordination with a Y-O bond length of 2.28 Å, which compared favourably to the average Y-O distance in Yttria with 8-fold co-ordination, 2.28 Å [20]. In chapter 7 the co-ordination environment of Y^{3+} is found to be greater than 8 and the Y-O distance was 2.309 Å.

The observed co-ordination environments of Zr^{4+} and Y^{3+} can be explained in terms of the position of the oxygen vacancies. Catlow et al stated that the oxygen vacancies must be preferentially sited adjacent to the Zr^{4+} ion and not the Y^{3+} as previously considered. Additionally, computer simulations indicated that vacancy-Zr^{4+} pairs were more energetically favourable than vacancy-Y^{3+} pairs. Within the ZrO_7 polyhedra, displacements of anions in the <100> and <111> directions were determined. The observations of Catlow et al were reiterated in a series of EXAFS studies by Li et al [18, 21, 22], with average Zr-O and Y-O distances of 2.15 Å and 2.33 Å respectively, with Zr^{4+} and Y^{3+} having 7 and 8-fold co-ordination. It would thus seem that at room temperature, Zr^{4+} in cubic YSZ is more stable in 7-fold co-ordination than in 8-fold, just as it is in the monoclinic room temperature form of ZrO_2.

Many structural studies have been made on cubic stabilised Zirconias. Room temperature neutron diffraction experiments on single crystals of YSZ by Steele and Fender [23] and CSZ (Calcia-stabilised Zirconia) by Moringa et al [24] and Cohen et al [25] concluded that oxygen atoms were displaced along the <100> direction by between 0 to 0.07 nm. However, Carter and Roth [26] and Horiuchi et al [27], studying CSZ and

YSZ respectively, reported displacements of 0 to 0.05 nm along the <111> direction. An example of the proposed displacement of oxygen ions in the <100> direction is shown in Figure 6.2. The displacements of anions determined from EXAFS and neutron diffraction studies are associated with a decrease in co-ordination number of the Zr^{4+}/Y^{3+} due to the introduction of an oxygen vacancy; a reduction in co-ordination number requires a decrease in mean bond length, which may be achieved by a displacement of oxygen ions from their ideal fluorite sites.

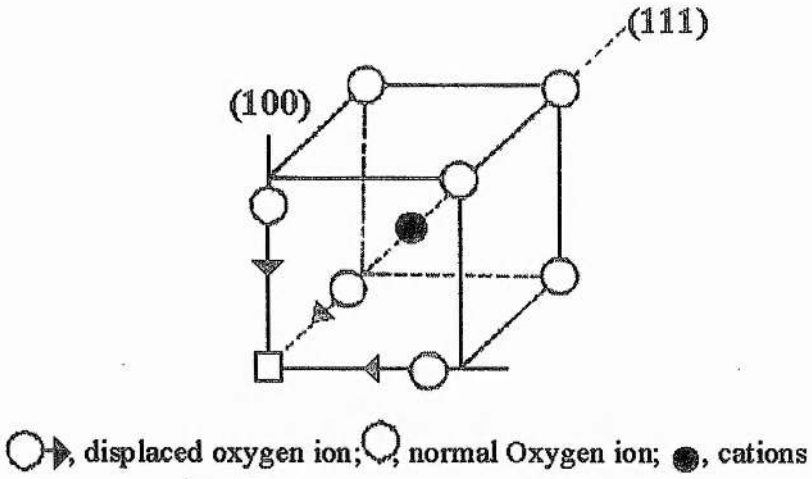

Figure 6.2. Part of the Fluorite structure showing displaced oxygens in the <100> direction around an oxygen vacancy [23].

Diffuse scattering or a modulated diffuse background was a significant feature of the neutron diffraction pattern obtained by Steele and Fender [23] and the displacement of the anions and the possible short range ordering by vacancy association was considered responsible. Similar observations were made by Hull et al [28] from diffuse scattering experiments using YSZ single crystals. They studied several Yttria stabilised Zirconias containing between 9 and 24 mol% Y_2O_3 at room temperature. Two regions of the crystals gave rise to neutron scattering. Firstly, a relatively vacancy-free, tetragonally-distorted fluorite structure, which gave rise to sharp peaks corresponding to reflections such as (112) and (114); the intensity and size decreased with increasing Yttria content and temperature. Secondly, a region where vacancies, vacancy pairs and aggregates of vacancy pairs occurred, producing different satellite peaks. The intensity of the peaks appeared to be independent of Yttria content, but the number of aggregates of vacancy

pairs increased with increasing Yttria content. Increasing the temperature resulted in a decrease in the intensity of the 'fluorite-forbidden' reflections indicating that the vacancies had become mobile.. Further work on YSZ and CSZ [25, 29-31] supports the concept of ordering of vacancy-cation complexes, or clusters, visible as diffuse scattering.

High temperature neutron diffraction experiments on YSZ [32] and CSZ [33] have recently been reported. Both studies examined the change in temperature factors (ITFs) of the cations and anions with increasing temperature. However, only a few data points were obtained in the temperature region 300-1000°C, where the deviation in activation energy of conduction is observed. Martin et al [34], studying CSZ, determined the change in oxygen isotropic temperature factor with temperature, B_{iso} (oxygen), between 25 and 1125°C. The plot of ITF versus temperature showed a deviation in the temperature-dependence of the O ITF at ~1000°C, which is close to the order-disorder transformation in CSZ [35]. Proffen et al [36], again studying CSZ, observed a decrease in the diffuse scattering as this temperature was approached.

The conductivity data obtained for YSZ has indicated a change in the bulk activation energy at ~550°C, due to the association/dissociation of the oxygen vacancy-cation complexes. Recent neutron diffraction work on CSZ and YSZ, previously discussed [30, 34, 36], suggests that a similar order-disorder transition may be observed in neutron diffraction studies of YSZ at 500-600°C. A detailed study on the effect of high temperatures on the diffuse background scattering was made by Irvine et al [37]. They determined that scattering intensities had virtually disappeared at approximately 650°C. The decrease in the modulated diffuse background was also accompanied by a deviation of the anion and cation ITFs and a deviation in thermal expansion coefficient between 600 and 700°C.

This chapter describes a more detailed neutron diffraction study of 8 mol% YSZ in the region of the order-disorder transition than that described by Irvine et al [37]. A much larger number of temperatures were studied in the temperature range 25-900°C. The effect of increasing temperature on the change in diffuse scattering, isotropic

temperature factor and lattice parameter are described and are compared to conductivity values.

6.2. Experimental

Stabilised Zirconias are cubic and diffract strongly but problems with absorption mean that high temperature X-ray diffraction cannot be utilised due to the unsuitable intensities for high temperature resolution work. Powder neutron diffraction data on 8 mol% YSZ were therefore collected on the high intensity, medium resolution diffractometer Polaris at the UK spallation source ISIS at the Rutherford Appleton Laboratory.

The studies were carried out on a large sample (~5g) of 8 mol% YSZ (Tosoh), contained in a Vanadium can, over the temperature range 20-900°C using a Vanadium wound furnace. A thermocouple was attached next to the sample can, ensuring temperature control of ± 1°C. Sixteen measurements were made on heating in order to give suitable data for direct comparison with the known conductivity characteristics. Further analysis focuses on the thermal parameters, looking for an anomaly in the rms displacement in temperature dependence at the transition.

The T.O.F. neutron diffraction experiments were carried out in a high temperature furnace attachment to the Polaris instrument. The experimental set-up was pre-programmed into the control computer. The sample was exposed to the neutron beam at room temperature (20°C) and 300°C for 100 μAhrs, (approximately half an hour). For the remaining temperatures, i.e. 450, 475, 500, 530, 560, 590, 620, 650, 680, 710, 740, 770, 800 and 900°C, the sample was exposed to the neutron beam for 200 μAhrs, (approximately 1 hour).

Data analysis was performed on the in-house software on the ISISE VAX mainframe situated at the Rutherford Appleton Laboratory. Structure refinements were carried out using the Rietveld method with the program TF14LS using data collected in the time-of-flight range 2500-19500 microseconds.

All refinements were carried out in the space group Fm3m using a similar approach to Argyriou et al [32], i.e. the refinements were carried out with the positions of Zr/Y and O fixed; if any displacement of anions or cations existed they would be detected in the form of diffuse scattering or as large values in the Isotropic Temperature Factor. No attempt was made to model any displacement of the anions in either the <111> and/or the <100> direction because this type of study requires the use of single crystals, which allows the measurement of intensities in three dimensions and allows accurate determination of atom displacement. The occupancy of the Oxygen site was determined by allowing the occupancy to refine from the theoretical value for 8YSZ, 0.96295. Background, lattice parameters and isotropic temperature factors for Zr/Y and Oxygen were then refined for all temperatures using the parameters in Table 6.1.

Table 6.1. The initial parameters which were fixed for 8 mol% YSZ ($Zr_{0.8515}Y_{0.1485}O_{1.926}$).

Parameter	Zr (Y)	O
X	0.0	0.25
Y	0.0	0.25
Z	0.0	0.25
Occupancy	0.8515 (0.1485)	0.96296
Scattering lengths [38]	0.7160 (0.7750)	0.5805

6.3. Results and Discussion

Part of the observed and calculated neutron diffraction patterns and their difference profiles observed at room temperature and 900°C are shown in Figures 6.3 and 6.4. At room temperature, additional, diffuse peaks are observed. These peaks do not correspond to expected reflections from the space group Fm3m. As the temperature was increased, the diffuse background eventually decreased until at 650°C it had effectively disappeared. At 900°C, the background appeared virtually flat and the difference profile showed only small deviations in 'allowed reflections'. Similar peaks were observed by Hull et al [28] and were attributed to oxygen displacement from their ideal fluorite sites. Steele et al [39] also observed additional forbidden reflections, satisfactory reflections based on a tetragonal structure could not be achieved. The temperature region where the diffuse peaks are observed corresponds to the region where the activation energy for

conduction is larger. This suggests that above 650°C, when the activation energy could be interpreted as arising solely from the enthalpy of migration , the cubic lattice no longer shows signs of local ordering. Refinements of the collected neutron diffraction patterns gave the data shown in Table 6.2.

Table 6.2. The refined data for 8 mol % Yttria stabilised Zirconia using the space group Fm3m.

T (°C)	Unit Cell (Å)	Y / Zr ITF (Å^2)	O ITF (Å^2)
20	5.1389(2)	0.70(1)	2.13(2)
300	5.1501(3)	0.88(1)	2.40(2)
450	5.1598(3)	1.02(1)	2.63(2)
475	5.1614(3)	1.04(1)	2.66(2)
500	5.1628(3)	1.06(1)	2.68(2)
530	5.1645(3)	1.08(1)	2.72(2)
560	5.1662(3)	1.11(1)	2.76(2)
590	5.1680(3)	1.13(1)	2.79(2)
620	5.1697(3)	1.16(1)	2.84(2)
650	5.1716(3)	1.18(1)	2.87(2)
680	5.1732(3)	1.21(1)	2.91(2)
710	5.1750(3)	1.23(1)	2.94(2)
740	5.1769(3)	1.25(1)	2.99(2)
770	5.1786(3)	1.29(1)	3.04(2)
800	5.1805(3)	1.31(1)	3.08(2)
900	5.1864(3)	1.39(1)	3.22(2)

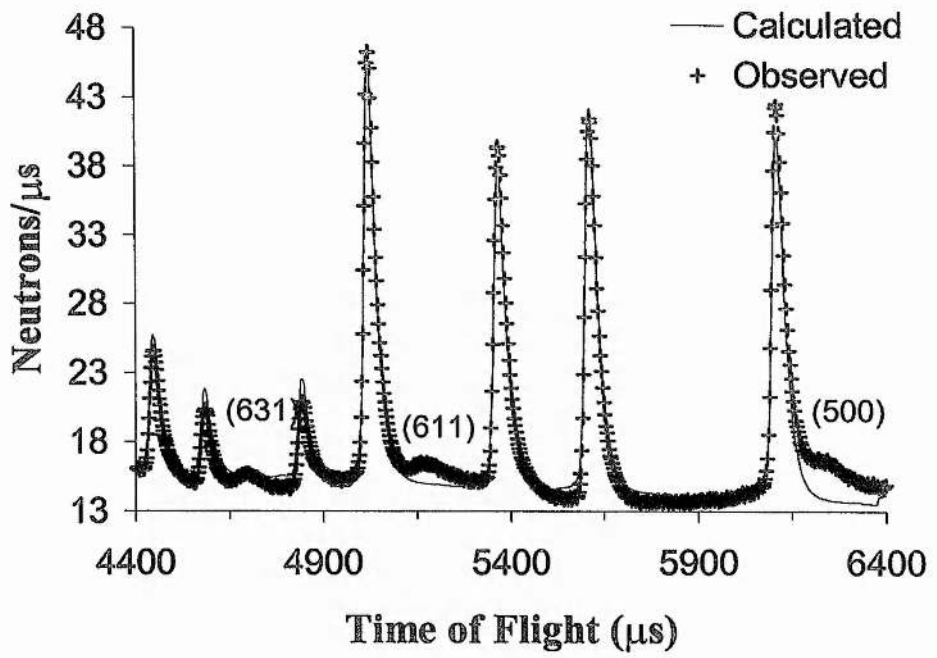

Figure 6.3. The calculated and observed neutron diffraction profiles for 8 mol% YSZ at 20°C. The fluorite forbidden reflections (631), (611) and (500) are indicated at the broad peaks caused by diffuse scattering.

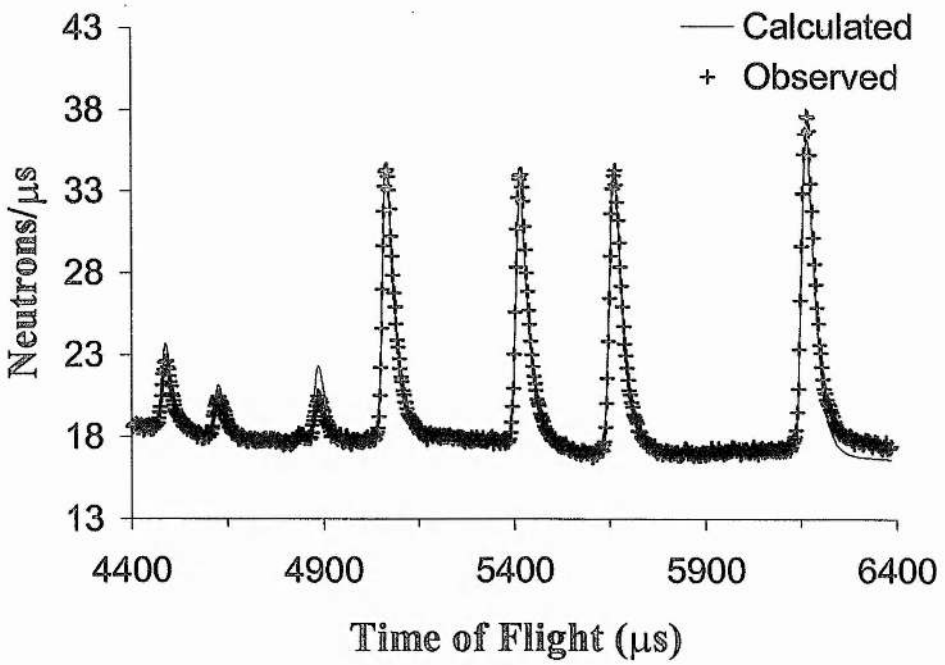

Figure 6.4. The calculated and observed neutron diffraction profiles for 8YSZ at 900°C. The fluorite forbidden reflections are no longer present.

6.3.1. The Oxygen Isotropic Temperature Factor

Figure 6.5 shows that there is a deviation from linearity in the plot of Oxygen isotropic temperature factor versus temperature. The six data points in the temperature region 723K to 863K (450°C to 590°C) form a straight line which can be described by the linear expression $y = (1.12 \times 10^{-3})x + 1.82$, i.e. the isotropic temperature factor for Oxygen at zero Kelvin is 1.82. However this is assuming that the relationship between the Oxygen ITF and temperature remains linear with decreasing temperature. Inclusion of the higher temperature data points at 893K and 923K (620°C and 650°C) in the straight line reduces the linear regression fit from $R^2 = 0.9998$ to $R^2 = 0.9951$ and 0.9968 respectively. This indicates that above 863K (590°C) the data deviates from linearity due to a change in the slope occurring. The six data points at higher temperatures, between 953K and 1173K (680°C and 900°C) also form a straight line which is described by the equation $y = (1.42 \times 10^{-3})x + 1.55$, i.e. the isotropic temperature factor extrapolated back to 0K is 1.55. Addition of a seventh data point at 650°C has no effect on the linear regression. However, addition of the data point at 620°C reduces the fit from $R^2 = 0.9993$ to 0.9976 indicating that there is deviation from linearity. Thus the region of curvature between the low temperature ordered state and the high temperature disordered state lies between 863K and 923K (590 and 650°C). The transition temperature determined from the intercept of the two linear fits is at 901.5K (628.5°C) which lies almost in the centre of the temperature range determined using the regression fit factor R^2.

Using the regression fit as a guide to the transition temperature, this study confirms the work of Irvine et al who reported that the order-disorder transition occurred at *ca.* 650°C. This study, however, shows that the transition is even more sharp than they described, i.e. the transition occurs over a region less than 60°C rather than over a region less than 100°C.

The observed linear dependence of the temperature factor upon temperature is in accord with a simple Debye-type model, although strictly this model is only applicable to monatomic solids with the atoms centred on their ideal crystallographic sites. An approximation developed by Martin et al [40] for YSZ is to split the temperature factor

into two components, giving a static term which is independent of temperature and a temperature dependent term which varies in accord with the Debye approximation, i.e.

$$B_k^{exp} = B_k^{static} + B_k^{thermal}$$

The observed dependence of the ITF on temperature factor can be interpreted using this model. The two linear equations determined for the high and low temperature regions have different intercepts at 0K. The ITF at 0K extrapolated from the low temperature data includes the ITF due to thermal vibrations and due to the static displacement of the anions from their ideal crystallographic sites. The ITF extrapolated from the high temperature data to 0K contains only the contribution from the thermal vibrations of the oxygen anions. Thus, the static displacement of the oxygens can be determined by

$$B_k^{static} = B_k^{static + thermal} - B_k^{thermal}$$

and is thus 0.27 $Å^2$ at 0K.

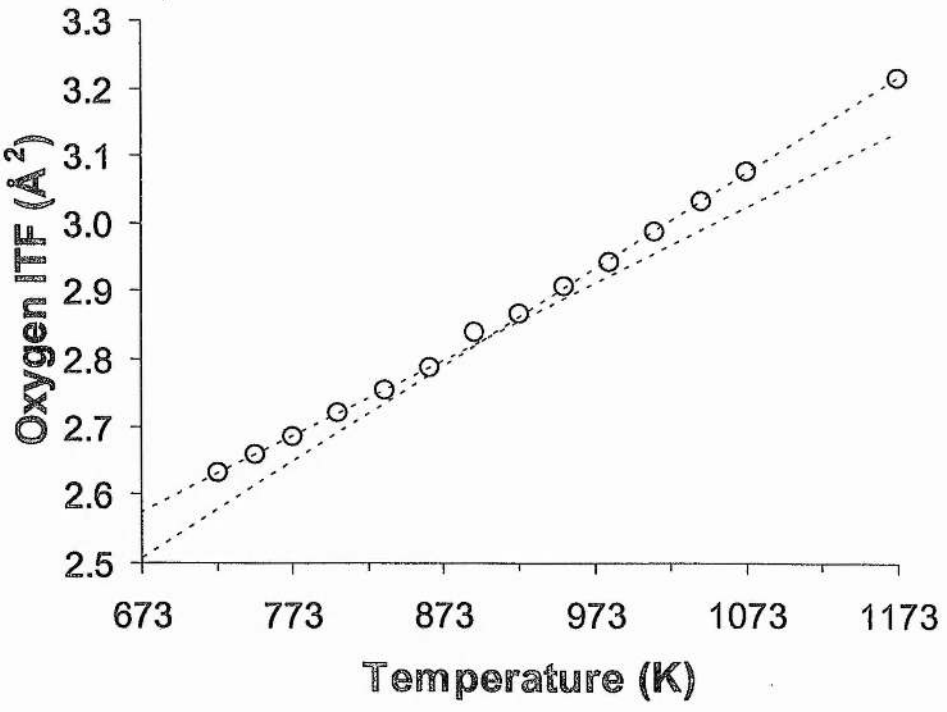

Figure 6.5. Plot of Oxygen ITF against temperature for 8 mol% YSZ (errors are smaller than points).

The low temperature behaviour of the Oxygen ITF can be explained in terms of ordering of oxygen vacancy/dopant cation clusters to form microdomains, which are evidenced by the presence of diffuse scattering peaks. At high temperature, the association of vacancies with defects breaks down, or at least becomes randomised, allowing vacancies to move more freely as indicated by the decrease in activation energy for conduction, (as shown by the conductivity plot in Figure 6.1). The static contribution to the total ITF is in reasonable accord with the value obtained by Irvine et al [37].

6.3.2. The Cation (Zr/Y) Isotropic Temperature Factor

Figure 6.6. shows that there is no deviation in the cation ITF with increasing temperature. The data fits a straight line, $y = (8.30 \times 10^{-4})x + 0.41$, i.e. the average static displacement of the cations at 0K is 0.41 $Å^2$. It was not possible to fit two intercepting lines to this data, which would have been indicative of a transition occurring, as was done by Irvine et al who suggested that the cations relaxed back to their ideal fluorite positions at a higher temperature than the oxygens, after the oxygens had disordered [37].

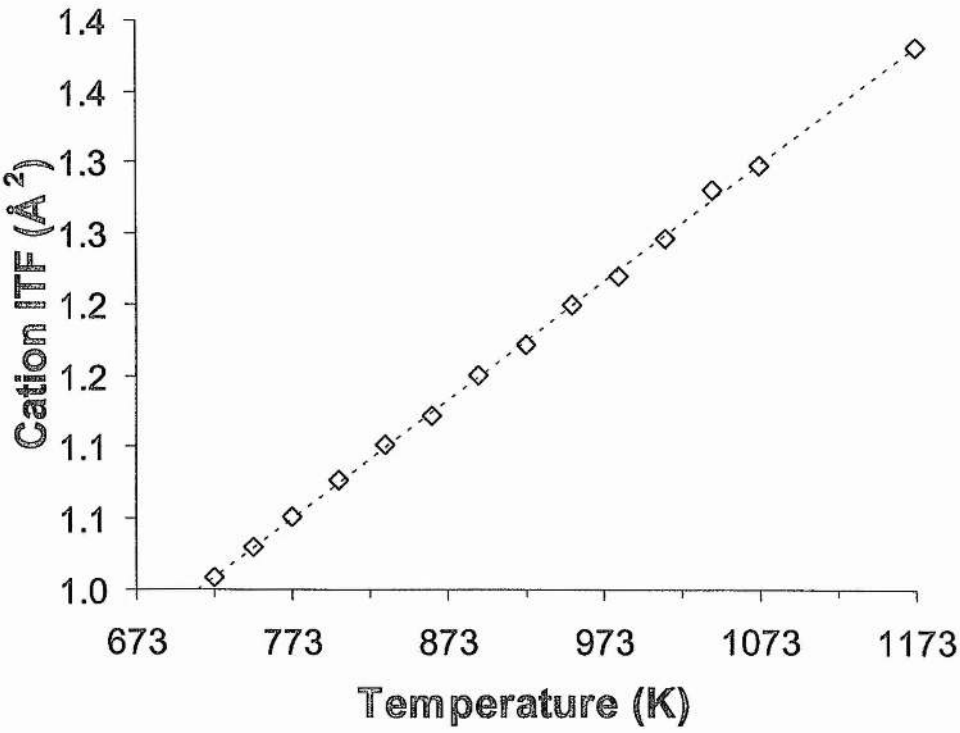

Figure 6.6. Plot of Zr/Y ITF against temperature for 8 mol% YSZ.

The plots of Oxygen and Zirconium/Yttrium ITFs are plotted together for comparison in Figure 6.7. The cation ITF is significantly lower than the Oxygen ITF, which is expected due to the high mobility of Oxygen in the fluorite structure.

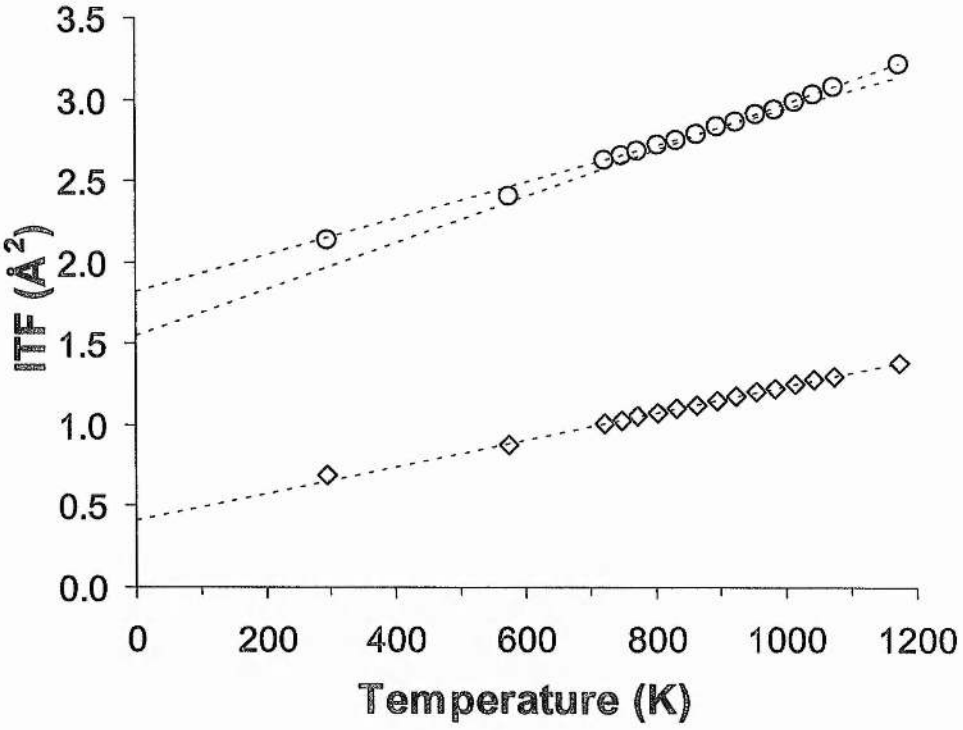

Figure 6.7. Comparison of Y/Zr ITF and O ITF against temperature for 8 mol% YSZ.

6.3.3. Thermal Expansion Coefficient

The unit cell parameter of 8YSZ is plotted against temperature in Figure 6.8. The plot clearly shows a subtle deviation from linearity in the region 863K-973K (590-700°C). This corresponds to a discontinuity in the thermal expansion coefficient, which is indicative of a second-order transition. In the low temperature region, below 863K (590°C), the cubic unit cell parameter increases from 5.1389 Å to 5.1680 Å for an increase in temperature from 20°C to 590°C. The linear coefficient of thermal expansion is calculated by comparing the change in length of a material with the change in temperature. Thus for 8 mol% YSZ which has a cubic crystal structure, the thermal expansion is isotropic and is represented by the equation:

$$\alpha_l = (T_f - T_o) \times (l_o / (l_f - l_o)$$

where α_l is the linear thermal expansion coefficient, T_f is the final temperature, T_o is the initial temperature and l_f and l_o are the final and initial unit cell parameters respectively.

The linear thermal expansion coefficient for the low temperature region, 273K to 863K (20°C to 590°C), is thus 9.935 x 10^{-6} K^{-1}. In the high temperature region, between 923K and 1173K (650°C and 900°C), the unit cell parameter increases from 5.1716 Å to 5.1864 Å, giving a thermal expansion coefficient of 11.447 x 10^{-6} K^{-1} ($°C^{-1}$). The high temperature and low temperature linear thermal expansion coefficients thus differ by 1.512 x 10^{6} K^{-1} ($°C^{-1}$), i.e. a difference of 15 %.

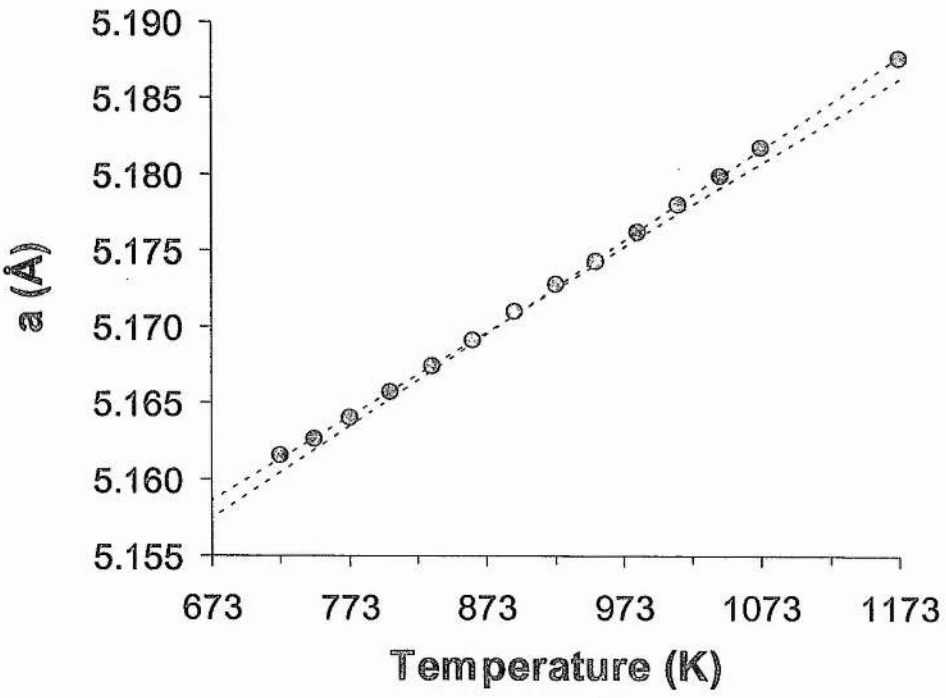

Figure 6.8. Plot of unit cell parameter, a, against temperature for 8 mol% YSZ.

The relationship between the unit cell parameter and temperature can be described by a second order polynomial to a high degree of accuracy because of the much more subtle change in unit cell parameter compared to the Oxygen isotropic temperature factor. However, using the Oxygen ITF versus temperature plot as a reference, two straight lines

can be applied to the unit cell versus temperature data, which show that the discontinuity in the unit cell parameter is centred around 894K (621°C).

6.3.4. Residual Factors

The decrease in the intensity of the fluorite-forbidden reflections with increasing temperature was also illustrated by a decrease in the refined residual factors as shown in Figure 6.9. It is more usual to see a small increase in R_{wp} with increasing temperature because the background increases. In the case of 8 mol% YSZ, the decrease in R_{wp} with increasing temperature is due to the improvement in the refinement due to the disappearance of the diffuse scattering peaks. The decrease in the residuals appears to be curved. However, upon closer inspection, particularly of the weighted profile R factor, there is a very clear 'step' between the data at 893K and 923K (620°C and 650°C), Figure 6.10. This step is even more obvious in the plot of χ^2 versus temperature, Figure 6.11, where $\chi^2 = (R_{wp} / R_{expected})^2$.

For a perfect refinement, the weighted and the expected R factors should be identical and hence a value of 1 would be obtained for χ^2. However, a number of things can affect the value of χ^2, such as the background associated with the Vanadium furnace, and hence the value should not be used solely on it's own as a guide to the quality of the refinement. The R factors obtained for the refinement are the best guide to the quality of the fitted profile. R may be artificially high for a number of reasons such as short counting times (this will lead to a systematic error in the background). Experiments performed in a specialist environment, such as a furnace in this case, can lead to a contribution to the background of the collected profile and hence will lead to a poorer than expected R factor. A value of 1% would normally be considered very good, however this is rarely seen. As a rule of thumb a value less than 5% is considered a very good fit.

All of the refinements carried out in this study had R factors well within 5%. All of the R factors obtained from the data refinements in this study are listed together in Table 6.2.

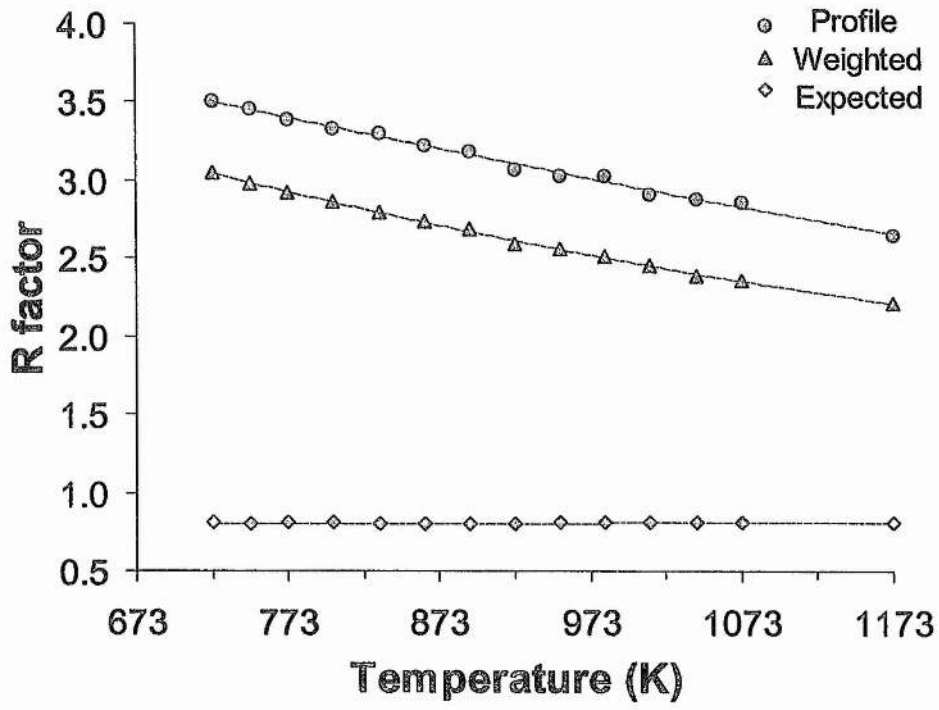

Figure 6.9. Plot of weighted profile Residual R_{wp} versus temperature for 8mol% YSZ.

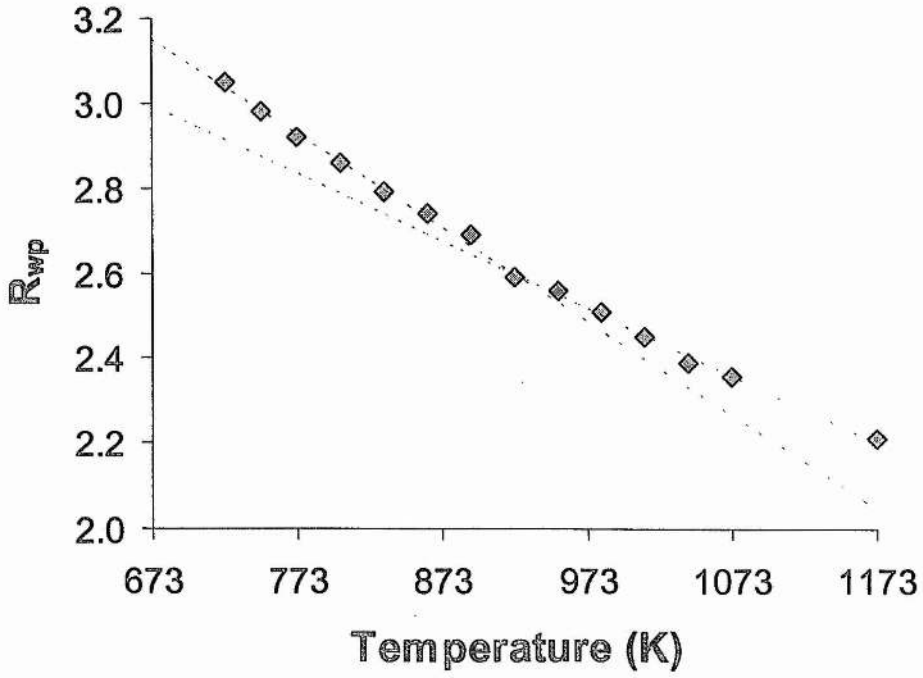

Figure 6.10. Plot of weighted profile Residual R_{wp} versus temperature for 8mol% YSZ.

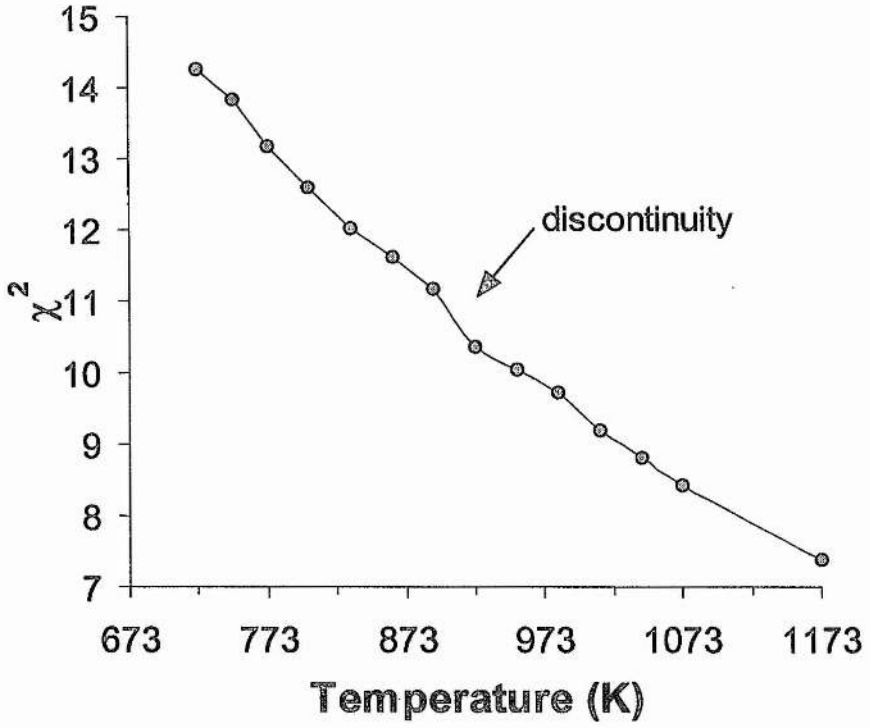

Figure 6.11. Plot of χ^2 versus temperature for 8 mol% YSZ.

Table 6.2. The Residuals for the refined high temperature data of 8 mol% YSZ.

T (°C)	$R_{profile}$	R_{wp}	$R_{expected}$	χ^2
20	4.30	4.10	0.59	48.7212
300	3.95	3.53	1.13	9.6772
450	3.50	3.05	0.81	14.2471
475	3.46	2.98	0.80	13.8212
500	3.39	2.92	0.81	13.1756
530	3.33	2.86	0.81	12.5963
560	3.30	2.79	0.80	12.0203
590	3.22	2.74	0.80	11.6173
620	3.18	2.69	0.80	11.1664
650	3.07	2.59	0.80	10.3558
680	3.03	2.56	0.81	10.0485
710	3.03	2.51	0.81	9.7160
740	2.91	2.45	0.81	9.1919
770	2.88	2.39	0.81	8.7987
800	2.86	2.36	0.81	8.4272
900	2.65	2.21	0.81	7.3852

6.3.5. Comparison with other studies of polycrystalline 8YSZ

Comparison of the ITF and unit cell parameter data obtained in this study with the previous study by Irvine et al shows that the values obtained in this study are slightly higher. Figure 6.12 compares the Oxygen ITF and the Zr/Y ITF for both studies. The discontinuity in the Oxygen ITF versus temperature plots occur at the same temperature in both plots and the two data sets do not converge at any point. The data obtained from this study has an Oxygen ITF of 1.82 $Å^2$ at 0K, compared to an Oxygen ITF of 1.70 $Å^2$ determined by Irvine et al. The Zr/Y ITF plots are linear and are essentially parallel for both studies, intersecting the axis at different points. The plot of unit cell parameter versus temperature is different from the previous study, Figure 6.13. Extrapolation of the unit cell data to 0K results in a difference in unit cell parameter of 0.0022 Å or 0.04% at 0K. The weighted profile R factors in this study are slightly lower than those found in the previous study, Figure 6.14.

It is unlikely that the differences were due to differences in the starting powders or sintering regime because both samples were prepared from the same batch of powder and both samples were sintered for several hours at 1500°C and cooled at 10°C/min from the sintering temperature. One would expect that if one sample had been cooled down more slowly than the other, microdomain formation would have occurred more readily than in the more quickly cooled sample. This would give rise to greater displacements in the cation and anion positions from the ideal fluorite sites (and thus larger ITF values and larger R factors) for the slow cooled sample, but would not account for differences in unit cell parameter.

Errors in the thermocouple readings may be considered as a possible source of error because the plots of Zr/Y ITF versus temperature for both studies are essentially parallel, with the difference in intercept between the two data sets being 0.042 $Å^2$.

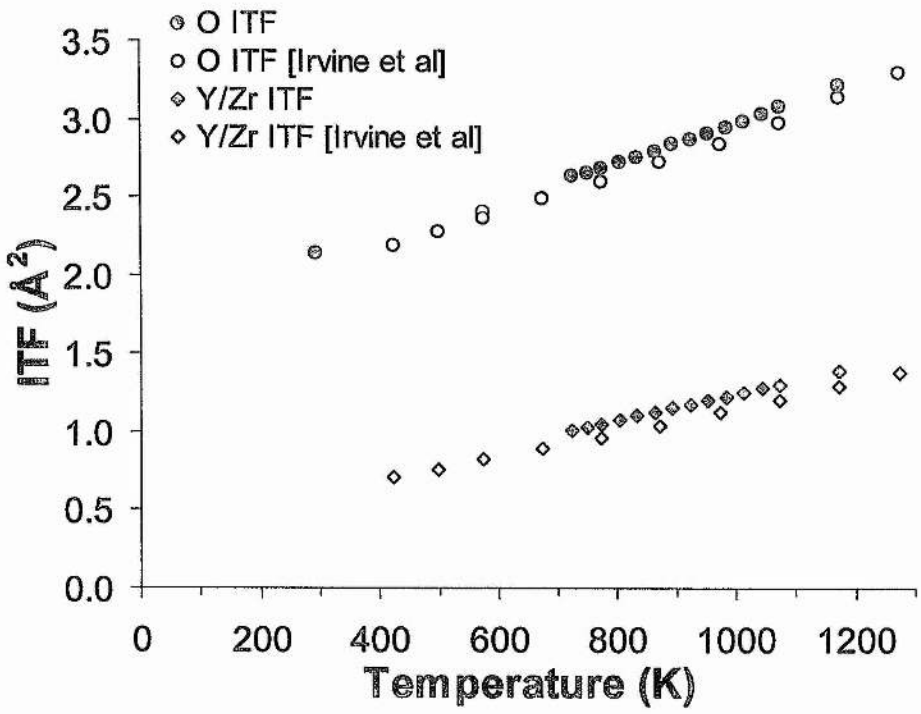

Figure 6.12. Comparison of the Oxygen and Zr/Y Isotropic Temperature Factors for 8YSZ, determined in this study and the previous study by Irvine et al [37].

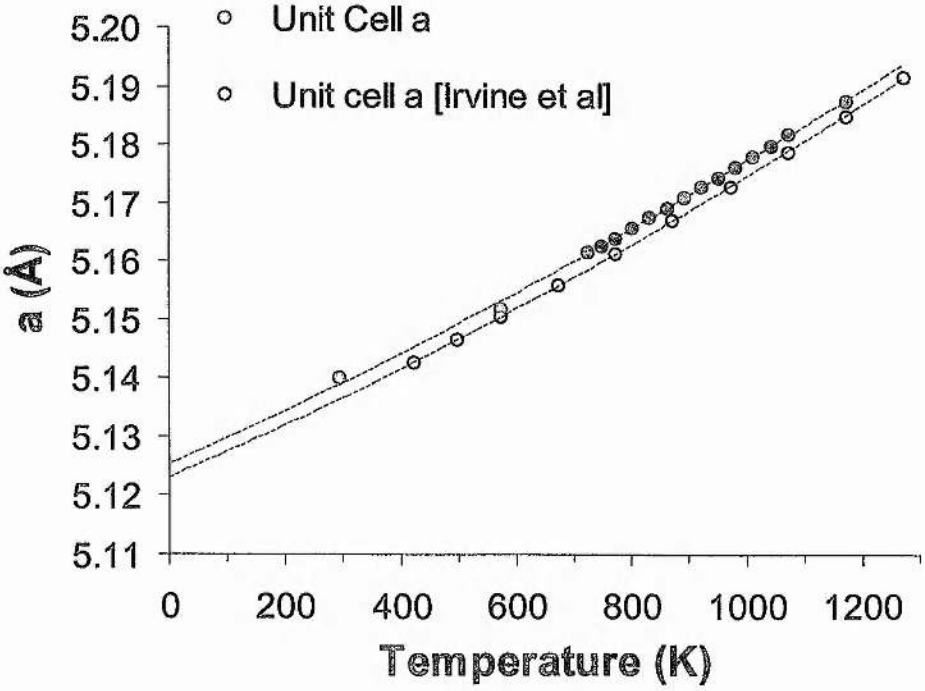

Figure 6.13. Comparison of the Unit Cell Parameter for 8 mol% YSZ, determined in this study and in the previous study by Irvine et al [37].

Another quite likely explanation for the differences in the absolute values of the obtained parameters in this study and the previous study is that the furnace alignment was slightly different in each experiment.

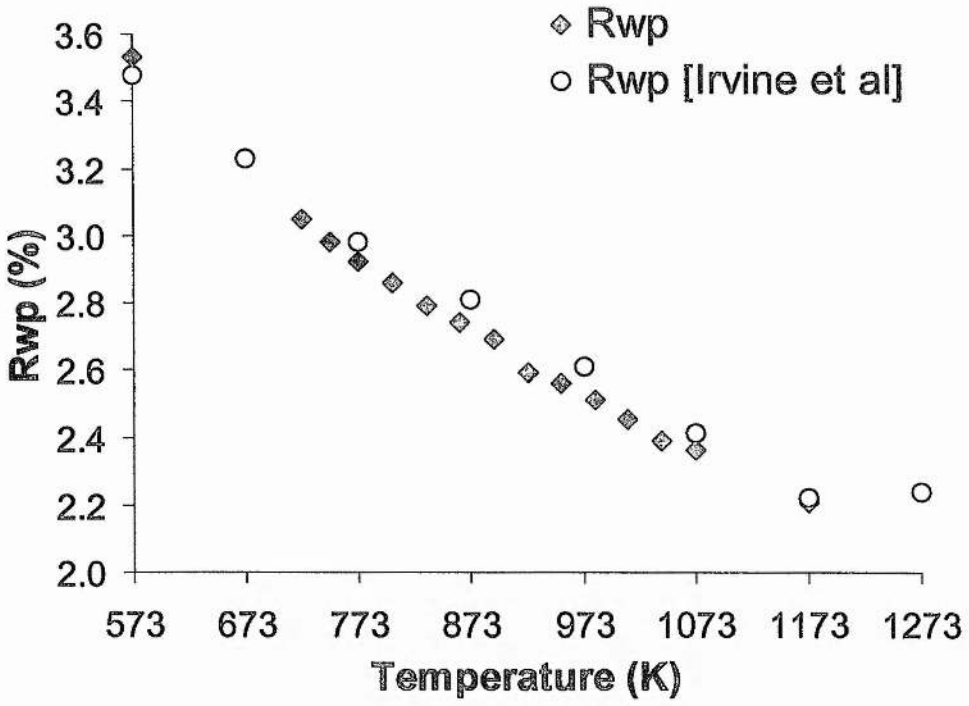

Figure 6.14. Comparison of R_{wp} for this study and the previous study by Irvine et al [37].

Another study carried out recently set out to determine if the low temperature ITF data , i.e. the data between 293 and 863K, could reliably be extrapolated to 0K to give a good estimate of the static displacement of the anions at 0K [41]. The study was carried out in the temperature range 4-500K and the data obtained correlates excellently with that of Irvine et al [37], Figure 6.15.

The low temperature study (<500K) showed that there is a deviation from linearity in both the cation and anion ITFs at very low temperatures. This was attributed to the persistence of thermal vibrations to very low temperatures, i.e. the zero-point energy of the anions is not zero. This zero-point state can be pictured as one in which the ions fluctuate incessantly around their equilibrium positions.Å

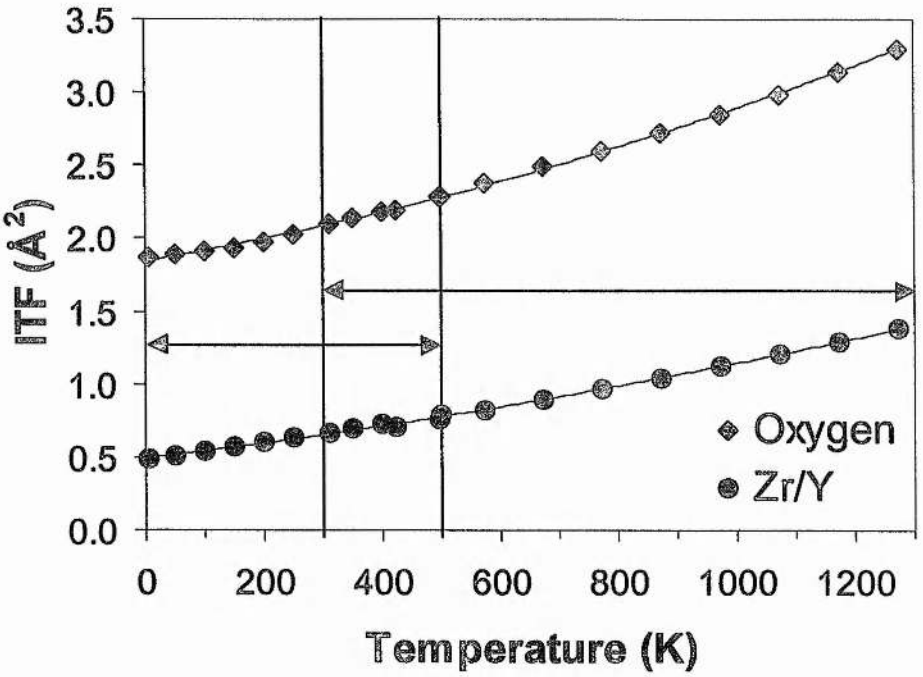

Figure 6.15. Combination of Oxygen and cation ITF data for 8mol% YSZ reported by Irvine et al [37, 41].

6.3.6. Comparison of Oxygen and Zr/Y ITF with Y_2O_3 content.

As the amount of stabilising Y_2O_3 dopant is increased, the number of oxygen vacancies increases and thus the average co-ordination number of the cations decreases. Microdomain formation is expected to increase with increased Yttria content due to greater lattice distortions associated with the Zirconium - Oxygen vacancy complexes. The increase in distortions in the local structure with increasing Yttria is very clear in the plots of Oxygen ITF and cation ITF versus temperature, Figures 6.15 and 6.16. The difference between the ITFs for the 8 and 11 mol% Y_2O_3 stabilised Zirconias is small but there is a very large difference between those compositions and the highly defective composition $Zr_{0.5}Y_{0.5}O_{1.75}$, indicating that there are large microdomains present in the sample which has an average long range fluorite structure.

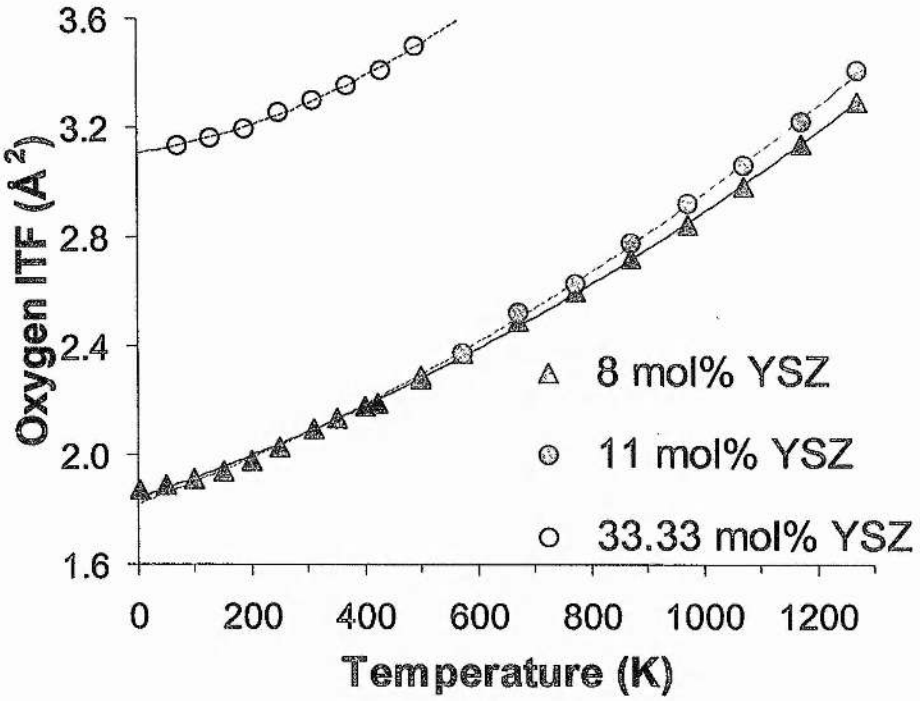

Figure 6.16. Oxygen ITF versus Temperature for 8, 11 and 33.33 mol% YSZ [37, 41].

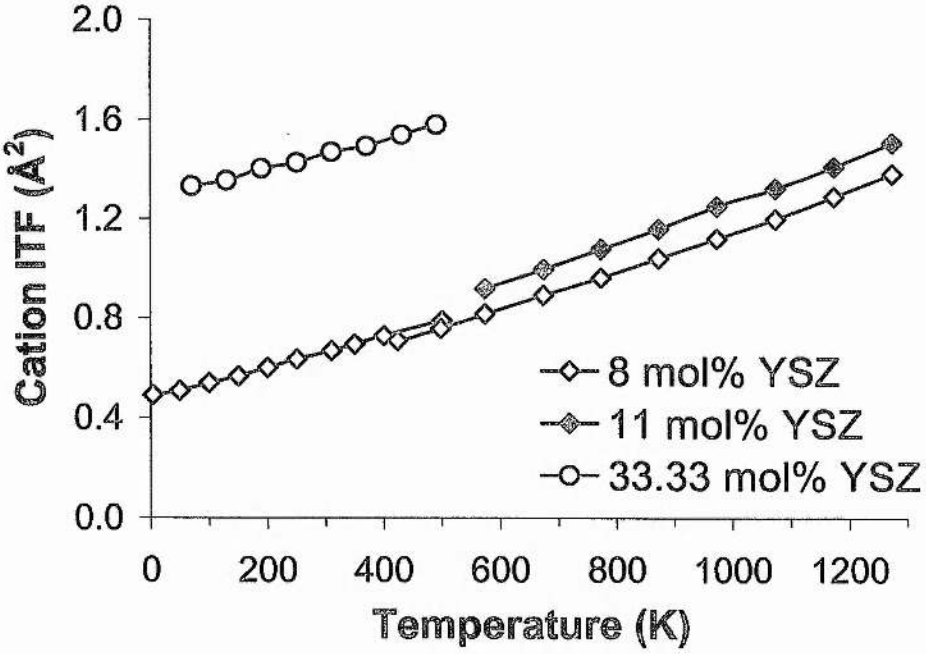

Figure 6.17. Zr/Y ITF versus Temperature for 8, 11 and 33.33 mol% YSZ [37, 41].

6.3.7. The Relationship between Conductivity and Structure

As described at the beginning of this chapter, there is a decrease in the activation energy for conduction of 8YSZ in the region of 650°C. The activation energy decreases from 1.17eV at low temperatures to 0.92eV at high temperatures, indicating that the oxygen ions have overcome the activation enthalpy associated with the cation-vacancy complexes which form at low temperatures and thus become mobile. The microdomains which form due to localised ordering on the nanometer scale have a tetragonally distorted structure compared to the average cubic structure which exists on the macroscale. The Oxygen ITF clearly shows an increase in the thermal contribution to the total ITF compared to the low temperature ITF. This relates to the oxygen ions breaking free from the Zirconium ions, which as described earlier, prefer 7-fold oxygen co-ordination. As the oxygens are no longer associated with any of the cations the randomisation of the oxygens results in the effective loss of local distortion and the loss of the diffuse scattering associated with the microdomains.

Upon increasing the Yttria content of the stabilised Zirconia, there is a transition form a low defect to a concentrated defect region. This transition appears to occur at around 20 mol% Y_2O_3 (33.33 atom% Y^{3+}), Figure 6.17. The conductivity rapidly decreases by 2 orders of magnitude from its maximum value of 10 Sm^{-1} to 0.1 Sm^{-1} for 8 and 20 mol% Y_2O_3 respectively. The conductivity continues to decrease with further Y_2O_3 addition. The activation energy follows a similar trend in that it reaches a maximum value above approximately 20 mol% Y_2O_3 . This indicates that the microdomains are so large above this level of stabilising dopant that the conductivity is occurring through the microdomains rather than the cubic fluorite matrix.

The relationship between the ITFs at room temperature and the high temperature conductivity are plotted in Figure 6.18. for 8, 11 and 33.33 mol% YSZ. The increase in both the Zr/Y and Oxygen ITFs with Y_2O_3 content are essentially linear, despite the discontinuity in the conductivity plot.

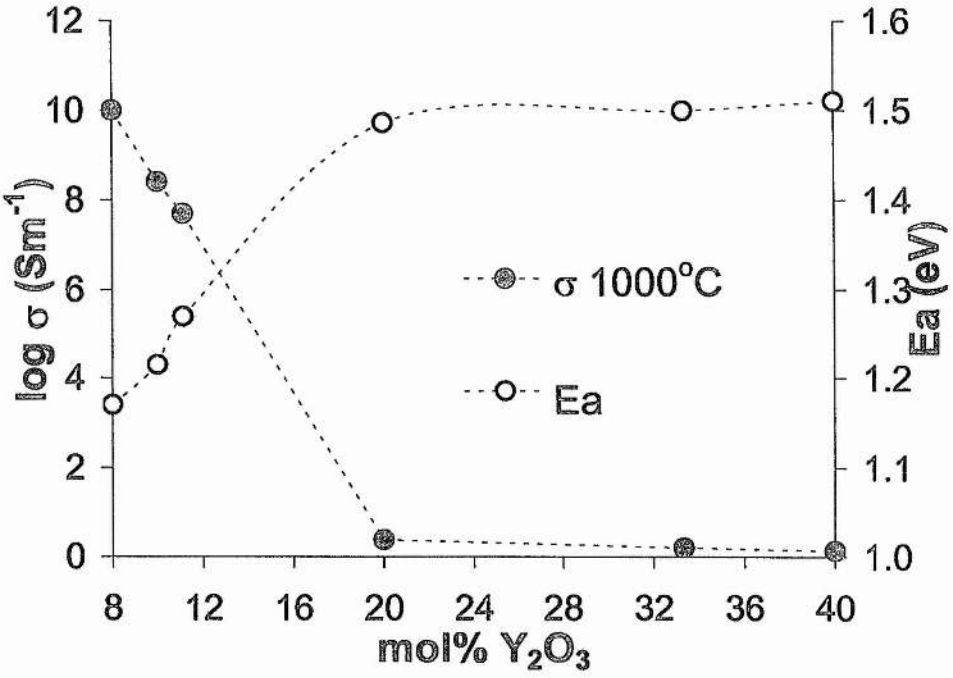

Figure 6.17. Trend in Ea and Conductivity at 1000°C versus Y_2O_3 content.

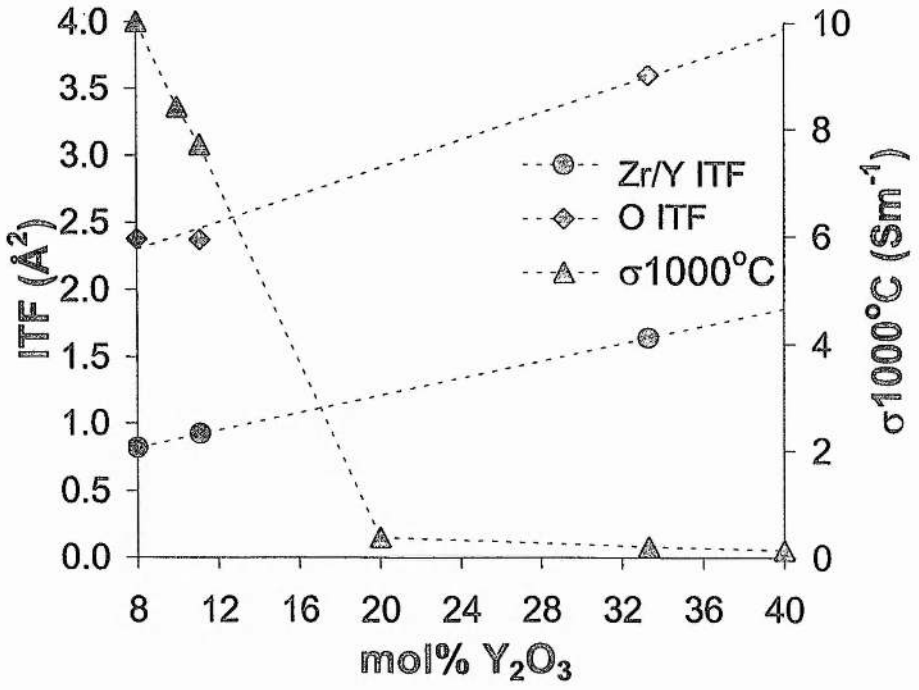

Figure 6.18. Comparison of ITFs derived by Irvine et al [37, 41] at room temperature with high temperature conductivity in 8, 11 and 33.33 mol% YSZ.

6.4. Conclusions

Structural studies link the decrease in activation energy for conduction at 650°C in 8 mol% Yttria-stabilised Zirconia to an order-disorder phenomenon in the lattice. In a lattice where these defects are ordered into microdomains the activation energy will be higher than in a lattice where the defect clusters are randomly arranged. The simplest explanation for the decrease in activation energy at 650°C would seem to be that disordering of the lattice facilitates ionic motion by reducing activation barriers. Higher levels of stabilising dopant cause larger displacements in both the anion and cation positions from the ideal fluorite positions due to the creation of distorted subcells containing ordered anions, resulting in larger ITF values for higher levels of dopant. A deviation in thermal expansion coefficient between 600 and 700°C suggested a transition which is second order in nature.

6.5. References

[1] S.P.S. Badwal, Solid State Ionics 52 (1992) 23-32

[2] J.F. Baumard and P. Abelard, in: Advances in Ceramics, Vol. 12, eds, N. Claussen, M. Rühle and A.H. Heuer (The American Ceramic Society, Columbus, OH, 1984) 555-571

[3] S. Ikeda, O. Sakurai, K./ Uematsu, N. Mizutani and M. Kato, J. Mat. Sci. 20[12] (1985) 4593-4600

[4] T. Takahashi, in: Physics of Electrolytes, Vol. 2, ed. J. Hladik (Academic Press, New York 1972 Chapter 4) 989-1046

[5] R.M. Dell and A. Hooper, in Solid Electrolytes, eds. P. Hagenmuller and W. van Gool (Academic Press, New York 1976) 395-412

[6] D.K. Honke, Solid State Ionics 5 (1981) 531-534

[7] S.P.S. Badwal, J. Mat.Sci. 19[6] (1984) 1767-1776

[8] J.E. Bauerle and J. Hrizo, J. Phys. Chem. Solids 30 (1969) 565-570

[9] C.R.A. Catlow, A.V. Chadwick, G.N. Greaves and L.M. Moroney, J. Am. Ceram. Soc., 69[3] (1986) 272-77

[10] J. A. Kilner and C. D. Waters, Solid State Ionics 6 (1982) 253-259

[11] A.S. Nowick and D.S. Park, in: Superionic Conductors, eds. G. Mahan and W. Roth (Plenum Press, New York 1976) 395-412

[12] J.A. Kilner and B.C.H. Steele, in : Non-stoichiometric Oxides, ed. O.T. S rensen (Academic Press, New York 1981) 233-269

[13] A. Ioffe, M. V. Inozemtsev, A. S. Lipilin, M. V. Perfilev and S. V. Karpachov, Phys. Status Solidi (A) 30 (1975) 87-95

[14] B.C.H. Steele, in: High Conductivity Solid Ionic Conductors, ed. T. Takahashi (World Scientific Publishing Co. London 1989) 402-447

[15] M. Weller and H. Schubert, Solid State Ionics, Proc. A2 Int. Conf. Adv. Mater. 1991 (Pub. 1992) eds. M. Balkanski, T. Takahashi and H. Tuller (North-Holland) Amsterdam, Neth.) 569-574

[16] C. R. A. Catlow, Solid State Ionics 12 (1984) 67-73

[17] J. A. Kilner and R.J. Brook, Solid state Ionics 6 (1982) 237-252

[18] P. Li, I-W. Chen and J. E. Penner-Hahn, Phys. Rev. B. 48[14] (1993) 10074-10081

[19] D.K. Smith and H. W. Newkirk, Acta Cryst. B36 (1965) 3209-3211

[20] M. Faucher and J. Pannetier, Acta Cryst. B36 (1965) 3209-3211

[21] P. Li, I-W. Chen and J. E. Penner-Hahn, J. Am. Ceram. Soc. 77[1] (1994) 118-128

[22] P. Li, I-W. Chen and J. E. Penner-Hahn, J. Am. Ceram. Soc. 77[5] (1994) 1289-1295

[23] D. Steele and B. E. F. Fender, J. Phys. C. Solid State Phys. Vol. 7 (1974) 1-11

[24] M. Moringa J. B. Cohen and J. Faber Jr., Acta Cryst. A35 (1979) 789-795

[25] J. B. Cohen, M. Moringa and J. Faber Jr., Solid State Ionics 3/4 (1981) 61-63

[26] R. E. Carter and W. L. Roth, in: Proc. Electromotive Force Measurements in High Temperature Systems, ed. C. B. Alcock (London Institution of Mining and Metallurgy, 1963) 125-144

[27] H. Horiuchi, A. J. Schultz, P. C. W. Leung and J. M. Williams, Acta Cryst. B40 (1984) 367-372

[28] S. Hull, T. W. D. Farley, M. A. Hackett, W. Hayes, R. Osborn, N. H. Anderson, K. Clauseen, M. T. Hutchings and W.G. Stirling, Solid State Ionics 28-30 (1988) 488-492

[29] B. Hudson and P. T. Moseley, J. Solid State Chem. 19[4] (1976) 383-389

[30] N. H. Anderson, K. Claussen, M. A. Hackett, W. Hayes, M. T. Hutchings and J. E. MacDonald and R. Osborn, in: Proc. 6th Risø Int. Symp. on Metallurgy and Materials Science, eds. F. W. Poulsen et al (London Institution of Mining and Metallurgy, 1985) 279-284

[31] R. Osborn, N. H. Anderson, K. Claussen, M. A. Hackett, W. Hayes, M. T. Huthchings and J. E. MacDonald, Mater. Sci. Forum 7 (1985) 55-62

[32] D. N. Argyriou, J. Appl. Cryst. 27 (1994) 155-158

[33] U. Martin, H. Boysen and F. Frey, D. A. Keen and C. M. E. Zeyen, Acta Cryst. B49 (1993) 605-610

[34] U. Martin, H. Boysen and F. Frey, Acta Cryst. A46 (1990) 799-809

[35] J. B. Cohen, M. Moringa and J. Faber Jr., Solid State Ionics 3/4 (1981) 61-63

[36] T. Proffen, R. B. Neder, F. Frey, D. A. Keen and C. M. E. Zeyen, Acta Cryst. B49 (1993) 650-610

[37] I. R. Gibson and J. T. S. Irvine, J. Mater. Chem., 6(5) (1996) 895-898

[38] V. F. Sears, Neutron News 3[3] (1992) 26-37

[39] D. Steele and B.E.F. Fender, J. Phys. C., Solid State Phys. Vol. 7 (1974) 1-11

[40] U. Martin, H. Boysen and F. Frey, Acta Crystallogr., Sect. B, 1993, 49, 403

[41] D. P. Fagg and J. T. S. Irvine, ISIS Experimental Report 1998, RB 9333

CHAPTER 7

EXAFS Spectroscopy Studies of Cation Co-ordination Environments in 8YSZ

7.1. Introduction

As was described in Chapter 1, electroneutrality is preserved in Y_2O_3 doped ZrO_2 by the creation of one anion vacancy in the cubic lattice for every pair of Y^{3+} dopant ions. Charge considerations suggest that the Y cation is the most likely nearest neighbour of oxygen vacancies. However, the use of extended X-ray absorption fine structure (EXAFS) spectroscopy enables the study of the immediate structural environment of the Y^{3+} and Zr^{4+} and hence can be used to locate which cation the anion vacancies are sited adjacent to. The ability of EXAFS spectroscopy to yield local structural information has been reviewed previously [1,2].

Several XAS studies have already been reported for this system, however there has been disagreement among investigators on the location of the oxygen vacancies. Goldman et al [3], Tuilier et al [4], Morikawa et al [5], and Shen et al [6] concluded that oxygen vacancies were associated with the aliovalent dopants. Catlow et al [7], Komyoji et al [8], and Veal et al [9] thought that the oxygen vacancies were removed from the stabilising dopant and most likely incorporated into the Zr-O shell. Catlow studied the local structural environment of 18 wt% Y_2O_3 stabilised ZrO_2 between -120°C and 770°C [7]. They reported that the cation-oxygen distances measured in the YSZ reflected those of the parent oxides, with the average Zr-O bond length 0.017 nm shorter than the average Y-O bond length. They found that the spread in the Zr-nearest neighbour and Zr-next-nearest-neighbour distances was considerably larger than observed for Y^{3+}. They attributed this to the anion vacancies being preferentially sited adjacent to the smaller Zr^{4+} cation which, with ensuing relaxations, permits a closer contact between Zr^{4+} and its oxygen neighbours. Thus in their study the structural environment was found to resemble that of 7-co-ordinate Zr^{4+} in monoclinic Zirconia. They also reported that increasing the temperature of the sample resulted in the local structural environments of the Y^{3+} and Zr^{4+} becoming more alike, suggesting that the anion vacancies become randomly distributed in the cubic fluorite matrix.

Local structures around Zr^{4+} ions were obtained for four Zirconia polymorphs by Li et al [10]. Their fitting results for Zr in Monoclinic, Tetragonal and stabilised Zirconia are shown in Table 7.1. The configuration of oxygen vacancies and the static

and thermal distortion of bonding in these polymorphs have also been elucidated [11, 12], e.g. the static distortion for the Zr-cation and Y-cation in 20 mol% YSZ are 0.0081 $Å^2$ and 0.0057 $Å^2$ respectively. The refined results for several stabilised Zirconia polymorphs at room temperature are summarised in Table 7.2. Local atomic structures of Zr^{4+} and dopant cations in Zirconia solid solutions with Fe_2O_3, Ga_2O_3, Y_2O_3 and Gd_2O_3 were also determined by Li et al [13]. They found that the dopant ionic size determined the preferred location of the oxygen vacancies. Vacancies introduced by oversized dopants such as Y^{3+} and Gd^{3+} are located as nearest neighbours to Zr^{4+} ions, leaving 8-fold co-ordination to dopant cations. Undersized dopants such as Fe^{3+} and Ga^{3+} compete with the Zr^{4+} ions for the oxygen vacancies in Zirconia, resulting in 6-fold oxygen co-ordination and a large disturbance to the surrounding next nearest neighbours.

Table 7.1. Fitting results of Zr for Zirconia polymorphs reported by Li et al [10]. The co-ordination numbers were fixed at the values shown.

Polymorph	Zr-O R (Å)	Zr-O CN	Zr-O σ^2 ($Å^2$)	Zr-Zr R (Å)	Zr-Zr CN	Zr-Zr σ^2 ($Å^2$)
Monoclinic	2.16	7.0	0.0100	3.46 4.01 4.55	7.0 4.0 1.0	0.0036 0.0060 0.0024
Tetragonal	2.10 2.33	4.0 4.0	0.0034 0.0090	3.62	12.0	0.0034
Stabilised Cubic	2.15	7.0	0.0074	3.55	12.0	0.0090

Table 7.2. EXAFS results of Yttria stabilised Zirconias at room temperature [11]. The co-ordination numbers were fixed at the values shown.

Y_2O_3 (mol%)	Shell	Zr K edge R (Å)	Zr K edge CN	Zr K edge σ^2 ($Å^2$)	Y K edge R (Å)	Y K edge CN	Y K edge σ^2 ($Å^2$)
3	Cat-O	2.10	4.0	0.0048	2.33	8.0	0.0080
	Cat-Cat	3.62	12.0	0.0076	3.62	12.0	0.0069
6	Cat-O	2.13	5.0	0.0064	2.33	8.0	0.0088
	Cat-Cat	3.62	12.0	0.0086	3.62	12.0	0.0069
10	Cat-O	2.15	7.0	0.0094	2.33	8.0	0.0088
	Cat-Cat	3.58	12.0	0.0108	3.62	12.0	0.0074
15	Cat-O	2.15	7.0	0.0088	2.33	8.0	0.0094
	Cat-Cat	3.56	12.0	0.0112	3.62	12.0	0.0083
20	Cat-O	2.15	7.0	0.0085	2.32	8.0	0.0108
	Cat-Cat	3.55	12.0	0.0125	3.62	12.0	0.0090

7.2. Experimental

A commercial powder of 8 mol% YSZ, produced by Tosoh, was used. The sample was fired at 1500°C for 48 hours to ensure complete reaction. Data were obtained using the Materials Science station (9.3) at the Daresbury Synchrotron Radiation Source where typical beam conditions were 2 GeV and 100mA. Data were obtained at the Y K absorption edge (17042 eV) and the Zr K absorption edge (18003 eV) between room temperature and 1000°C. Spectra were also obtained for the parent oxides cubic Y_2O_3 and monoclinic ZrO_2.

The first step in analysing the EXAFS spectra was to normalise the data using the program EXCALIB. The data is then background subtracted and Fourier transformed using the program EXBACK. The refinement program EXCURV92 was then used to create and fit a theoretical model to the experimental data. For the refinement, Xalpha phaseshifts were used, the VPI value was set to -4 and the AFAC value was set to 0.8. The cation-cation co-ordination numbers were fixed to 12 and for the Y-edge refinements the first shell co-ordination number was fixed at 8. The Debye Waller factors were refined with the bond distances and E0 until a satisfactory fit was obtained. The individual parameters were then refined separately. The Zr-edge refinements were carried out in the same manner except that the first shell co-ordination environment was initially fixed to a value of 7.7.

7.3. Model Compounds Y_2O_3 and ZrO_2

Y_2O_3 has a cubic unit cell parameter of 10.604 Å and the cations, which have 6-fold oxygen co-ordination, occupy two crystallographically distinct sites in the ratio of 1:3. The Y-O distances range from 2.24 to 2.31 Å with a mean Y-O distance of 2.28 Å. The EXAFS data reflect the average Yttrium structural environment and it has previously been found that resolving the four component Y-O distances is not possible [7]. Similarly for monoclinic ZrO_2, which has unit cell parameters a = 5.145 Å, b = 5.2075 Å, c = 5.3107 Å, α =90°, B = 99.23° and γ = 90°, there are seven different Zr-O distances ranging from 2.05 to 2.29 Å contributing to the one resolvable shell of Zr nearest neighbours in the EXAFS of monoclinic Zirconia. EXAFS not only reflects the

environment of the average cation but also, because of the inverse dependence of the amplitude with R^2 and the tendency of the Debye Waller factor to increase with R, the measured radial distance for a single shell encompassing a large static spread of component distances tends to be weighted accordingly in favour of the shorter distances [7].

7.4. Cation Local Environment in 8 mol% YSZ at 20°C

7.4.1. Local Structure of Yttrium

The X-ray absorption spectra obtained for 8YSZ is shown in Figure 7.1a. The absorption edge at 17042 eV is the Y K edge and the absorption at 18003 eV is the Zr K edge. The Fourier Transform of the Y edge data shown in Figure 7.1b. Analysis of the Y edge was carried out by fixing the co-ordination numbers of the Y-O, Y-Zr and Y-Y shells to their theoretical values of 8, 10.2 and 1.8 respectively. The Debye Waller factor, a, the bond lengths, r, and the E0 parameters were refined. When a satisfactory refinement had been carried out, the co-ordination numbers were allowed to refine together but were constrained so that the Y-cation co-ordinations shells did not deviate from the theoretical value of 12. Refinement carried out in this manner resulted in the Y-Oxygen co-ordination number increasing to 8.1. This same value was obtained by Catlow who fixed the Y-cation co-ordination number to 12. The result of the refinement of the Y edge are shown in Tables 7.3.

Table 7.3. Refined Y edge data for 8YSZ at 20°C.

Shell	Theoretical CN	Refined CN	Average Crystallographic Distance	Refined Distances (r)	Debye Waller Factor (a)
Y - O	8.00	8.1 ± 0.4	2.2253	2.300 ± 0.002	0.0171 ± 0.0007
Y - Zr	10.22	10.2 ± 1.5	3.6336	3.562 ± 0.001	0.0150 ± 0.0003
Y - Y	1.78	1.8 ± 1.1	3.6336	3.654 ± 0.002	0.0040 ± 0.0005

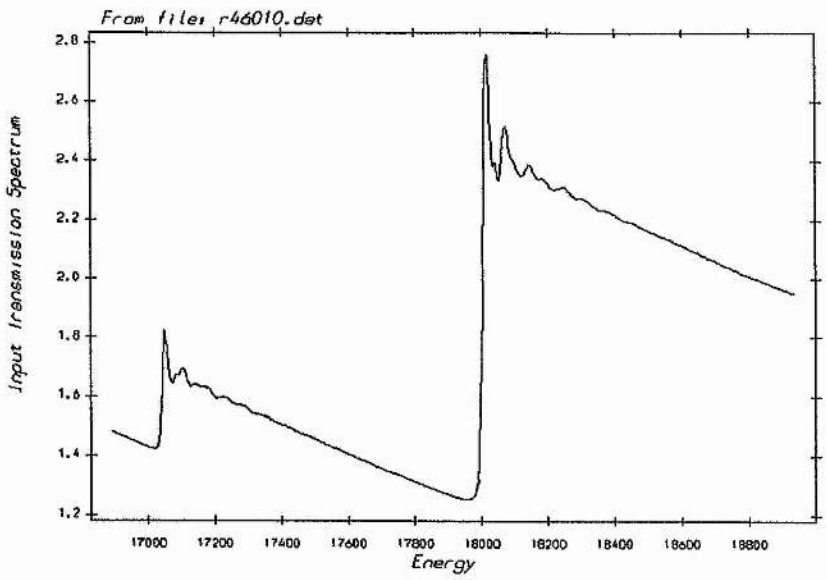

Figure 7.1a. X-ray absorption spectra for the Y K edge and the Zr K edge of 8YSZ.

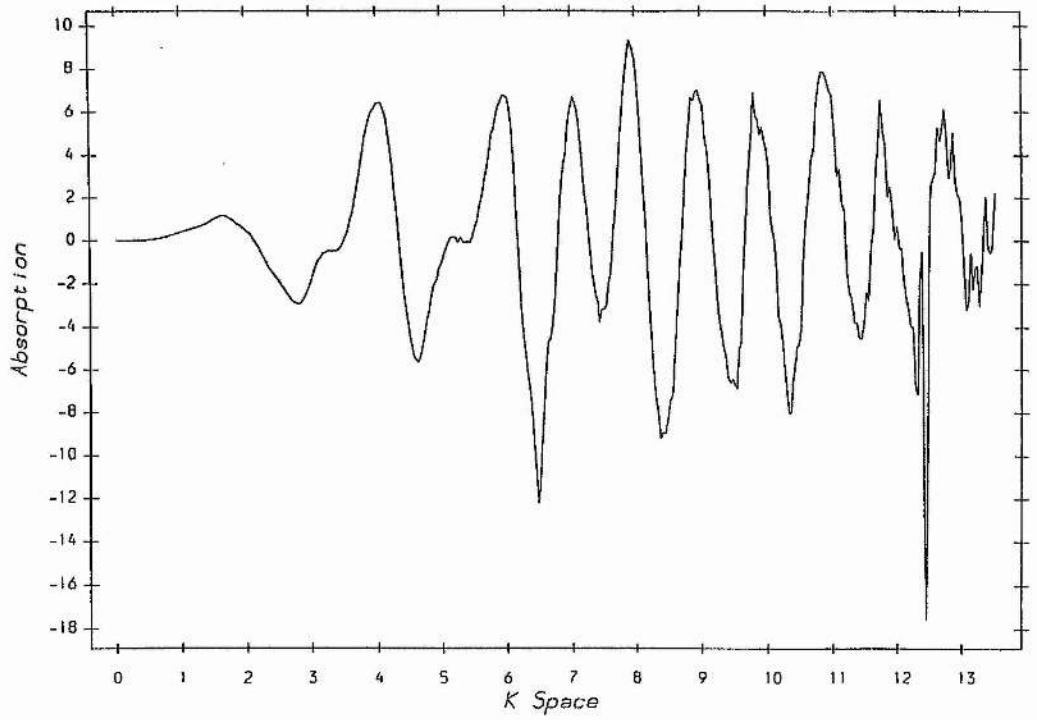

Figure 7.1b. Fourier Transform of Y edge data versus k.

There are some obvious differences between the average crystallographic and measured distances. The refined average bond length for the Y-O shell is 0.0739 Å larger than the expected average crystallographic cation-oxygen bond length for 8YSZ. Catlow et al found that in 18 wt Y_2O_3 stabilised Zirconia (~11 mol% YSZ) the average Y-O distance was 2.28 Å [7]. Li et al reported the same Y-O distance of 2.33 Å for 3, 6, 10, 15 and 20 mol% Y_2O_3 stabilised Zirconia, i.e. the local environment of the Y^{3+} ions in Zirconia was determined to be insensitive to the composition or the phase [11]. Their value is in good agreement with other studies [4-6]. Tuilier et al also reported a similar Y-O mean distance of 2.30 Å [3]. As this distance is larger than that for Y-O in Y_2O_3 (2.28 Å), this implies a higher co-ordination number for the Yttrium ion in stabilised Zirconias, as is reflected in the refined Y-O co-ordination number of 8.1 in this study.

The weighted mean Y-Zr and Y-Y distances are smaller than the average crystallographic Y-cation distances predicted from the unit cell parameter of 8YSZ. The average of the Y-Zr and the Y-Y distances is 3.58 Å. The mean Y-cation value determined by Catlow was 3.59 [7], however Ping et al determined that the Zr-cation and the Y-cation shells both had the same distance of 3.62 Å, i.e. only one shell could be resolved. Catlow did, however, find from the Zr edge EXAFS that the Zr-cation distance was 3.55 Å, which is in good agreement with the Y-Zr distance found in this study. The results of Ping et al are more similar to the Y-Y distance found in this study (which is close to the average crystallographic cation-cation distance) than to the Y-Zr distance found in this study.

Thus the refinement of two cation shells instead of one is possible for 8YSZ at 20°C despite the fact that there is only one Y-cation shell observed in the Fourier Transform. The errors, however, are larger for both the Y-Y co-ordination number than for the co-ordination numbers and radial distances in the two inner shells, which is reasonable due to the lower Y-Y co-ordination number.

7.4.2. Local Structure of Zirconium

The results of the Zr K edge refinements are given in Table 7.4. The first shell was found to contain less than 8 oxygens and the refined value was the same as the

theoretical value of 7.7 for Zr in 8YSZ. This is higher than the value given by Li et al who reported 7 fold co-ordination [10]. Catlow et al found that by allowing the Zr-O co-ordination number to float during refinement, the co-ordination number was only 5.9. They therefore fixed the co-ordination number at the theoretical value of 7.5 for their YSZ refinements. The Zr-O bond length of 2.125 Å is in good agreement with Catlow et al (2.11 Å) and Li et al (2.15 Å) [7, 11]. The average Zr-cation distances is in good agreement with Catlow et al who reported a mean value of 3.55 Å [7].

Table 7.4. Refined Zr edge data for 8YSZ at 20°C.

Shell	Theoretical CN	Refined CN	Average Crystallographic Distance	Refined Distance (r)	Debye Waller Factor (a)
Zr - O	7.70	7.7 ± 0.6	2.2253	2.125 ± 0.016	0.022 ± 0.005
Zr - Zr	10.22	10.2 ± 1.0	3.6336	3.51 ± 0.04	0.035 ± 0.0013
Zr - Y	1.78	1.8 ± 0.7	3.6336	3.57 ± 0.03	0.0061 ± 0.0016

Thus the mean Zr-O bond length of 2.12 Å and the mean Y-O bond length of 2.30 Å are different from each other by 0.18 Å and also differ from the average crystallographic cation-oxygen bond length of 2.2253 Å. Catlow found the difference between the Zr-O and Y-O distances to be 0.17 Å [7]. The Debye Waller factor for the Y-O distance is 0.017 $Å^2$ compared to the larger value of 0.022 $Å^2$ for the Zr-O shell, which indicates that there is greater dispersion in the Zr-O bonds and thus greater structural distortion around the Zirconium cation. The Zr-Zr distance is also significantly lower than the Y-Zr distance and the Y-Y distance, however there is excellent agreement between the Zr-Y distance of 3.5698 Å obtained from the Y edge refinement and the Y-Zr distance of 3.5623 Å obtained from the Zr edge refinement, which indicates that fitting two shells to the single cation-cation peak in the Fourier transform is possible. The amount of disorder is also reflected in the cation-cation Debye Waller factors. The Zr-Zr and Zr-Y values are significantly larger than the Y-Zr and Y-Y values.

These observations indicate that, as has been previously reported, the oxygen vacancies in 8YSZ are preferentially sited adjacent to the Zirconium cations. Thus for this sample of stoichiometry $Zr_{0.852}Y_{0.148}O_{1.9259}V_{0.0741}$, in which the vacancies are preferentially sited adjacent to the Zr^{4+} ions, 37% of the Zr ions are 7 co-ordinate and

thus displaced from the centrosymmetric site. The remaining 63% of the Zr^{4+} ions will be 8-coordinate. Only that fraction of the 8-coordinate Zr^{4+} ions which have 8-coordinate Zr^{4+} or Y^{3+} second neighbours would have close to the expected $\sqrt{2}/2a_o$ cation-cation distance of 3.6336 Å. The remaining 7-coordinate Zr to cation, and 8-coordinate Zr to 7-coordinate Zr cation-cation distances will deviate from this distance, i.e. there will be a large static spread of component Zr-cation distances making up the Zr second shell EXAFS. On the other hand, if Y is 8-coordinate and therefore not displaced too much from the centrosymmetric cation site, only the Y to 7-coordinate Zr contributions to the overall Y-cation EXAFS will deviate from the expected distance of $\sqrt{2}/2a_o$. There are thus 'ordered' and 'disordered' Y-cation distances contributing to the second shell peak. We can thus infer the existence of these different distances in the different values of σ^2 of the second shell for the two cations.

7.5. Temperature Dependence of Cation Local Structure in 8YSZ

7.5.1. Effect of Temperature on the Local Structure of Yttrium

For 8YSZ at 20°C, it was possible to successfully refine the Y-Zr and Y-Y shells separately even though there was only one peak attributable to the Y-cation distance. Refining the data in this manner becomes increasingly difficult with increasing temperature, thus the high temperature data was refined by fitting only one shell of cations around the Yttrium ion and compared to a similarly refined 20°C data set. Refinement of the Y-cation distances for 20, 250, 500, 750 and 1000°C shows that there is a gradual decrease in the Y-cation distance with temperature, even though the unit cell parameter and thus the average crystallographic cation-cation distance increases, Figure 7.2.. The average crystallographic cation-cation distances, determined from the neutron diffraction data in Section 6.3, are included in Figure 7.2 for comparison.

The difference between the average crystallographic Y-cation and actual Y-cation distances increases with temperature, perhaps indicating that the structural distortion of Yttrium increases with temperature. There is an apparent discontinuity in the plot between 750 and 1000°C, however the error for the 1000°C data is large and so the change in slope may not be real. Also, the data at 1000°C is for only one EXAFS

scan whereas all other data points are the average of two scans. The discontinuity may, however, be representative of the fact that at higher temperature the oxygen vacancies are more mobile and thus become increasingly dissociated from the Zirconium ions, i.e. the oxygen vacancies become increasingly statistically distributed between sites first neighbour to Yttrium ions and the Zirconium ions, thus tending to bring the local structural environments of Y closer to that of Zr at higher temperatures. The Y-Oxygen distance also decreases with increasing temperature, Figure 7.3. The Y-Oxygen distance at 750°C is near to the average crystallographic distance calculated from the unit cell parameter which may suggest that as the defects disorder, the Yttrium ions in the Yttrium sublattice take up the average crystallographic positions.

The error bars in Figures 7.2 and 7.3 show that there are obvious changes in the magnitude of the errors with increasing temperature. The errors in the Y-cation distance increase from 0.03 % to 0.3 % by increasing the temperature from 20 to 1000°C. The errors in Y-O distance increase with increasing temperature from 0.06 % to 0.13 %.

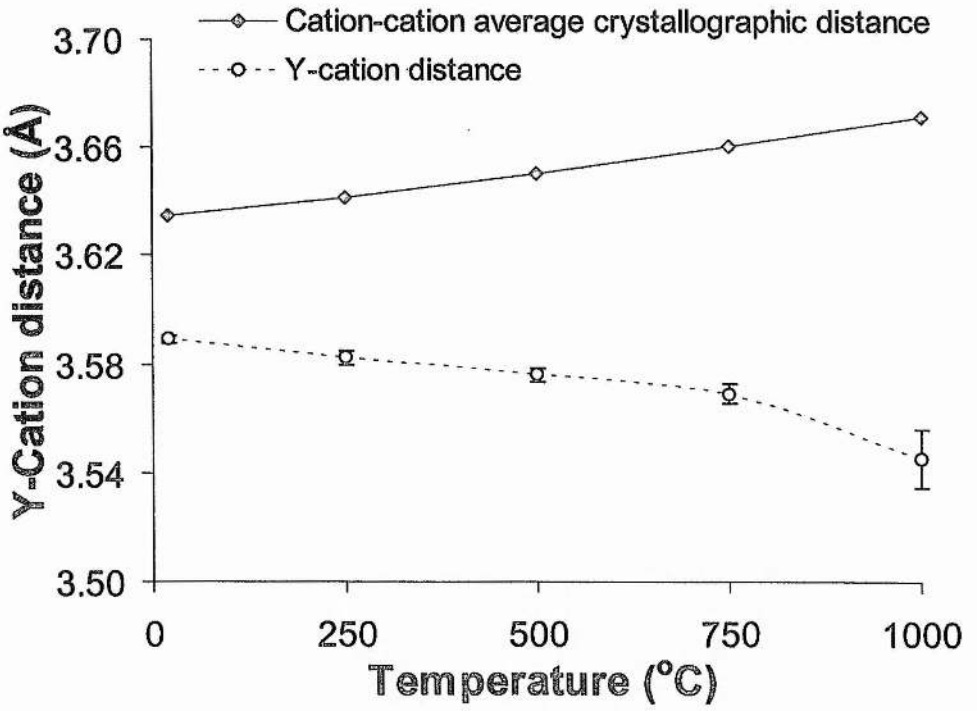

Figure 7.2. Comparison of the actual Y-cation distance with the average crystallographic cation-cation distance in 8YSZ with temperature.

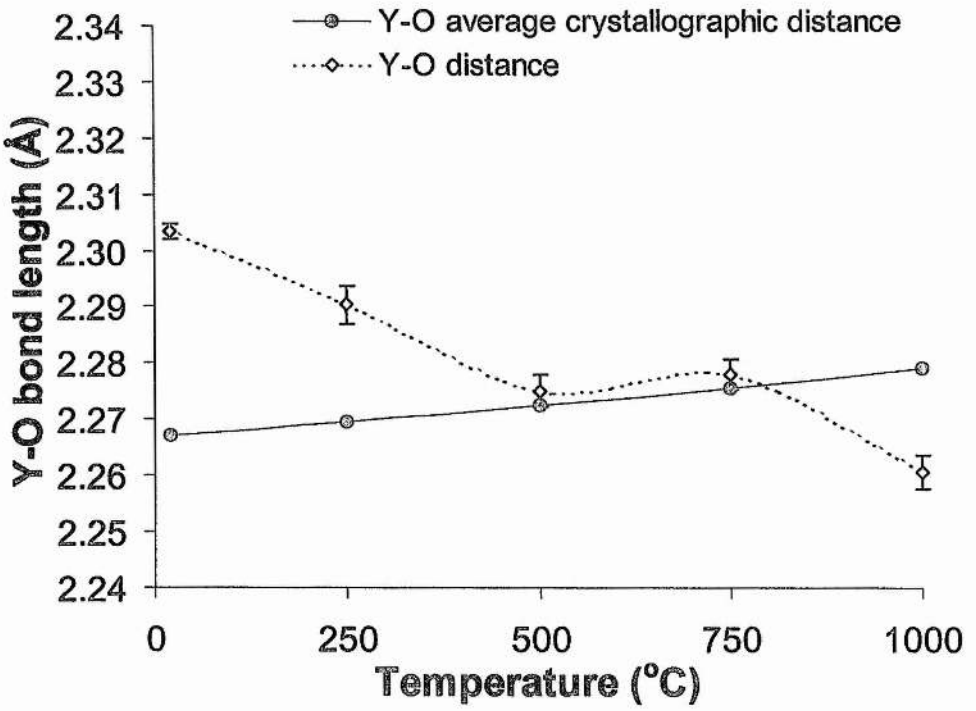

Figure 7.3. Comparison of the actual Y-oxygen bond length with the average crystallographic cation-oxygen bond length for 8YSZ with increasing temperature.

The Debye Waller factors for the Y-O and Y-cation shells for 8YSZ are plotted against temperature in Figure 7.4 an d 7.5 respectively. The Debye Waller factor for the Y-cation shell clearly shows a linear increase in mean-square deviation in the average distance between the absorbing Y ion and the scattering cations with temperature, Figure 7.4. No discontinuity is observed in the Y-cation disorder. This is in good agreement with the trend in cation isotropic temperature factor as determined by high temperature neutron diffraction (Chapter 6) for which no discontinuity was observed with increasing temperature. The errors in the Y-cation Debye Waller factors increase with temperature from 1.6 % at room temperature to 3% at 1000°C.

The Debye Waller factor for the Y-Oxygen shell also increases with temperature, however, there is a slight discontinuity in the plot between 500 and 750°C, Figure 7.5. The Neutron Diffraction studies described in Chapter 6 indicate that there is a discontinuity in the oxygen isotropic temperature factor between 590 and 650°C,

which is indicative of the order-disorder transition that occurs in 8YSZ. It is reasonable to assume that the change in slope observed in the plot of Y-Oxygen Debye Waller factor between 500 and 750°C is also due to the disordering of the oxygen ions occurring in this temperature region. The increase in temperature from 20 to 1000°C results in a slight decrease in the error from 4% at room temperature to 3% at 1000°C.

The structural distortions reflected in the Debye Waller factors are caused by both thermal vibration and static distortions. However without data close to 0K, it is not possible to determine the static contribution to the total displacement as was done for 8YSZ by studying the isotropic temperature factors using Neutron Diffraction, Section 6.3.5.

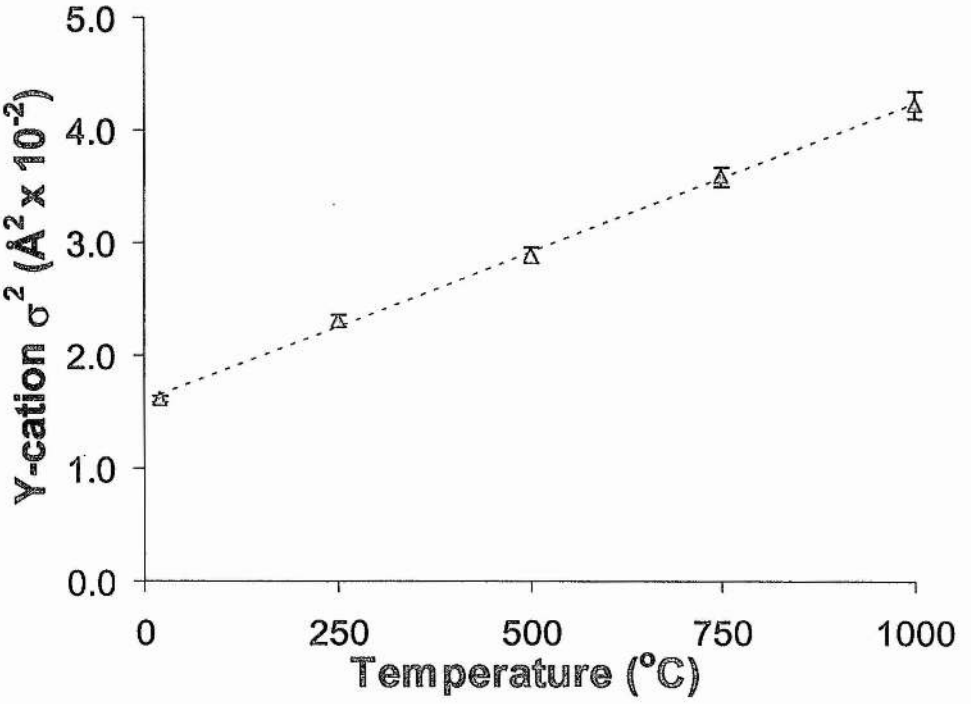

Figure 7.4. Increase in Y-Cation Debye Waller factor with increasing temperature.

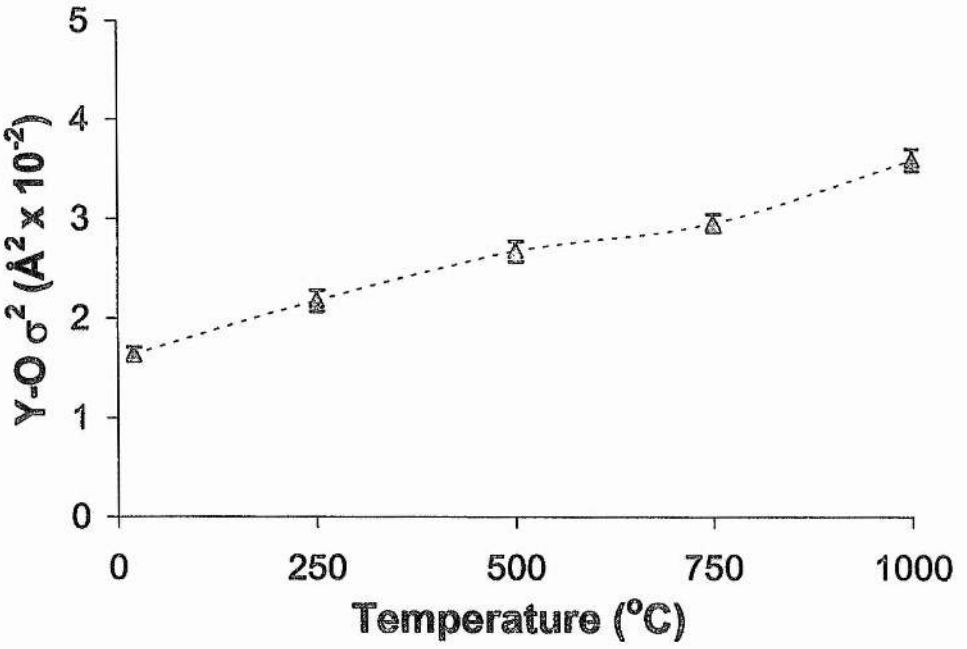

Figure 7.5. Increase in Y-Oxygen Debye Waller factor with increasing temperature.

All of the above data obtained from the Y edge spectra were refined by fixing the Yttrium-Oxygen co-ordination number to 8. This accurately reflects the nearest neighbour environment of Yttrium at low temperatures. However, as the oxygen vacancies are known to become mobile above 550°C, the co-ordination number of the Yttrium cation should decrease and become equal to that of the Zirconium ions. For this reason, all of the data sets described above were also refined with the Y-Oxygen co-ordination number fixed to the theoretical cation-cation value of 7.7. This gave rise to negligible differences in the refined parameters but resulted in small increases in the R factor for all temperatures, indicating that the fit between the experimental data and the fitted model were not as good as for a Yttrium-Oxygen co-ordination number of 8.

7.5.2. Effect of Temperature on the Local Structure of Zirconium

The change in Zr-cation distance with temperature is shown in Figure 7.6. The Zr-cation distance decreases with temperature in a non-linear manner. Fitting a line to the data at 20, 250 and 500°C and another line to the high temperature data results in an intercept at 565°C. Possibly this is linked to the order-disorder transition observed by

Neutron Diffraction (Chapter 6), however, the error at 1000°C is large so no strong conclusion should be drawn.

The change in Zr-Oxygen distance is plotted in Figure 7.7. This plot also shows the same trend as the cation-oxygen and cation-cation distances in that it decreases with increasing temperature. There appears to be a discontinuity between 500 and 750°C data.

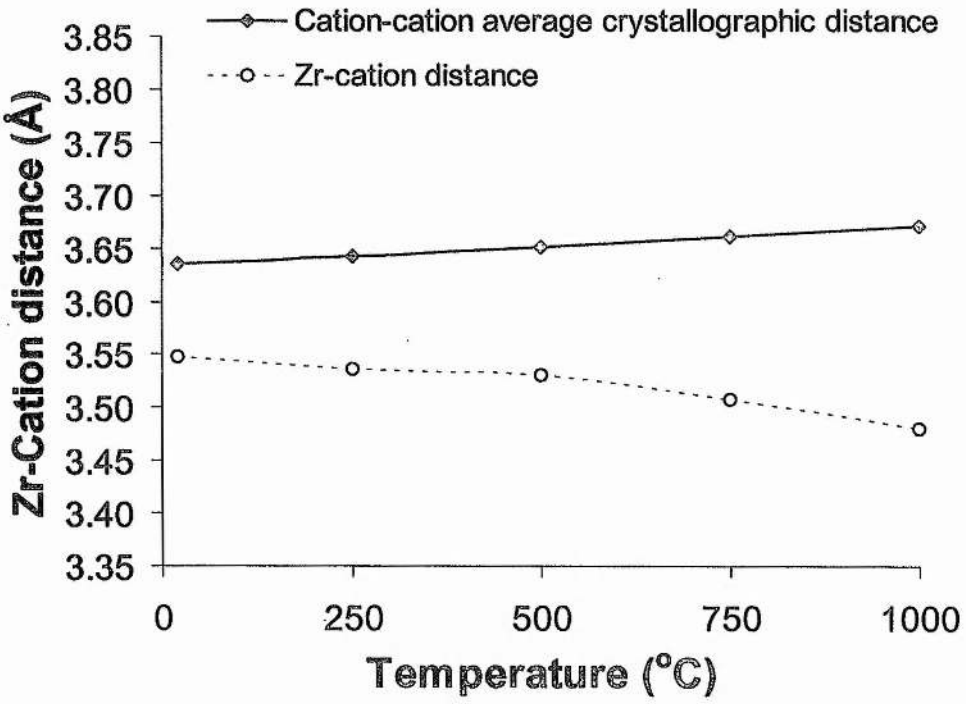

Figure 7.6. Comparison of the actual Zr-cation distance with the average crystallographic cation-cation distance for 8YSZ with increasing temperature.

The Debye Waller factors determined for the Zr-cation and Zr-Oxygen shells are plotted in Figures 7.8 and 7.9 respectively. The plot of Zr-cation Debye Waller factor shows that the disorder increases with temperature and that there is a change in slope between 500 and 750°C. The errors for the Zr-cation data increase from 2.5% at 20°C to 9.8 % at 1000°C. The Zr-Oxygen Debye Waller factor seems to exhibit a large change between 500 and 750°C indicating that there may be a large change in the disorder. The errors for the Zr-Oxygen data vary between 3.4 and 4.8%.

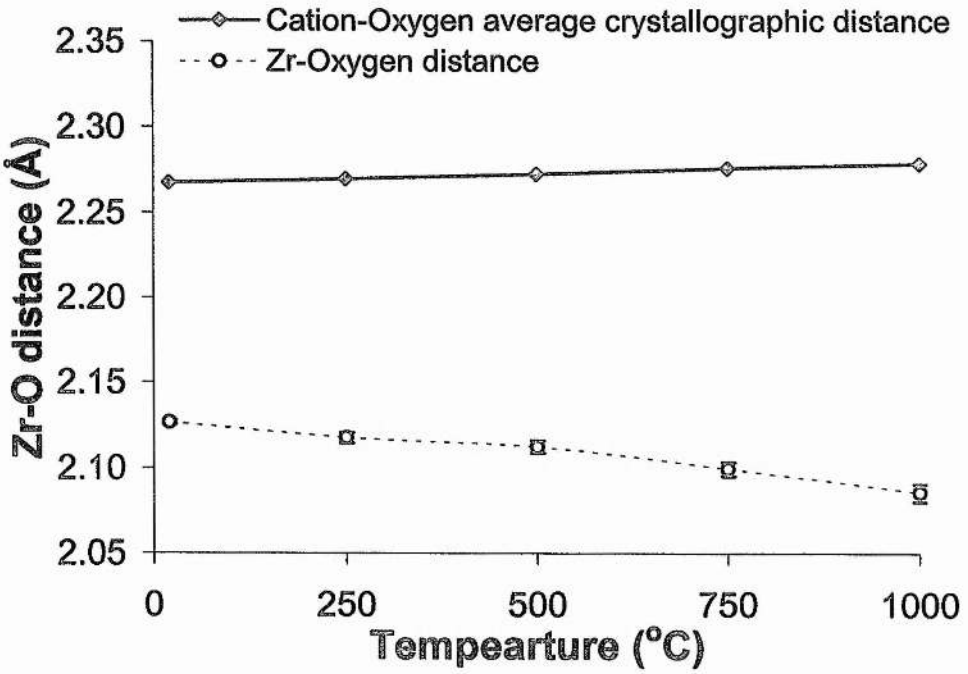

Figure 7.7. Comparison of the measured Zr-oxygen bond length with the average crystallographic cation-oxygen bond length for 8YSZ with increasing temperature.

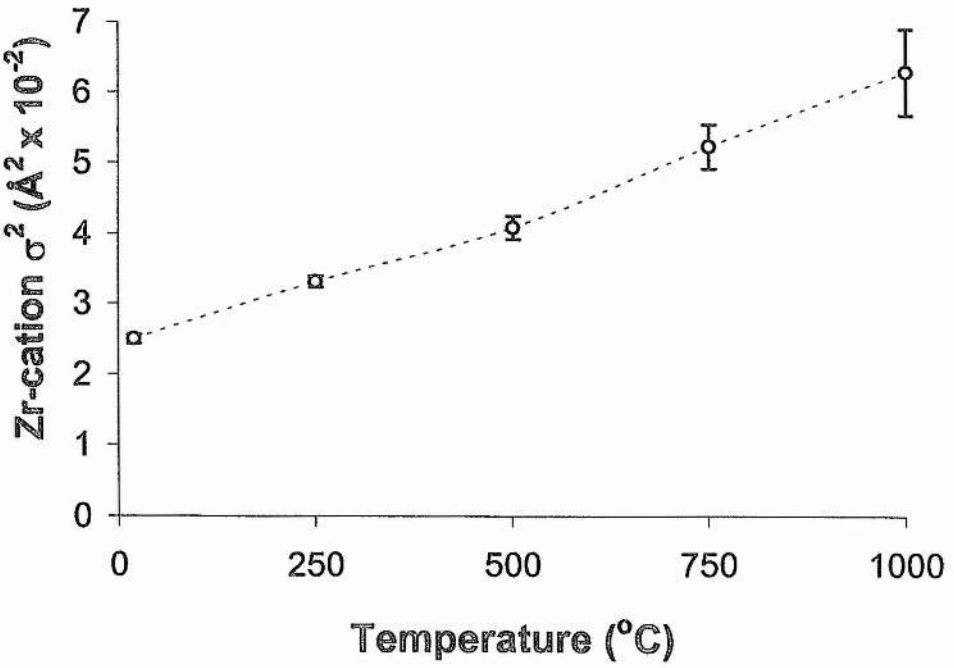

Figure 7.8. Increase in Zr-cation Debye Waller factor with increasing temperature.

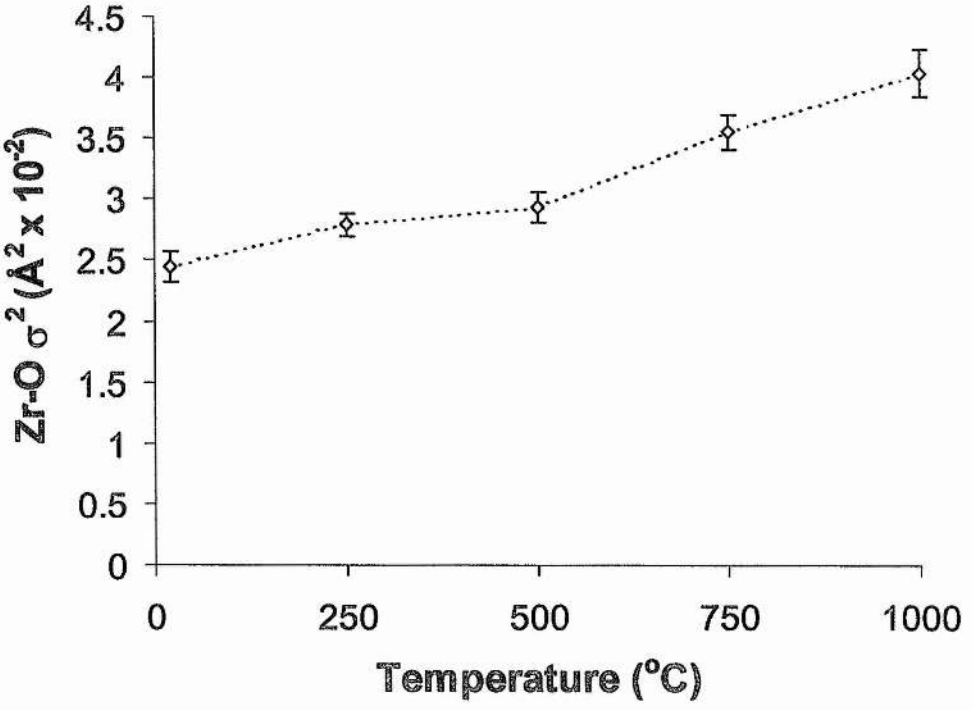

Figure 7.9. Increase in Zr-Oxygen Debye Waller factor with increasing temperature.

The mean Zr-O co-ordination number should in theory increase from 7.7 at low temperatures to 7.85 at high temperatures. By allowing only the Zr-O shell co-ordination number to refine without constraint, similar values to the theoretical values are obtained, Figure 7.10. The co-ordination numbers for Zr-O at 20 and 250°C are both 7.70 and 7.75 respectively. Increasing the temperature to 500°C results in a small increase in oxygen co-ordination to 7.78. At 750 and 1000°C the Zr-Oxygen co-ordination number has increased to near theoretical values of 7.81 and 7.82 respectively. The calculated errors vary from between 0.57 to 0.72 (7.4 to 9.2%), much larger than the changes themselves.

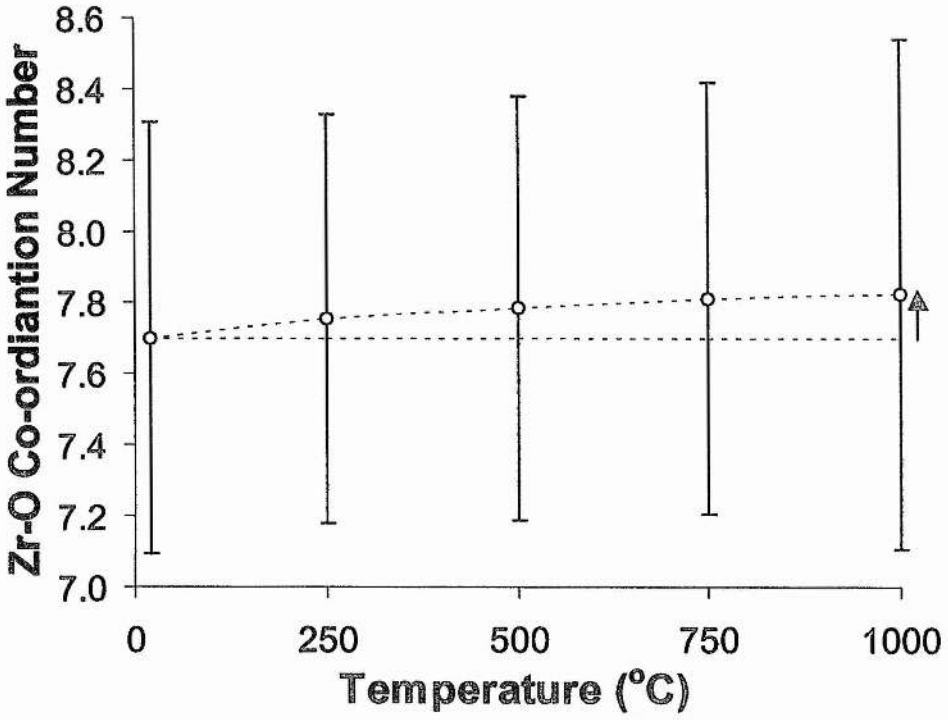

Figure 7.10. Increase in Zr-O co-ordination number with increasing temperature.

7.6. Conclusion

Catlow explained the apparent contraction in the Y-O distance and the decrease in the Y-cation distance with temperature as being due to the EXAFS being dominated by the sharpest feature in the radial distribution function. This is dependent upon the disorder within a shell being represented by a Gaussian spread of distances via the Debye Waller term $\exp(-2\sigma^2k^2)$. This assumption is clearly not a valid description of the static displacement arising in the lattice in response to an anion vacancy nor can it accommodate anisotropic thermal motions at elevated temperatures [7]. The increasing asymmetry in the radial distribution function manifests itself as an apparent contraction in the measured distance between the Yttrium ion and the backscatterer, i.e. it is the form of the distributions that change more so than the static bond distances. Catlow et al thus measured increasing disorder by plotting peak area against temperature rather than using the approach used in this study [7].

In this study EXAFS spectroscopy has been used to determine the change in local environment of the Y and Zr cations in 8YSZ with temperature. Plots of Y-cation, Y-Oxygen, Zr-cation and Zr-Oxygen distance versus temperature all show a change in slope between 500 and 750°C which are indicative of the order-disorder transition which is known to occur in that temperature region.

The changes in Debye Waller factor for the Y-Oxygen, Zr-cation and Zr-Oxygen shells also indicate that there is a transition in the temperature region 500-750°C. The fact that there is no change in slope observed in the Y-cation Debye Waller factor but that there is in the Zr-cation Debye Waller factor may simply be due to the large differences in the concentration of the ions, i.e. the changes occurring in the Zr shells will be more easily detected due to the higher concentration of Zr. The oxygen co-ordination environment of Yttrium could not be successfully refined and always had a tendency to increase to a value greater than 8 and so the co-ordination number was always fixed at the theoretical value of 8.

The change in the oxygen co-ordination environment of Zirconium with temperature was detected despite the very small theoretical changes which were expected to occur. Although the errors are large in comparison to the very small change in co-ordination number, all data were refined in the same manner and the Zr-O co-ordination number was allowed to refine freely.

In summary, the main points are that M-O and M-M distances are different to those predicted from the average crystallographic structure. Differences in M-M may reflect the radial distribution function, however, Zr-O bond lengths are much smaller and Y-O bond lengths much larger than expected. The Y-O distances decrease to those expected from crystallography whereas the Zr-O distances do not approach the crystallographic values at all. This strongly indicates that Y-O local order breaks down but that Zr-O order does not. $Y_2Zr_2O_7$ would not exhibit these changes as a function of temperature and would thus confirm this hypothesis.

7.7. References

[1] T. M. Hayes and J. B. Boyce, Solid State Physics, 37, 173-384 (1984) [3]

[2] P. A. Lee, P. H. Citrin, P. Eisenberger and B. M. Kincaid, Rev. Mod. Phys. 53[4] 769-803 (1981)

[3] A. I. Goldman, E. Canova, Y. H. Kao, W. L. Roth and R. Wang, in EXAFS and Near Edge Structure III, edited by K. O. Hodgson, B. Hedman and J. E. Penner-Hahn (Springer-Verlag, New York, 1984), pp. 442-444

[4] M. H. Tuilier, J. Dexpert-Ghys, H. Dexpert, and P. Lagarde, J. Sol. State Chem. 69, 153 (1987)

[5] H. Morikawa, Y. Shimizugawa, F. Marumo, T. Harasawa, H. Ikawa, K. Tohji, and Y. Udagawa, J. Jpn. Ceram. Soc. 96, 253 (1988)

[6] Z. J. Shen, T. K. Li, K. Q. Lu and Y. Q. Zhao, J. Chin. Silic. Soc. 16 270 (1988)

[7] C. R. A. Catlow, A. V. Chadwick, G. N. Greaves and L. M. Moroney, J. Am. Ceram. Soc. 69 272 (1986)

[8] D. Komyoji, A. Yoshiasa, T. Moriga, S. Emura, F. Kanamaru and K. Koto, Solid state Ionics 50, 291 (1992)

[9] B. W. Veal, A. G. McKale, A. P. Paulikas, S. J. Rothman, and L. J. Nowicki, Physica B 150, 234 (1988)

[10] P. Li, I-W. Chen and J. E. Penner-Hahn, Phys Rev B, 48[14] 10063-73 (1993)

[11] P. Li, I-W. Chen and J. E. Penner-Hahn, Phys Rev B, 48[14] 10074-81 (1993)

[12] P. Li, I-W. Chen and J. E. Penner-Hahn, Phys Rev B, 48[14] 10082-89 (1993)

[13] P. Li and I-W Chen, J. Am. Ceram. Soc., 77[1] 118-28 (1994)

CHAPTER 8

Conclusions

There were essentially three aims of this research. The first was to determine the effect of TiO_2 doping on the electrical properties of Zirconias stabilised in the face centred cubic structure by the cubic oxides Gd_2O_3 and Y_2O_3. The second was to determine the effect of Al_2O_3 additions on the ionic conducting properties of 8 mol% Yttria stabilised Zirconia and the third was to determine the extent of structural distortion caused by short range ordering in 8 mol% Yttria stabilised Zirconia.

8.1. Phase Relations and Electrical Conductivity in the Ternary System ZrO_2 - Y_2O_3 - TiO_2

The determination of the ternary phase diagram ZrO_2-Y_2O_3-TiO_2 was carried out by preparing a large number of ternary compositions by doping Y_2O_3 stabilised Zirconias with TiO_2. This was carried out by standard solid state mixing of the three oxides, sintering at 1500°C until complete reaction had occurred and then rapidly cooling the samples. The study concentrated particularly on the single phase compositions containing low Yttrium and high Titanium concentrations. These compositions required ball milling to achieve phase purity. This low Yttrium, high Titanium region is where one would expect the optimum mixed ionic and electronic conducting properties to occur for this system.

A large face centred cubic region with the cubic fluorite structure was determined. X-ray diffraction showed that up to 18 atom% Ti^{4+} dissolved substitutionally into the cubic fluorite lattice for Zirconias stabilised by Yttrium contents between 15 and 20 atom%. No solid solution was found to exist between the cubic fluorite ZrO_2-Y_2O_3 system and the pyrochlore compositions in the Y_2O_3-TiO_2 system. The experimental phase diagram determined in this study was found to differ considerably from the phase diagram calculated by Yokokawa et al [1].

The ternary system was conveniently divided into four regions of high oxide ion conductivity. The maximum oxide ion conduction determined for this system was 10 Sm^{-1} for the composition 8 mol% YSZ. The ionic conductivity of the Yttria stabilised Zirconia system was found to decrease rapidly with increasing Y_2O_3, increasing TiO_2 and both increasing Y_2O_3 and TiO_2 content. The TiO_2 content was found to have a particularly deleterious effect on ionic conduction due to the effect of the relatively

small Ti^{4+} ion. A straightforward analysis of the 'trapping' effect of the relatively small Ti^{4+} ion on the oxygen vacancies was used to predict a rapid decrease in oxygen ion conductivity with increasing titanium concentration. The predicted decrease in conductivity was closely reproduced experimentally. It was found that almost 50% of the conductivity was lost by the addition of only 4 atom% titanium. This is approximately the concentration of titanium ions required to theoretically 'trap' all of the oxygen vacancies thus allowing all Ti^{4+} to assume its preferred 6-fold oxygen co-ordination.

Electronic conduction was introduced into the TiO_2 doped Yttria stabilised Zirconias at low oxygen partial pressures due to the formation of Ti^{3+}. However, the maximum electronic conductivity for this system, i.e. 20 Sm^{-1} for the compositions containing 18 atom% Titanium, is not sufficient for TiO_2 doped YSZ to become a viable alternative to Ni/YSZ cermets as Solid Oxide Fuel Cell anode materials. The electronic component of the mixed conductivity was found to follow a $P(O_2)^{1/4}$ dependence at low oxygen partial pressures.

The effect of density on the mixed conducting properties of TiO_2 doped YSZ has also been determined and has been found to have a major influence on both the electronic and ionic conductivities. The electronic conductivity undergoes large hysteresis effects in dense samples which have poor ionic conducting properties. This was shown to be related to the poor oxygen ion transport in highly Titanium doped samples and the resulting difficulty in re-oxidising the sample after reduction. The ionic conductivity was also shown to be affected considerably by porosity and the extent to which the data for porous samples can be corrected for density was investigated and found to be in excellent agreement with the value determined in a previous study by Bluementhal et al [2].

8.2. The Ternary System ZrO_2 - Gd_2O_3 - TiO_2

The face centred cubic region of the ZrO_2-Gd_2O_3-TiO_2 phase diagram was found to be much larger than the single phase fluorite region determined in the ternary system ZrO_2-Y_2O_3-TiO_2. It also differed in that a complete solid solution was formed between the binary systems ZrO_2-Gd_2O_3 and G_2O_3-TiO_2. The face centred cubic region exhibited

the pyrochlore structure for near stoichiometric compositions and exhibited the fluorite structure for high levels of deviation from $Gd_2M_2O_7$ stoichiometry. The transition between the pyrochlore and fluorite regions was shown to be continuos by plotting the ratio of the superstructure (311) reflection to the fluorite (111) reflection. No evidence of a two phase region between the pyrochlore and fluorite regions was found indicating that the two structures are very closely related and differ only in the extent of ordering. This transition between the pyrochlore and fluorite structure has been related to the amount of ordered pyrochlore microdomains and disordered fluorite microdomains within these single phase materials.

The highest ionic conductivity of this system is one order of magnitude lower than 8 mol% YSZ, i.e. 1 Sm^{-1}. The ionic conductivity showed slightly different behaviour to the ZYT system. The maximum conductivity was found to occur for the stoichiometric pyrochlore composition $Gd_2Zr_2O_7$ which was near the centre of the face centre cubic region. This contrasts with the ZrO_2-Y_2O_3-TiO_2 system where the maximum conductivity was found to be near the edge of the face centred cubic region. Increases and decreases in Gd_2O_3 content of the stabilised ZrO_2 resulted in a decrease in ionic conductivity despite the increase in disorder with increasing deviation from stoichiometry. The increase in TiO_2 content to the cubic stabilised compositions showed the same effect as TiO_2 addition to the ZrO_2-Y_2O_3 system in that the ionic conductivity rapidly decreased. This can be related to the fact that the small Titanium ions force the pyrochlore ordering to occur much more readily than occurs in the ZrO_2-Y_2O_3 system where the similar ionic radii of Zr^{4+} and Y^{3+} results in a highly disordered system.

The electronic conducting properties increased with increasing TiO_2, however, the electronic conductivity was poorer than for the ZrO_2-Y_2O_3-TiO_2 system indicating that compositions within this system are also unsuitable for anode materials in Solid Oxide Fuel Cells. However, due to the nature of the pyrochlore structure, there is scope to further develop this system by doping with other ions which could improve the ionic and/or electronic conductivity. In principle it would be possible to create an entire electrochemical system with anode, electrolyte and cathode based on the same pyrochlore system. Differing levels of cation doping and non-stoichiometry could be used to control the different properties of each component material [3].

8.3. Effect of Alumina Additions on the Electrical Properties of 8 mol% Yttria-Stabilised Zirconia

In the study of the effect of alumina addition on the conductivity of 8 mol% YSZ, an Al_2O_3 powder of relatively large particle size was added to a commercial 8 mol% YSZ in quantities between 0 and 23 wt%. The multiphase alumina was found to irreversibly transform to the α phase (corundum) above 1000°C and remain essentially as a second phase. The composite materials were found to be of relatively poor percentage theoretical density due to the large particle size of the alumina and the relatively low temperatures used (<1600°C) which resulted in poor sintering.

The materials were characterised by A.C. impedance spectroscopy and X-ray diffraction. Powder X-ray diffraction indicated that less than 1 wt% (1.2 mol%) Al_2O_3 dissolves into the cubic fluorite 8YSZ structure. The solubility limit of Al_2O_3 into the 8YSZ was initially detected by the very small decrease in the unit cell parameter, equal to 0.12% of the unit cell parameter for 8YSZ. The low solubility of Al_2O_3, presumably due to the small ionic radii of Al^{3+}, was also detected by low temperature impedance studies. The bulk conductivity at 300°C decreased by almost 40% upon addition of up to 1wt% Al_2O_3. The solubility limit was also detectable in the bulk capacitance at 300°C. The decrease in bulk capacitance was equal to ~1pFcm^{-1}. The solubility limit was also detectable by the change in slope in the capacitance versus composition plot. Increasing Al_2O_3 content below the solubility limit caused a change in capacitance which differed in slope from the decrease in capacitance caused by an increase in porosity above the solubility limit.

The susceptibility of 8YSZ to hydrothermal degradation was investigated and the degradation in ionic conductivity was found to decrease with increasing Al_2O_3 content. The degradation in conductivity was found to be substantially reduced by around 1wt% alumina and then remained fairly constant above this value. Thus this study has shown that Al^{3+} has a stabilising effect on 8YSZ similar as an increase in Y^{3+} by dissolving substitutionally into the cubic matrix. This stabilising of the cubic structure could result in lower costs for the solid oxide fuel cell electrolyte, i.e. rather than using 8 mol% YSZ and alumina, up to 1mol% of which will dissolve into the

8YSZ, it would be cheaper to use a slightly lower quantity of Yttria so that the total concentration of the aliovalent dopants Y^{3+} and Al^{3+} was between 8.5 and 9mol%. This range was recommended in a previous ageing study of YSZ by Gibson et al [4].

The conductivity at 1000°C of the 8YSZ to which Al_2O_3 had been added was found to remain essentially constant at ~10 Sm^{-1} for Al_2O_3 contents of up to 10wt%. The conductivity of composites with higher alumina content rapidly decreased with further additions due to the increases in porosity, cracking and the breakdown in conduction pathways in the grains. The high and low temperature impedance studies and the degradation study suggests that the optimum range for alumina addition to 8YSZ, in terms of electrical performance is between 5 and 10wt% alumina. However, the processing of these composite materials had not been optimised, thus optimisation of the processing and sintering conditions and the use of an Al_2O_3 powder which had a much finer grain size than that used in this study may allow more alumina to be added to the 8YSZ without such extensive deleterious effects on the density and conductivity. The most recent study of alumina additions to YSZ suggested that around 30 mol% alumina would make a significant difference to the solid oxide fuel cell electrolyte plates [5].

8.4. Neutron Diffraction Studies of 8 mol% YSZ ($Zr_{0.8515}Y_{0.1485}O_{1.926}$)

High temperature neutron diffraction studies of the crystal structure of 8YSZ, which has an average cubic fluorite structure, has shown that the change in activation energy for ionic conduction that occurs between 550 and 650°C is structural in origin. The structural changes that occur can be related to an order-disorder transition. At low temperatures, i.e. below 550°C, the oxygen ions are associated with a particular cation. Diffuse scattering was observed at low temperatures due to the microdomains of local order. Increasing the temperature results in the oxygen ions becoming highly mobile and thus are no longer associated with any particular cation but are instead disordered throughout the structure. This resulted in no fluorite forbidden reflections being observed as diffuse scattering. This order-disorder transition was observed by a change in the slopes of the Oxygen isotropic temperature factor, the unit cell parameter and the weighted profile residual factor as was reported by Irvine et al [6].

The parameters determined from neutron diffraction of Zirconias stabilised in the cubic structure with higher Y_2O_3 contents were also compared with electrical properties. A gradual increase in the Oxygen isotropic temperature factor with increasing Yttria suggests that the ordered microdomains either increase in number or become larger so that eventually, the oxygen ions must pass through the ordered microdomains rather than through the disordered regions.

Low temperature studies of stabilised Zirconias showed that at low temperatures there is significant static displacement of the cations and anions from their ideal fluorite positions. There is also some distortion in the thermal isotropic temperature factor at low temperatures due to the zero point energy of the ions. Thus at low temperatures the local structure of the ions differ considerably from the average long range, crystallographic structure.

8.5. EXAFS Spectroscopy Studies of Cation Co-ordination Environments in 8YSZ

Extended X-ray absorption fine structure spectroscopy has been used to show that the oxygen vacancies are associated with the smaller Zirconium ions rather than the Yttrium ions in 8YSZ. The co-ordination numbers of the cations could not be determined accurately due to the intrinsically high errors involved in EXAFS analysis. Two and three shell models were determined for the room temperature data despite the fact that only two shells are observed in the Fourier Transforms. The three shell model was found to give a slightly lower R factor than the two shell model indicating that a better fit was achieved.

Fitting a three shell model to the experimental data became increasingly difficult as the temperature was increased, therefore for comparison of data between 20 and 1000°C only the two shell models were used to fit the data. The model fitting was carried out using Zirconium as the dominant cation it was the most abundant ion. The bond lengths and cation-cation distances were found to differ considerably from the average crystallographic distances indicating that there are significant distortions on the local scale. Changes were found to occur in the cation-oxygen bond lengths, cation-

cation distances and the Debye Waller factors between 500 and 750°C, i.e. in the same temperature region as the order-disorder transition determined by neutron diffraction. Thus EXAFS spectroscopy indicated that there are changes in the local structure of the cations as the oxygen ions disorder with increasing temperature.

8.6. References

[1] Yokokawa H, Horita T., Sakai N., Dokiya M., Van Herle J. and Kim S. G. , Denki Kagaku, 1996, Vol.64, No.6, pp.690-691

[2] F. S. Brugner and R.N. Bluementhal, J. Am. Ceram. Soc., 54 (1971) 57

[3] P.K. Moon and H.L. Tuller, in: Solid Oxide Fuel Cells, Proc. 1st Intern. Symp. Hollywood, FL, 1989, Vol. 89-11, ed. S.C. Singhal (Electrochem. Soc., Pennington, NJ, 1989) p. 30.

[4] I.R. Gibson, G.P. Dransfield, J.T.S. Irvine, J. Eur. Ceram. Soc., 18[6] (1998) 661-667

[5] A. Yuzaki, A. Kishimoto and Y. Nakamura, Solid state Ionics 109 (1998) 273-277

[6] I.R. Gibson and J.T.S. Irvine, J. Mater. Chem., 6(5) (1996) 895-898